

Copyright Warning & Restrictions

The copyright law of the United States (Title 17, United States Code) governs the making of photocopies or other reproductions of copyrighted material.

Under certain conditions specified in the law, libraries and archives are authorized to furnish a photocopy or other reproduction. One of these specified conditions is that the photocopy or reproduction is not to be “used for any purpose other than private study, scholarship, or research.” If a user makes a request for, or later uses, a photocopy or reproduction for purposes in excess of “fair use” that user may be liable for copyright infringement,

This institution reserves the right to refuse to accept a copying order if, in its judgment, fulfillment of the order would involve violation of copyright law.

Please Note: The author retains the copyright while the New Jersey Institute of Technology reserves the right to distribute this thesis or dissertation

Printing note: If you do not wish to print this page, then select “Pages from: first page # to: last page #” on the print dialog screen



The Van Houten library has removed some of the personal information and all signatures from the approval page and biographical sketches of theses and dissertations in order to protect the identity of NJIT graduates and faculty.

ABSTRACT

STATISTICAL STUDY OF SOLAR RADIO BURSTS

by
Gelu-Marius Nita

The peak flux distribution of 40 years of solar radio burst data recorded by NOAA, as a function of frequency and time over a wide range of frequencies, was investigated to quantify the potential impact of radio bursts on wireless systems. Tables of fit parameters, which can be used to find burst occurrence rates in a number of frequency ranges, are presented. The typical power-law index of number density distribution, ~ -1.8 , is similar to that found in many hard X-ray studies. Significant changes were found in power-law index with frequency. The results may be useful for designers of current and future wireless systems.

A set of 412 flares detected by OVSA during 2001–2002 was analyzed. Distributions of the spectral parameters were investigated and the correlations between them discussed, adding to the understanding of particle acceleration and flare energetics. The observed microwave bursts were classified according to their spectral and temporal characteristics, and the natural limits of different emission mechanisms were empirically inferred.

An analysis of spectral peak evolution of microwave bursts found that, generally, the peak frequency is very well correlated with the intensity of microwave bursts, in agreement with theoretical predictions following from the gyrosynchrotron self-absorption origin of the low frequency turnover of the spectrum. However, for some events the peak frequency increase is much smaller than expected or even absent. It was found that the peak frequency almost always increases on the late decay phase of strong long duration events. For 60% of the cases, the spectral dynamics of peak frequency around the peak time is caused by gyrosynchrotron self-absorption, but in

70% of cases, Razin suppression is dominant at some time during the burst, especially on the early rise and late decay phases.

The properties of decimetric spike bursts occurring simultaneously with microwave gyrosynchrotron continuum bursts were analyzed. The spike cluster flux density was found to be tightly correlated with the high-frequency spectral index of the microwave continuum for each event, while the flux-to-flux correlation may not be present. It was concluded that the findings strongly support the electron cyclotron maser mechanism of spike emission.

STATISTICAL STUDY OF SOLAR RADIO BURSTS

by
Gelu-Marius Nita

**A Dissertation
Submitted to the Faculty of
New Jersey Institute of Technology and
Rutgers, The State University of New Jersey - Newark
in Partial Fulfillment of the Requirements for the Degree of
Doctor of Philosophy in Applied Physics**

Federated Department of Physics

January 2004

Copyright © 2004 by Gelu-Marius Nita

ALL RIGHTS RESERVED

APPROVAL PAGE

STATISTICAL STUDY OF SOLAR RADIO BURSTS

Gelu-Marius Nita

Dr. Dale E. Gary, Dissertation Advisor
Professor of Physics, NJIT

Date

Dr. Ken Chin, Committee Member
Professor of Physics, NJIT

Date

Dr. Philip Goode, Committee Member
Distinguished Professor of Physics, NJIT

Date

Dr. Haimin Wang, Committee Member
Professor of Physics, NJIT

Date

Dr. Louis J. Lanzerotti, Committee Member
Distinguished Research Professor, NJIT

Date

Dr. Zhen Wu, Committee Member
Associate Professor of Physics, Rutgers University

Date

BIOGRAPHICAL SKETCH

Author: Gelu-Marius Nita
Degree: Doctor of Philosophy
Date: January 2004

Undergraduate and Graduate Education:

- Doctor of Philosophy,
New Jersey Institute of Technology, Newark, USA, 2004
- Bachelor of Science,
University of Bucharest, Romania, 1987

Major: Applied Physics

Publications:

- Fleishman, G. D., Gary, D. E., Nita, G. M. "Decimetric Spike Bursts versus Microwave Continuum" 2003, *The Astrophysical Journal*, 593, 571.
- Shneidman, V. A., Nita, G. M. "Nucleation Preexponential in Dynamic Ising Models at Moderately Strong Fields" 2003, *Phys. Rev. E*, 68, 021605.
- Lee, J., Gallagher, P. T., Gary, D. E., Nita, G. M., Choe, G. S., Bong, S., Yun, H. S., "Extreme-Ultraviolet, and Microwave Observations of the 2000 March 22 Solar Flare and Spontaneous Magnetic Reconnection" 2003, *The Astrophysical Journal*, 585, 524L.
- Nita, G. M., Gary, D. E., Lanzerotti, L. J., Thomson, D. J. "The Peak Flux Distribution of Solar Radio Bursts" 2002, *The Astrophysical Journal*, 570, 423.
- Shneidman, V. A., Nita, G. M. "Modulation of the Nucleation Rate Preexponential in a Low-Temperature Ising System" 2002, *Phys. Rev. Lett.*, 89, 5701S.
- Cretu, N., Delsanto, P. P., Nita, G., Rosca, C., Scalerandi, M., Sturzu, I. "Ultrasonic Pulse Propagation in Inhomogeneous One-Dimensional Media" 1998, *The Journal of the Acoustical Society of America*, 104, 57C.

Cretu, N., Nita, G., Sturzu, I., Rosca, C. "A Semianalytical Method for Studying the Acoustic Pulse Propagation in Elastic Inhomogeneous 1-D Media" in *Integral Methods in Science and Engineering 1998.*, 107-112, Chapman & Hall in The Pitman Research Notes in Mathematical Series.

Nita, G., "About a Conservation Law Specific to the Homogeneous Linear Differential Equation of 2nd Order with Variable Coefficients" 1997, Bulletin of the Transilvania University of Brasov 4(39), 41.

Cretu, N., Nita, G. "On The Mathematical Method of Filter Disturbing Voltages in Hall Effect Measurements" 1995, Bulletin of the Transilvania University of Brasov 2(37), 61.

Presentations:

Melnikov, V. F., Gary, D. E., Nita, G. M. "Spectral Dynamics of Solar Broadband Microwave Bursts", 34th Meeting of the Solar Physics Division, John Hopkins University, Columbia, MD, 16-20 June 2003.

Nita, G. M., Gary, D. E., Lee, J. "Statistical Study of Flare Radio Spectra obtained with OVSA", 34th Meeting of the Solar Physics Division, John Hopkins University, Columbia, MD, 16-20 June 2003.

Lee, J., Gallagher, P. T., Gary, D. E., Nita, G. M., Choe, G. S. "Ha , EUV, and Microwave Observations of a Large Flare as Evidence for Spontaneous Magnetic Reconnection", 34th Meeting of the Solar Physics Division, John Hopkins University, Columbia, MD, 16-20 June 2003.

Shneidman, V. A., Nita, G. M., "Modulation of the Nucleation Rate Pre-Exponential in Low-Temperature Dynamic Ising Systems", Annual American Physical Society March Meeting 2003, Austin, TX, 3-7 March 2003.

Gary, D. E., Lanzerotti, L. J., Nita, G. M., Thomson, D. J. "Solar Radio Bursts and their Effects on Wireless Systems", 200th Meeting of the American Astronomical Society, Albuquerque, NM, 2-6 June 2002.

Gary, D. E., Schmahl, E. J., Nita, G. M. "First Results of Joint OVSA and HESSI Observations", 200th Meeting of the American Astronomical Society, Albuquerque, NM, 2-6 June 2002.

Lanzerotti, L. J., Gary, D. E., Nita, G. M., Thomson, D. J., MacLennan, C. G., "Noise in Wireless Systems from Solar Radio Bursts", XXVII General Assembly, Nice, France, 21-26 April 2002.

Nita, G. M., Gary, D. E., Lanzerotti, L. J., Thomson, D. J., "Effect of Solar Bursts on Wireless Communication Systems", Boulder, Co, 16-19 April 2002.

Nita, G, Gary, D. E., Lanzerotti, L. J., Thomson, D. J. "40 Years of Solar Microwave Burst Flux Measurements", American Geophysical Union, Spring Meeting 2001, Boston, MA, 29 May–2 June 2001.

Cretu, N., Nita, G., Sturzu, I., Rosca, C., "A Semianalytical Method for Studying the Acoustic Pulse Propagation in Elastic Inhomogeneous 1-D Media", IMSE98, Mich. Tech. University, Houghton, MI, 10–13 August 1998.

*With all my love and gratitude,
to my wife Dana, and my daughter, Alexandra*

ACKNOWLEDGEMENT

First of all I would like to thank Dale Gary for being my advisor during all my graduate work. I deeply appreciate his willingness to spend a lot of time introducing me to a field of Physics that was totally new for me before meeting him. I was impressed from the beginning by his knowledge and love for his work, and I am thankful for him seeding and patiently waiting to grow my passion for this field. He was not only a teacher, but also a friend who listened, understood, and tried to find solutions for any difficulties I encountered during these years. I am also thankful to him for giving me the opportunity to meet a lot of peoples whose help and friendship were critical for this accomplishment.

One of them was Louis Lanzerotti, who impressed me by his encyclopedic knowledge and his professional achievements. I am thankful to him for our collaboration during my first project in this field and for his suggestion regarding the subject of this thesis.

I want to thank my friend Jeongwoo Lee, who impressed me by his talent and knowledge, most of the time hidden behind an unusual modesty. The collaboration with him was fruitful, and the lunch breaks, during which he used to write formulas on tiny pieces of napkins, or to tell great jokes without a smile on his face, were unforgettable.

Although short, the visit of Gregory Fleishman was decisive for the start of this project. I want to thank him for his help in the initial classification of solar radio bursts recorded by OVSA, and for his scientific expertise who led us in a short time to very interesting results.

I am also thankful to Victor Melnikov who had a decisive contribution to the core of this thesis. During his visit, I learned a lot about the underlying physics of solar radio bursts, and how the secrets behind the data can be uncovered. He was

a very pleasant presence, and I really enjoyed our walks around the campus, during which we talked about Physics, cultural customs, or World History.

I thank Philip Goode, Haimin Wang, Carsten Denker, Jiong Qiu, and all my fellow students, for the friendly environment found inside the Center for Solar and Terrestrial Research. I also want to thank Christine Oertel and Jimei Cao for the support I received any time I needed.

I would not forget to thank the person without whose diligent work no OVSA data would have been available for this project. I met Kjell Nelin during my visit at OVSA site, and I was really impressed about his one-man-band capabilities and his dedicated work to keep the instrument running on daily basis.

I could not end this list before thanking to all the persons who influenced my future in a way that allowed me to reach this point in my career.

First of all, I would like to thank Ken Chin who advised me every time I needed and recommended me to Dale Gary. During these years, I have always found the door of his office widely open, and him ready to offer his generous help.

I am thankful to Voicu Grecu, Dean of Physics Faculty of Bucharest University, Mircea Rusu, my undergraduate advisor, and Spiridon Dumitru, former Chair of Physics Department of Transilvania University, for trusting and recommending me to enter the graduate school.

I might have never thought to start my graduate studies without the confidence given by my previous research work. For this reason I want to thank my friends and first research fellows Nicolae Cretu and Ioan Sturzu.

To start a new life far away from your homeland would not have been a smooth transition without the help of the old friends already here, or of the new ones I met during these years. I would like to thank for their support and friendship Lucia and Sorin Stegaru, Andreea and Ciprian Suciu, Mirela and Sorin Teodorescu, Ruxandra

and Vali Balescu, Carmen and Ionut Zaharia, Nicoleta and Gheorghita Cadar, Raluca and Florin Neagu, Doina and George Dragoi, and Radu Damboianu.

Although the research work I carried out these years provided me with great satisfaction, I could have never found the resources needed for such a demanding work without the constant support of my family.

I thank Gina and Ioan Neculaie whose great generosity allowed my wife and my daughter to join me here from the beginning of my studies.

I am deeply thankful to Dana for being with me all these years, for her love, understanding, and personal sacrifice. I also thank Alexandra whose love and constant joyousness refilled my soul everyday, giving me the strength to start a new day of work. Not finding enough words to express my love and gratitude, I dedicate this work to them.

TABLE OF CONTENTS

Chapter	Page
1 INTRODUCTION	1
1.1 Solar Flares	1
1.2 Statistical versus Case Studies of Solar Radio Bursts	3
1.3 Thesis Overview and Important Results	4
2 THE PEAK FLUX DISTRIBUTION OF SOLAR RADIO BURSTS	8
2.1 Introduction	8
2.2 Data Description	10
2.3 Data Analysis	14
2.3.1 Assigning Entries to Events	14
2.3.2 Geographical Correction Factor	22
2.3.3 Computing Number Density Distributions	26
2.3.4 Power-Law Fitting Algorithm	28
2.4 Results	35
2.4.1 Occurrence Rate of Solar Radio Bursts	37
2.4.2 Time and Frequency Dependence of Power-Law Distributions	40
2.5 Conclusion	45
3 STATISTICAL STUDY OF TWO YEARS OF SOLAR FLARE RADIO SPECTRA OBTAINED WITH OVSA	50
3.1 Introduction	50
3.2 Description of Data Set	52
3.3 Spectral Peak Distribution of Microwave Bursts	56
3.4 Spectral Types and their Characteristics	63
3.4.1 Definition of Spectral Types	63

TABLE OF CONTENTS
(continued)

Chapter	Page
3.4.2 Absolute Peak Distribution of Spectral Types	66
3.4.3 Peak Flux Distribution of Spectral Types	67
3.4.4 The Peak Frequency Distribution of Spectral Types	70
3.4.5 The Spectral Slope Distribution	74
3.4.6 Time scale of microwave bursts	81
3.4.7 Summary of Spectral Type Characteristics	82
3.5 Statistics of Microwave Bursts with Multi-Spectral Components	88
3.5.1 Peak Frequency Ratio	88
3.5.2 Peak Flux Ratio	92
3.5.3 Time Delay of Spectral Components	96
3.6 Conclusion	96
4 PEAK FREQUENCY DYNAMICS IN SOLAR MICROWAVE BURSTS	100
4.1 Introduction	100
4.2 Observational Data	103
4.3 Peak Frequency Dynamics	105
4.3.1 Magnitude of Peak Frequency Variations	116
4.3.2 Peak Frequency Evolution on the Rising Phase of Bursts	116
4.3.3 Peak Frequency Evolution on the Decay Phase of Bursts	123
4.4 Discussion and Model Simulations	138
4.4.1 Gyrosynchrotron Spectrum Formation	138
4.4.2 Influence of Self-Absorption	139
4.4.3 Influence of High Plasma Density: Razin Effect	140
4.4.4 Razin Effect and Electron Power Law Index	143
4.4.5 Plasma Density Increase on the Late Decay Phase	145
4.5 Conclusion	151

TABLE OF CONTENTS
(continued)

Chapter	Page
5 NONTHERMAL ELECTRONS IN SOLAR FLARES DERIVED FROM MICROWAVE SPECTRA	155
5.1 Introduction	155
5.2 Data and Strategy	157
5.3 The Relationship between Flux and Brightness Temperature Inferred from NoRH Data	162
5.4 Analysis of the OVSA Data	165
5.4.1 Electron Power-law Index	165
5.4.2 Total Number and Total Energy	166
5.4.3 Derived Total Energy vs. Directly Measured Parameters	169
5.5 Discussion	170
5.5.1 Our Diagnostic Procedure	170
5.5.2 Upper Limit in the Nonthermal Energy Distribution	171
5.5.3 Statistical Properties of Flare Parameters	172
5.5.4 Electron Acceleration	173
6 DECIMETRIC SPIKE BURSTS VERSUS MICROWAVE CONTINUUM .	180
6.1 Introduction	180
6.2 Observations	184
6.3 Theoretical Background	185
6.4 Data Analysis	187
6.4.1 25-mar-01 event	188
6.4.2 24-aug-01 event	193
6.4.3 30-aug-01 event	196
6.4.4 05-oct-01 event	199
6.4.5 02-apr-01 event	202
6.4.6 19-oct-01 event	205

TABLE OF CONTENTS
(continued)

Chapter	Page
6.5 Discussion	206
7 CONCLUSION	213
REFERENCES	228

LIST OF TABLES

Table	Page
2.1 Statistics of the Data Set	13
2.2 Statistics of Optical Flares	13
2.3 Parameters for Max Flux Approach	48
2.4 Parameters for Selected Peak Approach	49
3.1 Statistics of Data Set	56
3.2 Statistics of Centimeter Spectral Types (Intensity, sfu)	84
3.3 Statistics of Decimeter Spectral Types (Intensity, sfu)	85
3.4 Statistics of Centimeter Spectral Types (Frequency, GHz)	85
4.1 Regression coefficients for events with $\Delta f_{peak}/f_{peak} > 0.3$	118
4.2 Regression coefficients for events with $\Delta f_{peak}/f_{peak} < -0.4$	123
4.3 Regression coefficients for events with $-0.3 < \Delta f_{peak}/f_{peak} < -0.1$	125

LIST OF FIGURES

Figure	Page
2.1 (a) The number of optical flares since 1965, as reported in the <i>Solar Geophysical Data</i> publication of the NGDC. (b) The number of radio events determined from the 40-year database of radio bursts considered in this paper. (c) A comparison of the two, where the light color represents the optical flares and the dark color represents the radio events. The numbers agree closely over most of the range (no scaling of numbers has been done). The radio bursts are likely under-counted before 1970.	11
2.2 A plot showing the distribution of observing frequencies represented in the database (black histogram), and the choice of frequency windows over which we accumulation data (gray). There are several gaps in which no observations are taken, hence our frequency ranges also reflect these gaps. The large range 15–37 GHz is kept, despite the large gap in coverage from 19 to 35 GHz, since splitting it into subranges would leave too poor statistics for the 35–37 GHz range.	15
2.3 Waiting time distribution of entries in the entire database, out to 60 minutes. The upper panel is a linear plot showing a rapid drop at small waiting times and a slower decay at longer waiting times. The lower panel shows the same information on a log-linear scale, along with an exponential fit corresponding to a decay time constant of 37 min.	17
2.4 Waiting time distribution of entries in the entire database, out to 10^5 min, plotted on a log-log scale with logarithmic binning. The distribution is similar to that found for soft X-ray events by Boffeta et al. (1999) and Wheatland (2000b). The dotted line shows the exponential fit of Fig. 2.3b, with time constant 37 min, for comparison. The solid line, which corresponds to a mean waiting time of 81 min, is the curve given by the Wheatland (2000b) model, which assumes an exponential distribution of flaring rates. Prominent features near 1, 2, and 3 days are likely artifacts due to human bias in the event reports.	19
2.5 Distribution of waiting times of subsequent entries relative to the Leader Entries, which are defined as having no preceding entries for at least 60 min earlier. The entries show a natural fall-off of 5.37 min time constant, merging with a general background of uncorrelated entries.	20

LIST OF FIGURES (continued)

Figure	Page	
2.6	Time-of-day distribution of (a) BATSE hard X-ray bursts, and (b) radio bursts from the NOAA database, for the period 1991-1999. The BATSE events are consistent with a uniform distribution, indicating that all Earth longitudes are equally well covered, while the radio events show a large non-uniformity with longitude, including a large peak at Universal Times corresponding to morning hours in Western Europe.	24
2.7	Time-of-day distribution of radio bursts from the NOAA database, for three complete solar cycles. Longitudes representing local noon in the continental United States are shown with hatched areas. The longitudinal coverage of radio events has clearly changed, especially for bursts at frequencies > 1000 MHz, with a dominance at Western Hemisphere longitudes in solar cycle 20 (upper left panel) giving way to a deficit at those longitudes by solar cycle 22 (lower left panel).	25
2.8	A schematic representation of the radio spectrum of a typical solar burst. The flux density S may be high at low frequencies due to plasma emission, then drops to a minimum near 2 GHz and rises again due to gyrosynchrotron emission to a peak near 5-10 GHz. At high frequencies, the emission is optically thin and decreases with increasing frequency. The example shows five entries with flux densities represented by dots at five frequencies. The vertical dashed lines divide the spectrum into several frequency ranges. . .	27
2.9	Example of the comparison of fits to the differential (ΔN) and cumulative (N) number distributions for Cycle 22, 8.4-11.8 GHz. (a) The solid lines are the fits to the differential distribution given in equation (2.2), for the flux range $10 - 10^{4.5}$ sfu. The dotted lines are the fits to the cumulative distribution over the same fit range. In (b) are shown the corresponding probability distributions for a range of values of λ . The two fits are both excellent, but are not mutually consistent. Panels (c), (d) show the same procedure using a slightly smaller flux range ($10^{1.2} - 10^{3.8}$ sfu), where the fit yields essentially identical results for both distributions, within the formal errors.	36
2.10	Cumulative number of bursts per day at frequencies > 2 GHz (a) during solar maximum years, and (b) during solar minimum. The histograms show the actual, observed distribution. The solid line shows the best power-law fit to the observed distribution, and the dotted line shows the fit after application of the geographical correction factor C_{geo} , which is 1.8 during solar max, and 1.7 during solar min epochs.	39
2.11	A plot of the absolute value of the slopes in Tables 2.4 (left panel—from the Selected Peak approach) and 2.3 (right panel—from the Max Flux approach) as a function of frequency.	41

LIST OF FIGURES
(continued)

Figure	Page	
2.12	Alternative plot of the same information that was plotted in Figure 2.11. The absolute value of the slopes in Tables 2.4 (left panel—from the Selected Peak approach) and 2.3 (right panel—from the Max Flux approach) for different frequency ranges as a function of epoch.	43
2.13	The number of events per year with flux density > 1000 sfu, as a function of epoch (abscissa of each plot) and frequency (in separate panels in each row). Data from the Selected Peak Table (2.4) are shown in the two upper rows. The two lower rows are for the Max Flux Table (2.3). The values for the three solar cycles are plotted as points connected by solid lines. The values for Solar Min years are plotted as a dotted line spanning all cycles, and the values for Solar Max years are plotted as a dashed line spanning all cycles.	44
3.1	A spectral fit example: In this case two spectral components were resolved and each spectral range was fitted using the generic function described in Equation 3.1. The fit parameters α and β were used to derive the spectral slopes α_{lf} and α_{hf} of each range. The function was computed for 100 equally spaced frequencies in the fitting range to interpolate the peak parameters ν_{peak} and S_{peak}	55
3.2	Synopsis of 2001-2002 OVSA data: The distribution of spectral peak at each recorded instant of time for 412 analyzed events, (500 spectral components, 50733 data points). The horizontal stripes represent a data artifact due to the observational OVSA frequencies. The horizontal dotted line at 2.62 GHz represents the empirical dividing line between dm and cm radio emission. The inclined dotted line approximately marks the frequency-dependent flux limitation discussed in the text.	58
3.3	The flux-frequency distribution of the spectral types. Each of the 500 spectral components of the 412 OVSA radio bursts is represented by one data point corresponding to its absolute peak. However, to compute the percentages corresponding to each type, C (diamonds)-79.37%, D (triangles)- 4.85%, and CD (squares)-15.78%, each burst has been counted only once. The irregular vertical curve at the left is the frequency-dependent 1σ RMS noise limit of the dataset. The horizontal and inclined dotted lines are the same as those shown in Fig.3.2.	60
3.4	Number density distributions of dm events, (a), and cm events, (b). A strong frequency range dependence of the power-law slope may be observed. The dm distribution is much flatter than the cm one, which implies a greater preponderance of strong events in the dm range.	62

LIST OF FIGURES
(continued)

Figure	Page	
3.5	Different types of dynamic spectra recorded by OVSA. Centimetric type (C): peak frequency only above 2.6 GHz. Decimetric type (D): peak frequency only below 2.6 GHz. Composite type (CD): at least one spectral component in each of the cm and dm frequency ranges.	65
3.6	Peak flux density distribution of spectral types: (a) C type, (b) D type, (c) cm components of CD type, (d) dm components of CD type. The median peak fluxes and the 50% probability ranges are indicated on each plot. . . .	68
3.7	Peak frequency distribution of event types: (a) All types, (b) C and D types, (c) CD type. The median peak frequencies of cm-types and 50% probability ranges are indicated on each plot. The equally logarithmic bin size was chosen to allow comparison with the previously reported results, which were based on fixed frequency observation separated by one octave.	72
3.8	The shift of the peak frequency with intensity level for the cm bursts. The median peak frequency of all cm bursts above a low cutoff limit of the absolute peak flux is plotted. The median values are plotted separately for different times during the bursts: at the absolute peak, (solid line), rise time, (dotted line), and decay time (dashed line).	73
3.9	Distribution of cm-type spectral slopes (a) versus peak flux and (b) peak frequency (diamonds-C type, squares-CD type). The positive values represent the low frequency spectral slope and the negative value the high frequency spectral slope.	76
3.10	The shift of cm-bursts spectral indices with the intensity level. The median low (positive values) and high (negative values) frequency spectral index of all cm bursts above a low cutoff limit of the absolute peak flux is plotted. The median values at the absolute peak, (solid line), rise time, (dotted line), and decay time (dashed line), shift to zero on both sides of the spectra. . . .	78
3.11	Distribution of spectral slopes for cm-type bursts. The positive values represent the low frequency spectral slope and the negative value the high frequency spectral slope: (a) the distribution of all cm-type bursts, (b) the distribution of C-type bursts, (c) the distribution of cm counterpart of CD-type bursts.	79
3.12	Duration above 80% of the peak flux: (a) C type, (b) D type, (c) cm components of CD type, (d) dm components of CD type. The median durations and the 50% probability ranges are indicated on each plot.	83

LIST OF FIGURES
(continued)

Figure	Page
3.13 The distribution of peak frequencies of multi-component bursts. (Events with peak frequency at 1.2 GHz were excluded from the statistics, since both frequency and flux density are not necessarily the true ones, which may lie outside of the OVSA frequency range.) (a) The high peak frequency versus the low peak frequency. The inclined lines represent the integer ratios from 1 to 10. (b) The distribution of high to low frequency ratios. (c) The distribution of 54 ratios randomly selected from the parent population of all possible OVSA frequency ratios. The similarity of the observed ratio distribution with the randomly selected one may be observed.	90
3.14 (a) The distribution of peak frequency ratios observed at any instant of time during the evolution of multi-component bursts. (b) The parent population of all possible ratios one may observe in the OVSA frequency range. The similarity of the two distributions suggests that the observed ratio distribution at any instant of time represents a random subset of the parent population.	94
3.15 (a) The high frequency component peak flux versus the low frequency component peak flux for 2-component C-type bursts. The inclined line corresponds to equal fluxes. (b) The high frequency (cm) component peak flux versus the low frequency (dm) component peak flux for the CD-type bursts. (c) Distribution of the ratio of high to low frequency component peak fluxes for C-type bursts. (d) Same as c, for CD-type bursts.	95
4.1 Spectral evolution of the first peak in the microwave multi-component burst of July 15, 2002, (a). Solid lines show the best fit with the generic function Eq. 4.1. An increase of the turnover frequency on the rising phase, (b), and a corresponding decrease on the decay phase, (c), is clearly seen.	106
4.2 Spectral evolution as in Figure 4.1 for a secondary peak in the microwave burst of July 15, 2002, (a). Note the remarkable stability of the peak frequency during the most of the burst, (b, c), and the equal rise and fall on both sides of the peak frequency, which yields a constant R . . .	107
4.3 Time profiles of several key parameters of the spectral evolution of the burst shown in Figure 4.1: (a) Flux density, (b) peak frequency, (c) ratio R of fluxes at two frequencies, one (13.2 GHz) on the high-frequency side and one (3.8 GHz) on the low-frequency side of f_{peak} , and (d) the high frequency spectral index, α_h . A strong correlation is seen among the top three panels, both on the rise phase and initial part of the decay phase. The dotted vertical lines in each panel mark the peak times in a.	109

LIST OF FIGURES
(continued)

Figure	Page
4.4	Distribution of correlation coefficients between the peak frequency f_{peak} and peak flux S_{peak} on the rise (upper panel) and decay (lower panel) phases of the bursts from our set of events. 110
4.5	Peak frequency evolution in the multi-component burst of 2001 April 22, for the same parameters as shown in Figure 4.3. 112
4.6	The same as on Figure 4.5, but for the event May 1, 2001. 113
4.7	The distributions of Δf_{peak} (<i>a</i>) on the rise and (<i>b</i>) decay phases. The corresponding flux density increase (decrease) is from (to) 25% of its maximum value. The total number of bursts used in the distributions is 25 in <i>a</i> and 36 in <i>b</i> 117
4.8	The same as in Figure 4.7, but normalized by the peak frequency $\Delta f_{peak}/f_{peak}$. Here f_{peak} is taken at the peak time of $S_{peak}(t)$ 117
4.9	Peak frequency vs. peak flux density on the rise phase of 7 events. The straight lines are the best linear fits (in logarithmic scale) near the peak of the bursts. The numbers indicate the events: 1–2001 Apr 22, 2–2001 Oct 19, 3–2001 Oct 22, 4–2001 Nov 04, 5–2001 Nov 22, 6–2002 Jul 15, 7–2002 Dec 04. 128
4.10	Time profiles as in Figure 4.3 for the burst of 2001 April 24. The peak frequency in <i>b</i> remains high and nearly constant except near the main peak in <i>a</i> . The ratio <i>R</i> in <i>c</i> also becomes high and constant during the decay. Note that the spectral index α_h in <i>d</i> increases all during the rise phase and is constant in most of the decay phase. 129
4.11	Time profiles as in Figure 4.3 for the bursts of 2001 Sep 14. This example shows a time delay between f_{peak} in <i>b</i> and S_{peak} in <i>a</i> . Note also that on the decay f_{peak} first decreases and then slightly increases. The α_h in <i>d</i> increases throughout the burst. 130
4.12	Simulation of the spectral evolution for a gaussian flux density profile (<i>a</i>) under the influence of hardening or softening of the electron spectrum, showing in <i>b</i> the leading or lagging of the time of maximum of f_{peak} . The assumed electron spectral index evolution is shown in <i>c</i> : solid line, $\delta = const$; dashed line, $\Delta\delta = -0.5$; dotted line, $\Delta\delta = -1.0$; dot-dashed line, $\Delta\delta = +0.5$. The peak frequency time profile leads the flux maximum if the electron spectrum flattens, and it lags if the electron spectrum steepens. 131

LIST OF FIGURES
(continued)

Figure	Page
4.13 Time profiles as in Fig. 4.3 for the burst of 2001 August 31. This example shows a rather complex time profile for f_{peak} , with a strong decrease of f_{peak} and R in the initial rise phase followed by more normal behavior. On the late decay phase, there is also a strong subsequent increase of the peak frequency and flux ratio. Note that for the ratio R the end of decrease and the beginning of the increase occur earlier than for the peak frequency. The high frequency spectral spectral slope flattens during all the main part of the burst, and keeps almost constant on the late decay phase.	132
4.14 Time profiles as in Fig. 4.3 for the second major peak of the burst of 2001 Nov 22. The turnover frequency in b is remarkably constant during the main part of the rise and decay. The same is true for the ratio R in c . On the late decay phase the peak frequency starts to increase.	133
4.15 Time profiles as in Fig. 4.3 for the burst of 2002 Jul 15. The turnover frequency in b is remarkably constant during the entire rise and decay of the second major peak of the burst. The same is true for the ratio R in c . Note also the gradual increase of f_{peak} and R after 2026 UT, while S_{peak} decreases gradually more than a factor of 4. The spectral evolution of this burst is shown in Fig. 4.2.	134
4.16 The relationship between the peak frequency, f_{peak} , and peak flux density, $S_{peak} = S(f_{peak})$ on the decay phase of 4 events with the highest values of $\Delta f_{peak}/f_{peak}$. The straight lines are the best linear fits (in logarithmic scale) near the peak of the bursts. The numbers indicate the events: 1 - 2001.08.30, 2 - 2001.08.31, 3 - 2001.10.22, 4 - 2002.08.28.	135
4.17 The relationship between the peak frequency, f_{peak} , and peak flux density, $S_{peak} = S(f_{peak})$ on the decay phase of 6 events with the moderate values of $\Delta f_{peak}/f_{peak}$ ($-0.3 < \Delta f_{peak}/f_{peak} < -0.1$). The straight lines are the best linear fits (in logarithmic scale) near the peak of the bursts. The numbers indicate the events: 1 - 2001.08.25, 2 - 2001.12.28, 3 - 2002.07.20, 4 - 2002.07.26, 5 - 2002.08.18, 6 - 2002.010.31. A change of the dependence slope on the late stage of decay is well seen for all the events.	136
4.18 Time profiles of the microwave burst of September 14, 2001. Strong increase of f_{peak} and R on the gradual decay phase of the last peak is accompanied by continuous flattening of the high frequency spectral slope (increase of α_h).	137

LIST OF FIGURES
(continued)

Figure	Page
<p>4.19 Spectral evolution of GS emission in a low density plasma ($n_0 = 5 \times 10^9 \text{ cm}^{-3}$, $B = 150 \text{ G}$, $t_m = 54 \text{ s}$, $t_0 = 12 \text{ s}$, $\delta = 4.0$, $L = 10^9 \text{ cm}$, $\phi = 17''$, $k = 10^4$). For these parameters, the low frequency turnover is determined by GS self-absorption. Panel (a): Flux density spectrum at different times on the rising (dotted lines) and decay (dashed lines) phases. Panel (b): Peak flux time profile $S_{peak} = S(f_{peak})$. Panel (c): Dependence of the peak frequency on the peak flux on a log scale (solid and dashed lines for the rise and decay, respectively). Panel (d): Peak frequency evolution. Panel (e): High frequency spectral index evolution. Spectral index is defined by fitting of a calculated spectrum (panel a) at frequencies $f > f_2$, $f_2 = 1.5f_{pabs}$ (see Eq. 4.6). Panel (f): Evolution of logarithm of the flux ratio R at $f_2 > f_{peak}$ and $f_1 < f_{peak}$.</p>	141
<p>4.20 Spectral evolution of GS emission in the presence of high density plasma: $n_0 = 5 \times 10^{10} \text{ cm}^{-3}$. The other parameters are same as in Figure 4.19. The low frequency turnover is determined by two effects: 1) by the Razin suppression on the initial rising phase and late decay phase, and 2) by the self-absorption near the maximum of the simulated burst. Note the high initial value and small range of the peak frequency and R variations.</p>	144
<p>4.21 Dependence of the GS peak frequency on plasma density, magnetic field and electron energy index δ. The peak frequency defined by the Razin effect is considerably larger for a harder electron energy spectrum.</p>	147
<p>4.22 Spectral evolution of GS emission in the presence of high density plasma and continuous electron spectrum hardening, $\delta = 4.0 - (t - t_{max})/t_{max}$. The other parameters are the same as in Figure 4.20 except $k = 10^3$ and $\phi = 45''$. Note the continuous increase of f_{peak} and R on the rise and decay phases. On panels (a) and (c) solid line is for the rising phase and dashed line for the decay phase.</p>	148
<p>4.23 Spectral evolution of GS emission in the presence of high density plasma and electron spectral hardening, $\delta = 4.0 - (t - t_{max})/t_{max}$. The other parameters are the same as in Figure 4.20. The increase and decrease of f_{peak} and R in the main part of the emission peak is due to GS self-absorption. A new increase of the peak frequency and the flux ratio with time is clearly seen on the decay phase when the source becomes optically thin at low frequencies and the Razin suppression becomes dominant in defining the spectral peak.</p>	149

LIST OF FIGURES
(continued)

Figure	Page
<p>4.24 Spectral evolution of GS emission in the case of plasma density increase on the decay phase: $n(t) = n_0[1 + 2(t - t_m)^2/t_m^2]$, where $n_0 = 5 \times 10^{10} \text{ cm}^{-3}$, $t_m = 200 \text{ s}$. The other parameters are the same as in Figure 4.20, except $\phi = 20''$. The increase of f_{peak}, R and α_h on the late decay phase is completely due to the influence of high plasma density (Razin effect).</p>	150
<p>4.25 Schematic representation of characteristic time profiles of the peak frequency expected from GS theory. The three curves in each panel are (solid line) self-absorption dominant throughout a burst, (dot-dashed line) Razin suppression dominant in the beginning and end of a burst, but self-absorption important near the burst maximum, and (dashed line) Razin suppression dominant throughout a burst. The panels show three cases: <i>a</i>) electron spectral index is constant, <i>b</i>) continuous hardening of the electron spectrum, <i>c</i>) stable electron index but Razin suppression (as expressed by $Y = f_p/f_B$) increases on the decay phase.</p>	153
<p>5.1 The distribution of peak flux density divided by the square of peak frequency. All cm bursts, (C-diamonds, CD-squares), and almost all D-type bursts (triangles), have the same limit of this ratio that we empirically set at $\sim 300 \text{ sfu/GHz}^2$, represented by the dotted vertical line. The dotted horizontal line represents the dm frequency limit of 2.6 GHz. No event has been recorded in OVSA data above these two empirical limits. The lack of events in the left-down corner of the plot is just an artifact due to the 1 sfu frequency-independent sensitivity limit of OVSA.</p>	159
<p>5.2 The S_{peak}/ν_{peak}^2 distribution from OVSA data above 2.6 GHz. The power-law index of this distribution is 1.56 ± 0.04 the same as, within the statistical limits, the one derived from NoRH observations at a single frequency. . . .</p>	175
<p>5.3 (a) The S_{peak}/ν_{peak}^2 distribution from NoRH data at 17 GHz. A power-law index of 1.63 ± 0.07 is found. (b) Source area distribution from NoRH. Area is expressed in units of NoRH beam area, which is about $20''$ at 17 GHz. The tail of the distribution obeys a power-law with an index of 2.57 ± 0.23. (c) Brightness temperature distribution from NoRH. The power-law index of this distribution is 1.65 ± 0.09. (d) The correlation plot of source area and S_{peak}/ν_{peak}^2 at 17 GHz from NoRH data. The distribution is best fitted by a power-law with an index of 0.32 ± 0.02.</p>	176
<p>5.4 Distribution of the electron power-law index derived from the optically-thin spectral slopes of the OVSA spectra. These index distributions are shown at three different groups according to the flux (left panel) and according to the scaled flux, $y \equiv S_\nu/\nu^2$ (right panel).</p>	177

LIST OF FIGURES
(continued)

Figure	Page
5.5	The total number (upper panels) and total energy (lower panels) distributions of nonthermal electrons derived from the OVSA microwave spectra. The slope of a power-law fit (lines) to the distribution and the lower bound energy E_0 used for integration are specified in each panel. 178
5.6	Derived total energy vs. directly observed flare parameters. In the top panels, total energies integrated above $E_0 = 10$ keV are used, and in the bottom panels, those integrated above $E_0 = 100$ keV are used for correlation with other parameters. From the left to right columns we show scatter plots of spectral index, peak frequency, and the scaled peaked flux, y , respectively, against the total energy, E_{tot} . The line in each panel represents a linear fit to the data and the slope of the fit is specified. 179
6.1	Distribution of optically thick spectral index of 6 spike-producing bursts (solid line) and the equivalent distribution obtained for 125 gyrosynchrotron bursts above 60 sfu observed by OVSA during 2001 (dashed line). 189
6.2	March 25, 2001: (a)-Dynamic spectrum recorded by OVSA at 40 frequencies between 1.2 and 18 GHz at 4 s time resolution. The solid line, 6.6 GHz, and the dashed line, 3.4 GHz, represent the optically thick frequency and, respectively, the upper integration limit of the spiky emission used to obtain the results displayed in Fig.6.3. (b)-The time averaged total power emission (squares) and Left-hand polarization data (triangles) for the same segment of time as in (a). (c)-The averaged polarization spectrum computed using the magnitudes displayed in (b). 191
6.3	March 25, 2001: (a)-Integrated spiky emission over [1.2 – 3.4] GHz (thin line) and the optically thick gyrosynchrotron emission at 6.6 GHz, (thick line). (b)- The linear correlation coefficient (symbols) between the magnitudes displayed in (a) for different time lags. A delay of 2.5 seconds of the high-frequency emission relative to the integrated low-frequency emission has been estimated using a spline interpolation (solid line). (c)- The natural logarithm of the ratio between optically thick and integrated spiky emissions (thin line) and the optically thin spectral index (thick line). (d) The correlation plot of the magnitudes displayed in (c). A linear correlation coefficient of +0.73 has been found. The probability for such a correlation coefficient to be the result of a random distribution is 0% to two decimal places. 192

LIST OF FIGURES
(continued)

Figure	Page
<p>6.4 August 24, 2001: (a)-Dynamic spectrum recorded by OVSA at 40 frequencies between 1.2 and 18 GHz at 4 s time resolution. The solid line, 5.4 GHz, and the dashed line, 2.0 GHz, represent the optically thick frequency and, respectively, the upper integration limit of the spiky emission used to obtain the results displayed in Fig.6.5. (b)-The time averaged total power emission (squares) and Left-hand polarization data (triangles) for the same segment of time as in (a). (c)-The averaged polarization spectrum computed using the magnitudes displayed in (b).</p>	194
<p>6.5 August 24, 2001: (a)-Integrated spiky emission over [1.2 – 2.0] GHz (thin line) and the optically thick gyrosynchrotron emission at 5.4 GHz, (thick line). (b)- The linear correlation coefficient (symbols) between the magnitudes displayed in (a) for different time lags. A delay of 9.6 seconds for the high-frequency emission relative to the integrated low-frequency emission has been estimated using a spline interpolation (solid line). (c)- The natural logarithm of the ratio between optically thick and integrated spiky emissions (thin line) and the optically thin spectral index (thick line). (d) The correlation plot of the magnitudes displayed in (c). A linear correlation coefficient of +0.80 has been found. The probability for such a correlation coefficient to be the result of a random distribution is again 0%.</p>	195
<p>6.6 August 30, 2001: (a)-Dynamic spectrum recorded by OVSA at 40 frequencies between 1.2 and 18 GHz at 4 s time resolution. The solid line, 5.4 GHz, and the dashed line, 3.2 GHz, represent the optically thick frequency and, respectively, the upper integration limit of the spiky emission used to obtain the results displayed in Fig.6.7. (b)-The time averaged total power emission (squares) and Left-hand polarization data (triangles) for the same segment of time as in (a). (c)-The averaged polarization spectrum computed using the magnitudes displayed in (b).</p>	197

LIST OF FIGURES
(continued)

Figure	Page
<p>6.7 August 30, 2001: (a)-Integrated spiky emission over [1.2 – 3.2] GHz (thin line) and the optically thick gyrosynchrotron emission at 5.4 GHz, (thick line). (b)- The linear correlation coefficient (symbols) between the magnitudes displayed in (a) for different time lags. Practically no delay between high-frequency emission and the integrated low-frequency emission has been found in this case. (c)- The natural logarithm of the ratio between optically thick and integrated spiky emissions (thin line) and the optically thin spectral index (thick line). (d) The correlation plot of the magnitudes displayed in (c). A linear correlation coefficient of +0.49 has been found. The probability for such a correlation coefficient to be the result of a random distribution is about 0.03%.</p>	198
<p>6.8 October 5, 2001: (a)-Dynamic spectrum recorded by OVSA at 40 frequencies between 1.2 and 18 GHz at 8 s time resolution. The solid line, 3.8 GHz, and the dashed line, 2.0 GHz, represent the optically thick frequency and, respectively, the upper integration limit of the spiky emission used to obtain the results displayed in Fig.6.9. (b)-The time averaged total power emission (squares) and Right-hand polarization data (triangles) for the same segment of time as in (a). (c)-The averaged polarization spectrum computed using the magnitudes displayed in (b). Only the polarization spectrum below 10 GHz is reliable due to a very weak emission above this frequency, as it can be seen in (b).</p>	200
<p>6.9 October 5, 2001: (a)-Integrated spiky emission over [1.2 – 2.0] GHz (thin line) and the optically thick gyrosynchrotron emission at 3.8 GHz, (thick line). (b)- The linear correlation coefficient (symbols) between the magnitudes displayed in (a) for different time lags. A delay of 5.9 seconds of the high-frequency emission relative to the integrated low-frequency emission has been estimated using a spline interpolation (solid line). (c)- The natural logarithm of the ratio between optically thick and integrated spiky emissions (thin line) and the optically thin spectral index (thick line). (d) The correlation plot of the magnitudes displayed in (c). A linear correlation coefficient of –0.46 has been found. The probability for such a correlation coefficient to be the result of a random distribution is about 0.18%.</p>	201

LIST OF FIGURES
(continued)

Figure	Page
<p>6.10 April 2, 2001: (a)-Dynamic spectrum recorded by OVSA at 40 frequencies between 1.2 and 18 GHz and 4 s time resolution. The solid line, 3.8 GHz, and the dashed line, 1.8 GHz, represent the optically thick frequency and, respectively, the upper integration limit of the spiky emission used to obtain the results displayed in Fig.6.11. (b)-The time averaged total power emission (squares) and Right-hand polarization data (triangles) for the same segment of time as in (a). (c)-The averaged polarization spectrum computed using the magnitudes displayed in (b).</p>	203
<p>6.11 April 2, 2001: (a)-Integrated spiky emission over [1.2 – 1.8] GHz (thin line) and the optically thick gyrosynchrotron emission at 3.8 GHz, (thick line). (b)- The correlation plot of the magnitudes displayed in (a). No reliable delay could be found. For the case shown (no time lag) there is practically no linear correlation ($r = 0.01$ corresponding to a 90% probability of a random distribution). (c)- The natural logarithm of the ratio between optically thick and integrated spiky emissions (thin line) and the optically thin spectral index (thick line). (d) The correlation plot of the magnitudes displayed in (c). A linear correlation coefficient of -0.61 has been found. The probability for such a correlation coefficient to be the result of a random distribution is 0% to two decimal places.</p>	204
<p>6.12 October 19, 2001: Dynamic spectrum recorded by OVSA at 22 frequencies between 1.2 and 14.8 GHz and 2 s time resolution. The solid line, 3.6 GHz, line represents the optically thick frequency used to obtain the results displayed in Fig.6.13. To analyze the spiky emission only one frequency, 1.2, GHz has been used in this case because a smoothed component becomes important for higher frequencies at the low frequency range. No polarization data are available for this event.</p>	207
<p>6.13 October 19, 2001: (a)-Emissions at 1.2 GHz (thin line) and the optically thick gyrosynchrotron emission at 3.6 GHz, (thick line). (b)- The linear correlation coefficient (symbols) between the magnitudes displayed in (a) for different time lags. A delay of 7.3 seconds of the high-frequency emission relative to the low-frequency emission has been estimated using a spline interpolation (solid line). (c)- The natural logarithm of the ratio between optically thick and spiky emissions (thin line) and the optically thin spectral index (thick line). (d) The correlation plot of the magnitudes displayed in (c). A linear correlation coefficient of -0.79 has been found. The probability for such a correlation coefficient to be the result of a random distribution is again 0%.</p>	208

LIST OF FIGURES
(continued)

Figure	Page
6.14 (a) Distribution of optically thin spectral index of the presumably quasi-transverse observed spike-producing bursts (solid line). (b) Distribution of optically thin spectral index of the presumably quasi-parallel observed spike-producing bursts (solid line). Both distributions are compared with that obtained for 125 gyrosynchrotron bursts above 60 sfu observed by OVSA during 2001 (dashed lines).	209

CHAPTER 1

INTRODUCTION

1.1 Solar Flares

Solar flares represent an important aspect of solar activity. They are explosive phenomena which suddenly emit radiation over the entire electromagnetic spectrum, ranging from meter radio waves to X and gamma-rays. Beside photons, high energy solar particles are released into the interplanetary medium and may reach the Earth. The energetic particles produced in solar flares may damage satellites, or may be hazardous for astronauts, while their interaction with Earth's ionosphere causes extra ionization, which may affect the radio communications. The radio emission of solar flares that penetrates the Earth ionosphere may also have a direct influence on wireless communications, which are exposed to interferences (Lanzerotti, Thomson & Macleannan 1999). All these effects that solar flares may have on Earth make particularly important their study from the point of view of Space Weather forecasting.

Beside this practical aspect, solar flares are studied for scientific reasons. The Sun is the closest natural plasma laboratory that can be used to test the theoretical predictions at scales impossible to be reached on Earth. In a generous manner, the Sun continuously offers natural experiments waiting to be analyzed. Among them, solar flares and coronal mass ejections, (CME), are the most spectacular events. Our present understanding of the physics behind solar flares may be generally pictured as a catastrophe responsible for a basic eruption that drives a reconnection process which releases the energy stored in the twisted magnetic field lines (Priest & Forbes 2002). This energy results in particle acceleration and plasma heating. The accelerated electrons, if injected from the top of the flaring loop, precipitate downwards, along the loop legs, spiraling around the magnetic field lines. This motion generates microwave radiation, (via gyrosynchrotron emission mechanism), while the electrons

hitting the dense upper chromospheric plasma from the loop footpoints generate hard X-rays. The plasma heated by this energy release fills the magnetic loop with hotter plasma which emits soft X-ray radiation. Optical radiation, the most common being the $H\alpha$ line (6536 Å), is produced by heated chromospheric plasma. Ultraviolet continuum, and extreme ultraviolet lines are also believed to be produced in the chromosphere, while nuclear gamma-rays and neutrons are produced deeper into the chromosphere, where accelerated protons interact with local dense plasma (Silva 1995).

Of course, the above scenario is neither a unique, nor a complete picture of the complicated processes related to the energy release during a solar flare. In particular, the radio emission associated with solar flares may be produced not only by moving electrons in closed flaring loops, but also by electron beams moving upward or downward along some open magnetic field lines. The radio emission produced by such electron beams usually spans the meter wavelength range, although it may be also observed in the dm- λ range. Unlike the incoherent microwave emission, the m, dm- λ radio emission is mainly due to coherent processes triggered by particle-plasma interactions (Bastian, Bentz & Gary 1998).

Beside these already *classical* radio emission mechanisms mentioned above, other emission mechanisms may play a role in solar flares. The electron cyclotron maser mechanism, which may explain the properties of dm-spike bursts accompanying microwave emission (Fleishman, Gary & Nita 2003), or the transition radiation, which may explain the dm-type IV counterpart of the gyrosynchrotron emission (Fleishman, Nita & Gary, in preparation), are just two examples of viable additions to the classical picture.

1.2 Statistical versus Case Studies of Solar Radio Bursts

A popular joke says that a sufficiently large database may be used to prove any hypothesis by statistical means. However, the other side of the coin may be even more dangerous. A single case study may lead one to conclusions that may not be generally true. Thus, none of these approaches should be used exclusively in order to get as close as possible to the true picture behind such a rich collection of observable phenomena related to the physics of solar flares.

Some of the answers one may seek related to solar activity are intrinsically statistical in their nature. Such an example is the occurrence rate of solar flares one should expect in a given intensity or frequency range, or solar activity stage. Information such as waiting time or intensity distributions, and their relationship with other flare or solar parameters, are essential in the complicated attempt of developing forecasting tools of the solar catastrophes. The same kind of statistic may demonstrate the power-law behavior of nonlinear dissipative processes, which is governed by self-organized criticality (Trimble & Aschwanden 2003). Chapter 2 of this thesis tries to answer some of the questions related to the above issues.

While the detailed study of a single event may allow one to derive unknown parameters from the observed ones, the results obtained by statistical means may help one to weight the significance of some parameters and to develop more or less simplified models ready to be applied in individual studies. Chapter 3 of this thesis is dedicated to the classification of microwave bursts according with their main spectral and temporal characteristics, while Chapter 4 presents a detailed analysis of temporal evolution of two microwave spectral parameters, i.e peak frequency and peak flux density, against the current theoretical expectations for their evolution and relationship.

An example about how a statistical study may suggest that a particular hypothesis, previously accepted just as a theoretical possibility, is a real component

of solar flare physics, is given by Chapter 6 of this thesis. In this case, although not initially intended, the process of classification of microwave bursts highlighted a particular subclass of radio bursts, experiencing a $dm-\lambda$ spectral component, eventually proven to be a manifestation of electron cyclotron maser mechanism triggered by the same electron population responsible for the accompanying gyrosynchrotron radiation.

1.3 Thesis Overview and Important Results

This thesis is organized in two parts. The first one, containing Chapters 2, 3, and 4, presents different aspects of a comprehensive statistical study of solar radio bursts, while the second one, Chapters 5 and 6, investigates the relationship between centimetric and decimetric components of some microwave bursts via the electron cyclotron maser emission mechanism and presents the estimated averaged gyrosynchrotron flare parameters derived from the OVSA dataset.

Chapter 2 presents the results of a statistical study based on 40 years of radio burst observations at a limited set of fixed frequencies, as compiled by the NGDC of NOAA from the worldwide network of radio stations. By its size, more than 500,000 records related to more than 150,000 radio bursts, and its time coverage, 1960–1999, this database is the best (and only) set of data of its kind available up to date. This study is focused on the distribution of the radio flux at the absolute peak time, although some other related investigations, on waiting time distribution, occurrence rates, or geographical coverage efficiency, are employed. The changes of statistical parameters in relation with different frequency ranges and time epochs are analyzed, in order to relate them to different emission mechanisms or to the solar cycle variability. The data set is analyzed to find correction factors for missed events, and evidence that nearly half of the events were missed by the worldwide network is found. The power-law fits to the differential (density) (dN/dS in events/sfu) and

cumulative ($N(> S)$ in events) distributions as a function of frequency, time, and phase of the solar cycle, are obtained. The typical power-law index, ~ -1.8 , is similar to that found in many hard X-ray studies. The average waiting time between bursts with flux density exceeding 1000 sfu is found to be 6 days at solar maximum, and 33 days at solar minimum. Taking account of missed events, the expected waiting time decreases to 3.5 days and 18.5 days, respectively. Bursts of this flux level can cause problems with wireless communication systems. Tables of fit parameters that can be used to find burst occurrence rates in a number of frequency ranges are presented. This study finds no significant variation of power-law index from one solar cycle to the next, or with phase of the solar cycle, but it finds significant changes of power-law index with the frequency band.

Chapter 3 presents the results of an analysis of 412 flares during 2001–2002 as detected by the OVSA instrument. This study involves temporal dependence of parameters and the more complete frequency coverage available with OVSA. This study analyzes the distributions of the burst parameters such as maximum flux density in the spectra, peak frequency, spectral slopes below and above peak frequency, duration, and total energy at selected frequencies. The correlations between these parameters, which help us to understand particle acceleration and flare energetics, are discussed. The microwave bursts, observed by OVSA at 40 frequencies in the 1–18 GHz range and with 4 seconds time resolution, are classified according with their spectral and temporal characteristics, and the natural limits of different emission mechanisms are empirically inferred. This is the first statistical study based on the upgraded OVSA instrument, and the differences and similarities with the previous studies based on the same instrument are discussed.

Chapter 4, based on the same OVSA dataset, focuses on the spectral evolution of the gyrosynchrotron bursts. It is found that, for majority of bursts, the peak frequency is very well correlated with the intensity of microwave bursts: it increases

on the rise phase and decreases on the decay phase, in agreement with theoretical predictions following from the self-absorption origin of the low frequency turnover of the gyrosynchrotron spectrum. However, for some events the peak frequency increase is much smaller than expected or even does not happen: it starts from high values from the very beginning of a burst and keeps almost constant during the considerable increase and decrease of the burst intensity. It is also found a type of spectral evolution that is characterized by the increase of the peak frequency starting in the middle of the decay phase just after the regular decrease of it. Another new finding is the peak frequency increase on the late decay phase of strong long-duration events.

The spectral peculiarities found are compared then with relevant theoretical expectations derived from model simulations of radio emission generation. It is shown that an analysis of the observable peak frequency temporal evolution helps determine the relative importance of the self-absorption and Razin suppression in a specific microwave source. It is found that in most of the bursts, (60%), the spectral dynamics of peak frequency, at least at intensities close to the maximum flux, is caused by the self-absorption. On the other hand, for some, quite large group of events (20-30%), Razin effect plays the dominant role in defining the spectral peak and dynamics of peak frequency, especially on the early rise phase and late decay phase of the bursts.

In Chapter 5 the solar flare parameters are derived using the microwave flux spectra of 412 flares measured with the Ownes Valley Solar Array (OVSA) in 2001-2002 and complementary data from Nobeyama Radioheliograph (NoRH). The analysis is carried out using the events selected as due to gyrosynchrotron emission based on the spectra measured with high spectral resolution ($\Delta\nu/\nu \leq 0.2$) over the range 1-18 GHz. The flux density and frequency of the spectral maximum and the spectral slope above the maximum frequency is measured, to obtain statistical distri-

butions of key parameters. The simplified expressions of gyrosynchrotron formulae by Dulk & Marsh (1982) are used to convert these statistical quantities to statistical distributions of physical parameters. The parameters include the power-law index of the nonthermal electron energy distribution, total number and total energy of the nonthermal electrons integrated over space and energy. The resulting parameters are briefly compared with the previous results based on X ray observations for insights into particle acceleration and flare energy release.

Chapter 6 focuses on the properties of decimetric spike bursts occurring simultaneously with microwave gyrosynchrotron continuum bursts. It is found that all of the accompanying microwave bursts were highly polarized in the optically thin range. The sense of polarization of the spike clusters is typically the same as the optically thin gyrosynchrotron emission, implying preferential extraordinary-wave-mode spike polarization. Optically thick spectral indices of the continuum in spike-producing events were not observed to be larger than 2.5, suggesting low or absent Razin suppression. This implies that the plasma frequency to gyro-frequency ratio is systematically lower in the spike-producing bursts compared to other bursts. The spike cluster flux density is found to be tightly correlated with the high-frequency spectral index of the microwave continuum for each event, while the flux-to-flux correlation may not be present. It is discovered a strong evidence that the trapped fast electrons producing the microwave gyrosynchrotron continuum have an anisotropic pitch-angle distribution of the loss-cone type in the spike-producing bursts. The spike clusters are mainly generated when the trapped electrons have the hardest and the most anisotropic distributions. The new properties are discussed against the currently available ideas about emission processes and models for spike generation. It is concluded that the findings strongly support the electron cyclotron maser mechanism of spike emission, with characteristics agreeing with expectations from the local-trap model.

CHAPTER 2

THE PEAK FLUX DISTRIBUTION OF SOLAR RADIO BURSTS

2.1 Introduction

The published frequency distributions of peak fluxes in solar flares were reviewed by Aschwanden, Dennis & Benz (1998), as observed in hard X-rays, soft X-rays, optical, radio, and energetic particles in interplanetary space. Since then, frequency distribution studies continue to be popular, with recent studies by Wheatland & Glukhov (1998), Isliker & Benz (2001), and Moon et al. (2001). The published distributions for microwaves were obtained solely from bursts during or prior to solar cycle 19 (1951-1962), by Akabane (1956), Kundu (1965), and Kakinuma, Yamashita & Enome (1969), as derived from observations by single instruments. Since 1960, the National Geophysical Data Center (NGDC) of the National Oceanic and Atmospheric Administration (NOAA) has compiled reports from a worldwide network of radio observing sites. We study the statistical properties of 40 years of radio bursts contained in these reports, from 1960-1999.

There are two main goals of this paper. The first goal is to determine the absolute rate of occurrence of radio bursts vs. flux density—the cumulative distribution. This is motivated by our interest in solar radio bursts as potential sources of interference in wireless communication systems. Evidence that solar radio bursts can cause such interference was given by Lanzerotti, Thomson & MacLennan (1999), in a review paper on Space Weather effects on technology, who showed that dropped call rates increased in a microwave antenna facing east at sunrise during a solar flare. Preliminary statistical results on this subject were given in an earlier paper, Bala et al. (2002), and an individual X-ray class X5.6 solar radio event was discussed in Lanzerotti et al. (2002). In this paper we extend the statistical results to lower flux densities and include corrections for missed events, which raises the occurrence rate by more than a factor of two.

The second goal of this work is to determine the parameters of the differential, or density distribution of radio bursts, as it may relate to the concept of Self-Organized Criticality (SOC – Bak, Tang & Wiesenfeld 1988; Lu & Hamilton 1991). Most studies of solar burst occurrence distributions have focused on hard X-ray bursts (e.g. Bromund, McTiernan, & Kane 1995; Kucera et al. 1997; Wheatland 2000*a*; Lin, Feffer & Schwartz 2001; Georgoulis, Vilmer & Crosby 2001), soft X-ray bursts (Boffeta et al. 1999; Wheatland 2000*b*; Moon et al. 2001) or EUV and soft X-ray brightenings (Shimizu & Tsuneta 1997; Berghmans, Clette, & Moses 1998; Krucker, & Benz 1998; Parnell & Jupp 2000; Aschwanden et al. 2000). Some early work (Akabane 1956; Kundu, 1965; Kakinuma, Yamashita & Enome, 1969) described power-law distributions of microwave radio bursts. To our knowledge, however, no study in microwaves has been done since these early papers, although Mercier & Trottet (1997) and Aschwanden et al. (1997) have looked at distributions of peaks during individual bursts at frequencies below 1 GHz. In this study, we wish to examine the microwave distributions as a function of solar cycle and radio observing frequency, in order to search for systematic changes in the distributions. Such changes would perhaps relate to the underlying physics of solar radio bursts. Since the radio emission mechanism (see, e.g. Dulk 1985) changes from predominantly gyrosynchrotron emission at high frequencies (> 2 GHz) to predominantly plasma emission below about 2 GHz, we are especially interested in solar cycle changes in these two frequency regimes.

In §2.2, we describe the data set and some general statistics of radio burst and flare occurrence rates. In §2.3, we detail the analysis procedure, including assigning of entries to events, and our method to account for missed events. In §2.4 we outline our method for obtaining a consistent power-law fit to the density and cumulative distributions. We present the results in §2.5, including tables of fit parameters that

can be used to calculate the occurrence rate of bursts in a number of frequency ranges and epochs. We list our conclusions in §2.6.

2.2 Data Description

The solar radio burst data that are analyzed for this study were obtained from the National Geophysical Data Center (NGDC) of the National Oceanic and Atmospheric Administration (NOAA), Boulder, Colorado. The original data set was a compilation of solar radio burst measurements supplied to NGDC by various solar radio observatories around the world during 1960 through 1999. Over this forty-year interval the number and location of radio observatories have changed, as did the frequencies of observation. Further, over this interval, it is likely that instrumentation has changed considerably. Thus, the data set could suffer from several types of bias.

One type of bias—incomplete observing coverage (missed events)—is illustrated in Figure 2.1, where the number of radio bursts is compared with the number of optical ($H\alpha$) flares reported to NGDC from 1965-2000. Although the radio burst reports began in 1960, during the decline of solar cycle 19, the total number of bursts reported in the rising phase of cycle 20, beginning in 1965, is obviously a small fraction of the actual number that occurred. This situation persisted until at least 1969. In general, with the exception noted for cycle 20, Fig. 2.1 shows that the number of radio bursts corresponds reasonably well with the number of optical flares, although there may be a tendency for the relative number of radio bursts to increase in the later phase of each cycle. We used two approaches for estimating the extent of missed events. The first is to examine the number of bursts as a function of hour of the day, which shows the extent of changes in longitudinal coverage by reporting observatories around the globe. The second is to examine waiting times between bursts. If considered a Poisson process, an estimate of the true occurrence

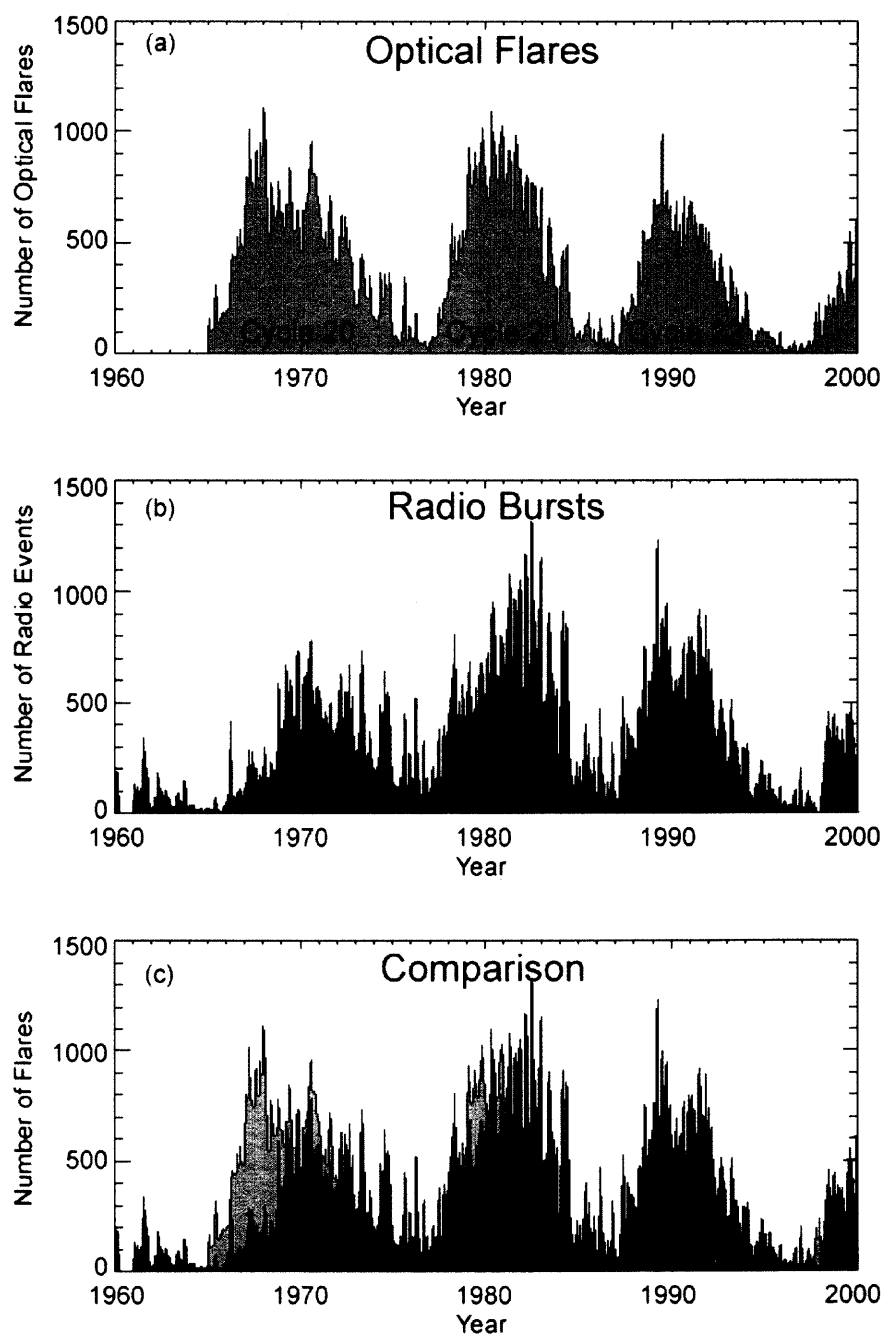


Figure 2.1 (a) The number of optical flares since 1965, as reported in the *Solar Geophysical Data* publication of the NGDC. (b) The number of radio *events* determined from the 40-year database of radio bursts considered in this paper. (c) A comparison of the two, where the light color represents the optical flares and the dark color represents the radio events. The numbers agree closely over most of the range (no scaling of numbers has been done). The radio bursts are likely under-counted before 1970.

rate can be established and then compared with the observed one. Both approaches are described in more detail in the next section.

Other biases to be expected are limitations in detection sensitivity (at small fluxes), and saturation of receivers (at large fluxes). These biases will change over the 40-year period, and with observing station. Obvious sensitivity biases are found in some frequency ranges (notably the low and high end), but they likely exist even at frequencies where they are not obvious. It is important to keep these caveats in mind during interpretation of the observations. Nevertheless, to the best of our knowledge, this is the best (and only) set of data of its kind available over such a long time span. It is therefore worth examining, both for what it can tell us about the Sun, and how the bursts may contribute to the expected noise levels in contemporary and future wireless communications technologies.

The reported quantities used for this study are the observing frequency, the peak flux at that frequency in solar flux units ($1 \text{ SFU} = 10^{-22} \text{ W m}^{-2} \text{ Hz}^{-1}$), and the start time of the burst, in UT. The time is not actually needed for the flux distributions themselves, but we use it to explore some statistical properties of the dataset, as we will detail below. The peak time for each burst was also reported, but we decided to use the start time because (i) not all entries include a peak time, (ii) the peak time can change considerably with frequency for a given event, and (iii) the start time was considered to more reliably represent the event occurrence time, for the purposes we use it here (see below).

Some statistics of the dataset are given in Table 2.1. In all, the database contains over a half-million entries. We group the entries into events following the procedures in the next section, which yielded 155396 events. These numbers imply an average time between entries, $\langle \Delta t_{\text{entries}} \rangle = 40.57$ minutes, and average time between events, $\langle \Delta t_{\text{events}} \rangle = 135.39$ minutes. The inverse of these times, expressed in hr^{-1} , gives the average occurrence rates 1.48 entries/hr, and 0.44 events/hr, respectively.

Table 2.1. Statistics of the Data Set

Epoch	N_{entries}	N_{events}	$\langle \Delta t_{\text{ent}} \rangle$ (min)	$\langle \Delta t_{\text{ev}} \rangle$ (min)	N_{ent}/T (ent/hr)	N_{ev}/T (ev/hr)	$N_{\text{ent}}/N_{\text{ev}}$
1960-1999 (All 40 yrs)	518606	155396	40.57	135.39	1.48	0.44	3.34
1966-1975 (Cycle 20)	129066	39074	40.75	134.60	1.47	0.44	3.30
1976-1985 (Cycle 21)	208661	59175	25.21	88.88	2.38	0.67	3.53
1986-1995 (Cycle 22)	155250	45391	33.88	115.87	1.77	0.52	3.42
12 solar max years (69-72, 79-82, 89-92)	327580	87516	19.27	72.11	3.11	0.83	3.74
12 solar min years (66-67, 74-77, 84-87, 94-95)	77034	28261	81.93	233.30	0.73	0.27	2.73

Table 2.2. Statistics of Optical Flares

Epoch	N_{flares} (min)	$\langle \Delta t_{\text{flares}} \rangle$ (min)	N_{flares}/T (flares/hr)	$N_{\text{flares}}/N_{\text{bursts}}$
1965-1999 (35 yrs)	155171	118.63	0.51	1.02
1966-1975 (Cycle 20)	56548	93.0	0.65	1.45
1976-1985 (Cycle 21)	53070	99.11	0.61	0.90
1986-1995 (Cycle 22)	36198	145.30	0.41	0.80
12 solar max years (69-72, 79-82, 89-92)	97188	54.12	1.12	1.11
12 solar min years (66-67, 74-77, 84-87, 94-95)	30743	171.08	0.35	1.09

Corresponding quantities for different time ranges (column 1 of the table) are also given. Note that the apparent occurrence rate varies significantly from one solar activity cycle to another. The rate for Cycle 21 (1976-1985) is significantly higher (0.67 events/hr) than for Cycles 20 (0.44 events/hr) and 22 (0.52 events/hr). Cycle 20 is likely undercounted, as indicated by Fig. 1, but the larger number of solar radio events observed in Cycle 21 over Cycle 22 is probably a real solar effect.

Some related statistics for optical flares are shown in Table 2.2, based on the information in Fig. 2.1. One can see the effect of undercounting of radio events in Cycle 20, where the ratio $N_{\text{flares}}/N_{\text{bursts}}$ is a factor 1.6 larger than for Cycle 21.

Later we will divide the events into several frequency ranges to investigate the frequency dependence of the burst occurrence rate and flux density distributions.

Figure 2.2 shows the way in which the burst reports were distributed in frequency. Because of gaps in the frequency coverage, we used non-adjoining frequency ranges as shown by the gray regions in the figure, with gaps indicated by the spaces between the gray regions. The ranges, in GHz, are: < 1 , 1–1.9, 2–3.8, 4.9–7, 8.4–11.8, and 15–37.

2.3 Data Analysis

2.3.1 Assigning Entries to Events

The dataset provided by NGDC consists of a series of reports (hereafter called *entries*), each representing one observatory’s observation at one frequency. Multiple entries exist for most bursts, due both to observations of the same burst at multiple observatories and to reports of multiple frequencies at a given observatory. In order to count bursts (hereafter referred to as *events*), we must identify those entries belonging to a given event. This is done routinely by NGDC in their list of “Radio Emission Outstanding Occurrences,” but the dataset available to us did not contain this information. Therefore, we examined several ways to automate the task of assigning entries to events, all based on the concept of a window of time in which all entries with a start time within the window are assigned to the same event, while the next following entry outside the window begins a new event. The key task is then to determine the most appropriate length of this time interval so that long-lasting bursts will not be subdivided and separate bursts that occur near the same time are not incorrectly combined.

Bala et al. (2002) estimated this interval by examining the cumulative distribution of durations given for all of the entries in the entire database. They showed that the distribution attained 50% at a duration of ~ 12 minutes, meaning that half the entries had durations less than 12 minutes and half lasted longer than 12 minutes.

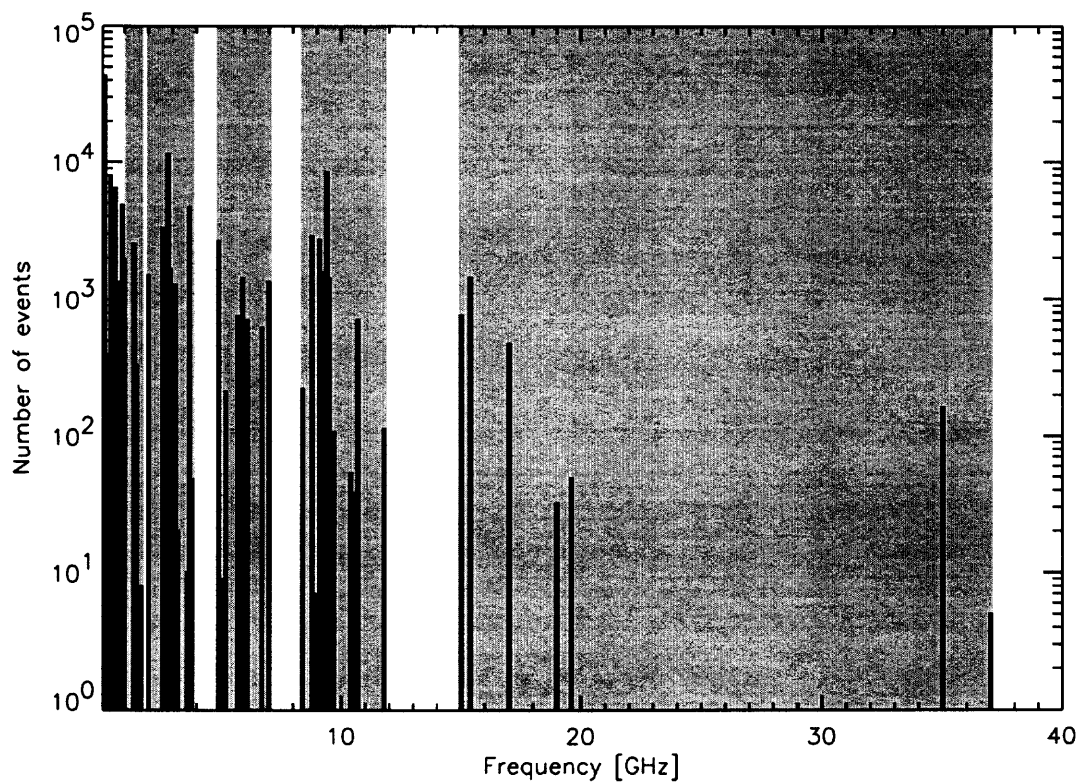


Figure 2.2 A plot showing the distribution of observing frequencies represented in the database (black histogram), and the choice of frequency windows over which we accumulation data (gray). There are several gaps in which no observations are taken, hence our frequency ranges also reflect these gaps. The large range 15–37 GHz is kept, despite the large gap in coverage from 19 to 35 GHz, since splitting it into subranges would leave too poor statistics for the 35–37 GHz range.

However, the question of duration is somewhat different from the question of time between events (i.e., the *waiting time*). To investigate further, we have analyzed the waiting time distribution corresponding to the entries in our data set. Treating entries as independent occurrences, one can use Poisson statistics to investigate the parent population. We expect to have two independent populations: entries belonging to the same event, which should occur close together in time, and entries belonging to new events, which should obey Poisson statistics. Figure 2.3 shows the distribution of waiting time between entries for entries separated by 60 minutes or less. The events are binned in 1 minute boxes.

A small, systematic quirk in the dataset is apparent in the histograms of Fig. 2.3. There tends to be a slight increase in the number of entries at time differences with approximately 5 minute spacing. That is, at or just prior to 10, 15, 20, 25, etc. minutes. This is likely a human bias in assigning the start times.

The figure shows the influence of at least three time-scales: (1) The bins from 0-4 minutes likely are due to slight differences in start time reported by independent observatories. (2) The intermediate times up to about 20-25 minutes likely are due to real solar processes, giving rise to multiple bursts from a single energy release. (3) The slower drop in the 30-60 minute time range is well fit by an exponential decay of time constant $\tau_b = 37$ min, which would be expected if the events were independent events that occur according to Poisson statistics. In this case, τ_b would be identified as the timescale for occurrence of independent events. However, it is well-known that solar bursts occur at vastly different rates at different times in the solar cycle, as shown, e.g., in Fig. 2.1. This *non-stationary* Poisson process produces other distributions than a simple exponential one (Boffeta, et al. 1999; Wheatland 2000b), which are more easily visible at longer waiting times.

We show in Figure 2.4 the distribution for longer waiting times, where the effect of the non-stationarity is more apparent. The data are plotted with log-log

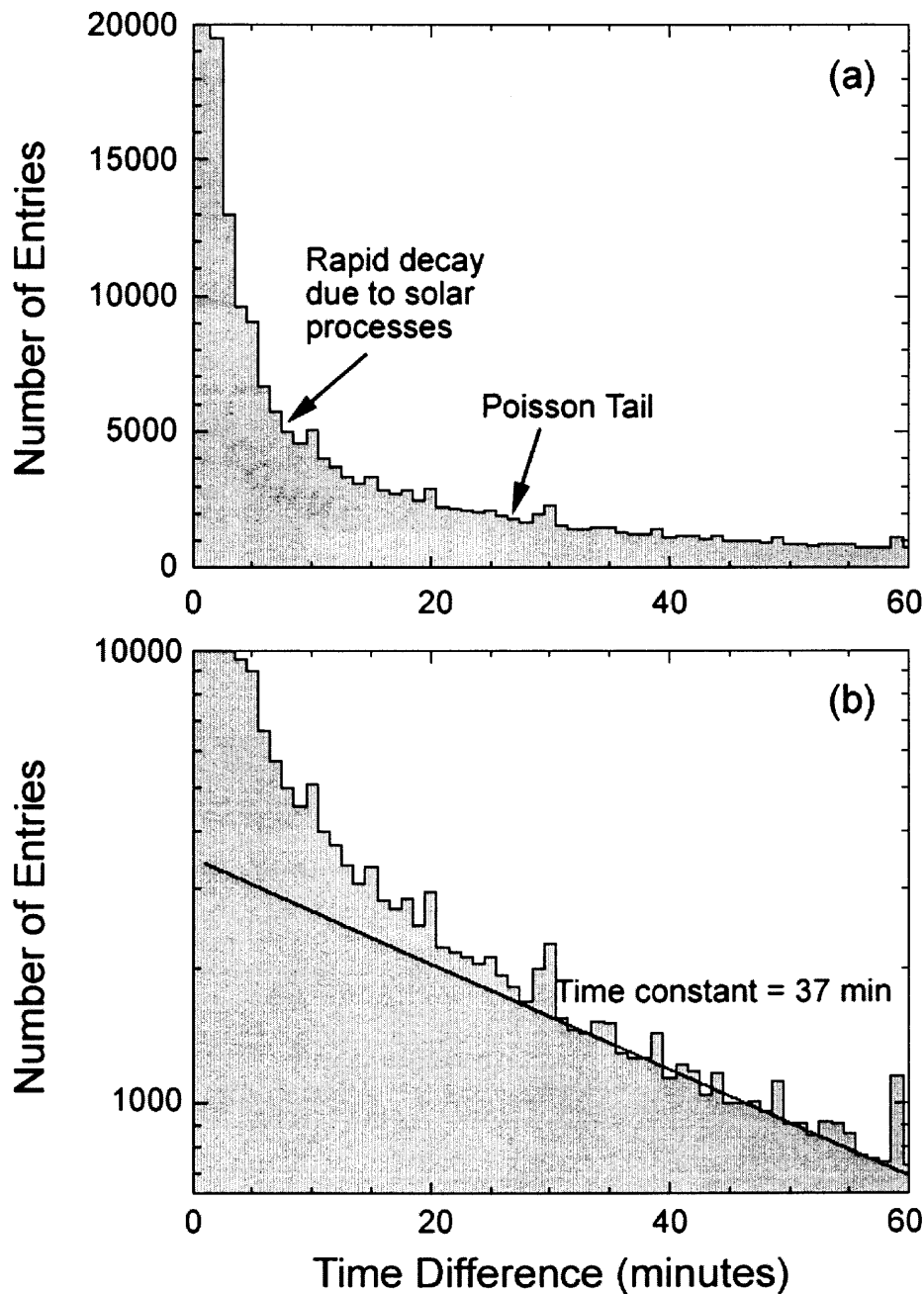


Figure 2.3 Waiting time distribution of entries in the entire database, out to 60 minutes. The upper panel is a linear plot showing a rapid drop at small waiting times and a slower decay at longer waiting times. The lower panel shows the same information on a log-linear scale, along with an exponential fit corresponding to a decay time constant of 37 min.

axes, and with logarithmic bins, following the approach of Wheatland (2000*b*). The logarithmic bins cause the distribution to be no longer monotonically decreasing, as in Fig. 2.3, but rather to slightly increase at short waiting times to a peak near 1 h. For comparison, the dotted line shows the exponential curve with 37 min time constant shown in Fig. 2.3*b*, and the solid line shows the function obtained by Wheatland (2000*b*) assuming an exponential distribution of flaring rates. The Wheatland model fit is parameterized in terms of λ_0 , the mean burst rate for the entire 40-year period, whose inverse corresponds to a mean waiting time of 81 min. This is about twice the 37 min inferred from the fit for a single Poisson rate that we found before, but still shorter than the 135 min mean waiting time shown in Table 2.1, which came from an average over the entire dataset. We will come back to this point later when we discuss missed events.

One implication of Fig. 2.4 is that a single time-constant cannot fit the longer waiting times, which are a consequence of the non-stationarity of the Poisson processes. However, the two curves in Fig. 2.4 agree closely over the 30-60 min range, and phenomenologically at least, the 37 minute time constant does describe the dominant scale at short waiting times. This 37 minute timescale is the relevant one for our purposes of distinguishing between multiple entries of a given burst and the occurrence of a new burst.

The rapid decay of entries at time differences ≤ 20 minutes in Fig. 2.3 we believe represents the time scale of multiple reports for a given solar burst, which should be ascribed to a single event. To get a better measure of this decay time, we line up events (epoch-folding) by identifying the first entry in an event and looking at the time differences of later entries relative to these events. We define as “leader entries” those that have no entries in the preceding 60 minutes, so that we can be reasonably sure that they are the first observed entries in some well-separated events. Figure 2.5 shows the distribution we obtained.

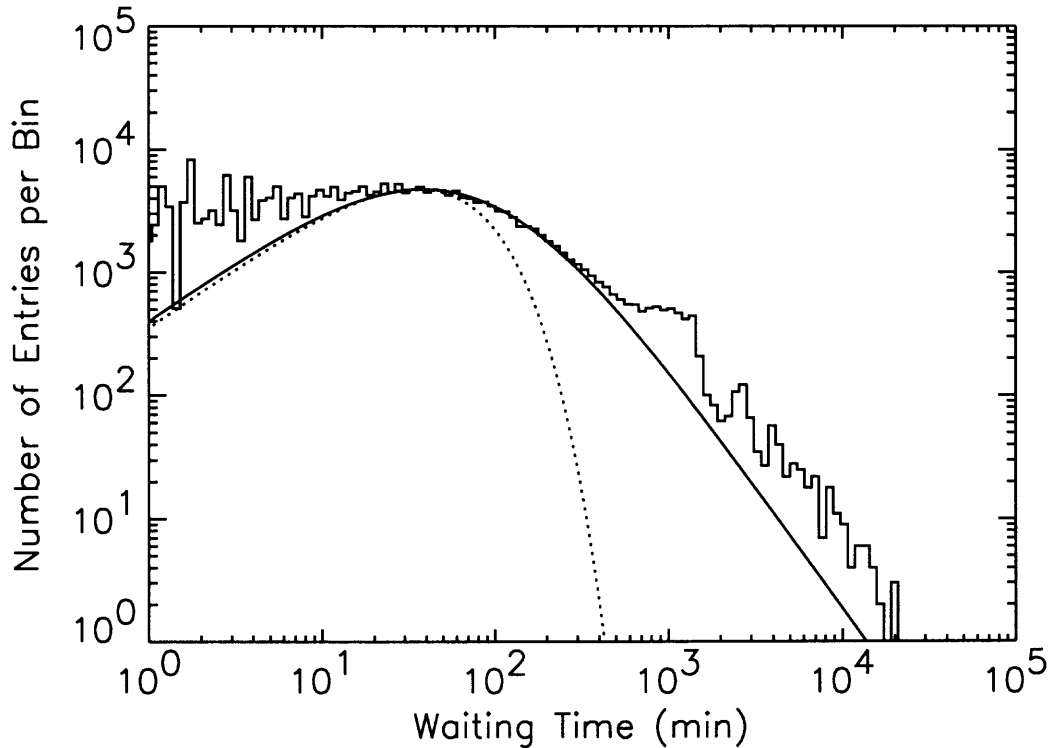


Figure 2.4 Waiting time distribution of entries in the entire database, out to 10^5 min, plotted on a log-log scale with logarithmic binning. The distribution is similar to that found for soft X-ray events by Boffeta et al. (1999) and Wheatland (2000*b*). The dotted line shows the exponential fit of Fig. 2.3*b*, with time constant 37 min, for comparison. The solid line, which corresponds to a mean waiting time of 81 min, is the curve given by the Wheatland (2000*b*) model, which assumes an exponential distribution of flaring rates. Prominent features near 1, 2, and 3 days are likely artifacts due to human bias in the event reports.

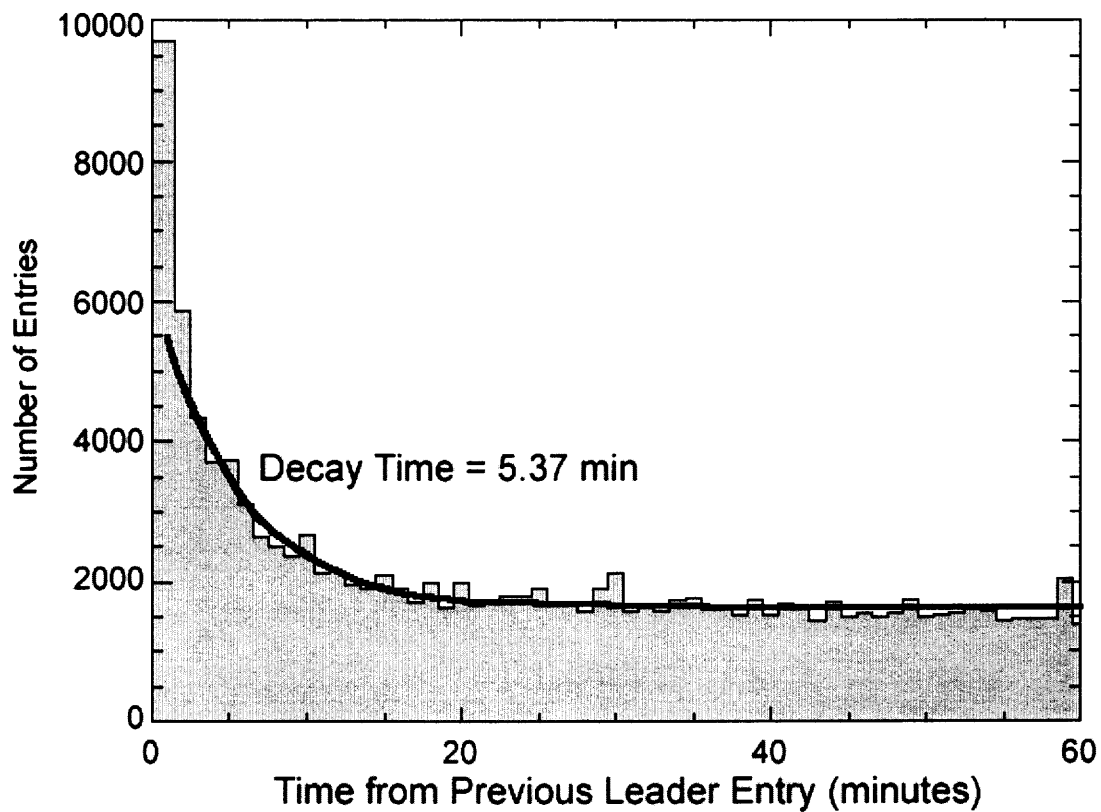


Figure 2.5 Distribution of waiting times of subsequent entries relative to the Leader Entries, which are defined as having no preceding entries for at least 60 min earlier. The entries show a natural fall-off of 5.37 min time constant, merging with a general background of uncorrelated entries.

In Fig. 2.5, those entries that are correlated with the leader entries have a natural decay. On the other hand, those entries that are uncorrelated with the leader entries are evenly distributed in time. Excluding the first 3 bins (which again we believe are affected by uncertainties in the reporting of start times) and fitting a function of the form $N(t) = Ae^{-\frac{t}{\tau_d}} + B$, we find an average decay constant of $\tau_d = 5.37$ minutes together with a flat distribution of $B = 1640$ entries representing the random occurrence of additional events.

We now have two competing time constants, one for entries to belong to an *old* event, $\tau_d = 5.37$ minutes, and one for entries to belong to a *new* event, *i.e.*, the dominant mean time between solar bursts, $\tau_b = 37$ minutes. After a first entry is observed, the probability that a subsequent entry belongs to the *old* event is a decreasing one:

$$P_{old}(t) = e^{-\frac{t}{\tau_d}},$$

while the probability that it belongs to a *new* event increases as:

$$P_{new}(t) = 1 - e^{-\frac{t}{\tau_b}}.$$

From these relationships, and the ratio of these probabilities, we find that after ~ 12 minutes an entry is 3 times more likely to belong to a new event as to belong to the leader event. Hence we choose $\Delta t = 12$ min for the time window, in agreement with the value adopted by Bala et al. (2002), arrived at by other means as previously explained.

Armed with the window width, we separated entries into events using the following algorithm:

1. The time window of length Δt is moved continuously over the data set sorted in chronological order.

2. The origin of the time window is fixed to the first observed entry, and all entries bounded by the window receive a numerical label specifying that they all belong to the same event.
3. The origin of the time window is then moved to the next following entry outside the window, and the process is repeated.

The above procedure is slightly different from that used by Bala et al. (2002). At step (2), above, they extended the length of the window until the next gap of at least 12 min, so that a series of bursts separated by less than 12 min, but having a total duration of more than 12 min, were counted as a single event. We believe that our algorithm better matches the waiting time approach that we have followed. However, we checked the total number of events obtained using both approaches and found little difference in practice.

The statistics of number of entries per event, and number of events per hour, are given in Table 2.1, where we see that the average of about 3.3 entries per event is nearly independent of solar cycle, although it is higher, 3.7, for the solar maximum years than for solar minimum, 2.7. This may indicate a decrease in diligence on the part of the reporting stations during solar minimum years.

2.3.2 Geographical Correction Factor

We are interested in the absolute rate of occurrence of bursts of a given flux density—that is, we want the offset as well as the slope of the distribution. We therefore want to determine whether a significant number of events were missed by the reporting observatories. Indeed, the larger number of optical flares relative to radio burst until about 1970 in Fig. 2.1 shows that many radio bursts were likely missed at least during that epoch. The results of the fit in Fig. 2.4 also suggests that there are missing events, since the 135 min mean waiting time from the data in Table 2.1 is longer than the inferred 81 min waiting time from the Wheatland (2000*b*) model.

One possible reason for missing events is uneven observational coverage at different longitudes on the Earth. To investigate this, we bin the events according to time of day, since the solar distribution should be uncorrelated with UT. Thus, bursts should be evenly distributed in time of day unless longitudinal coverage were non-uniform. As a test of this idea, we first plot the distribution of events vs. time of day from the BATSE flare catalog. The BATSE instrument on the Compton Gamma-Ray Observatory orbited the Earth many times during a day, so its longitudinal coverage over the entire mission could be expected to be uniform. Figure 2.6 shows a comparison of BATSE X-ray data (Fig. 2.6a) and our radio events (Fig. 2.6b) for the same period, 1991 – 1999. For BATSE, the observed standard deviation (dotted horizontal lines in Fig. 2.6a) agrees quite well with that expected from Poisson statistics (dashed horizontal lines), for a flat distribution. In contrast, it is obvious that radio data do not obey a flat distribution in UT, having a standard deviation much greater than the square root of the mean number.

We interpret the variations in this figure as variations in the efficiency of radio observing and reporting vs. Earth longitude. To see how the longitudinal coverage may have changed over the three solar cycles covered by these data, we plot in Figure 2.7 the radio events vs. time of day for bursts > 1000 MHz (left-hand panels) and bursts < 1000 MHz (right-hand panels).

We use the results of Figure 2.7 to form a *geographical correction factor*, in order to estimate and correct for the proportion of missed events. We assume that the peaks in the distribution represent 100% efficiency. This is likely to be an overestimate, meaning that the correction factor is underestimated and the proportion of missed events is even higher than we derive. The correction factor is

$$C_{geo} = \frac{N_{\text{peak}}}{N_{\text{mean}}},$$

where N_{peak} is the number at the peak of the distribution and N_{mean} is the mean number of events over the 24 h period. The correction factor varies from year to

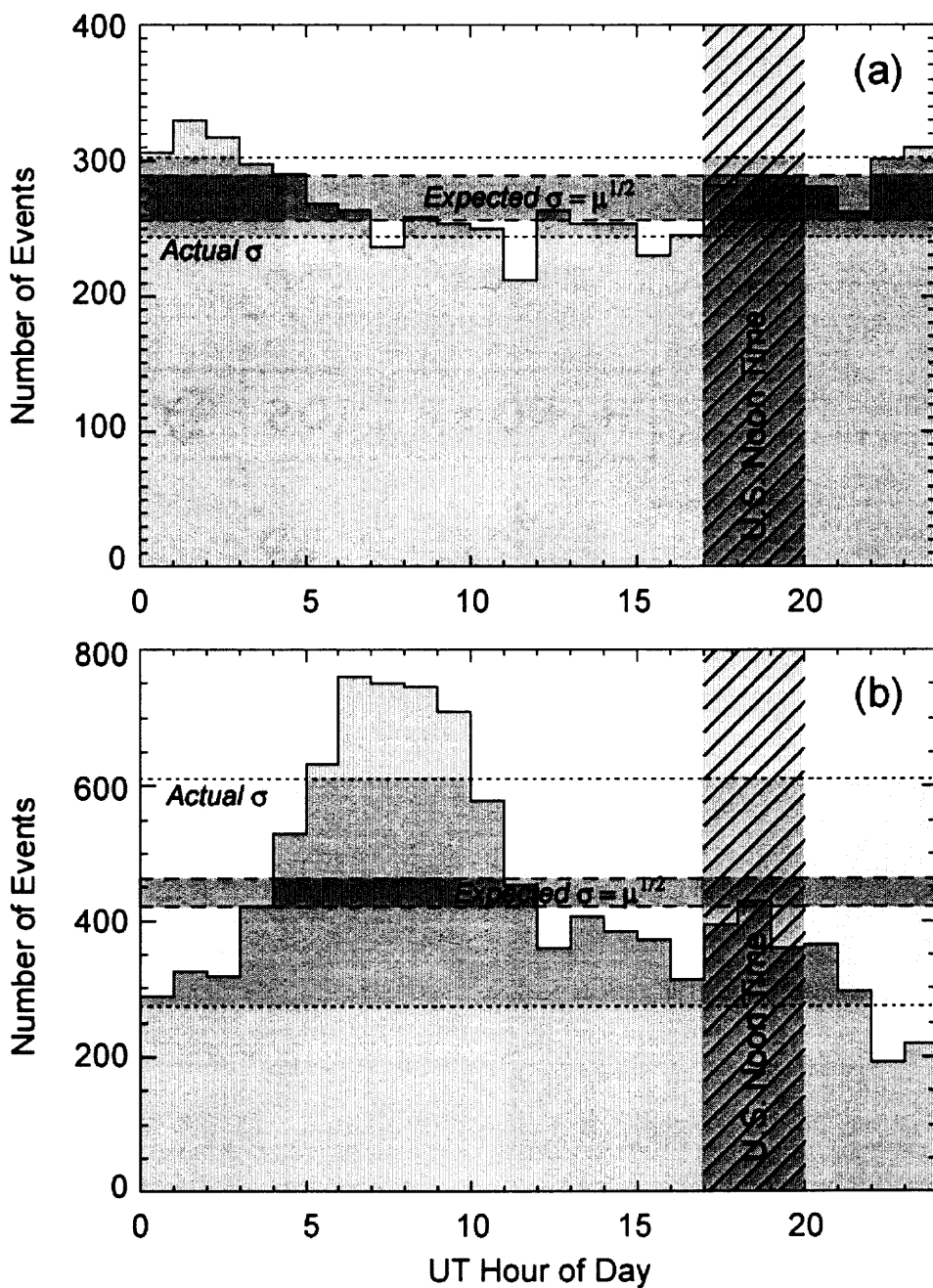


Figure 2.6 Time-of-day distribution of (a) BATSE hard X-ray bursts, and (b) radio bursts from the NOAA database, for the period 1991-1999. The BATSE events are consistent with a uniform distribution, indicating that all Earth longitudes are equally well covered, while the radio events show a large non-uniformity with longitude, including a large peak at Universal Times corresponding to morning hours in Western Europe.

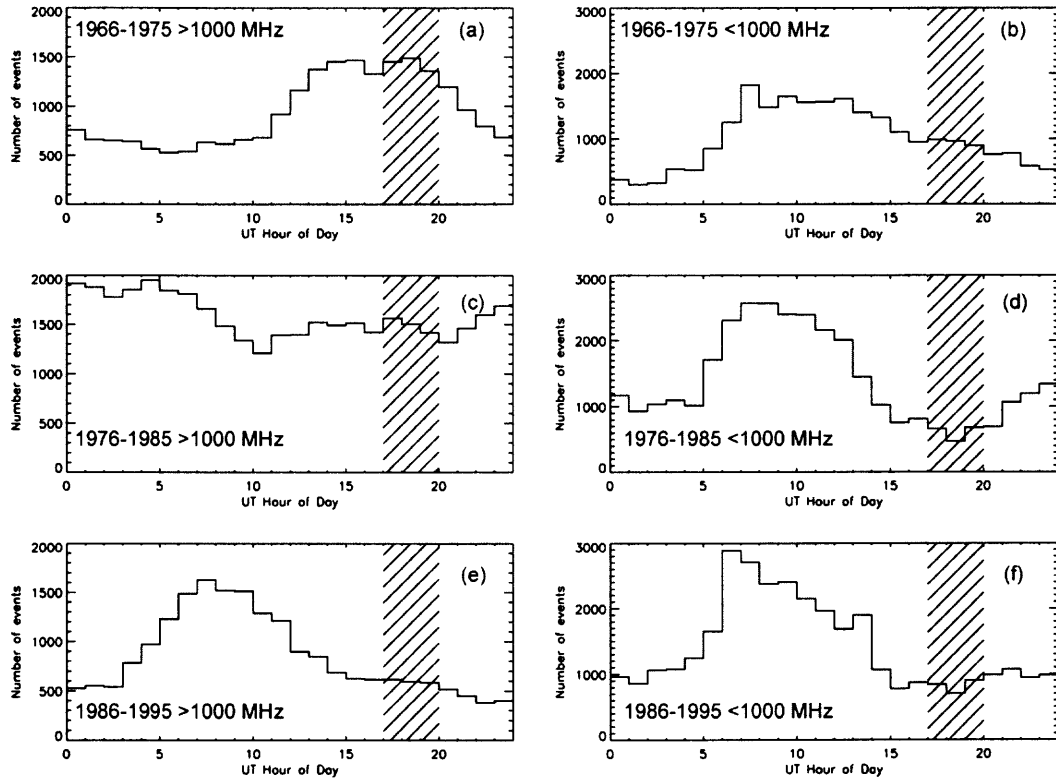


Figure 2.7 Time-of-day distribution of radio bursts from the NOAA database, for three complete solar cycles. Longitudes representing local noon in the continental United States are shown with hatched areas. The longitudinal coverage of radio events has clearly changed, especially for bursts at frequencies > 1000 MHz, with a dominance at Western Hemisphere longitudes in solar cycle 20 (upper left panel) giving way to a deficit at those longitudes by solar cycle 22 (lower left panel).

year and is frequency dependent, but remains about 2, in near agreement with the ratio of mean waiting times $135/81 = 1.67$ obtained from the dataset and from the Wheatland (2000b) model.

2.3.3 Computing Number Density Distributions

Having organized the entries in our data set into events, we are ready to compute the number density and cumulative distributions for the events in various frequency ranges and epochs. To do this, each event must be represented by a single flux value. However, an event can be represented by more than one entry because it may have been detected in several frequency ranges. Consider the schematic representation of the radio spectrum of a typical solar burst (e.g. Guidice & Castelli 1975), shown in Figure 2.8. Assume that this event is reported in 5 separate entries in the data, shown at 5 different frequencies by the dots. Further assume that we are considering several different frequency ranges with edges given by the vertical dashed lines.

To decide what representative flux value to use for each event in each frequency range, we developed two different approaches:

1. For each frequency range, choose the entry with the maximum flux density. The schematic event in Fig. 2.8 would be included in the distributions in 4 frequency ranges, represented by entries 1, 2, 3 and 5. Entry 4 would be dropped because it has a lower flux density in the same frequency range as entry 3. This we call the *Max Flux* approach, and it is suitable for looking at the likelihood of solar radio interference on wireless devices (goal 1 of the Introduction).
2. For each event, choose the entry with the maximum flux regardless of the frequency, and throw out all other entries. Then each event is represented only in the frequency range where the event peaks. In the example in Fig. 2.8, only entry 2 is counted (retaining information about both the peak amplitude

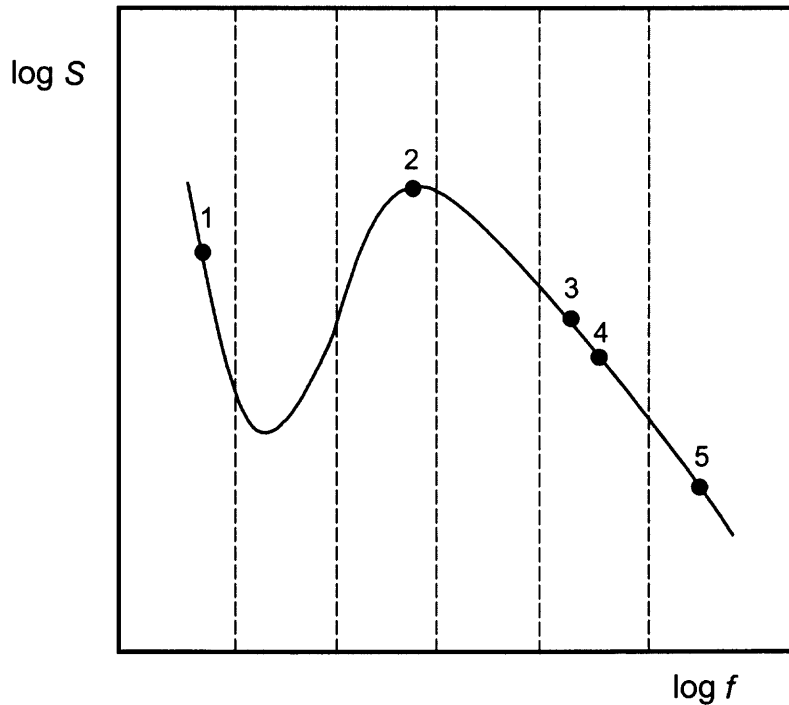


Figure 2.8 A schematic representation of the radio spectrum of a typical solar burst. The flux density S may be high at low frequencies due to plasma emission, then drops to a minimum near 2 GHz and rises again due to gyrosynchrotron emission to a peak near 5-10 GHz. At high frequencies, the emission is optically thin and decreases with increasing frequency. The example shows five entries with flux densities represented by dots at five frequencies. The vertical dashed lines divide the spectrum into several frequency ranges.

and frequency). Thus, an event is counted only once, no matter how many frequency entries are reported. This we call the *Selected Peak* approach, and we believe it may give more suitable number density distributions for investigating systematic changes of solar bursts vs. frequency or solar cycle (goal 2 of the Introduction).

The Selected Peak approach, applied strictly, would not count each event more than once over whole frequency range of the data set. However, because different radio emission mechanisms tend to dominate on either side of ~ 2 GHz (plasma emission below ~ 2 GHz and hyperresonance emission above ~ 2 GHz), we allowed each event to be represented in both low-frequency (below 2 GHz) and high-frequency (above 2 GHz) ranges. This allows us (roughly) to consider these two mechanisms separately.

Because the Selected Peak approach does not count an event above 2 GHz more than once, the distributions in different frequency ranges (above 2 GHz) can be added to obtain the distributions corresponding to an enlarged frequency range. This is *not* true of the distributions obtained by the Max Flux Approach.

To determine reliable distributions we filtered data using the peak time qualifiers recorded in the catalog for each entry. That is, we used only those entries that had a valid peak flux entry. Although, generally, this operation dropped only some of the unreliable entries belonging to the same event (keeping the reliable ones), some events were dropped completely from the statistics. The number of dropped unreliable events represents 9.76% of the total number of events reported in Table 2.1 for the 40-year interval.

2.3.4 Power-Law Fitting Algorithm

2.3.4.1 Number Density and Cumulative Distributions

Assuming that the number of events versus radio flux density (expressed in SFU) follows a power-law

distribution, as expected under the influence of Self-Organized Criticality,

$$\frac{dN}{dS} = \frac{dN}{dS} \Big|_{S=1} S^\lambda, \quad (2.1)$$

the number of events expected to be counted in a given, discrete flux range is

$$\Delta N(S_1, S_2) = \frac{1}{\lambda + 1} \frac{dN}{dS} \Big|_{S=1} (S_2^{\lambda+1} - S_1^{\lambda+1}). \quad (2.2)$$

In order to compute from experimental data the parameters describing (2.1), one has to count the number of events, ΔN , recorded in different flux bins ΔS . In accord with equation (2.2), one may write the ratio of these discrete magnitudes corresponding to the i^{th} bin as:

$$\left[\frac{\Delta N}{\Delta S} \right]_i = \frac{1}{\lambda + 1} \frac{dN}{dS} \Big|_{S=1} \frac{S_{i+1}^{\lambda+1} - S_i^{\lambda+1}}{S_{i+1} - S_i} \quad (2.3)$$

We now choose to bin the data in logarithmic flux ranges such that

$$S_{i+1} = kS_i, \quad (2.4)$$

where k is a constant factor related to the logarithmic bin size s by $k = 10^s$. Using (2.4), equation (2.3) becomes

$$\left[\frac{\Delta N}{\Delta S} \right]_i = \frac{1}{\lambda + 1} \frac{k^{\lambda+1} - 1}{k - 1} \frac{dN}{dS} \Big|_{S=1} S_i^\lambda. \quad (2.5)$$

Comparing equation (2.5) with (2.1), it is clear that a power-law fit to $\Delta N/\Delta S$ will yield the correct slope, but the intercept will be incorrect by the bin-size-dependent factor $\frac{1}{\lambda+1} \frac{k^{\lambda+1}-1}{k-1}$, and should be corrected by the inverse *discrete correction factor*

$$C_{disc} = (\lambda + 1) \frac{k - 1}{k^{\lambda+1} - 1}. \quad (2.6)$$

Then the correct intercept is given from the fitted one by:

$$\frac{dN}{dS} \Big|_{S=1} = C_{disc} \left[\frac{\Delta N}{\Delta S} \right]_{S=1}. \quad (2.7)$$

Although the correction is small for small logarithmic bin sizes (only about 10% for $k = 1.12$ and $\lambda = -1.8$), it is nevertheless exactly calculable and should be applied.

In addition to the number density distribution (2.1), we are also interested in the cumulative distribution,

$$N(S) = \int_S^\infty \frac{dN}{dS} dS = -\frac{1}{\lambda + 1} \frac{dN}{dS} \Big|_{S=1} S^{\lambda+1}, \quad (2.8)$$

which is used to estimate the number of events one should expect to be produced above a certain flux limit. Being an integral distribution up to infinity, this function should provide an upper limit for the integral distribution up to the maximum flux observed, and also may be used to estimate the number of events missed in the tail of experimental distribution.

2.3.4.2 Fitting to Functions Obeying Poisson Statistics One may use the standard *Least Square Method* to find the best fit parameters to the power-law distribution. This method, however, when applied to data that obey Poisson statistics, systematically underestimates the area under the curve by an amount equal to the minimum value of the χ^2 function (Bevington & Robinson 1992). The error becomes increasingly important in the case of poor statistics. Moreover, if the fit is intended to be extrapolated beyond the fitting range, the induced error may become important even when negligible in the fitting range.

There is another reason to try another approach. In applying the *Least Square Method* with Poisson statistics, one has no other choice than to use the square root of the number of events in each bin as their estimated errors instead of the *true* errors, which are the square root of the unknown function evaluated for each data bin. Bai (1993) came to a similar conclusion, and was led to develop an alternative approach to fitting the distribution using a maximum likelihood approach similar to that given in Bevington & Robinson (1992). His method uses an arbitrary lower cutoff to the distribution, without an unbiased way of choosing it. His method also fits the data

to infinity without an upper cutoff. This is a special case that may not be valid for observable events, which may have a cutoff due to instrumental saturation or perhaps physical limitations of the energy released in solar bursts (the “finite-size” effect noted by Bak et al., 1988).

We have independently developed a distinct approach that is appropriate to fit data obeying Poisson statistics. Our approach is equivalent to the more general form of the Maximum Likelihood method of Bevington & Robinson (1992), which takes account of both upper and lower cutoffs, but our approach extends this method by taking into account Poisson statistics. We have also developed an unbiased criterion for choosing both upper and lower cutoff.

The number of observed events y_i counted in each bin of the histogram should obey Poisson statistics with a mean, μ_i , that according to (2.2) may be written as

$$\mu_i(a, \lambda) = a \frac{1}{\lambda + 1} (S_{i+1}^{\lambda+1} - S_i^{\lambda+1}), \quad (2.9)$$

where $a \equiv \left. \frac{dN}{dS} \right|_{S=1}$ and λ are the two parameters to be estimated. The probability that all data points are distributed as observed is the product of Poisson probabilities corresponding to each bin of the given histogram:

$$P_d(a, \lambda) = \prod \frac{\mu_i^{y_i}}{y_i!} e^{-\mu_i}. \quad (2.10)$$

The probability of the density distribution, $P_d(a, \lambda)$, should reach its maximum value for those parameters a and λ that give the best estimate for the unknown distribution μ_i . These parameters are the solutions of a generally nonlinear set of equations derived from the condition that partial derivatives of P_d 's logarithm with respect to each parameter must vanish:

$$\sum \left(\frac{y_i}{\mu_i} - 1 \right) \frac{\partial \mu_i}{\partial a} = 0$$

$$\sum \left(\frac{y_i}{\mu_i} - 1 \right) \frac{\partial \mu_i}{\partial \lambda} = 0 \quad (2.11)$$

Equations (2.11) may be generally solved using one of the numerical algorithms available. The uncertainties of the most probable parameters may be evaluated by inspecting the behavior of the probability function $P_a(a, \lambda)$ in the parameter space around its maximum. The standard deviation of each parameter may be defined as the point where the probability's logarithm drops to one half of its maximum value. Since the shape of the probability distribution is not necessarily Gaussian, the standard deviation range may not be centered on the most probable value.

In the special case of a power-law distribution, the problem of finding the most probable distribution reduces to the problem of finding the root of one nonlinear equation instead of solving a system of two equations. Indeed, when the distribution is linear in one of its parameters, as happens to be our case,

$$\mu(a, \lambda) = af(\lambda), \quad (2.12)$$

where

$$f(\lambda) = \frac{1}{\lambda + 1}(S_{i+1}^{\lambda+1} - S_i^{\lambda+1}), \quad (2.13)$$

the system (2.11) becomes

$$a = \frac{\sum y_i}{\sum f_i} \quad (2.14)$$

$$\sum \left(\frac{y_i}{f_i} - \frac{\sum y_i}{\sum f_i} \right) \frac{\partial f_i}{\partial \lambda} = 0 \quad (2.15)$$

and the problem reduces to that of solving a single nonlinear equation, (2.15) for parameter λ , after which a is uniquely determined by (2.14). Note that the uncertainties in the fit parameters a and λ are not independent, and that (2.14) can be used to determine the uncertainty in a for a given uncertainty in λ .

Equation (2.14) offers a direct interpretation of the final results. Using (2.12), (2.14) becomes

$$\sum \mu_i = \sum y_i, \quad (2.16)$$

which means that the total number of events in the observed histogram, $\sum y_i$, is exactly the same as the area of the most probable histogram $\sum \mu$.

Thus, our direct Poisson approach provides the density distribution that is the most probable one to generate exactly the observed number of events in the fit range. This result, of course, is independent of how the data are binned, so it must apply separately to both the density and cumulative distributions. The last observation allows a direct estimate of the probability to observe the given total number of events in the investigated range. This probability is not the same as the probability (2.10) that we maximized before. Rather, it is the Poisson probability of observing in a certain flux range a number of events equal to the mean of the distribution corresponding to this range:

$$P(\sum y_i) = \frac{[\int_{S_{min}}^{S_{max}} \frac{dN}{dS} dS]^{\sum y_i}}{(\sum y_i)!} e^{-\int_{S_{min}}^{S_{max}} \frac{dN}{dS} dS} \quad (2.17)$$

The magnitude of this probability depends on the number of events observed, being different for different fit ranges. If the number of events is very large, this probability is very close to its maximum but, in the case of very small number of events observed, as in the tail of the power-law distribution, the probability may be significantly different from the most probable value. Equation (2.17) may be also used to evaluate the probability to observe a given number of events outside the fitting range, as an alternative test of the goodness of fit, or to test if the discrepancy in the number of events outside the fitted range is due to acceptable statistical fluctuations or to other nonstatistical reasons.

2.3.4.3 Self-Consistent Fits to the Two Distributions Although the fitting procedure described above provides the most probable distribution to generate the observed set of data, the result may be affected by nonstatistical errors that may affect the number of events reported in each bin. If relative nonstatistical errors

may be assumed to be equal for all bins, such in the case of geographical correction discussed before, equations (2.14) and (2.15) show that the real slope cannot be affected and the intercept may be corrected by applying the geographical correction factor to the value resulting from the fit. However, there could be other kinds of nonlinear errors that bias the final results. Several authors have analyzed these sources of bias for power-law distributions. One of the most important is the possibility of missing events at both ends of the distribution—at the low flux density end due to instrumental sensitivity limits, and at the high end due to instrumental saturation or perhaps physical limitations of the energy released in solar bursts (the “finite-size” effect noted by Bak et al., 1988). Due to these biases, which cause deviations from a power-law fit at both ends of the distribution, it is necessary to choose an appropriate range over which to do the fitting. By adjusting the range over which the fit is done, the fit parameters can be appreciably changed. This procedure may be dangerous if one does not have an unbiased criterion to choose the right fitting range. Note that Bai (1993) had no solution to this problem, and simply provided a set of fits for different low-energy cutoffs. Fortunately the method described above also provides a test of self-consistency. This test consists in a comparison between fit results derived from two different ways of binning the same data points. One alternative way to bin the data is through the cumulative distribution, defined as the number of events counted above a certain flux, up to the right edge of the fitting range:

$$w_i = \sum_{i=1}^n y_i. \quad (2.18)$$

Using the same algorithm, the fitting parameters for the cumulative distribution are provided by equations of the same form as (2.14) and (2.15) by replacing y_i with w_i and $f(\lambda)$ with $g(\lambda)$ given by

$$g(\lambda) = \frac{1}{\lambda + 1} (S_{n+1}^{\lambda+1} - S_i^{\lambda+1}). \quad (2.19)$$

The probability maximized in this case is not the same as (2.10), but because the data sets were produced by the same parent population, the probabilities should reach their maximum values for the same parameter λ .

By slowly changing the fit ranges, we were able to find the range that gave the best agreement between fits, within their statistical errors. Figure 2.9 shows an example of the procedure. The lower solid line in Fig. 2.9a is the best fit to the density distribution for the range $10 - 10^{4.5}$ sfu. The same fit parameters predict the upper solid line representing the cumulative distribution. The upper dotted line is the corresponding best fit to the cumulative distribution over the same range, and the two fits do not agree. In Fig. 2.9b the relative probability distributions for λ show the same disagreement. In Fig. 2.9c, d, the procedure is repeated, but fit over a slightly smaller flux range ($10^{1.2} - 10^{3.8}$ sfu). This fit yields essentially identical results for both distributions, within the formal errors. The final fits were obtained by trying different fit ranges, by an automated procedure, until an acceptable agreement was found in the fits to the two distributions. The automated procedure was simply to try every possible fit range in steps of the bin size, and keep all of those with a difference in λ for the two distributions that was less than 0.01. The final fit range was then chosen to be the largest fit range giving this level of agreement (on the general grounds that one should fit the widest possible range of data). In most cases the formal agreement was within 0.001, far smaller than the error in λ for each individual fit.

2.4 Results

We have performed the fits to the number density and cumulative distributions according to the procedure outlined in the previous section, ensuring consistency in the fits between the two distributions in each case. We binned the flux densities using a logarithmic bin size of 0.1, corresponding to the factor $k = 1.12$ in equation

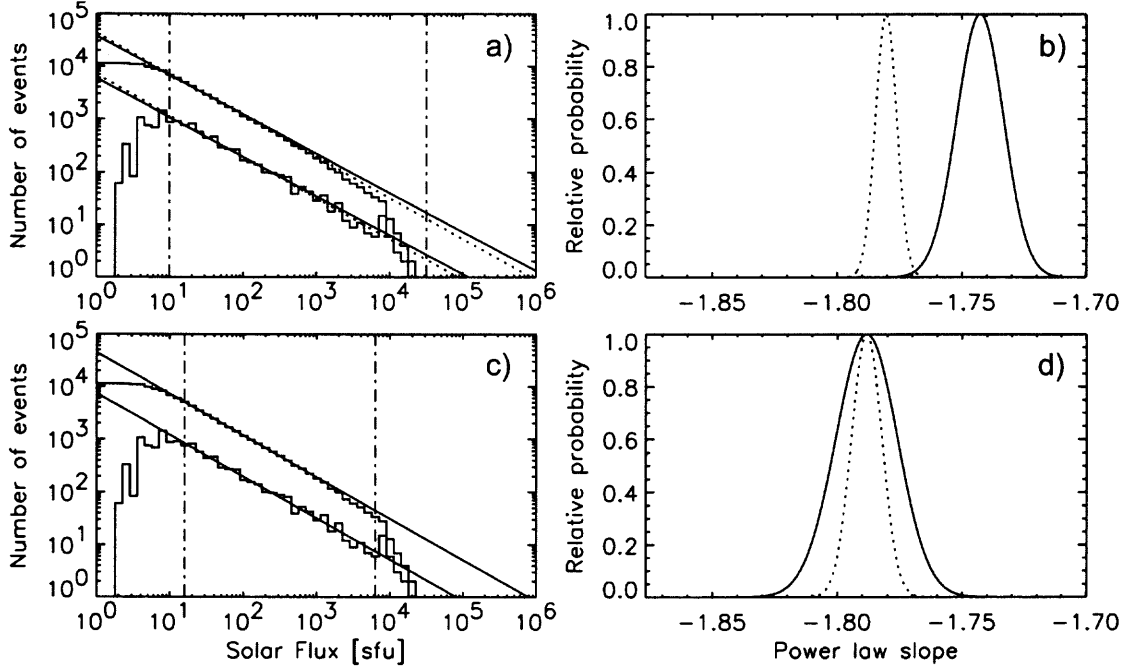


Figure 2.9 Example of the comparison of fits to the differential (ΔN) and cumulative (N) number distributions for Cycle 22, 8.4-11.8 GHz. (a) The solid lines are the fits to the differential distribution given in equation (2.2), for the flux range $10-10^{4.5}$ sfu. The dotted lines are the fits to the cumulative distribution over the same fit range. In (b) are shown the corresponding probability distributions for a range of values of λ . The two fits are both excellent, but are not mutually consistent. Panels (c), (d) show the same procedure using a slightly smaller flux range ($10^{1.2} - 10^{3.8}$ sfu), where the fit yields essentially identical results for both distributions, within the formal errors.

(2.5). The fit parameters are listed in Table 2.3 for the *Max Flux* approach, and in Table 2.4 for the *Selected Peak* approach. The actual number of bursts that entered into the histogram distributions is shown in column 3. For the results in the tables, data were accumulated separately over the time periods listed in Table 2.1—that is, over year ranges corresponding to three solar cycles (Solar Cycle 20–1966-1975, Solar Cycle 21–1976-1985, and Solar Cycle 22–1986-1995); twelve Solar Max years (1969-1972, 1979-1982, and 1989-1992); twelve Solar Min years (1966-1967, 1974-1977, 1984-1987, and 1994-1995); and all 40 years (1960-1999). For each time period, the data were selected in the following frequency ranges in GHz: (below 1, 1-1.7, 2-3.8, 4.9-7, 8.4-111.8, above 15), as well as in ranges designed to separate plasma emission (below 2 GHz) and gyrosynchrotron emission (above 2 GHz). The correction for missed events due to non-uniform longitudinal coverage has *not* been applied. To apply the correction, as estimated by the geographical correction factor C_{geo} , the parameters in columns 4 and 5 must be multiplied by the factor in column 7.

2.4.1 Occurrence Rate of Solar Radio Bursts

As laid out in the Introduction, the first goal is to determine the occurrence rate of bursts as a function of radio flux density for the purpose of quantifying the likelihood of interference in wireless communication systems. The total number of bursts exceeding a given flux density, S_1 , in a given frequency range $[\nu_1, \nu_2]$, is just the cumulative flux density

$$N(S > S_1, \nu_1, \nu_2) = N(S > 1, \nu_1, \nu_2) S_1^{\lambda+1}, \quad (2.20)$$

where the normalization for cumulative number $N(S > 1)$ is related to the normalization of number density $dN/dS|_{S=1}$ by

$$N(S > 1, \nu_1, \nu_2) = -\frac{1}{\lambda + 1} \left. \frac{dN}{dS} \right|_{S=1}. \quad (2.21)$$

Using the parameters in the 4th and 6th columns of Table 2.3 (optionally multiplied by the correction factor in column 7), one can estimate the number of

solar bursts that occurred above any flux density value S_1 , within any of the listed frequency ranges, using (2.20). To obtain the *occurrence rate*—e.g. number per day—one must divide by the number of days in the range, as listed in column 1.

As a concrete example, we estimate the daily rate of radio bursts above 100 sfu during the Solar Max epoch, at frequency > 2 GHz as,

$$N(S > 100 \text{ sfu}, \nu > 2 \text{ GHz}) = \frac{(216124) 100^{-1.82+1}}{4383 \text{ days}} = 1.13(1 \pm 0.02) \text{ events/day}$$

Applying the correction factor C_{geo} , which in this case is ~ 1.7 , the event rate becomes 1.93 events/day above 2 GHz during solar maximum. The quoted formal error above includes the correlation between a and λ given by (2.14), and also adds the \sqrt{N} Poisson uncertainties.

To aid in the use of these results for estimation of the occurrence rate of solar bursts, we show in Figure 2.10 the cumulative distribution in events per day above 2 GHz, as observed (histogram), as fitted (solid line), and after application of the geographical correction, C_{geo} (dotted line), for both Solar Max and Solar Min epochs. The fits predict considerably more events at high fluxes than actually observed. This may be due to an actual paucity of large events, but there may also be a contribution by instrumental saturation of observed events. The roll-over at low flux densities is due to the instrumental sensitivity limits, which appear to begin having an effect below 20 sfu at solar maximum and about 10 sfu at solar minimum.

It is of interest to compare the results of Fig. 2.10 with those reported by Bala et al. (2002). In that paper it was found that the number of bursts above 1000 sfu was one every 10-20 days, averaged over an entire solar cycle. The more precise results in Fig. 2.10 show that the average waiting time between 1000 sfu events before geographical correction is 6 days at solar maximum, and 33 days at solar minimum. After correction these become 3.5 days and 18.5 days, respectively. Use of the parameters in Table 2.3 allows these values to be determined for other epochs and frequency ranges.

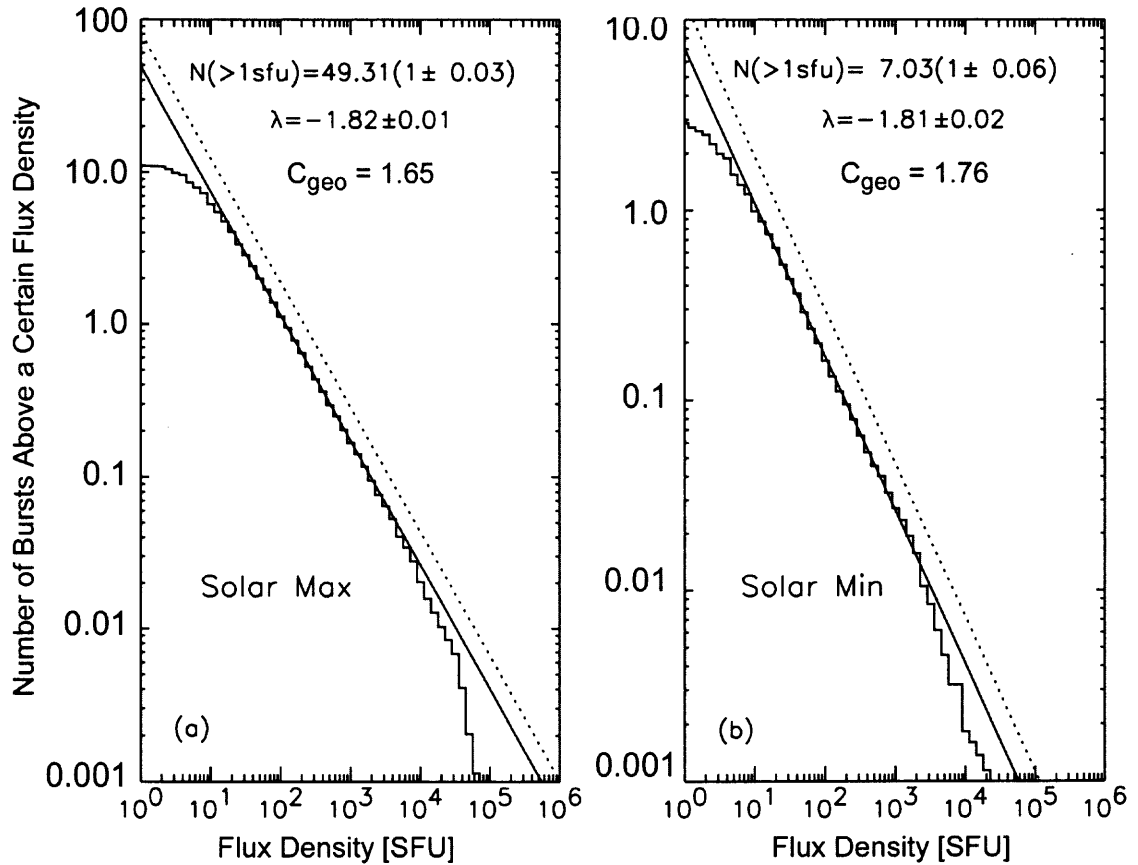


Figure 2.10 Cumulative number of bursts per day at frequencies > 2 GHz (a) during solar maximum years, and (b) during solar minimum. The histograms show the actual, observed distribution. The solid line shows the best power-law fit to the observed distribution, and the dotted line shows the fit after application of the geographical correction factor C_{geo} , which is 1.8 during solar max, and 1.7 during solar min epochs.

2.4.2 Time and Frequency Dependence of Power-Law Distributions

The concept of Self Organized Criticality (Bak et al. 1988), suggests that power-law distributions are to be expected in many systems, and that the slope of the distribution may in some way depend on the underlying parameters of the physical process. We find, as indicated in Tables 2.3 and 2.4, that the distributions are indeed well fit by power laws over a significant range in flux density. We assume that the fall-off at low flux densities is simply an instrumental effect. As noted above, the fall-off at the high end may be undercounting in some way, or it may be due to solar physics. Aschwanden et al. (1997) suggested that the fall off at high flux densities may express a limitation in the size scale of solar flares, which is a general consequence of the finite-size effect mentioned by Bak et al. (1988).

We wish to plot the results of Tables 2.3 and 2.4 to facilitate a search for possible systematic differences in power-law slope as a function of phase of the solar cycle, or from cycle to cycle, and as a function of frequency. We plot in Figure 2.11 the magnitude of the fitted power-law indexes as a function of frequency for the epochs shown. The left panel is for the Selected Peak approach, which we have argued is more suited to showing solar activity variations, since each event is counted only once. The average indexes are in all cases between -1.7 and -1.8, but in the left panel there is a clear tendency for the slopes to be slightly steeper for intermediate frequencies (approximately 2-11 GHz) and flatter both high and low frequencies. The effect is nearly absent in the Max Flux approach of the right panel.

In Figure 2.12, we plot the same information that was plotted in Figure 2.11, but now the slopes are plotted for each frequency versus epoch. Here it appears that there is little or no systematic variation with solar cycle or epoch in either Selected Peak or Max Flux approaches. This agrees with earlier findings (Crosby et al. 1993; Biasecker 1994; Bromund et al. 1995) that the parameters of the distribution functions from hard X-rays are insensitive to the phase of the solar

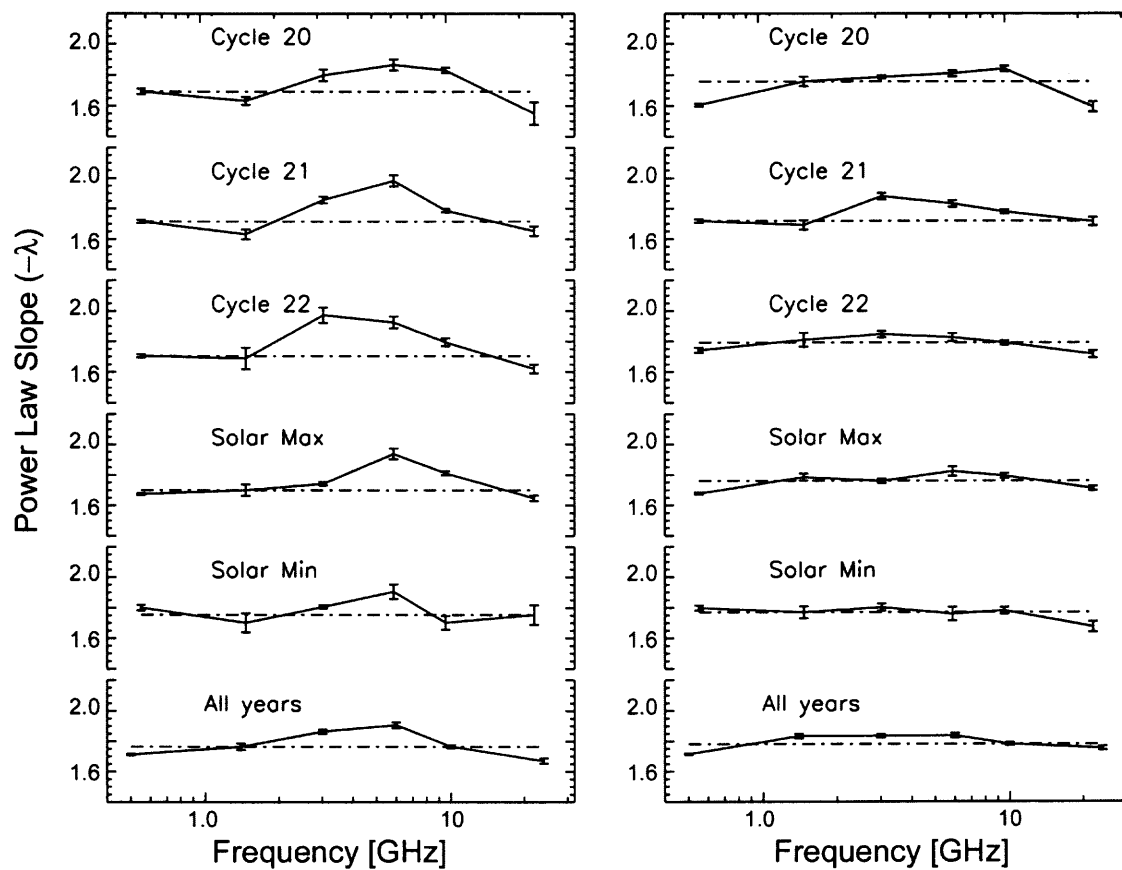


Figure 2.11 A plot of the absolute value of the slopes in Tables 2.4 (left panel—from the Selected Peak approach) and 2.3 (right panel—from the Max Flux approach) as a function of frequency.

cycle. However, from the average slopes (dot-dashed lines) in the Selected Peak approach (left panel) it is again clear that there is a systematic trend in the slopes at different frequencies. The slope of the distribution in the frequency range 4.9-7 GHz is consistently steeper, with an average slope of almost -1.9, than at the lowest and highest frequency ranges, where the slope is consistently about -1.7 or less.

In Figure 2.13, we plot the number of events per year that occurred with flux density > 1000 sfu, as a function of epoch (abscissa of each plot) and frequency (in separate panels in each row). The two upper rows are for the Selected Peak approach, and the two lower rows are for the Max Flux approach. The first and third rows are the numbers as measured, while the second and fourth rows have had the geographical correction factor applied. The first panel in each row has a larger vertical range to accommodate the large number of events measured in the 0.1-0.9 GHz range. All of the other panels in each row have the same vertical range, to facilitate comparison.

The Selected Peak panels give a grand overview of relative tendency for events to peak in each frequency range. It is somewhat unexpected that the number of events that peak in the range 4.9-7 GHz is significantly lower (by about a factor of 2-3) than adjacent ranges 2-3.8 and 8.4-11.8 GHz. Guidice and Castelli (1975) concluded that microwave bursts typically peak in the range 5-10 GHz. Stähli, Gary & Hurford found 7 GHz was the most probable peak for some 40 bursts observed during 1981. Nor is this due to lack of entries in the dataset, since the numbers in the Max Flux approach (lower rows of panels) show no such deficit. We must conclude that, according to this dataset, a relatively small number of bursts with flux densities > 1000 sfu actually peak in the range 4.9-7 GHz. This is in part a corroboration of the steeper power-law slope at 4.9-7 GHz, which predicts fewer large events in this frequency range. At lower fluxes (say 100–1000 sfu) the number peaking in the 4.9-7 GHz range increases faster than adjacent ranges (although apparently not enough

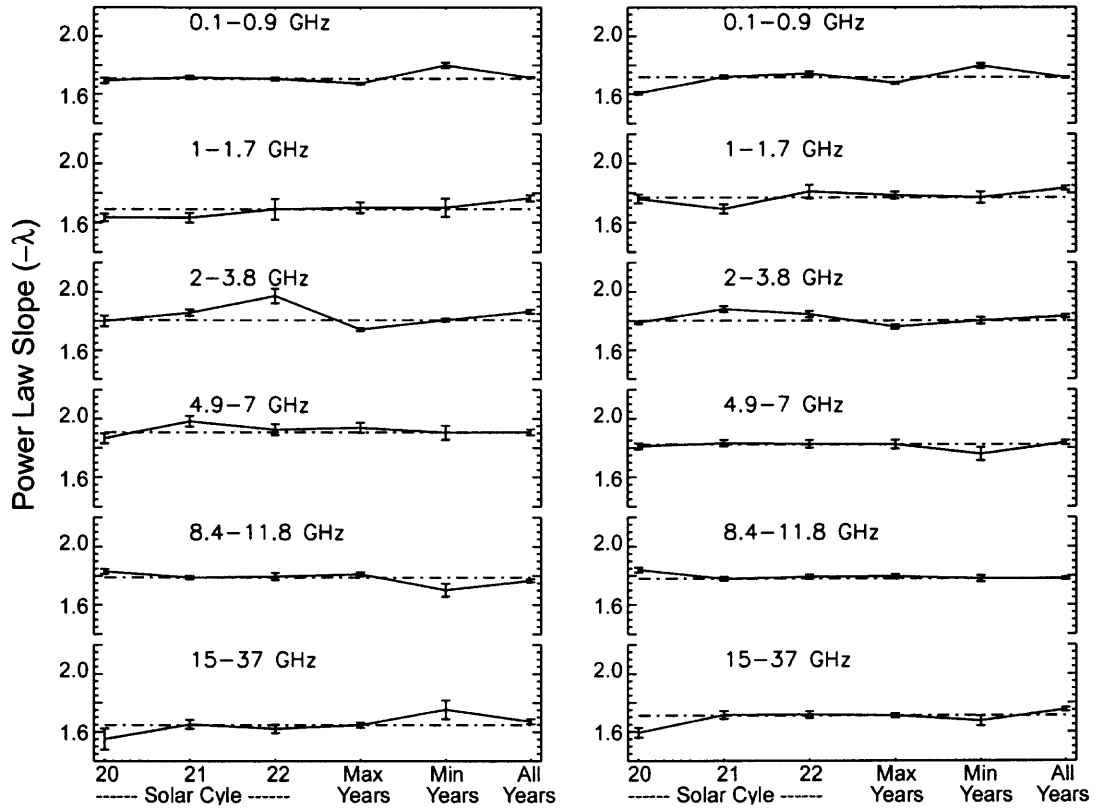


Figure 2.12 Alternative plot of the same information that was plotted in Figure 2.11. The absolute value of the slopes in Tables 2.4 (left panel—from the Selected Peak approach) and 2.3 (right panel—from the Max Flux approach) for different frequency ranges as a function of epoch.

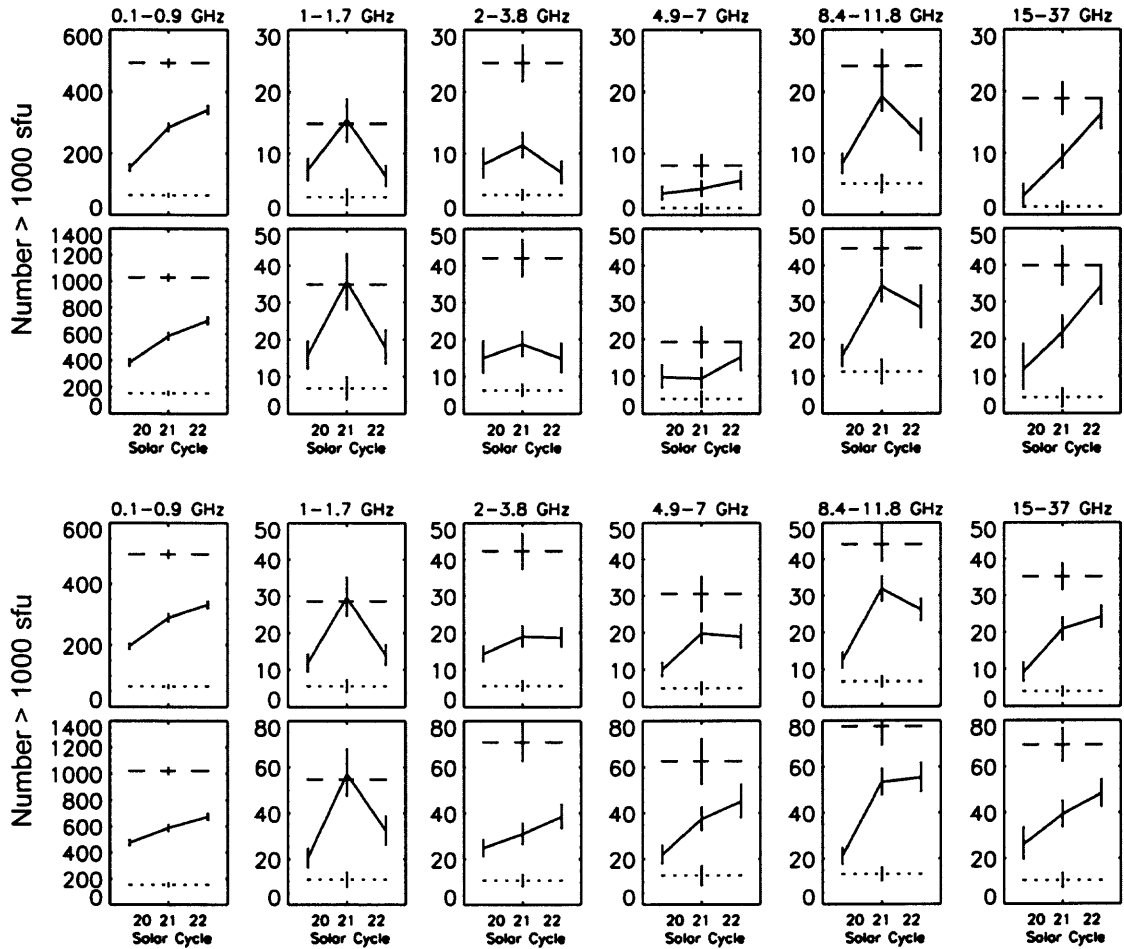


Figure 2.13 The number of events per year with flux density > 1000 sfu, as a function of epoch (abscissa of each plot) and frequency (in separate panels in each row). Data from the Selected Peak Table (2.4) are shown in the two upper rows. The two lower rows are for the Max Flux Table (2.3). The values for the three solar cycles are plotted as points connected by solid lines. The values for Solar Min years are plotted as a dotted line spanning all cycles, and the values for Solar Max years are plotted as a dashed line spanning all cycles.

to make up the difference). We suggest that the conclusions of Guidice & Castelli (1975) and Stähli, Gary & Hurford (1989) were obtained with datasets dominated by bursts with smaller flux densities. Our results suggest that at higher flux densities the bursts have a strong tendency to peak somewhat higher in frequency, above 8.4 GHz, or lower, below 3.8 GHz.

Another tendency that can be seen in Figure 2.13 is for cycle 20 to have fewer events than the other cycles in all frequency ranges. This is merely another confirmation, as in Table 2.2 that the dataset has many missed events in cycle 20 that cannot be completely corrected by application of the geographical correction factor.

2.5 Conclusion

We have examined the statistical properties of the flux density distribution of 40 years of solar radio bursts collected by the NOAA National Geophysical Data Center. The time period covered by the data includes more than 3 complete solar activity cycles (cycle 20, 21 and 22). We find that the distributions are well fit by power laws over a wide range of flux densities, but diverge from a power law at both high and low flux densities. The divergence of the distribution from the fit at low flux density probably is due to sensitivity limits of the recording instruments. This limit ranges from about 10 sfu during solar minimum to nearly 20 sfu at solar maximum. At high flux densities, the number of observed bursts again falls off relative to the fit, which may be due to instrumental limitations (e.g. saturation), or may be due to solar limitations such as the physical size of the interaction region, or total number of electrons available for energization.

During the course of our study, we found evidence that the database undercounts the true number of bursts by up to a factor of two, despite the world-wide coverage. We used the time of day distribution of reports to quantify the missed number of bursts, assuming that the peak of this distribution corresponds

to longitudes where 100% of the bursts were observed. Thus, our *geographical correction factor* is a lower limit to the true correction. Even so, the correction factors we deduced average around 1.7, indicating that almost half of all events were not observed. An investigation of a non-stationary Poissonian waiting time between events using Wheatland's (2000b) model remarkably predicts the same factor of 1.7 based on the ratio of observed (135 min) to predicted (81 min) mean waiting times.

We developed a new approach to fitting the power-law distributions that is better for data obeying Poissonian statistics than the more widely used least squares method. The key result is that it provides a self-consistent criterion for choosing the appropriate range over which to fit the powerlaw function based on agreement of the fits for the density and cumulative distributions. Without such a criterion, the fitting parameters depend on the arbitrary choice of fit range.

The observed occurrence rate was examined during periods of solar maximum and solar minimum, as well as separately for the three complete solar cycles. The average waiting time between occurrences of >1000 sfu events, before geographical correction, is 6 days at solar maximum, and 33 days at solar minimum. This is consistent with the estimate of one event every 10-20 days given by Bala et al. (2002). After correction these become 3.5 days and 18.5 days, respectively. Table 2.3, with equation (2.20) allows precise calculation of rates for any frequency range.

We searched for a systematic trend in the distributions as a function of epoch and frequency. We found no significant change in the power-law index from one solar cycle to the next, or phase of the solar cycle. The power-law index remained remarkably constant near -1.8 , which is also remarkably close to the slope found for hard X-ray bursts. Note that Bai (1993) reported a slight solar-cycle dependence in power-law index at two phases of the solar cycle, amounting to a difference of 0.07 from 1980-1981 to 1982-1984. He further investigated changes on a 153.8 day cycle. Our analysis over a wider range of time failed to verify a solar cycle dependence in the

radio data. We did not investigate changes on the 153.8 day timescale. Significantly, however, we did find a clear trend in power-law index as a function of frequency. Low (< 2 GHz) and high (> 15 GHz) frequencies displayed a shallower slope of near -1.7 , while the distribution in the range 4.9-7 GHz is steeper with a slope of -1.9 . This same trend appears to account at least partially for a deficit in number of bursts with flux density > 1000 sfu in the 4.9-7 GHz range.

Table 2.3. Parameters for Max Flux Approach

<i>Epoch</i>	ν GHz	N_{Events}	$N(> 1 \text{ sfu})$	$dN/dS(> 1 \text{ sfu})$	λ	C_{geo}	
Cycle 20 (3652 days)	0.1 – 0.9	19025	128987($1^{+0.05}_{-0.04}$)	78096($1^{+0.06}_{-0.06}$)	-1.61 ± 0.01	2.4	
	1.0 – 1.7	6738	22315($1^{+0.12}_{-0.10}$)	16948($1^{+0.15}_{-0.13}$)	-1.76 ± 0.03	1.7	
	2.0 – 3.8	16064	32980($1^{+0.02}_{-0.02}$)	25984($1^{+0.02}_{-0.02}$)	-1.79 ± 0.01	1.7	
	4.9 – 7.0	6209	26859($1^{+0.07}_{-0.07}$)	21769($1^{+0.09}_{-0.08}$)	-1.81 ± 0.02	2.2	
	8.4 – 11.8	9392	41459($1^{+0.05}_{-0.05}$)	34846($1^{+0.07}_{-0.06}$)	-1.84 ± 0.02	1.7	
	15.0 – 37.0	1645	5505($1^{+0.10}_{-0.09}$)	3270($1^{+0.15}_{-0.13}$)	-1.59 ± 0.03	2.9	
	<i>below</i> 2	21282	113920($1^{+0.08}_{-0.07}$)	66123($1^{+0.10}_{-0.09}$)	-1.58 ± 0.01	2.3	
	<i>above</i> 2	20219	67809($1^{+0.05}_{-0.04}$)	57803($1^{+0.06}_{-0.06}$)	-1.85 ± 0.02	1.7	
	Cycle 21 (3652 days)	0.1 – 0.9	29930	412298($1^{+0.06}_{-0.06}$)	296180($1^{+0.08}_{-0.07}$)	-1.72 ± 0.01	2.0
		1.0 – 1.7	9482	35103($1^{+0.11}_{-0.10}$)	24268($1^{+0.15}_{-0.13}$)	-1.69 ± 0.03	1.9
2.0 – 3.8		26479	83592($1^{+0.08}_{-0.08}$)	73662($1^{+0.10}_{-0.09}$)	-1.88 ± 0.02	1.6	
4.9 – 7.0		9009	61738($1^{+0.10}_{-0.09}$)	51313($1^{+0.12}_{-0.11}$)	-1.83 ± 0.02	1.9	
8.4 – 11.8		17072	69038($1^{+0.04}_{-0.04}$)	53743($1^{+0.06}_{-0.05}$)	-1.78 ± 0.01	1.7	
15.0 – 37.0		4444	29097($1^{+0.13}_{-0.11}$)	20799($1^{+0.16}_{-0.14}$)	-1.71 ± 0.03	1.9	
<i>below</i> 2		33794	423360($1^{+0.07}_{-0.07}$)	304169($1^{+0.09}_{-0.08}$)	-1.72 ± 0.01	1.9	
<i>above</i> 2		34581	122139($1^{+0.06}_{-0.06}$)	100244($1^{+0.08}_{-0.07}$)	-1.82 ± 0.02	1.5	
Cycle 22 (3652 days)		0.1 – 0.9	29900	555261($1^{+0.10}_{-0.09}$)	411812($1^{+0.13}_{-0.11}$)	-1.74 ± 0.02	2.0
		1.0 – 1.7	3561	37485($1^{+0.24}_{-0.19}$)	30371($1^{+0.30}_{-0.23}$)	-1.81 ± 0.05	2.3
	2.0 – 3.8	10676	64909($1^{+0.10}_{-0.09}$)	54968($1^{+0.12}_{-0.11}$)	-1.85 ± 0.02	2.1	
	4.9 – 7.0	8042	56986($1^{+0.11}_{-0.10}$)	47094($1^{+0.14}_{-0.12}$)	-1.83 ± 0.03	2.4	
	8.4 – 11.8	11678	62080($1^{+0.06}_{-0.06}$)	49161($1^{+0.07}_{-0.07}$)	-1.79 ± 0.01	2.1	
	15.0 – 37.0	4780	34282($1^{+0.12}_{-0.10}$)	24584($1^{+0.15}_{-0.13}$)	-1.72 ± 0.02	2.0	
	<i>below</i> 2	30729	515924($1^{+0.09}_{-0.08}$)	374838($1^{+0.11}_{-0.10}$)	-1.73 ± 0.02	2.0	
	<i>above</i> 2	19666	116394($1^{+0.06}_{-0.05}$)	96159($1^{+0.07}_{-0.06}$)	-1.83 ± 0.01	2.0	
	Solar Max (4383 days)	0.1 – 0.9	48900	639671($1^{+0.03}_{-0.03}$)	432891($1^{+0.04}_{-0.04}$)	-1.68 ± 0.01	2.1
		1.0 – 1.7	12765	77377($1^{+0.11}_{-0.10}$)	60685($1^{+0.14}_{-0.12}$)	-1.78 ± 0.02	1.9
2.0 – 3.8		33045	96363($1^{+0.04}_{-0.04}$)	73194($1^{+0.06}_{-0.06}$)	-1.76 ± 0.01	1.7	
4.9 – 7.0		16315	107880($1^{+0.12}_{-0.11}$)	88800($1^{+0.16}_{-0.14}$)	-1.82 ± 0.03	2.0	
8.4 – 11.8		26960	127566($1^{+0.07}_{-0.06}$)	101300($1^{+0.09}_{-0.08}$)	-1.79 ± 0.02	1.8	
15.0 – 37.0		8382	57235($1^{+0.06}_{-0.05}$)	40672($1^{+0.07}_{-0.07}$)	-1.71 ± 0.01	2.0	
<i>below</i> 2		53329	647709($1^{+0.03}_{-0.03}$)	437594($1^{+0.04}_{-0.04}$)	-1.68 ± 0.01	1.9	
<i>above</i> 2		48432	216124($1^{+0.03}_{-0.03}$)	176661($1^{+0.04}_{-0.04}$)	-1.82 ± 0.01	1.6	
Solar Min (4383 days)		0.1 – 0.9	14708	196329($1^{+0.09}_{-0.08}$)	156604($1^{+0.11}_{-0.10}$)	-1.80 ± 0.02	2.3
		1.0 – 1.7	3464	13694($1^{+0.16}_{-0.13}$)	10535($1^{+0.21}_{-0.17}$)	-1.77 ± 0.04	2.0
	2.0 – 3.8	10151	17279($1^{+0.08}_{-0.07}$)	13853($1^{+0.10}_{-0.09}$)	-1.80 ± 0.02	1.9	
	4.9 – 7.0	2832	11193($1^{+0.17}_{-0.14}$)	8482($1^{+0.22}_{-0.18}$)	-1.76 ± 0.05	2.6	
	8.4 – 11.8	5124	17652($1^{+0.08}_{-0.08}$)	13766($1^{+0.11}_{-0.10}$)	-1.78 ± 0.02	2.0	
	15.0 – 37.0	925	5051($1^{+0.13}_{-0.11}$)	3405($1^{+0.17}_{-0.15}$)	-1.67 ± 0.03	2.6	
	<i>below</i> 2	15955	207048($1^{+0.09}_{-0.08}$)	166570($1^{+0.11}_{-0.10}$)	-1.80 ± 0.02	2.2	
	<i>above</i> 2	12607	30834($1^{+0.07}_{-0.06}$)	24920($1^{+0.09}_{-0.08}$)	-1.81 ± 0.02	1.8	
	All years (14610 days)	0.1 – 0.9	87101	1194373($1^{+0.03}_{-0.03}$)	853984($1^{+0.03}_{-0.03}$)	-1.72 ± 0.00	2.1
		1.0 – 1.7	20661	148576($1^{+0.07}_{-0.06}$)	123728($1^{+0.08}_{-0.08}$)	-1.83 ± 0.01	2.0
2.0 – 3.8		55245	178956($1^{+0.05}_{-0.04}$)	149166($1^{+0.06}_{-0.06}$)	-1.83 ± 0.01	1.8	
4.9 – 7.0		25083	161079($1^{+0.07}_{-0.06}$)	134705($1^{+0.08}_{-0.08}$)	-1.84 ± 0.02	2.2	
8.4 – 11.8		39032	174357($1^{+0.04}_{-0.04}$)	136082($1^{+0.05}_{-0.05}$)	-1.78 ± 0.01	1.8	
15.0 – 37.0		11232	90978($1^{+0.06}_{-0.05}$)	68504($1^{+0.07}_{-0.07}$)	-1.75 ± 0.01	2.1	
<i>below</i> 2		94374	1209983($1^{+0.03}_{-0.03}$)	864002($1^{+0.03}_{-0.03}$)	-1.71 ± 0.00	2.0	
<i>above</i> 2		77907	303974($1^{+0.03}_{-0.03}$)	246222($1^{+0.04}_{-0.03}$)	-1.81 ± 0.01	1.7	

Table 2.4. Parameters for Selected Peak Approach

<i>Epoch</i>	ν GHz	N_{Events}	$N(> 1 \text{ sfu})$	$dN/dS(> 1 \text{ sfu})$	λ	C_{geo}
Cycle 20 <i>(3652 days)</i>	0.1 – 0.9	18064	184119($1^{+0.09}_{-0.08}$)	127682($1^{+0.12}_{-0.11}$)	-1.69 ± 0.02	2.5
	1.0 – 1.7	3218	5869($1^{+0.08}_{-0.07}$)	3720($1^{+0.10}_{-0.09}$)	-1.63 ± 0.03	2.1
	2.0 – 3.8	11168	20705($1^{+0.10}_{-0.09}$)	16556($1^{+0.14}_{-0.13}$)	-1.80 ± 0.04	1.8
	4.9 – 7.0	2764	13953($1^{+0.12}_{-0.11}$)	12084($1^{+0.16}_{-0.14}$)	-1.87 ± 0.03	2.8
	8.4 – 11.8	5896	25944($1^{+0.05}_{-0.05}$)	21563($1^{+0.06}_{-0.06}$)	-1.83 ± 0.02	1.9
	15.0 – 37.0	391	1395($1^{+0.23}_{-0.18}$)	768($1^{+0.36}_{-0.26}$)	-1.55 ± 0.07	3.7
	<i>below</i> 2	21282	113920($1^{+0.07}_{-0.07}$)	66123($1^{+0.10}_{-0.09}$)	-1.58 ± 0.01	2.3
<i>above</i> 2	20219	67809($1^{+0.05}_{-0.04}$)	57803($1^{+0.06}_{-0.06}$)	-1.85 ± 0.02	1.7	
Cycle 21 <i>(3652 days)</i>	0.1 – 0.9	29019	399413($1^{+0.06}_{-0.06}$)	285826($1^{+0.08}_{-0.07}$)	-1.72 ± 0.01	2.0
	1.0 – 1.7	4775	12353($1^{+0.12}_{-0.11}$)	7826($1^{+0.17}_{-0.15}$)	-1.63 ± 0.03	2.3
	2.0 – 3.8	18002	42551($1^{+0.08}_{-0.08}$)	36504($1^{+0.11}_{-0.10}$)	-1.86 ± 0.02	1.6
	4.9 – 7.0	3712	38171($1^{+0.15}_{-0.13}$)	37547($1^{+0.19}_{-0.16}$)	-1.98 ± 0.04	2.2
	8.4 – 11.8	11242	44627($1^{+0.04}_{-0.04}$)	35177($1^{+0.05}_{-0.05}$)	-1.79 ± 0.01	1.8
	15.0 – 37.0	1625	8501($1^{+0.14}_{-0.12}$)	5546($1^{+0.15}_{-0.15}$)	-1.65 ± 0.03	2.3
	<i>below</i> 2	33794	423360($1^{+0.07}_{-0.07}$)	304169($1^{+0.09}_{-0.08}$)	-1.72 ± 0.01	1.9
<i>above</i> 2	34581	122139($1^{+0.06}_{-0.06}$)	100244($1^{+0.08}_{-0.07}$)	-1.82 ± 0.02	1.5	
Cycle 22 <i>(3652 days)</i>	0.1 – 0.9	29494	447445($1^{+0.07}_{-0.05}$)	315690($1^{+0.09}_{-0.07}$)	-1.71 ± 0.01	2.0
	1.0 – 1.7	1235	7412($1^{+0.45}_{-0.30}$)	5121($1^{+0.58}_{-0.36}$)	-1.69 ± 0.07	2.8
	2.0 – 3.8	6636	57007($1^{+0.24}_{-0.19}$)	55482($1^{+0.31}_{-0.23}$)	-1.97 ± 0.05	2.2
	4.9 – 7.0	3573	33626($1^{+0.15}_{-0.15}$)	31146($1^{+0.22}_{-0.22}$)	-1.93 ± 0.04	2.7
	8.4 – 11.8	7242	31654($1^{+0.08}_{-0.07}$)	25196($1^{+0.11}_{-0.10}$)	-1.80 ± 0.03	2.2
	15.0 – 37.0	2215	12080($1^{+0.15}_{-0.13}$)	7515($1^{+0.19}_{-0.16}$)	-1.62 ± 0.03	2.1
	<i>below</i> 2	30729	515924($1^{+0.09}_{-0.08}$)	374838($1^{+0.11}_{-0.10}$)	-1.73 ± 0.02	2.0
<i>above</i> 2	19666	116394($1^{+0.06}_{-0.05}$)	96159($1^{+0.07}_{-0.06}$)	-1.83 ± 0.01	2.0	
Solar Max <i>(4383 days)</i>	0.1 – 0.9	47480	624632($1^{+0.03}_{-0.03}$)	421411($1^{+0.04}_{-0.04}$)	-1.67 ± 0.01	2.1
	1.0 – 1.7	5849	22645($1^{+0.17}_{-0.14}$)	15885($1^{+0.23}_{-0.18}$)	-1.70 ± 0.04	2.3
	2.0 – 3.8	21139	50116($1^{+0.02}_{-0.02}$)	37245($1^{+0.03}_{-0.03}$)	-1.74 ± 0.01	1.7
	4.9 – 7.0	6880	63908($1^{+0.15}_{-0.13}$)	60062($1^{+0.19}_{-0.16}$)	-1.94 ± 0.03	2.4
	8.4 – 11.8	17056	79437($1^{+0.06}_{-0.05}$)	64560($1^{+0.07}_{-0.06}$)	-1.81 ± 0.01	1.8
	15.0 – 37.0	3357	19872($1^{+0.08}_{-0.07}$)	12865($1^{+0.10}_{-0.09}$)	-1.65 ± 0.02	2.1
	<i>below</i> 2	53329	647709($1^{+0.03}_{-0.03}$)	437594($1^{+0.04}_{-0.04}$)	-1.68 ± 0.01	1.9
<i>above</i> 2	48432	216124($1^{+0.03}_{-0.03}$)	176661($1^{+0.04}_{-0.04}$)	-1.82 ± 0.01	1.6	
Solar Min <i>(4383 days)</i>	0.1 – 0.9	14223	196477($1^{+0.10}_{-0.09}$)	157340($1^{+0.13}_{-0.11}$)	-1.80 ± 0.02	2.4
	1.0 – 1.7	1732	4479($1^{+0.26}_{-0.20}$)	3143($1^{+0.35}_{-0.26}$)	-1.70 ± 0.06	2.3
	2.0 – 3.8	7570	10426($1^{+0.02}_{-0.02}$)	8413($1^{+0.02}_{-0.02}$)	-1.81 ± 0.01	1.9
	4.9 – 7.0	1221	7277($1^{+0.17}_{-0.14}$)	6591($1^{+0.22}_{-0.18}$)	-1.91 ± 0.05	3.4
	8.4 – 11.8	3446	7867($1^{+0.21}_{-0.17}$)	5530($1^{+0.28}_{-0.22}$)	-1.70 ± 0.05	2.2
	15.0 – 37.0	370	2888($1^{+0.24}_{-0.19}$)	2177($1^{+0.33}_{-0.24}$)	-1.75 ± 0.06	3.2
	<i>below</i> 2	15955	207048($1^{+0.09}_{-0.08}$)	166570($1^{+0.11}_{-0.10}$)	-1.80 ± 0.02	2.2
<i>above</i> 2	12607	30834($1^{+0.07}_{-0.06}$)	24920($1^{+0.09}_{-0.08}$)	-1.81 ± 0.02	1.8	
All years <i>(14610 days)</i>	0.1 – 0.9	84691	1168245($1^{+0.03}_{-0.03}$)	833154($1^{+0.03}_{-0.03}$)	-1.71 ± 0.00	2.1
	1.0 – 1.7	9683	48341($1^{+0.10}_{-0.09}$)	36954($1^{+0.12}_{-0.11}$)	-1.76 ± 0.02	2.3
	2.0 – 3.8	37287	111047($1^{+0.06}_{-0.05}$)	95989($1^{+0.07}_{-0.06}$)	-1.86 ± 0.01	1.8
	4.9 – 7.0	11388	79708($1^{+0.09}_{-0.08}$)	72292($1^{+0.11}_{-0.10}$)	-1.91 ± 0.02	2.5
	8.4 – 11.8	24897	96908($1^{+0.03}_{-0.03}$)	74284($1^{+0.04}_{-0.04}$)	-1.77 ± 0.01	2.0
	15.0 – 37.0	4335	27951($1^{+0.08}_{-0.07}$)	18746($1^{+0.10}_{-0.09}$)	-1.67 ± 0.02	2.4
	<i>below</i> 2	94374	1209983($1^{+0.03}_{-0.03}$)	864002($1^{+0.03}_{-0.03}$)	-1.71 ± 0.00	2.0
<i>above</i> 2	77907	303974($1^{+0.03}_{-0.03}$)	246222($1^{+0.04}_{-0.03}$)	-1.81 ± 0.01	1.7	

CHAPTER 3

STATISTICAL STUDY OF TWO YEARS OF SOLAR FLARE RADIO SPECTRA OBTAINED WITH OVSA

3.1 Introduction

The early statistical studies of solar microwave bursts were limited to single-frequency observations, (Covington 1951; Dodson, Hedeman & Covington 1954; Akabane 1956; Kundu 1965; Kakinuma, Yamashita & Enome 1969). The first published distributions of microwave peak fluxes were obtained by Akabane (1956), Kundu (1965), and Kakinuma, Yamashita & Enome (1969) using data recorded during Solar Cycle 19. The distribution of number of bursts versus frequency range of the spectral peak, and in some respects with intensity level, has been reported by Castelli & Guidice (1972) and Guidice & Castelli (1975) using data recorded at Sagamore Hill from 1968 to 1971. A study of large flares using the same instrument was presented by Cliver, McNamara & Gentle (1985). More recently, Nita et al. (2002) have studied the peak flux distribution in different frequency ranges of more than 150,000 solar radio bursts, recorded at fixed frequencies from 1960 to 1999 by a world-wide network and compiled by NOAA.

Although valuable for their contribution to a better understanding of general characteristics of such distributions, all of these studies lacked the frequency and temporal resolution required to derive accurate peak parameters. The observing frequencies contain gaps of an octave or more, and the peak fluxes reported at different frequencies often occur at different times. Therefore, neither the peak flux nor the peak frequency derived by these means represent the true spectral parameters at a given time.

A better approach is to use simultaneous observations at multiple frequencies, preferably from the same instrument. Some of the first statistical studies of this kind were done by Takakura & Kai (1966) and Kai (1968) using radio data recorded at up

to 5 frequencies from Toyokawa and Mitaka. Frequency agile observations from Bern, although over a restricted frequency range (6-8 GHz) were reported by Bruggmann et. al. (1990).

Since it began observations in 1981, OVSA has offered a more complete picture of microwave spectra, due to its frequency agile operation. However, since the results of Stähli, Gary & Hurford (1989), based on a set of 49 events observed with the 27-m antennas, and Stähli, Gary & Hurford (1990), based on selection of 14 events from the same dataset, no other statistical studies have been done involving the spectral peak parameters derived from OVSA data. The current study, based on a complete survey of OVSA data from 2001-2002, involves not only a much larger dataset, 412 events, but also performs the spectral analysis at every recorded instant of time, yielding more than 50,000 spectral fits. This study thus places the earlier results into context and provides a clearer picture of how the sometimes disparate results of earlier studies arise. Some of the results of this work are used in a companion paper, Lee, Nita & Gary (2003), to estimate the distribution of physical parameters such as electron power-law index, effective temperature, magnetic field strength, average number of electrons and mean electron energy.

In §3.2 we describe the improved OVSA instrument and the dataset used in this study. In §3.3 we analyze the distribution of spectral maxima of microwave bursts with respect to peak flux density and peak frequency. In §3.4 we introduce our classification scheme—a somewhat simplified version of the scheme by Guidice & Castelli (1975)—and discuss the main spectral and temporal characteristics of each spectral type. In §3.5 we study the properties of microwave bursts with more than one spectral component. In §3.6 we present the conclusions of this study.

3.2 Description of Data Set

OVSA (Hurford, Read & Zirin 1984) is a solar-dedicated interferometer array, and takes daily observations roughly covering the time range 16:00-24:00 UT. After some upgrades (Gary & Hurford 1999), the array now consists of two 27-m antennas and four 2-m antennas that can observe the Sun at up to 86 frequencies in the range 1 – 18 GHz. The radio bursts reported here are those observed by OVSA during the years 2001-2002, at typically 40 frequencies roughly logarithmically spaced over the 1.2-18 GHz frequency range. The 27-m antennas are equipped with two broadband feeds, which provide dual polarization with 8 s time resolution. The 2-m antennas are equipped with log-periodic linear dipole feeds, which provide total intensity with 4 s time resolution.

Although the main purpose of the instrument is to provide imaging data, in order to study such a large number of bursts we restrict ourselves to total power (integrated flux density) data without spatial resolution. Because of difficulties with absolute flux calibration of the 27-m dishes due to various effects arising from their restricted field of view, we further restrict our analysis to data from the 2-m antennas, and hence discuss only total intensity (Stokes I).

The 2-m flux calibration is based on the quiet Sun total flux density as reported by the National Oceanic and Atmospheric Administration (NOAA). Each day near local noon at OVSA, the quiet Sun flux is determined by measuring the spectrum at Sun center and again on the blank sky at a declination 10 degrees north of Sun center. The difference in these spectra represents the increment due to the Sun, as viewed by the 2-m antennas. The measured increment is corrected for the field of view of the 2-m antennas, which is $\sim 10.5/f_{\text{GHz}}$ degrees FWHM. The correction factor increases with frequency, reaching about 1.25 at 18 GHz. The corrected increment is then compared with the NOAA flux values for the day, and calibration factors are determined and applied for the entire day. On days when the calibration failed for

any reason, calibration factors from previous or following days were applied. The fluxes reported by NOAA can disagree from station to station by amounts up to 10%, with typical disagreement of a few percent. In addition, the OVSA gain can vary by 5% during the course of an 8-hour observing day. Thus, when we compare our burst flux densities with those reported by the Air Force Radio Solar Telescope Network (RSTN), they typically agree to within about 10% at all frequencies. In rare cases, larger errors are possible due to a burst occurring in an active region far from the OVSA pointing location. Such errors are worst at high frequencies, and can be more than a factor of 2 at 18 GHz in a few cases. Although such errors are correctable on a case-by-case basis, we have made no attempt to do so in this statistical study due to the very large number of bursts that we study.

The sensitivity limit and saturation level for the 2-m antennas will affect the smallest and largest bursts that can be measured by the instrument. The sensitivity limit is best determined from the dataset itself, which we do by determining the rms fluctuations averaged over quiet time periods just before the bursts. The 1σ RMS limit changes slightly with frequency (see §3.3), but ranges from 3-7 sfu (solar flux units: $1 \text{ sfu} = 10^4 \text{ Jy} = 10^{-22} \text{ W m}^{-2} \text{ Hz}^{-1}$). Thus, the 3σ limit is roughly 10 sfu over most of the range, going up to about 20 sfu above ~ 14 GHz. As for the saturation limit, no saturation due to the A/D converter is expected for solar bursts measured with the 2-m antennas. A flux density of 1 sfu corresponds to 5 A/D units out of a maximum 4096, and each antenna is equipped with a front-end programmable attenuator that automatically provides up to 35 dB of attenuation. Thus, saturation of the A/D nominally occurs at 2.6×10^6 sfu, far above the highest flux densities in our dataset. Saturation of the first stage amplifier (17 GHz bandwidth, gain 25 dB, gain compression 10 dBm, on a 2-m dish) occurs at $> 6 \times 10^6$ sfu, so again is not an issue for this study.

The basic data for each burst consists of a dynamic spectrum for each of the four 2-m antennas, with 40 frequencies and 4 s time resolution. The four equivalent dynamic spectra are first compared for consistency, and data from any antenna experiencing problems is discarded. After selecting the set of reliable antennas in each case, we compute an averaged dynamic spectrum to be used for the analysis. This approach provided us a qualitatively better data set compared with those used in other previous total power studies, (e.g. Stähli, Gary & Hurford 1989, 1990), based on the OVSA instrument.

The frequency resolution of OVSA allows us, for each event, to identify the main spectral components and divide the spectral range when multiple components are present. Following Stähli, Gary & Hurford (1989), at each instant of time we fit the resolved spectral ranges using a generic function described by

$$S = e^A \nu^\alpha [1 - \exp(-e^B \nu^{-\beta})] \quad (3.1)$$

Although this generic function has been found appropriate to fit gyrosynchrotron-like spectral shapes, (Stähli, Gary & Hurford 1989), its general form, which gives a spectral maximum and power-law asymptotic behavior below and above the peak frequency, makes it useful as a fitting model for all of the spectral components we considered, independent of the actual emission mechanism involved. This allows us to compute the spectral slopes at low ($\alpha_{lf} \equiv \alpha$) and high ($\alpha_{hf} = \alpha - \beta$) frequency ranges, and spectral parameters corresponding to the local spectral peak, i.e. peak frequency, ν_{peak} , and peak flux density, S_{peak} . An illustrative example of such a fit is shown in Fig.3.1, where two spectral components have been resolved.

For bursts with multiple temporal peaks, in each spectral range we separate the main temporal peaks by visual inspection. For each peak, we then further divide the bursts automatically into rising and decaying intervals defined as those temporal ranges in which the flux density ranged between 20% and 80% of the corre-

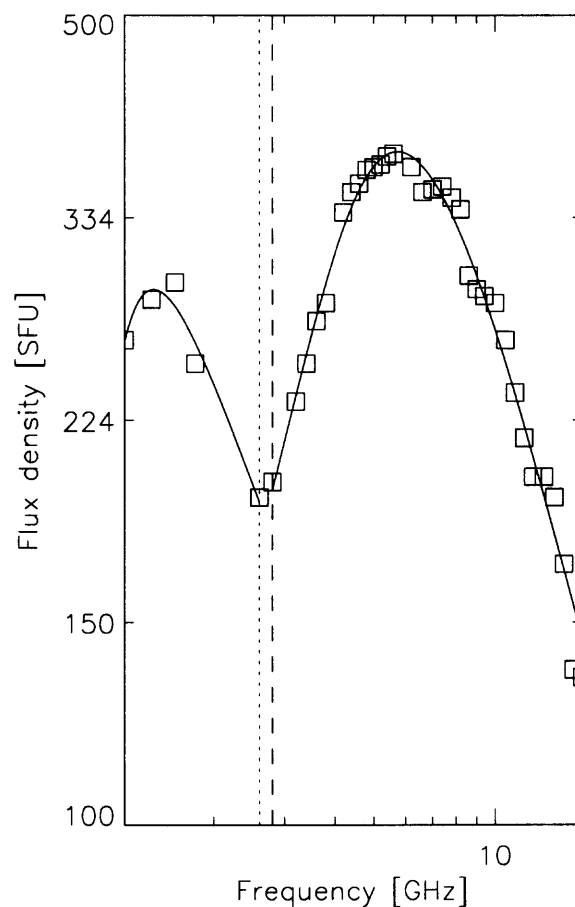


Figure 3.1 A spectral fit example: In this case two spectral components were resolved and each spectral range was fitted using the generic function described in Equation 3.1. The fit parameters α and β were used to derive the spectral slopes α_{lf} and α_{hf} of each range. The function was computed for 100 equally spaced frequencies in the fitting range to interpolate the peak parameters ν_{peak} and S_{peak} .

Table 3.1. Statistics of Data Set

Year	Events	Spectral components (1; 2; ≥ 3)%	Temporal peaks (1; 2; ≥ 3)%	Snapshots
2001	228	285 (76.8; 21.5; 1.8)	672 (38.2; 25.4; 36.4)	29682
2002	184	215 (83.2; 16.8; 0.0)	450 (40.8; 25.0; 34.2)	21051
Total	412	500 (79.6; 19.4; 1.0)	1122 (39.3; 25.2; 35.4)	50733

sponding peak flux. No attempt was made to remove the decay of preceding temporal components from later ones, since we know of no objective way to do this.

Table 3.1 describes the data set that was ultimately used for analysis. We have investigated in detail a total of 412 events recorded by OVSA during 2001-2002. Our selection was based on the data quality needed to obtain reliable spectral fits. A percentage (19.4%) of the events we analyze display two spectral components, while only 1% display more than two spectral components. About 40% of the 500 spectral components display simple time structures involving a single temporal peak, while 60% display complex time structures. The total number of temporal peaks over all spectral ranges is 1122. The detailed analysis we carry out involves a total of 50,733 spectral fits, each of which provides the four parameters describing the spectral shape for each time sample.

3.3 Spectral Peak Distribution of Microwave Bursts

Figure 3.2 displays a synopsis of the entire data set. It shows the spectral peak distribution—that is, peak frequency versus peak flux density—for all times when the flux density was above 20% of the absolute peak flux of each of 500 spectral components, resolved from the dynamic spectra of 412 radio bursts identified in the

raw data. This two-dimensional distribution offers at a glance a rather complete picture of some of the main issues addressed in earlier studies.

First of all, the distribution highlights a clear division (horizontal dotted line) of centimetric (cm) and decimetric (dm) emission into two distinct populations. We set this empirical division at 2.6 GHz, near but somewhat lower than the 3 GHz (10 cm) implied by a strict definition of “decimeter” based on wavelength. Above 2.6 GHz, no event exceeding ~ 1000 sfu was observed in the adjacent region of the cm range. In addition, a frequency dependent flux density limit for cm emission is apparent in the figure. We find this limit to be well described by a ν^2 -power law, with an offset of ~ 300 sfu at 1 GHz, as shown by the sloping dotted line. The frequency dependence of this flux density upper-limit and its particular value of offset will be discussed in greater detail elsewhere (Lee, Nita & Gary 2003).

The superposition of these two populations, one limited in frequency and the other in intensity, results in a well delimited region in which no high intensity emission can be observed. A similar result was reported by Nita et al. (2002), who noticed a lack of events above 1000 sfu at intermediate cm wavelengths. However, their result, based only on observations at frequency bands separated by roughly octave-wide gaps, indicated [4.9 – 7] GHz as the range with the fewest events above 1000 sfu, while the number of the events recorded in their next lower range, 2 – 3.8 GHz, was relatively greater. From Figure 3.2, we can see that the 2 – 3.8 GHz range includes bursts on both sides of the dividing line, and so the number of large bursts was inflated, making the [4.9 – 7] GHz range appear anomalous. In fact, the number of bursts > 1000 sfu above 2.6 GHz grows monotonically as frequency increases. This result is also in agreement with Castelli & Guidice (1972) who found in the case of U-shaped bursts (bursts with both dm and cm components) reaching > 1000 sfu that the weakest emission (the minimum in the U) lies around 2.8 GHz.

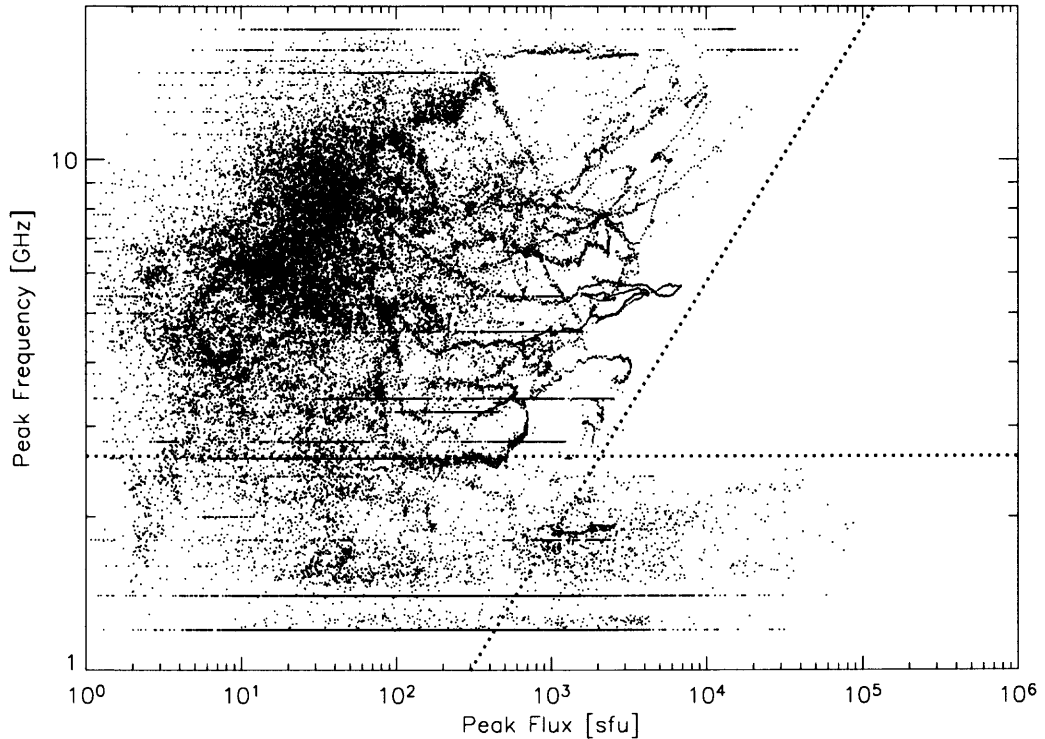


Figure 3.2 Synopsis of 2001-2002 OVSA data: The distribution of spectral peak at each recorded instant of time for 412 analyzed events, (500 spectral components, 50733 data points). The horizontal stripes represent a data artifact due to the observational OVSA frequencies. The horizontal dotted line at 2.62 GHz represents the empirical dividing line between dm and cm radio emission. The inclined dotted line approximately marks the frequency-dependent flux limitation discussed in the text.

In Figure 3.3 we show the same information as in Fig.3.2, but now plotting only one point for each burst component, corresponding to the time of absolute peak flux density. The different symbols represent different burst types, as will be defined shortly. Included on Figure 3.3 is the average 1σ flux limit for the dataset, as a function of frequency. A few points appearing near this limit are weak bursts whose spectra were measured with the 27-m antennas.

The median peak flux density of the entire cm distribution in Fig.3.3 is 52_{-26}^{+85} sfu¹, and the median peak frequency is $6.6_{-1.7}^{+2.4}$ GHz. This value of median peak frequency agrees with the average values previously reported by Castelli & Guidice (1972) and Stähli, Gary & Hurford (1989). At the same time, it may be observed that the bulk of cm emission shifts to higher frequencies as the intensity of the events increases. A similar result was reported by Castelli & Guidice (1972) who noted that the C-type bursts (bursts with a single spectral maximum in the microwave range), peak at higher frequencies as their peak flux density increases. Looking at the individual tracks associated with an event, which can be distinguished in some cases in Fig.3.2, we see that this correlation is often seen throughout the burst, not just at the peak time. This finding disagrees with Stähli, Gary & Hurford (1989) who concluded that in most cases the peak frequency remains remarkably constant during the evolution of the bursts. However, we believe that this is likely an artifact of the use by Stähli, Gary & Hurford (1989) of data from the 27-m antennas, whose restricted field of view truncates the high-frequency emission and artificially restricts the spectral shape. We have demonstrated this effect for many of our events by comparing the spectral shape observed with the 2-m and 27-m dishes. A detailed analysis of the time-dependent behavior of the peak frequency leads to many interesting results, which we report elsewhere (Melnikov, Gary & Nita 2003).

¹We use this notation throughout this paper, where the lower and upper limits represent the range that contains 50% of the burst population. For example, 50% of the bursts have peak fluxes ranging from $52 - 26 = 26$ sfu to $52 + 85 = 137$ sfu.

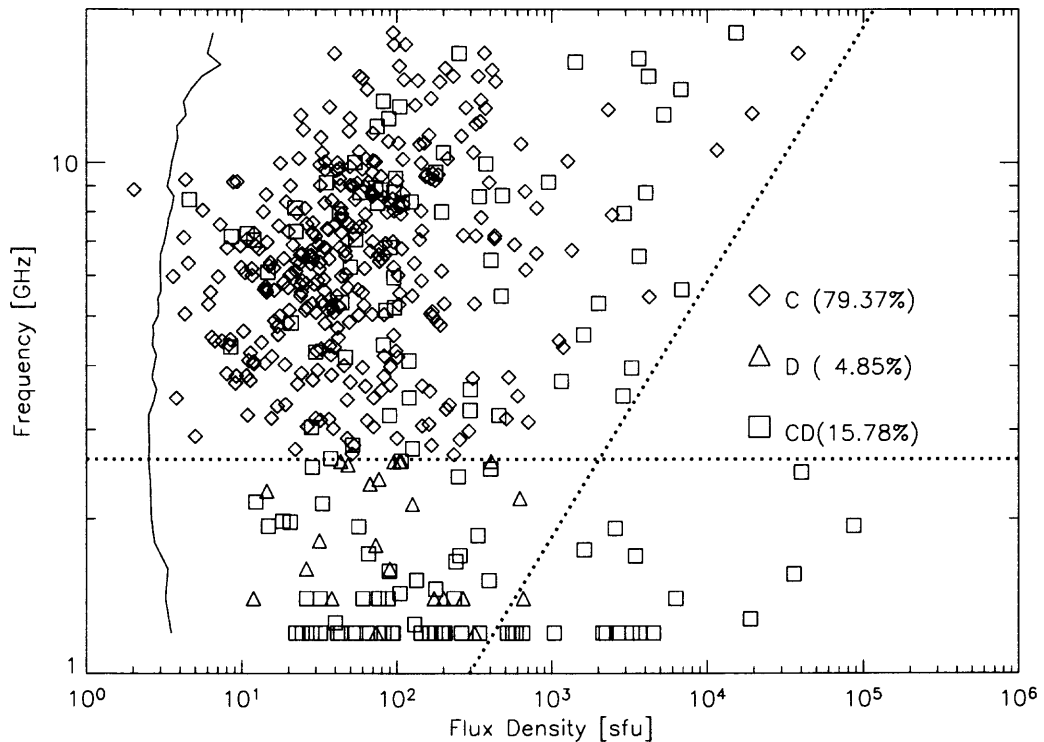


Figure 3.3 The flux-frequency distribution of the spectral types. Each of the 500 spectral components of the 412 OVSA radio bursts is represented by one data point corresponding to its absolute peak. However, to compute the percentages corresponding to each type, C (diamonds)-79.37%, D (triangles)- 4.85%, and CD (squares)-15.78%, each burst has been counted only once. The irregular vertical curve at the left is the frequency-dependent 1σ RMS noise limit of the dataset. The horizontal and inclined dotted lines are the same as those shown in Fig.3.2.

In their previous study, Nita et al. (2002) found that the number density distribution of microwave events shows a powerlaw with a slope close to the predicted universal value of ~ 1.8 obtained from simulations done by Lu & Hamilton (1991). However, a detailed analysis in different frequency ranges showed a slight but statistically significant frequency dependence, the number density distribution being steeper in those frequency ranges with fewer high flux density events. They thus showed that the lack of high-flux-density events was accompanied by a simultaneous increase in the number of low-flux-density ones.

This conclusion is supported by an analysis of Fig.3.3 as shown in Figure 3.4. The OVSA dm events below the empirical limit of 2.6 GHz (Fig.3.4a) have a power-law slope of -1.42 ± 0.09 , while cm events above the limit (Fig.3.4b) have a slope of -1.73 ± 0.04 . These slopes agree quantitatively with the results of Nita et al. (2002) obtained for similar frequency ranges.

To conclude this section, we find that the spectral peak distribution of solar radio bursts in the 1 – 18 GHz range is the result of at least two different populations: dm bursts with an upper frequency limit of about 2.6 GHz, but with no special intensity limit or frequency dependence, and cm bursts that show a frequency dependent flux limit and a steeper flux distribution, with characteristic peak parameters that evolve in a correlated manner.

The differences between these two populations likely reflect the underlying emission mechanisms responsible for their generation. As generally accepted now, (Bastian, Benz & Gary 1998), the cm bursts are dominated by the gyrosynchrotron emission mechanism, while the dm bursts are dominated by coherent emission mechanisms such as plasma emission or electron cyclotron maser (ECM) emission. However, other mechanisms such as transition radiation (TR), may compete in this frequency range. Recent case studies based on the same dataset

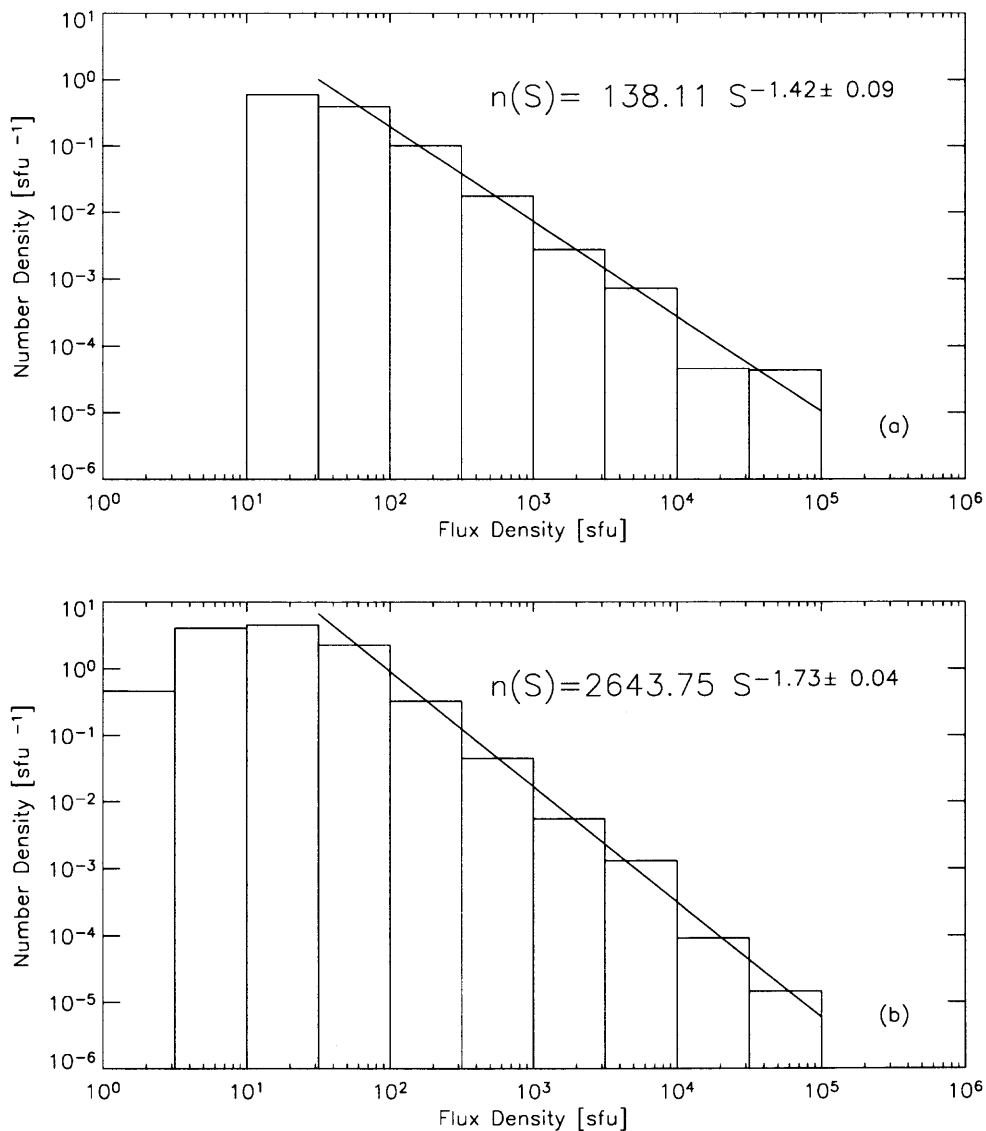


Figure 3.4 Number density distributions of dm events, (a), and cm events, (b). A strong frequency range dependence of the power-law slope may be observed. The dm distribution is much flatter than the cm one, which implies a greater preponderance of strong events in the dm range.

have identified some events whose dm component is produced by ECM (Fleishman, Gary & Nita 2003) and TR (Fleishman, Nita & Gary in preparation).

We interpret the observed characteristics of cm bursts—the frequency-dependent flux density limit, the correlation of peak frequency with increasing flux density, and the steeper number density distribution—as general characteristics of gyrosynchrotron emission, while those associated with dm bursts—higher peak flux densities, lack of characteristic frequency dependence, and flatter number density distribution—belong to coherent emission mechanisms. However, the possibility is not excluded of gyrosynchrotron peaks occurring in the dm range, say from loops with low magnetic field strength. But the extrapolated flux limit of gyrosynchrotron radiation to the dm range suggests that there is a severe flux limit for such events—a limit unlikely to exceed 300 sfu at 1 GHz.

3.4 Spectral Types and their Characteristics

3.4.1 Definition of Spectral Types

Classifying microwave bursts based on the frequency range in which the spectral peak of a radio burst occurs is just a first step. In fact the two main populations identified in the previous section overlap in the dm range and some of the events may have more than one spectral component in one or both frequency ranges. The spectral shape of a microwave burst is a valuable criterion that allows for a more precise classification. In their previous work, Castelli & Guidice (1972), Guidice & Castelli (1975) and Cliver, McNamara & Gentle (1985) used a classification scheme initially developed for internal use at AFCRL. This scheme contained three basic spectral shapes denoted A, C and G. The A shape represents a spectrum that monotonically increases with increasing frequency, the C shape represents a spectrum with a spectral peak in the microwave range, while the G shape represents a spectrum that monotonically increases with decreasing frequency. Combinations of these basic types have also

been considered, the main one being the G-C combination which, in the case of very strong events (above 1000 sfu), was defined as a U-type burst.

Since it is obvious that any spectrum of A or G type cannot indefinitely increase, but must have a maximum somewhere outside of the observed frequency range, we adopted a somewhat simplified scheme in which any observed spectrum is considered to be a combination of different components, each having a spectral peak that may or may not be seen in the observed range. However, to distinguish the frequency range in which the spectral peak of a microwave burst may occur, we introduced two basic types, the pure cm C-type and the pure dm D-type, along with the combined CD-type having at least one spectral component in each of the two frequency ranges defined by our empirically-determined limit of 2.6 GHz. So, one should distinguish between our C type and the AFCRL type having the same name, and be aware that our C or D types may include bursts with peaks outside of our range of 1–18 GHz, which would correspond to A and G types, respectively, in the AFCRL scheme.

Figure 3.5 displays six examples of dynamic spectra corresponding to our classification. The first row shows two pure cm, C-type spectra, one with a single frequency component above 2.6 GHz (left panel) and one with two spectral components in the cm range (right panel). The second row displays two pure dm D-type spectra, one with smooth time variation and unresolved spectral peak (left panel) and one with a spiky time profile (right panel). The third row displays two CD-type spectra. The one represented in the left panel has two well defined spectral components, one in the cm range and one in the dm range. In the right-hand panel is displayed a more complex composite burst. In the early stage, the smooth cm emission is accompanied by spiky emission close to 1.2 GHz and maybe below. Later on, the smooth cm emission is accompanied by a well resolved smooth dm component. The early stage of this burst corresponds with the classical definition of a U-type burst.

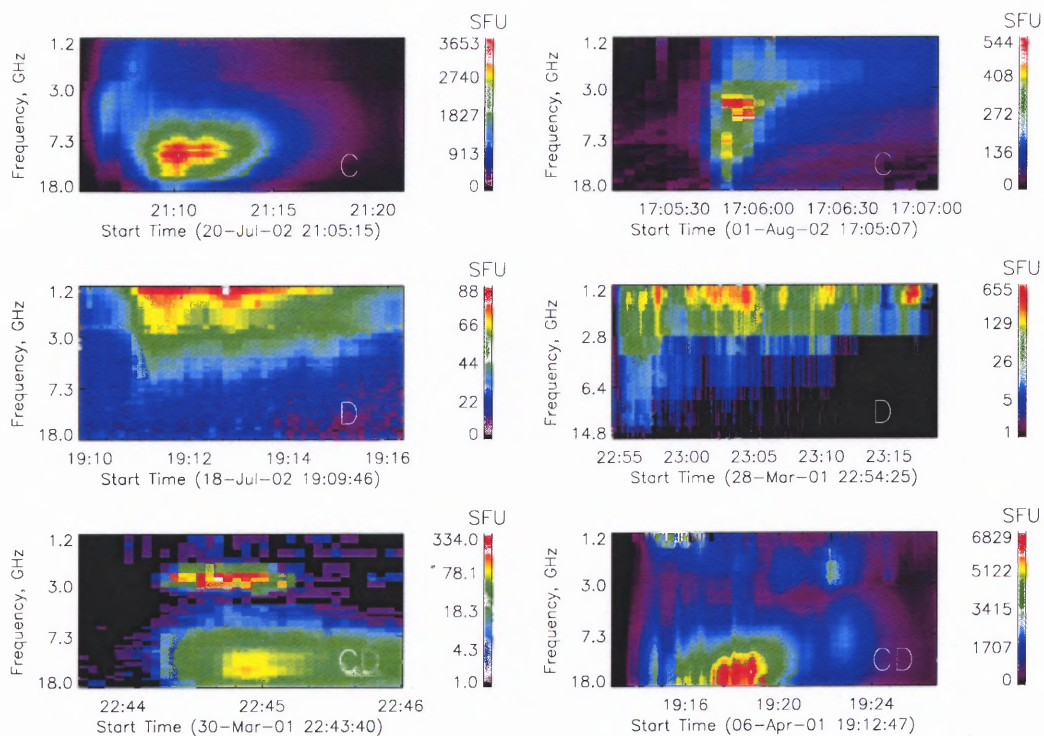


Figure 3.5 Different types of dynamic spectra recorded by OVSA. Centimetric type (C): peak frequency only above 2.6 GHz. Decimetric type (D): peak frequency only below 2.6 GHz. Composite type (CD): at least one spectral component in each of the cm and dm frequency ranges.

According to Table 3.1, about 80% of the analyzed bursts are single component bursts of pure C or D types, while about 18% of them, having two spectral components, are of C, D or CD types. The four bursts (1%) with three spectral components were classified as CD type with two components in the cm range and one in the dm.

3.4.2 Absolute Peak Distribution of Spectral Types

To have a better picture of how the different types are distributed according with their peak flux and peak frequency, we plot in Figure 3.3 the distribution of the absolute spectral peaks as derived from our dataset. In this diagram each event is represented using one data point corresponding to the absolute spectral peak of each resolved spectral component, so that some bursts appear more than once. However, to compute the percentage corresponding to each class, each burst was counted only once. The pure cm C-type (diamonds) bursts represent 79.4% of the total of 412 analyzed bursts, while the pure dm D-type (triangles) bursts represent only 4.9%. The composite CD-type bursts (squares) represent 15.9% of the observed bursts. This result is close to the percentage of about 14% of composite bursts reported by Castelli & Guidice (1972).

The shift of high peak frequencies to higher flux densities is evident for both C and CD types. It is remarkable that, although not intended, the flux limit of the cm emission is also obeyed by the pure dm D-type bursts. All but one of the high flux dm bursts to the right of the demarcation line represent low frequency components of the composite CD-type bursts. This result agrees with the picture in which the low frequency component of composite CD bursts is produced by a different emission mechanism, and shows that high intensity bursts, above several hundred sfu in the dm range, are essentially always U-type bursts with a cm- λ counterpart. There is a tendency for high flux cm bursts to have a dm counterpart, but this is not always

the case. Although three of the most intense cm bursts appear to be of C type as observed in OVSA frequency range, there remains the possibility that there is were unseen dm counterparts below the 1.2 GHz OVSA limit. In fact, we examined the NOAA event lists and found that two of the three events did have low frequency components below 1.2 GHz. However, since we have not done such a check for all of our C-type bursts, we do not change the classification as inferred from the OVSA frequency coverage.

One should be aware that our reported peak frequencies of 1.2 GHz for the CD-type bursts and their associated peak fluxes are not necessarily the true ones, since they are at the low frequency limit of OVSA. In fact, 43.47% of CD-type bursts (30 events out of 69) have unresolved peaks at this frequency. If we had data below 1.2 GHz, this would likely increase the percentage of composite bursts with fluxes above 1000 sfu. The same situation seems unlikely for the pure dm D-type bursts. In this case, only 15% (3 out of 20 events) have unresolved spectral peaks at 1.2 GHz. When combined with the flux limit observed for the group as a whole, it seems unlikely that much larger fluxes would be seen below 1.2 GHz for most D-type events.

3.4.3 Peak Flux Distribution of Spectral Types

Figure 3.6 displays the peak flux distribution of spectral types. The median flux corresponding to each type and the range in which 50% of the events are distributed is indicated on each plot.

The C-type bursts (Fig.3.6a) peak around 46 sfu, while 50% of these bursts have an absolute peak flux between 24 and 105 sfu. However, the distribution has a tail at high fluxes. The classification of these high flux bursts as C-type may be correct, but as we mentioned above, some may be CD bursts whose low frequency component is not in the OVSA frequency range. We compare this distribution with the cm component of the CD-type emission (Fig.3.6c). The latter has a larger median

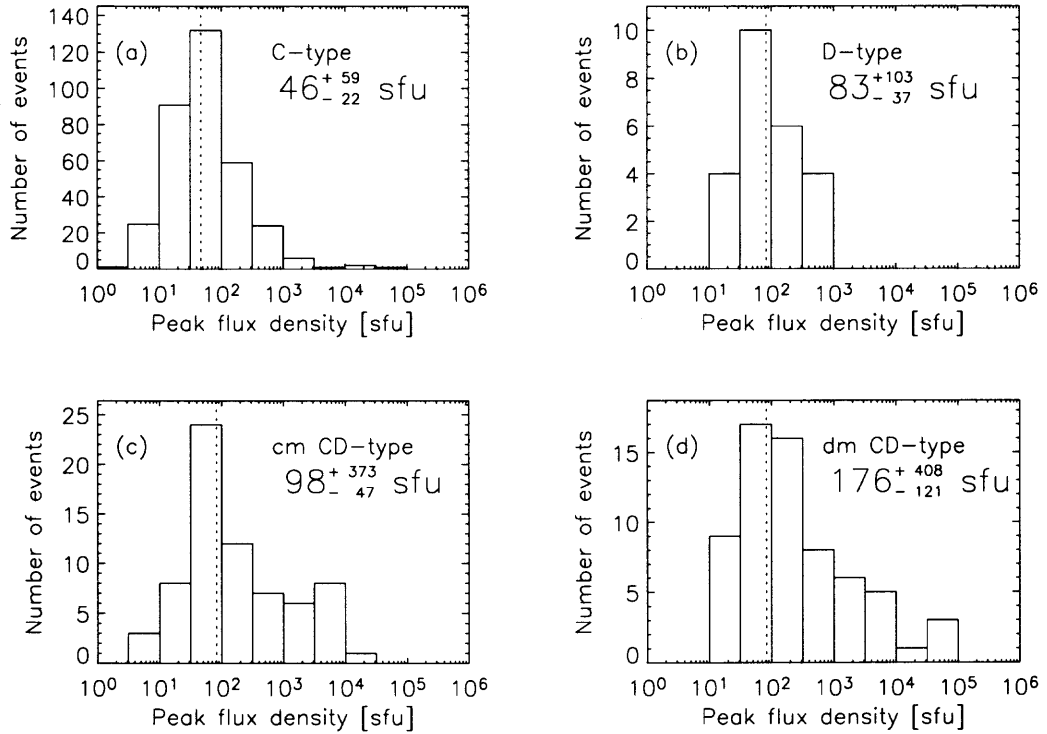


Figure 3.6 Peak flux density distribution of spectral types: (a) C type, (b) D type, (c) cm components of CD type, (d) dm components of CD type. The median peak fluxes and the 50% probability ranges are indicated on each plot.

value, 98 sfu, half of the events are distributed in the range [52 – 471] sfu and its high flux tail decreases slower than that of the C-type distribution. The immediate conclusion is that, on average, the cm branch of CD-type bursts tends to be stronger than the pure cm C-type bursts.

The pure dm D-type bursts (Fig.3.6b) are strictly confined below 1000 sfu, while the dm CD-type distribution (Fig.3.6d) is the only burst type responsible for high flux emission in the dm range. The 50% probability ranges are [46 – 186] sfu for the D-type bursts and [55 – 584] sfu for the dm branch of CD-type bursts. Just as in the cm range, the strongest emission in the dm range is due to the composite CD-type bursts.

Finally we compare the cm and dm components of CD-type bursts in Figures 3.6*b, c, d*. The median flux of the dm component, 176 sfu, is larger than for the cm component and its distribution is wider due to the higher fluxes. This implies that on average, the low frequency component of CD-type bursts tends to be stronger than the high frequency one. As we will show in a later section, this is true in 61.5% of cases. The true percentage may be even higher, since the events that have unresolved low frequency peaks at 1.2 GHz are excluded from these statistics.

We also looked at the peak flux distribution of spectral types in a similar manner as Castelli & Guidice (1972), defining three intensity levels. However, since we found the median value of C-type flux density to be around 50 sfu, and the flux limit of cm emission to become important above 1000 sfu, we adopted 100 and 1000 sfu as dividing lines between our intensity levels, instead of 50 and 500 sfu that they used. The numbers of events of each type in each intensity range are listed in Tables 3.2 and 3.3. From these tables it can be seen that, indeed, the percentage of CD-type bursts increases with intensity in both frequency ranges, becoming 60% in the cm range and 100% in the dm for the bursts above 1000 sfu.

Although the tendency of intense bursts to show both cm and dm emission may be considered just the result of the *Big Flare Syndrome*, (Cliver, McNamara & Gentle 1985, and references therein), we believe that in some cases there is a physical connection between the two spectral components of the CD-type bursts. This is shown by looking at correlations between certain parameters associated with each of the spectral components. Indeed, in a separate study based on the same dataset, Fleishman, Gary & Nita (2003) found a strong correlation between the slope of the optically thin gyrosynchrotron spectrum and the flux ratio of cm to dm components of CD-type bursts. They used this finding to support the idea that spike production is directly related to the energy and pitch angle distribution of the trapped electrons responsible for the accompanying microwave gyrosynchrotron emission, in agreement with the expectations of the Electron Cyclotron Maser theory.

3.4.4 The Peak Frequency Distribution of Spectral Types

In Figure 3.7 we present the absolute peak frequency distribution of the microwave bursts as observed in the OVSA frequency window. The equal logarithmic bins have been chosen to allow an easy comparison with previously reported results (Castelli & Guidice 1972; Guidice & Castelli 1975), which were based on observations at fixed frequencies separated by about one octave. Note that any burst with actual peak frequency above 18 GHz, which is the high frequency limit of OVSA, would appear in the last bin.

The overall distribution has a “U” shape with a minimum near 1.6 GHz. The continuity in the C- and D-type distributions across the dividing line in Fig.3.7b suggests that the D-type distribution is merely an extension of the C-type one. This is further supported by the frequency-dependent flux limit discussed previously, which appears to be obeyed by all gyrosynchrotron bursts whether peaking in the cm or dm range. In contrast, the CD distribution in Fig.3.7c monotonically decreases in

the dm range, and is responsible for the “U” shape of the overall distribution. In the cm range, the CD distribution is nearly uniform up to about 7 GHz, where it has a local maximum at a higher frequency than the maximum of the C-type distribution. These distributions have been obtained using all of the observed events, regardless of magnitude. To see how these distributions change with the intensity level, we list in Tables 3.2 and 3.3 the median peak frequency and the 50% probability range corresponding to each spectral type in the three flux density ranges.

None of the dm types (Table 3.3) show a significant change in their median peak frequency with intensity level. However, the dm components of CD-type bursts have, in any given intensity range, a median peak frequency lower than the pure D-type bursts. The median peak frequency of the former may be even lower, since almost 50% of these bursts actually have unresolved spectral peaks at 1.2 GHz.

In the cm range (Table 3.2) for both C and CD types, an increase in peak frequency with intensity level is evident. Although this effect seems to be stronger for the C-type events, we do not consider this result significant since, as we mentioned before, at least some of the C-type bursts may have dm components undetected by OVSA. Rather, we consider this effect to be a common feature of gyrosynchrotron emission, occurring equally in both C and cm component of CD spectral subclasses. In order to better quantify the shift of peak frequency with the intensity level of cm bursts, we plot in Figure 3.8 the median peak frequency of the cm bursts above a running low cutoff peak flux limit. Along with the values corresponding to the peak time (solid line), we also plot the median values corresponding to the rise and decay phases, as defined earlier in §3.2. To represent each spectral component by a single value in each of its phases, we used the median peak frequency corresponding to all of the time samples in a given phase.

Figure 3.8 shows that the median peak frequency has an overall shift through higher values as the low cut off limit of peak flux increases. There is a slight local

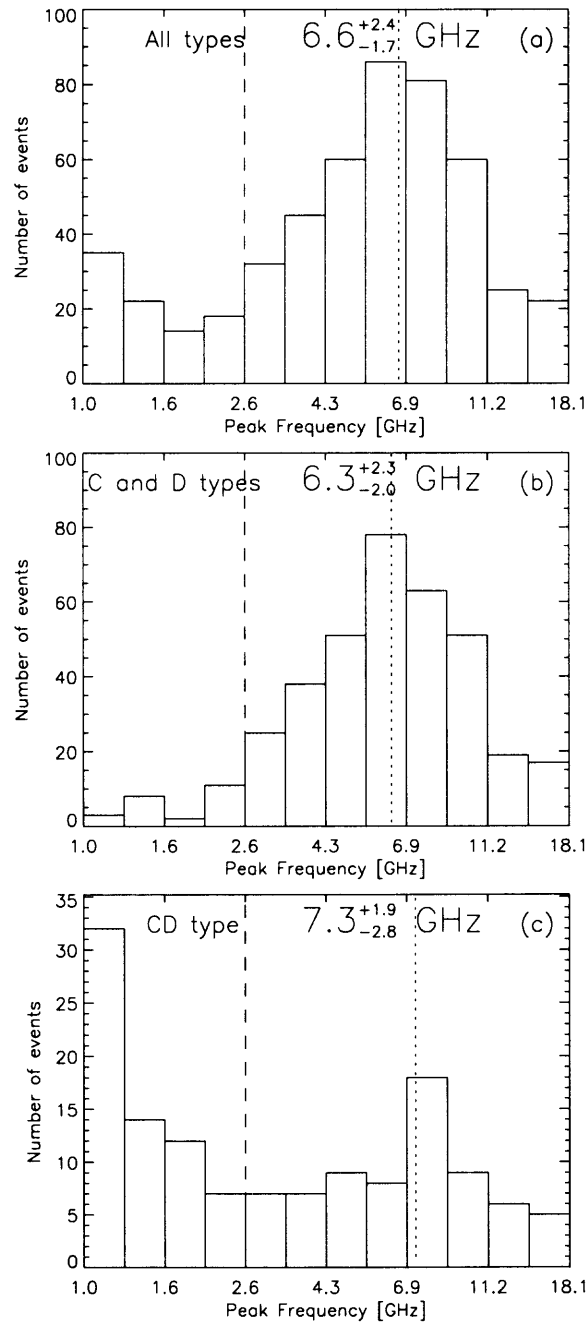


Figure 3.7 Peak frequency distribution of event types: (a) All types, (b) C and D types, (c) CD type. The median peak frequencies of cm-types and 50% probability ranges are indicated on each plot. The equally logarithmic bin size was chosen to allow comparison with the previously reported results, which were based on fixed frequency observation separated by one octave.

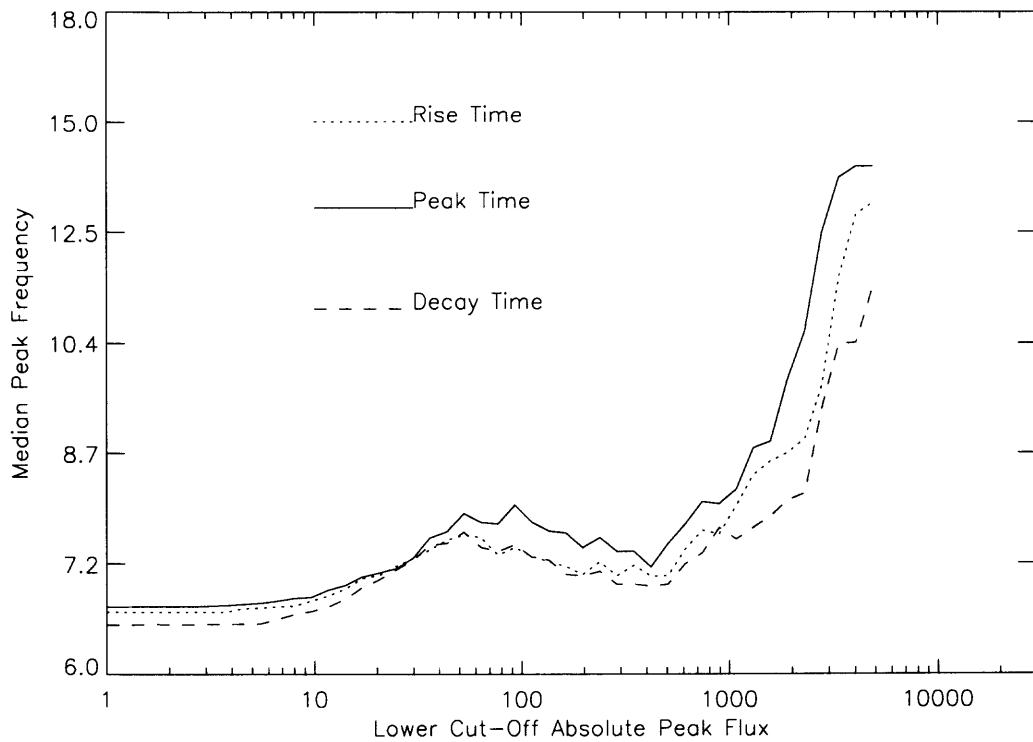


Figure 3.8 The shift of the peak frequency with intensity level for the cm bursts. The median peak frequency of all cm bursts above a low cutoff limit of the absolute peak flux is plotted. The median values are plotted separately for different times during the bursts: at the absolute peak, (solid line), rise time, (dotted line), and decay time (dashed line).

rise in median peak frequency above ~ 100 sfu, followed by a much sharper increase as we limit the measurement to bursts with still higher fluxes. The explanation for the local peak is seen in the two-dimensional distribution shown in Fig.3.2, where the bulk centroid of the cm bursts is seen to shift to higher frequencies for higher fluxes. For bursts at yet higher fluxes, however, the frequency-dependent limit of the peak flux (indicated by the inclined dotted line) begins to have an increasing effect on the median peak frequency. Whether the two effects are related remains to be further investigated.

Although they follow the same trend, the median peak frequency in the rising and decaying phases always remains below the value at the peak time. This result is consistent with the general picture of gyrosynchrotron emission, (Dulk & Marsh 1982), according to which the peak frequency is expected to increase during the rise phase and decrease during the decay phase. Our result disagrees with the similar one reported by Stähli, Gary & Hurford (1989), who found no significant change of the peak frequency during the gyrosynchrotron burst evolution. Moreover, their averaged values in the rise and decay phases were higher than the averaged values at the peak time, suggesting an opposite dynamic behavior than we found. We should mention that our result pertains to the average behavior of bursts. Many individual bursts actually display very different behaviors, as can be discerned in the trails evident for stronger bursts in Fig.3.2 (see also Melnikov, Gary & Nita 2003).

3.4.5 The Spectral Slope Distribution

The statistics of spectral slopes below and above the peak frequency, especially in the case of gyrosynchrotron emission mechanisms, is of special interest due to the diagnostic tools provided by these measures. The low frequency slope may provide valuable information about the mechanism responsible for the low frequency turnover of the radio spectrum, (e.g. free-free absorption, self-absorption or Razin

suppression), while the high frequency spectral slope may be related to the energy distribution of the electrons responsible for the gyrosynchrotron radiation. However, one should be cautious when using diagnostics based on a restricted set of fixed frequencies. Without good frequency resolution, the inferred slopes may appear less steep than the true ones, as pointed out by Castelli & Guidice (1972) or Stähli, Gary & Hurford (1989).

Using fixed frequency data from Sagamore Hill, 1968, Castelli & Guidice (1972) analyzed the distribution of spectral slopes of microwave bursts and found a low frequency spectral index between 2.5 and 4.5, and a high frequency spectral index between -1.5 and -5.5. Using the multi-frequency observations offered by OVSA, Stähli, Gary & Hurford (1989) found, for a set of 49 events, the average low frequency slope at the peak time to be 3.1 ± 0.2 and an average high frequency spectral slope of -3.7 ± 0.2 . They also reported similar averaged values for the rising and decaying phases of the microwave bursts. The low-frequency slopes may be compared with the expected optically thick slope from a homogeneous source (Dulk & Marsh 1982) of 2.9. However, many bursts are from inhomogeneous sources, for which the optically thick source size will itself be frequency dependent. Therefore, the spatially integrated spectrum below the peak frequency will be flatter than for a corresponding homogeneous source—sometimes significantly so. For bursts with measured “size spectra”, e.g. Gary & Hurford (1990), the size is typically proportional to $\sim f^{-1}$, flattening the slope below the spectral peak to 1.9. For some bursts the inhomogeneity can be even larger, and the spectral slope can be essentially zero in large flares (Lee et al. 1994).

Using our data set, obtained with the upgraded OVSA instrument, we analyzed the distribution of spectral slopes and their possible relationship with the other two peak parameters, peak flux and peak frequency. In Figure 3.9 we plot the distribution of spectral slopes of C-type bursts (diamonds), and cm-CD-type (squares), versus

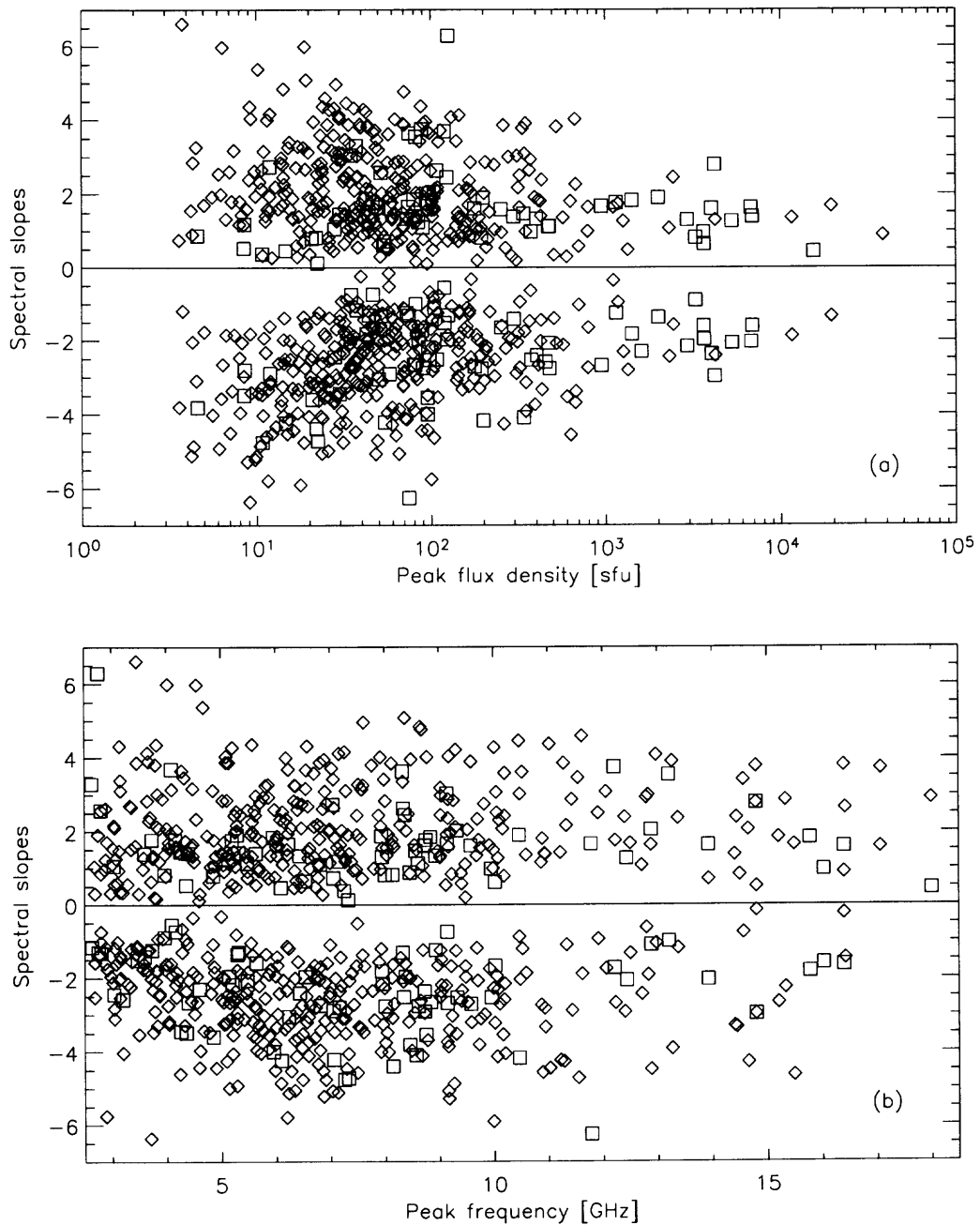


Figure 3.9 Distribution of cm-type spectral slopes (a) versus peak flux and (b) peak frequency (diamonds—C type, squares—CD type). The positive values represent the low frequency spectral slope and the negative value the high frequency spectral slope.

the absolute peak flux (upper panel), and absolute peak frequency (lower panel), at the absolute peak time. The butterfly-diagram appearance of the upper panel shows that the spectral slopes on both sides of the cm-type burst spectral peak become less steep with increase of intensity level. A similar result, involving only the low frequency slope, was pointed out by Stähli, Gary & Hurford (1989).

To better quantify the flattening of gyrosynchrotron spectra with the increase of the intensity level, we plot in Figure 3.10 the median indices calculated for cm bursts having a peak flux above a low cut-off limit. The continuous shift of the median values at the peak time, rise or decay phase, on both sides of the spectra, is evident.

The decrease of low frequency slope with increase of peak flux suggests greater source inhomogeneity for the largest bursts, while the hardening of the high frequency side of the spectrum suggests the presence of higher energy electrons on average in the strong bursts. No correlation is seen between the spectral slopes and the absolute peak frequency, (Fig.3.9b). The lack of correlation with high frequency slope suggests that the peak frequency does not depend on the mean energy of the electrons.

In Figure 3.11 we plot the distributions of spectral slopes for all cm bursts (*a*), and separately for the pure cm C-type bursts (*b*), and for the cm components of CD-type bursts (*c*).

The overall distribution gives a median value of low frequency slope of 1.79 and a median value of high frequency slope of -2.51 . These values are in strong disagreement with the average values reported by Stähli, Gary & Hurford (1989), who reported much steeper slopes on both sides of the gyrosynchrotron spectrum. A partial explanation may be the low overall intensity level of the previous data base, since only 2 out of 49 events had peak fluxes above 100 sfu. Figure 3.9 shows that the weak bursts tend to have steeper slopes than strong ones—slopes averaged over a more extended database are expected to be somewhat flatter. Another explanation,

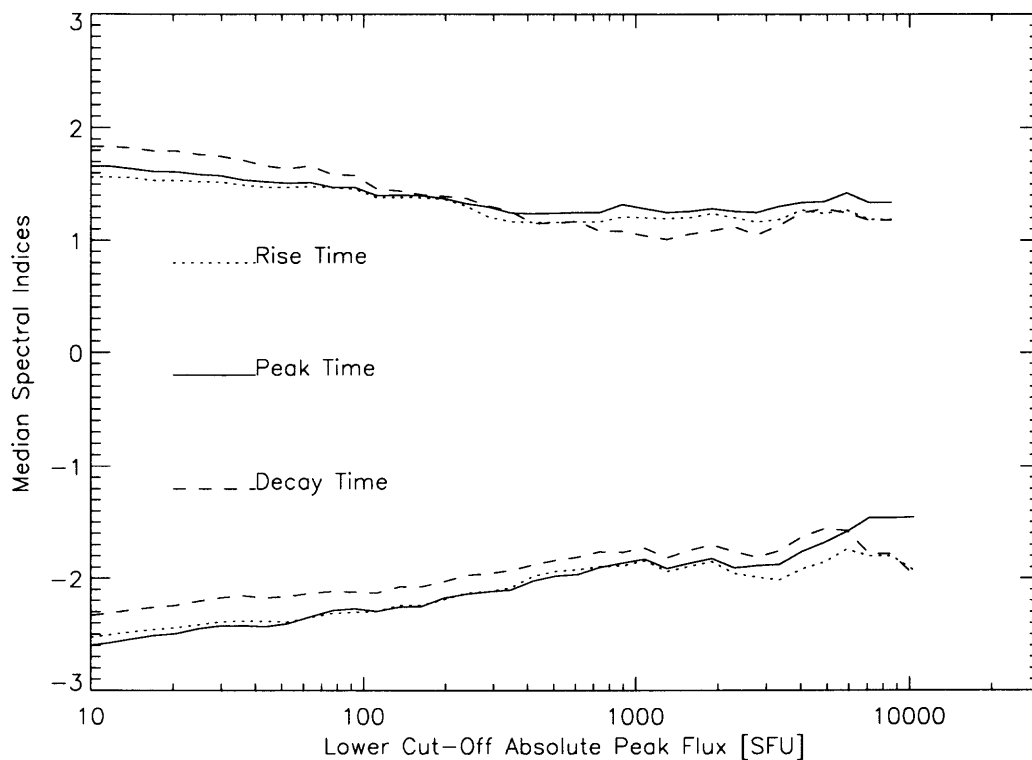


Figure 3.10 The shift of cm-bursts spectral indices with the intensity level. The median low (positive values) and high (negative values) frequency spectral index of all cm bursts above a low cutoff limit of the absolute peak flux is plotted. The median values at the absolute peak, (solid line), rise time, (dotted line), and decay time (dashed line), shift to zero on both sides of the spectra.

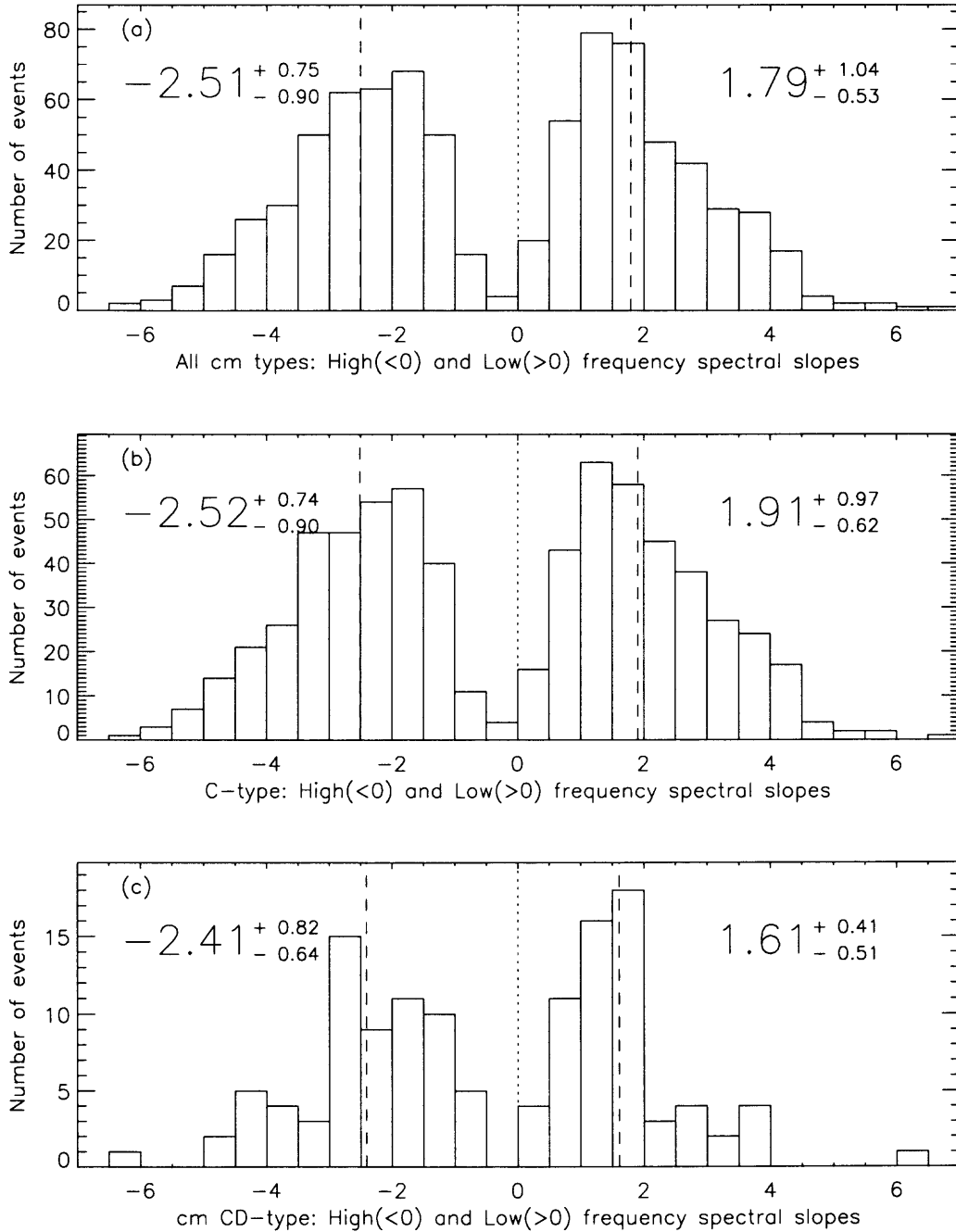


Figure 3.11 Distribution of spectral slopes for cm-type bursts. The positive values represent the low frequency spectral slope and the negative value the high frequency spectral slope: (a) the distribution of all cm-type bursts, (b) the distribution of C-type bursts, (c) the distribution of cm counterpart of CD-type bursts.

valid only for the high frequency side of the spectra, may be instrumental. The spectra used by Stähli, Gary & Hurford (1989) were obtained only with the 27-meter antennas available at that time. The restricted field of view of these antennas at high frequencies may introduce a considerable error in the case of a flare occurring at some distance from the targeted point. In such a case, the high frequency side of the observed spectrum may experience a severe attenuation unrelated to the source spectrum itself. This also would explain the constancy of peak frequency they reported, as discussed in the previous section. Our results based on data recorded by the 2-meter antennas are far less affected by any slight off-pointing. We do not have an additional instrument-based explanation for the differences on the low frequency part of the spectrum.

The distribution of pure C-type bursts (Fig.3.11b) is not significantly different from the overall distribution (Fig.3.11a). The cm component distribution for CD-type bursts (Fig.3.11c) on the other hand, reveals some peculiarities possibly related to plasma conditions favorable for generation of the accompanying dm component. A remarkable 75% of CD bursts have low frequency slopes less than 2, which likely indicates a high degree of inhomogeneity for these radio sources. However, the distribution of the remaining 25% seems to extend to steeper slopes than the overall distribution. This may be an indication of the prevalence of Razin suppression. On the high frequency side, the slope distribution of cm CD-type bursts has a median value close to the overall one, but displays both a local peak around -4 and an excess of events with shallow slopes. Bursts with steeper than usual high frequency slopes were related by Fleishman, Gary & Nita (2003) to dm spikes observed in a quasi-parallel geometry, while the flatter ones were related to spikes observed in quasi-transverse geometry.

A similar analysis done for the D-type bursts and the low frequency components of CD-type bursts, revealed no correlation between their spectral slopes and their

peak flux or peak frequency. We also found on average much steeper spectral slopes associated with these events. These differences between dm and cm parameters simply reflect their different emission mechanisms.

The median values of the spectral slopes of each spectral type, binned by flux level, are listed in Tables 3.2 and 3.3. The median values corresponding to cm bursts peaking in different frequency bands are listed in Table 3.4.

3.4.6 Time scale of microwave bursts

Besides the spectral parameters discussed above, the time scale of microwave bursts may offer valuable information about statistical properties of different spectral types. Performing this kind of analysis, one may choose different time-related parameters to define the time scale of radio bursts, such as the rise time or decay time constants. However, such a choice may not be appropriate for bursts with multiple peaks, when one or both phases may be a mixture of separate burst episodes. For our database we found it more appropriate instead to use the peak duration, defined as the time interval during which the flux density at the local peak frequency is above 80% of the corresponding peak flux. Although we made measurements for each resolved temporal peak, we use in this analysis only data referring to the main peak.

The dynamic spectra plotted in Figure 3.5 illustrate different time behaviors corresponding to each spectral type. The first row displays, in the left panel, a gradual rise and fall C-type burst and, in the right panel, an impulsive C-type burst. The left panel of the second row displays a D-type burst having a smooth time profile, while the right panel displays a pure D-type burst having a spiky time profile. The third row displays two different varieties of CD-type bursts—on the left a burst with both components of short duration and on the right a burst with a more complex time profile with both impulsive and gradual components.

Figure 3.12 displays the peak duration distributions corresponding to each of our spectral types. The pure cm C-type bursts (Fig.3.12a), are mainly impulsive, with a median duration above 80% of the peak value of about 20 s. However, 25% of the C-type bursts are gradual rise and fall bursts, with a peak duration from 40 s up to more than few hundred s.

The pure dm D-type distribution (Fig.3.12b) has a broad distribution (the two peaks are not statistically significant). The broad distribution, much wider than the C-type distribution, may reflect the mixture of different emission mechanisms responsible for radio emission in the dm range.

Just as we found for other characteristics of C and cm CD-type bursts described earlier, the time scales of the two types show no essential differences. The dm component of CD-type bursts, however, tend to be more impulsive than their cm counterpart. This is likely due to different emission mechanisms—gyrosynchrotron emission in the cm range, and short duration coherent emission in the dm range. However, about 25% of the low frequency CD-type components have a smooth time profile that is unlikely to be produced by a coherent emission mechanism. In agreement with our earlier findings about flux distributions, the smooth low frequency components of some CD-type bursts may be produced by gyrosynchrotron emission from weak magnetic fields, synchrotron emission by relativistic electrons, or even transition radiation (Lee et al. 2003; Fleishman, Nita & Gary in preparation).

A summary of the temporal characteristics of the spectral types we defined, in relation with the intensity level or frequency range, is given in the next section.

3.4.7 Summary of Spectral Type Characteristics

In Tables 3.2, 3.3 we give the number of events of a given type and the median values of the analyzed parameters in three flux density levels: $S_{\text{peak}} < 100$ sfu, $100 < S_{\text{peak}} < 1000$ sfu, and $S_{\text{peak}} > 1000$ sfu. For the cm-type bursts, we also present

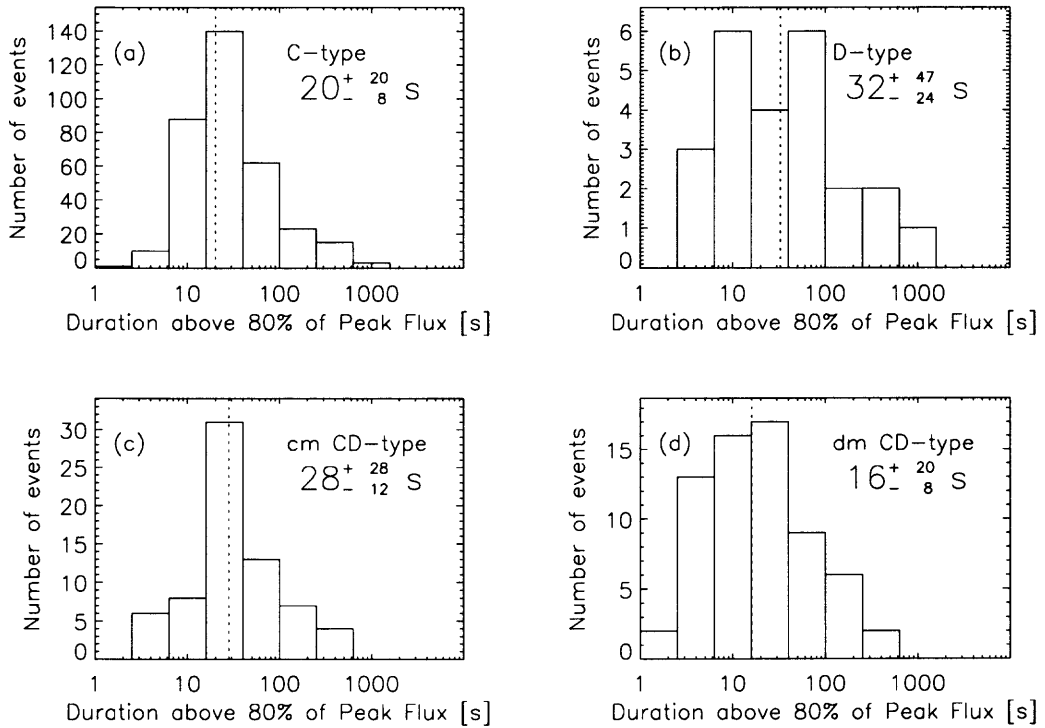


Figure 3.12 Duration above 80% of the peak flux: (a) C type, (b) D type, (c) cm components of CD type, (d) dm components of CD type. The median durations and the 50% probability ranges are indicated on each plot.

Table 3.2. Statistics of Centimeter Spectral Types (Intensity, sfu)

Type	Parameter	Any flux	< 100	100 – 1000	≥ 1000
Any	Number of events	411(100.00%)	284	102	25
	Peak Freq. (GHz)	$6.6^{+2.4}_{-1.7}$	$6.3^{+1.8}_{-1.6}$	$8.0^{+2.9}_{-3.0}$	$7.9^{+4.8}_{-3.0}$
	Low Freq. Slope	$1.8^{+1.0}_{-0.5}$	$1.9^{+1.0}_{-0.6}$	$1.6^{+0.8}_{-0.6}$	$1.4^{+0.4}_{-0.4}$
	High Freq. Slope	$-2.5^{+0.8}_{-0.9}$	$-2.7^{+0.8}_{-0.9}$	$-2.1^{+0.6}_{-0.7}$	$-2.0^{+0.5}_{-0.4}$
	Peak Duration (s)	24^{+20}_{-12}	22^{+22}_{-10}	24^{+9}_{-12}	40^{+80}_{-24}
C	Number of events	342(83.21%)	249	83	10
	Peak Freq. (GHz)	$6.5^{+2.3}_{-1.7}$	$6.2^{+1.8}_{-1.5}$	$7.9^{+3.0}_{-2.8}$	$9.0^{+3.5}_{-3.5}$
	Low Freq. Slope	$1.9^{+1.0}_{-0.6}$	$2.1^{+1.0}_{-0.7}$	$1.6^{+0.7}_{-0.6}$	$1.3^{+0.3}_{-0.3}$
	High Freq. Slope	$-2.5^{+0.7}_{-0.9}$	$-2.7^{+0.8}_{-0.9}$	$-2.1^{+0.6}_{-0.9}$	$-1.9^{+0.5}_{-0.6}$
	Peak Duration (s)	20^{+20}_{-8}	20^{+21}_{-8}	24^{+8}_{-12}	22^{+18}_{-10}
CD	Number of events	69(16.79%)	35	19	15
	Peak Freq. (GHz)	$7.3^{+1.9}_{-2.8}$	$7.1^{+1.7}_{-2.2}$	$8.3^{+1.0}_{-4.7}$	$7.9^{+6.4}_{-3.3}$
	Low Freq. Slope	$1.6^{+0.4}_{-0.5}$	$1.5^{+0.3}_{-0.7}$	$1.6^{+1.0}_{-0.3}$	$1.5^{+0.3}_{-0.5}$
	High Freq. Slope	$-2.4^{+0.8}_{-0.6}$	$-2.7^{+1.0}_{-0.9}$	$-2.5^{+0.9}_{-0.2}$	$-2.0^{+0.4}_{-0.3}$
	Peak Duration (s)	28^{+28}_{-12}	24^{+8}_{-10}	20^{+13}_{-4}	64^{+88}_{-32}

in Table 3.4 similar statistics in three frequency bands. These bands, 2-6-4.3 GHz, 4.3-11.2 GHz, and 11.2-18 GHz, are chosen to divide the cm range accessible to OVSA in three equal logarithmic bins. Although our database contains 412 microwave bursts, we base the analysis summarized in these tables on the total of 500 spectral components we resolved, to which we refer for this purpose as *events*. Since 60.7% of the bursts have more than one temporal peak, in order not to bias the results by multiple contributions from the same event we include only the main peak of each spectral component.

3.4.7.1 Characteristic Parameters of Centimetric Bursts The first section of Table 3.2 presents the most probable parameters associated with cm bursts, which also may be regarded as gyrosynchrotron bursts. From the total of 411 spectral components in this frequency range, 69% (284) peak below 100 sfu, 25% (102)

Table 3.3. Statistics of Decimeter Spectral Types (Intensity, sfu)

Type	Parameter	Any flux	< 100	100 – 1000	≥ 1000
Any	Number of events	89(100.00%)	40	34	15
	Peak Freq. (GHz)	$1.4^{+0.4}_{-0.2}$	$1.4^{+0.5}_{-0.2}$	$1.4^{+0.3}_{-0.2}$	$1.3^{+0.4}_{-0.1}$
	Low Freq. Slope	$3.6^{+2.3}_{-2.5}$	$1.2^{+2.5}_{-0.5}$	$6.5^{+4.3}_{-3.6}$	$4.3^{+1.0}_{-2.6}$
	High Freq. Slope	$-3.1^{+1.1}_{-3.0}$	$-2.4^{+0.7}_{-1.4}$	$-3.9^{+1.9}_{-2.1}$	$-5.7^{+2.6}_{-10.6}$
	Peak Duration (s)	16^{+32}_{-8}	22^{+46}_{-14}	12^{+16}_{-8}	20^{+40}_{-16}
D	Number of events	24(26.97%)	14	10	0
	Peak Freq. (GHz)	$1.8^{+0.7}_{-0.4}$	$1.8^{+0.6}_{-0.4}$	$1.8^{+0.8}_{-0.4}$...
	Low Freq. Slope	$0.9^{+1.7}_{-0.4}$	$0.7^{+0.9}_{-0.3}$	$2.0^{+2.7}_{-1.1}$...
	High Freq. Slope	$-2.9^{+1.1}_{-1.1}$	$-2.6^{+0.7}_{-0.6}$	$-3.1^{+1.3}_{-1.7}$...
	Peak Duration (s)	32^{+47}_{-24}	44^{+68}_{-36}	26^{+14}_{-14}	...
CD	Number of events	65(73.03%)	26	24	15
	Peak Freq. (GHz)	$1.3^{+0.4}_{-0.1}$	$1.4^{+0.4}_{-0.2}$	$1.2^{+0.4}_{-0.0}$	$1.3^{+0.4}_{-0.1}$
	Low Freq. Slope	$4.7^{+4.0}_{-1.7}$	$3.4^{+1.2}_{-2.3}$	$10.4^{+0.8}_{-5.4}$	$4.3^{+1.0}_{-2.6}$
	High Freq. Slope	$-3.6^{+1.5}_{-3.2}$	$-2.3^{+0.6}_{-2.2}$	$-4.5^{+2.3}_{-1.8}$	$-5.7^{+2.6}_{-10.6}$
	Peak Duration (s)	16^{+20}_{-8}	18^{+38}_{-10}	8^{+4}_{-4}	20^{+40}_{-16}

Table 3.4. Statistics of Centimeter Spectral Types (Frequency, GHz)

Type	Parameter	Any freq.	2.6 – 4.3	4.3 – 11.2	11.2 – 18.0
Any	Number of events	411(100.00%)	77	287	47
	Peak Flux (sfu)	52^{+85}_{-26}	51^{+94}_{-29}	43^{+55}_{-20}	166^{+203}_{-91}
	Low Freq. Slope	$1.8^{+1.0}_{-0.5}$	$1.7^{+1.2}_{-0.7}$	$1.8^{+1.0}_{-0.6}$	$2.4^{+0.7}_{-0.8}$
	High Freq. Slope	$-2.5^{+0.8}_{-0.9}$	$-1.8^{+0.5}_{-0.7}$	$-2.7^{+0.7}_{-0.8}$	$-2.1^{+0.7}_{-1.6}$
	Peak Duration (s)	24^{+20}_{-12}	24^{+28}_{-8}	24^{+22}_{-12}	20^{+14}_{-10}
C	Number of events	342(83.21%)	63	243	36
	Peak Flux (sfu)	46^{+59}_{-22}	47^{+52}_{-30}	41^{+49}_{-19}	149^{+191}_{-87}
	Low Freq. Slope	$1.9^{+1.0}_{-0.6}$	$1.6^{+1.1}_{-0.6}$	$1.9^{+1.0}_{-0.6}$	$2.4^{+0.8}_{-0.8}$
	High Freq. Slope	$-2.5^{+0.7}_{-0.9}$	$-1.9^{+0.4}_{-0.7}$	$-2.7^{+0.7}_{-0.8}$	$-2.7^{+1.4}_{-1.6}$
	Peak Duration (s)	20^{+20}_{-8}	24^{+20}_{-8}	20^{+20}_{-8}	18^{+14}_{-6}
CD	Number of events	69(16.79%)	14	44	11
	Peak Flux (sfu)	98^{+373}_{-47}	122^{+332}_{-71}	87^{+270}_{-48}	1418^{+3314}_{-1329}
	Low Freq. Slope	$1.6^{+0.4}_{-0.5}$	$2.9^{+4.9}_{-1.4}$	$1.4^{+0.4}_{-0.5}$	$1.7^{+0.8}_{-0.4}$
	High Freq. Slope	$-2.4^{+0.8}_{-0.6}$	$-1.3^{+0.2}_{-1.2}$	$-2.7^{+0.7}_{-0.8}$	$-1.8^{+0.2}_{-0.3}$
	Peak Duration (s)	28^{+28}_{-12}	37^{+62}_{-29}	24^{+8}_{-8}	34^{+17}_{-14}

between 100 and 1000 sfu, and only 6% (25) above 1000 sfu. The first section of Table 3.4 shows that 70% (287) of the cm bursts peak in the [4.3-11.2] GHz frequency range, while only 19% (77) and 11% (47) peak below or above this frequency range, respectively.

These results roughly define the most probable flux and frequency ranges in which one should expect a cm burst to be observed. An alternative way to define these ranges is given by the median values and their associated 50% probability ranges. According to these tables, 50% of the cm bursts peak in the 52_{-26}^{+85} sfu flux range, and $6.6_{-1.7}^{+2.4}$ GHz frequency range.

Considering all the cm spectral components without regard to their peak flux, the median values of spectral slopes are $1.8_{-0.5}^{+1.0}$ for the low frequency side, and $-2.5_{-0.9}^{+0.8}$ for the high frequency side, both values being less steep than the averaged values previously reported by Stähli, Gary & Hurford (1989) for reasons already discussed.

Associated with an increase in intensity level of cm bursts is seen both an increase in peak frequency and a flattening of both spectral slopes. Whether or not the rising peak frequency is largely due to a change in magnetic field strength, as suggested by Guidice & Castelli (1975), cannot be decided without supplemental information. It is definitely clear, however, that the flattening of spectral slopes indicates that the strongest flares come from the most inhomogeneous sources and are produced by electrons with harder energy distributions. We also observe an increase in the time scale with intensity level for cm bursts (both C and cm-CD types, which are combined in the row marked "Any"). The time scales are 22_{-10}^{+22} s for events below 100 sfu, 24_{-12}^{+9} s for events between 100 and 1000 sfu, and 40_{-24}^{+80} s for those above 1000 sfu, which indicates that the most intense bursts tend to be gradual bursts, while most of the impulsive cm bursts do not exceed 1000 sfu. There is no significant relationship between time scale and peak frequency.

Similar trends may be observed for the individual cm classes, C and CD. The most evident difference revealed by the summary tables is related to the peak durations associated with each class. The time scale of the pure cm C-type bursts does not change significantly with intensity level, which suggests that the C-type bursts are mainly impulsive bursts at any intensity level. This is not the case for the cm components of CD-type bursts. Their time scale changes significantly, from 24_{-10}^{+8} s below 100 sfu, up to 64_{-32}^{+88} s above 1000 sfu, being solely responsible for the change of the time scale of the cm emission. Since the high flux CD-type bursts are in fact U-shape bursts, we conclude that most of the U-shape bursts have a gradual rise and fall component in the cm range.

3.4.7.2 Characteristic Parameters of Decimetric Bursts In Table 3.3 we list the characteristic parameters of dm bursts (D and dm-CD, denoted by Any) versus intensity level. Since the bursts falling in this category may be produced by several different emission mechanisms, there is no direct interpretation of the median values associated with the peak frequency— $1.4_{-0.2}^{+0.4}$ GHz, low frequency slope— $3.6_{-2.5}^{+2.3}$, and high frequency slope— $-3.1_{-3.0}^{+1.1}$, although these parameters may be used as diagnostic tools in some case-based analyses that assume a particular emission mechanism. However, the much steeper slopes of dm spectra compared to the cm case suggest that in many cases the radiation is the result of some coherent mechanism. The same conclusion is suggested by the much shorter time scale, 16_{-8}^{+32} s, of such events or spectral components. However, there are significant differences between the pure D-type bursts and the dm components of CD-type bursts. The most evident is the total absence of pure dm emission above 1000 sfu, which suggests that strong dm emission is always accompanied by cm emission. Thus, the coherent mechanism responsible for intense dm emission seems to be closely associated with

the cm emission process. One should also note that the pure D-type bursts have a time scale larger on average than the dm component of CD bursts.

3.5 Statistics of Microwave Bursts with Multi-Spectral Components

3.5.1 Peak Frequency Ratio

In a previous study based on OVSA data, Stähli, Gary & Hurford (1990) found from a sample of 49 events that $\sim 80\%$ displayed multiple spectral components. Moreover, they found that most of the bursts showed a frequency ratio between spectral peaks of a given event that fell between 3 and 4, with an average value of 3.4 ± 0.3 . This finding suggested a possible harmonic structure of the microwave bursts, which could not be explained. However, after the previous study was published, an instrumental effect was discovered, a slight third harmonic response of the mixer, that could produce spurious secondary peaks in the OVSA spectra (Bastian, Benz & Gary 1998) with a frequency ratio of 3, an amplitude ratio of 10 or more (i.e. the low-frequency peak would have at least 10 times lower flux density than the high-frequency peak), and identical time profiles for the two components.

Bastian, Benz & Gary (1998) speculated that this effect might explain the harmonic structure of multi-component bursts detected in the previous study. However, based on our work we must conclude that the results of Stähli, Gary & Hurford (1990), although anomalous, result from some other cause. Being now aware of this instrumental effect, we paid special attention to the process of resolving the spectral components in the present dataset. We carefully removed any frequency suspected to be affected by occasional external interference or reduced sensitivity, and manually selected the frequency ranges used to fit the spectral components in the dynamic spectra.

The present study revealed that only about 20% of the 412 analyzed events displayed more than one significant spectral component, most of them having one

spectral component in the dm range, and one in the cm range, i.e. CD-type events. However, 15 C-type events displayed two resolved spectral components in the cm range, and 4 of the CD-type events displayed, beside the dm component, two spectral components in the cm range.

One of the goals of this section is to check if the multi-component bursts reveal any harmonic structure. For this purpose, we analyzed the distribution of peak frequency ratios, defined as the ratio of the high to low peak frequency, whatever the absolute peak time in each frequency range associated with a given multi-component event. Since a low peak frequency of strictly 1.2 GHz indicates an unresolved low frequency spectral peak, we discarded from our analysis all such events as irrelevant, ending up with ratios for 15 C-type and 39 CD-type events. In Figure 3.13a we plot the high versus low peak frequency for the C-type (diamonds) and CD-type (squares) events. Although the distribution is scattered over the semi-plane corresponding to supra-unitary ratios, an apparent clustering of some data points is seen along the lines representing integer ratios, represented by solid lines. It seems remarkable that all the C-type events and many CD-type events have associated frequency ratios close to integer ratios of 2 or 3, while some of the CD-type events display ratios close to 4 or 5. Since a possible harmonic structure may be suspected, we proceed further to investigate the statistical significance of such clustering of the peak frequency ratio distribution.

In Figure 3.13b we plot the frequency ratio distribution with division into bins purposely chosen to better reveal the clustering around integer ratios. Three relatively prominent peaks at integer ratios of 2, 3 and 5, are evident. Although the possibility of a true harmonic may be supported by this result, we checked the probability to obtain such a distribution just as the result of a random process. To perform this test we generated all possible combinations of two spectral ranges provided by the finite set of observational OVSA frequencies, under the same constraints as those

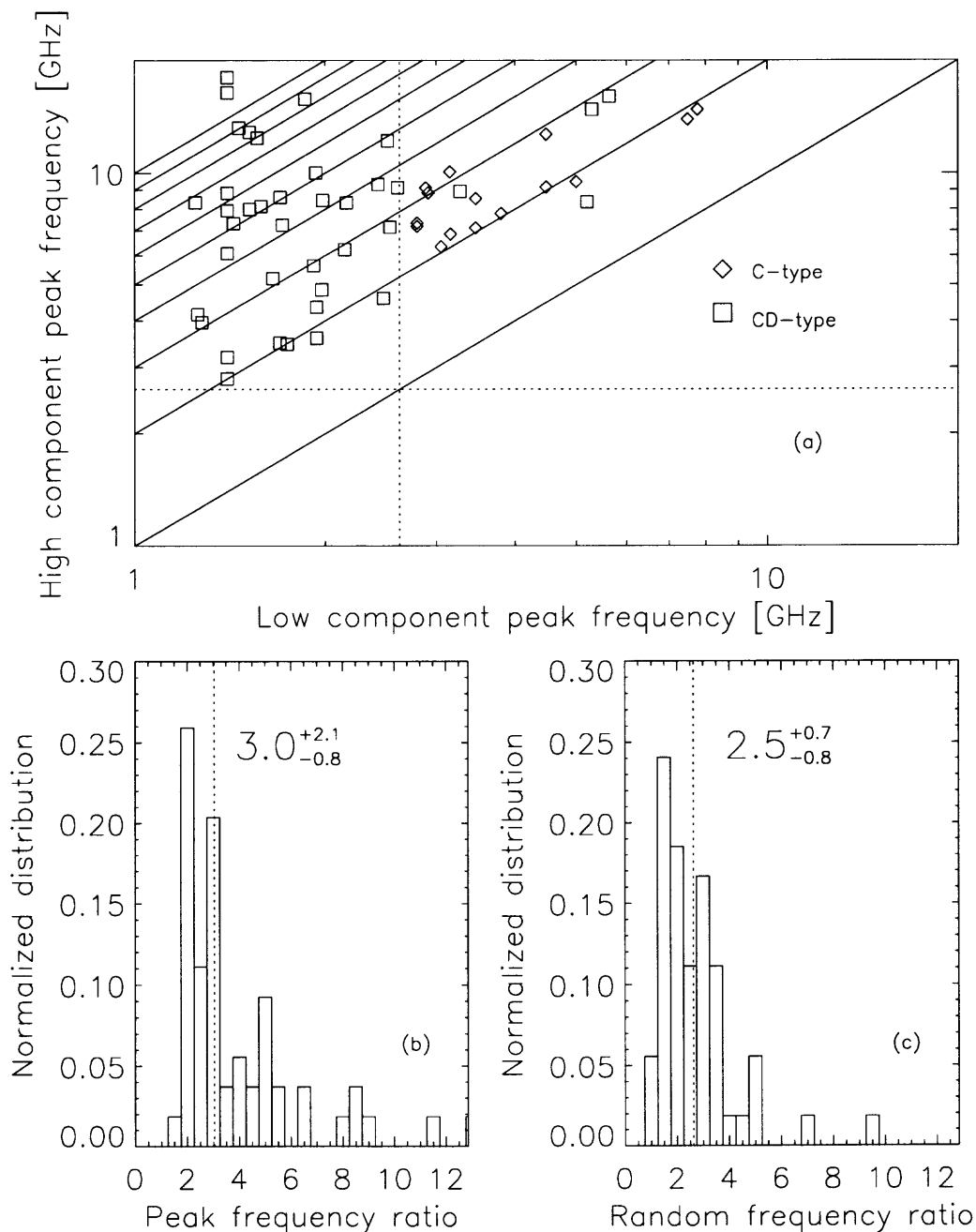


Figure 3.13 The distribution of peak frequencies of multi-component bursts. (Events with peak frequency at 1.2 GHz were excluded from the statistics, since both frequency and flux density are not necessarily the true ones, which may lie outside of the OVSA frequency range.) (a) The high peak frequency versus the low peak frequency. The inclined lines represent the integer ratios from 1 to 10. (b) The distribution of high to low frequency ratios. (c) The distribution of 54 ratios randomly selected from the parent population of all possible OVSA frequency ratios. The similarity of the observed ratio distribution with the randomly selected one may be observed.

imposed by the fitting algorithm we used. We allowed the realization of only those frequency ranges containing at least four discrete OVSA frequencies, (the minimum number of points able to give a fitting solution involving four parameters), and we generated inside each of these ranges 100 equally spaced frequencies. Finally we computed all possible frequency ratios, building the parent distribution from which any subset of observed ratios might have been randomly selected. Figure 3.13c displays one of the random distributions obtained by random selection of 54 ratios, the same number as in our dataset, from the parent distribution. It may be seen that this distribution also contains local peaks that happen to correspond to some integer ratios. A Student's T test performed to compare the observed distribution with the random one, returned an essentially 100% probability for these distributions to belong to the same parent population. In consequence, we conclude that the harmonic structure suggested by Figs.3.13a,b may be just the result of a random selection.

Besides this pure statistical argument, we also checked the full spectral data corresponding to the individual events responsible for these local peaks in the frequency ratio distribution. However, we did not find any peculiarities in the dynamic spectra to suggest a harmonic structure of the radio emission. True harmonic structure should be present at any time during the evolution of the flare, not just the peak time. Instead, in most of the cases we found that the frequency ratio actually changes randomly during the event. Using the full dynamic spectrum for each event, we computed the frequency ratios at any instant of time, and built a similar distribution as those presented in Figure 3.13a,b. The resulted distribution is shown in Figure 3.14a. In Figure 3.14b we present the parent population of the possible frequency ratios one may obtain using the fitting algorithm we used. The similarity of the two distributions suggests that the distribution of observed

frequency ratios at any instant of time represents a random subset of the parent population.

We do not want to rule out the possibility that the OVSA dataset may contain some particular events displaying a true harmonic structure, but such a conclusion should be based only on detailed case studies, not intended here.

3.5.2 Peak Flux Ratio

Related to the multi-component bursts, we have also investigated the relationship between the absolute peak fluxes of the high and low frequency components. Figure 3.15a displays the correlation plot of the two fluxes for C-type bursts on a logarithmic scale. The plot reveals a strong correlation, with a linear correlation coefficient of 0.97. The dotted line shown on the plot representing equal fluxes is close to the actual distribution of the data points, which are best fit with a power law of index 1.13 ± 0.07 (solid line). This is to be compared with a slope of about 3 that would be expected if the harmonic ratios were due to the mixer adding one-tenth of S_{peak} to the typical spectrum. Figure 3.15b displays the distribution of individual ratios. The strong peak near a ratio of unity is evident, while the actual ratios are in the range 0.4-2.76. Although generally close to unity, in 73% of cases the C-type bursts display a flux ratio greater than one.

In the case of CD-type bursts, Figure 3.15c, d, a correlation between peak fluxes is again present, although some events with large dm fluxes are strongly scattered from the general trend. The linear correlation coefficient in logarithmic scale is in this case only 0.81, while the best power law fit gives an index of 0.71 ± 0.09 . However, we consider these results strongly affected by the few events having large scatter. In fact, excluding the four CD-type events having dm fluxes above 10^4 sfu, the remaining events display a correlation of 0.85 and a power law index of 0.99 ± 0.11 which, in the limit of the statistical errors, represents basically the same power law dependence

as in the case of the C-type events. In fact, the perfect unity ratio, shown by the dotted line, seems to more naturally fit the bulk of the distribution than the strict least squares fit. The distribution shown in Figure 3.15d reveals that in the case of CD-type events, in 61.54% of the cases the dm component is more intense than the cm component. The true percentage may be even higher, since some bursts likely peak below 1.2 GHz. The minimum and maximum peak flux ratios are in this case 0.003 and 6.09, respectively. Again, we notice that the largest ratio is the same order of magnitude as for C-type events, while the smallest ratio, 2 orders of magnitude smaller, is from the most intense burst.

We interpret the strong correlation of spectral component peak fluxes as an indication of a real physical connection between them, which seems to be present in most of the cases. In the case of C-type bursts, when both spectral components of a given burst are likely produced by gyrosynchrotron emission mechanisms, the two spectral components may come from two interacting loops, or from source structure contained inside a single loop. Both pictures may explain a low frequency component having, on average, a lower peak flux than the high frequency one, being emitted from a weaker magnetic field present in a larger loop or, respectively, at the top of the same loop. This same interpretation may also apply to many CD-type events, excluding those with the more intense dm component. This fits our earlier suggestion that the dm component of some CD-type bursts are produced by gyrosynchrotron emission from weaker magnetic fields. Again, the exceptions may be explained by coherent emission mechanisms acting in the dm range. Even here, however, a physical connection between the spectral components of CD-type bursts may be required. Indeed, Fleishman, Gary & Nita (2003) showed that some of these events are produced by electron cyclotron maser mechanism based on a strong correlation between other spectral parameters, such as spectral slopes, associated with dm and cm spectral components of these bursts.

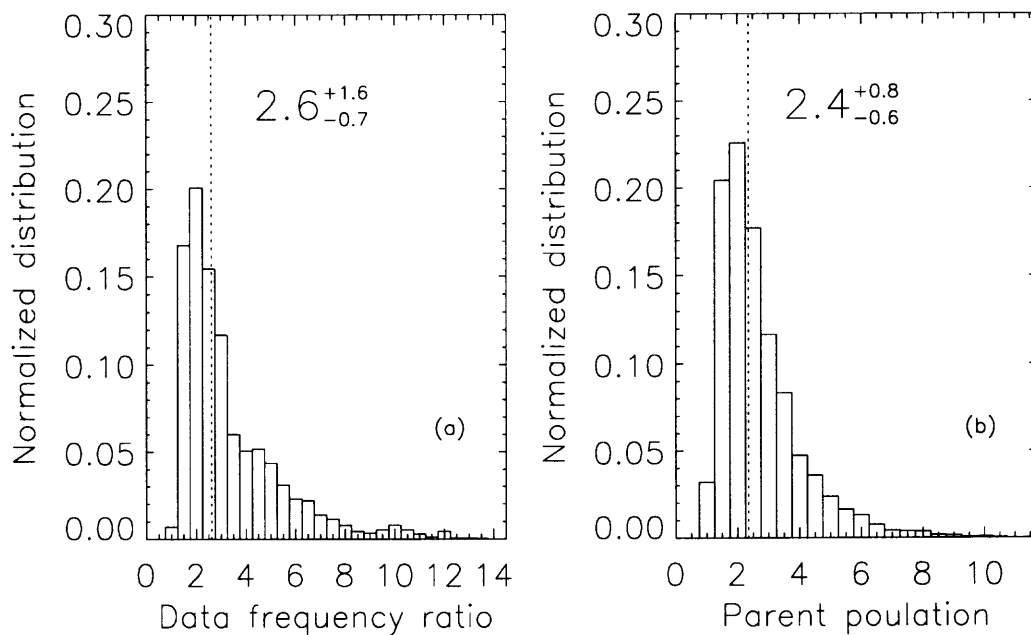


Figure 3.14 (a) The distribution of peak frequency ratios observed at any instant of time during the evolution of multi-component bursts. (b) The parent population of all possible ratios one may observe in the OVSA frequency range. The similarity of the two distributions suggests that the observed ratio distribution at any instant of time represents a random subset of the parent population.

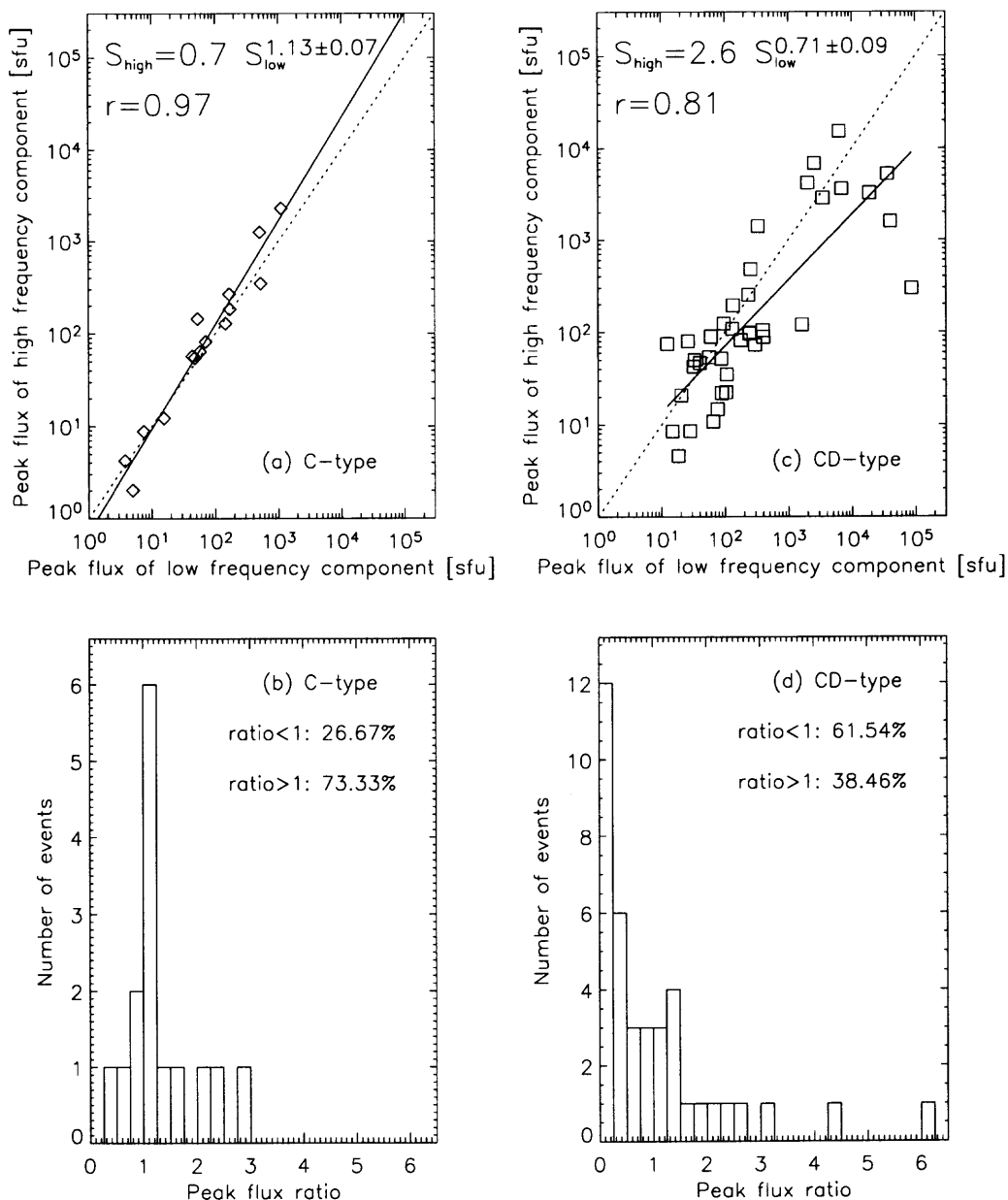


Figure 3.15 (a) The high frequency component peak flux versus the low frequency component peak flux for 2-component C-type bursts. The inclined line corresponds to equal fluxes. (b) The high frequency (cm) component peak flux versus the low frequency (dm) component peak flux for the CD-type bursts. (c) Distribution of the ratio of high to low frequency component peak fluxes for C-type bursts. (d) Same as c, for CD-type bursts.

3.5.3 Time Delay of Spectral Components

Reliable statistics of time delays between the spectral components of the same burst would require a cross-correlation analysis performed in each particular case. Since such detailed analysis was performed only occasionally, we cannot make rigorous statements regarding this subject. However, from the cross-correlation data we performed, from the analysis of the absolute peak time of all analyzed events, and from the visual analysis of their dynamic spectra, we may conclude that in general the C-type and CD-type spectra display an opposite delay trend. The low-frequency components of the C-type bursts tend to peak later than the high frequency ones, while in the case of the CD-type bursts, the dm component tends to peak before the cm one.

The general trend of C-type bursts may be explained as gyrosynchrotron emission produced from two different sources involving different magnetic fields. If we associate the weaker magnetic field with a higher altitude in the corona, the delay of the low frequency component may be explained by much longer trapping time in the larger loop, or by the time needed by a radio source to evolve to greater heights. However, spatially resolved data are needed to avoid speculation on this point.

In the case of CD-type bursts, six selected bursts have been analyzed in detail by Fleishman, Gary & Nita (2003) who found the cm emission to be delayed between 5 and 30 seconds in respect to the dm one. This result has been interpreted by the underlying kinetics of the same fast moving electron population. The low energy electrons, which are poorly trapped, produce dm spikes, while the better-trapped high-energy electrons accumulate to produce delayed gyrosynchrotron emission.

3.6 Conclusion

We have investigated the microwave spectra of 412 solar radio bursts observed by OVSA during the years 2001-2002 at 40 frequencies in the 1.2–18 GHz frequency

range with 4 s time resolution. For each spectrum, we have identified the main spectral and temporal components. Each spectral component has been analyzed and the main spectral parameters, i.e peak frequency, peak flux density, and spectral slopes below and above the peak frequency, have been derived at any instant of time.

We found the distribution of these parameters to be the result of a superposition of at least two distinct populations: the dm radio emission, which has a upper frequency limit of about 2.6 GHz and no characteristic flux size, and the cm radio emission, which in 50% of the cases has its spectral peak in the range defined by [4.9, 9.0] GHz and [26, 137] sfu limits, and has a frequency dependent limit of the peak flux density described by a $\sim \nu^2$ power law with an offset of ~ 300 sfu at 1 GHz. We found the superposition of these two populations to be responsible for the lack of strong radio emission at intermediate frequencies and for the frequency dependence of the peak flux distribution power-law slope, previously reported by Nita et al. (2002). We found the power-law slope of the peak flux number density distribution to be -1.42 ± 0.09 for the dm events, and -1.73 ± 0.04 for the cm ones, consistent with the Nita et al. (2002) results.

The increase of the average peak frequency with increasing flux density of the cm emission, previously reported by Castelli & Guidice (1972), is now confirmed by the OVSA data set. Some 50% of the cm bursts have an absolute peak frequency in the [4.7, 8.1] GHz range, when their absolute peak flux is below 100 sfu, but this rises to [5.0, 10.9] GHz, for flux densities between 100 and 1000 sfu, and further to [4.9, 12.7] GHz, for flux densities above 1000 sfu.

We have also found an evident spectral flattening on both optically thick and optically thin sides of the gyrosynchrotron spectra for increasing peak flux density ranges. The 50% probability ranges are [1.3, 2.9] for the low frequency spectral slope and $[-3.6, -1.9]$ for the high frequency spectral slope below 100 sfu, [1.0, 2.4] and $[-2.8, -1.5]$ between 100 and 1000 sfu, [1.0, 1.8] and $[-2.4, -1.5]$ above 1000 sfu. We

interpret this result as an indication that statistically the strongest flares come from the most inhomogeneous sources (which flattens the low-frequency slope) and are simultaneously produced by electrons with statistically harder energy distributions (which flattens the high-frequency slope).

We have divided our data base into three main spectral classes based on the frequency range of the absolute peak frequency, below or above the empirical 2.6 GHz dividing line: (1) the pure cm bursts, C-type, (2) the pure dm bursts, D-type, and (3) the composite CD-type. We have carried out a detailed analysis of the spectral and temporal characteristics of these classes, presenting tables that list the most probable spectral and temporal parameters of each class in different frequency and intensity ranges.

We find that the pure cm C-type is mainly composed of impulsive bursts, while the pure dm D-type contains two populations corresponding to smooth or rapidly changing times profiles. Remarkably, we find that the frequency-dependent flux-density limit seen for cm emission also limits the peak flux of pure dm D-type bursts. In contrast, all dm bursts peaking above this limit, i.e. > 1000 sfu, are low-frequency counterparts of composite CD-bursts, and thus satisfy the criteria to be classified as U-shaped bursts (Cliver, McNamara & Gentle 1985). We interpret this finding as an indication that the gyrosynchrotron emission mechanism may produce the weaker dm bursts, with a flux density limit unlikely to exceed ~ 300 sfu at 1 GHz, while the coherent emission mechanisms, which are likely responsible for the rest of the dm bursts, seem not to be very efficient except when accompanied by a cm- λ counterpart.

We have investigated the properties of multi-spectral component bursts and find that the percentage of CD-type bursts, 17% for the whole database, increases with the flux density of the microwave bursts, being 12% below 100 sfu, 19% between 100 and 1000 sfu, and 60% above 1000 sfu. These percentages may be even larger

when taking into account the possibility of undetected low frequency components below the 1.2 GHz lower frequency limit of OVSA. We find no significant evidence for the harmonic structure of multi-component bursts previously suggested by Stähli, Gary & Hurford (1990). However, we find in most cases a strong correlation between peak fluxes of the spectral components of multi-component bursts, which suggests a physical connection between them, investigated in detail elsewhere (Fleishman, Gary & Nita 2003; Fleishman, Nita & Gary in preparation).

CHAPTER 4

PEAK FREQUENCY DYNAMICS IN SOLAR MICROWAVE BURSTS

4.1 Introduction

Microwave broadband emission of solar flares can give us valuable information about processes of particle acceleration and transport, as well as about magnetic field and plasma density in solar flaring loops (see for review Bastian, Benz & Gary 1998; Fleishman & Melnikov 2003; Lee 2003).

Studies of the shape of observed solar microwave spectra started in the early 1960's (Takakura & Kai 1961, 1966). The most complete analysis of the shape of microwave flux density spectra was done by Guidice & Castelli (1975). Their analysis was based on data obtained at fixed, well-separated frequencies. Theoretical studies, motivated by the observational findings, developed a clear understanding that the solar broadband microwave bursts are generated by nonthermal electrons via the gyrosynchrotron (hereafter GS) emission mechanism (Takakura & Kai 1966; Ramaty 1969; Takakura 1972; Petrosian 1981) and provided some simplified schemes for microwave diagnostics of solar flares (Dulk & Marsh 1982; Gary 1985; Klein 1987).

The spectrum of such emission usually has a characteristic shape, with a single peak at the peak frequency f_{peak} (Figure 4.1). The high frequency turnover of this peak is due to the emission becoming optically thin, with the spectral slope being determined chiefly by the electron energy distribution, while the low frequency slope may be determined by self-absorption (Twiss 1954) or by Razin suppression (Razin 1960a).

These two processes are fundamentally different in the underlying physics. The self-absorption is the absorption of the emitted gyrosynchrotron radiation by the fast electrons themselves, so the effect of self-absorption is proportional to the source length. The Razin effect is the suppression of the gyrosynchrotron emissivity itself because of the difference of wave dispersion in plasma and vacuum. Accordingly,

the role of Razin suppression is defined mainly by the plasma density and does not depend on the source size.

Different parts of the microwave burst spectrum give different tools for flaring loop diagnostics. For example, the high frequency slope, flux density, and polarization of emission at $f > f_{peak}$ can provide information about the spectral index of nonthermal electrons, total number of high energy electrons, and also about pitch-angle anisotropy. The low frequency slope and intensity of emission at $f < f_{peak}$ strongly depend on magnetic field inhomogeneity in the radio source and also on the magnetic field strength and effective energy of emitting electrons. They also may depend on the ratio of plasma density and magnetic field if Razin suppression is important for a specific flaring loop.

One of the key parameters of a solar microwave burst is the frequency of spectral maximum (peak frequency f_{peak}). Together with the peak flux, S_{peak} , it gives information about magnetic field strength and column number density of nonthermal electrons. In the case of strong Razin suppression these parameters can also provide information about plasma density in a flaring loop.

Possibly the most striking results were obtained in the comprehensive study by Stähli, Gary & Hurford (1989). They studied 49 bursts and found that for majority of the bursts the deviation of f_{peak} during the rise and decay phases of bursts was much less than that predicted by the theory of GS radiation (Dulk & Marsh 1982). Using the simplified expressions for GS emission from a homogeneous radio source, (Dulk & Marsh 1982), they analyzed the influence on the peak frequency of such parameters as 1) magnetic field strength B , 2) column number density of nonthermal electrons along line of sight nL , 3) the viewing angle θ in respect to magnetic field direction, and 4) the size of a radio source Ω . They pointed out that a change in the burst source size has no effect on the peak frequency, but that an increase in any other source parameter results in an increase in the peak frequency.

As an explanation of the constancy of f_{peak} during a burst, the authors suggested that for most of the events the source parameters (number of energetic electrons and/or magnetic field strength) may vary over the course of a burst in such a way that the peak frequency did not change.

A comprehensive analysis of the peak frequency evolution for one particular flare was done by Belkora (1997). In her analysis she used OVSA observations with spatial resolution, so it was possible to derive the brightness temperature spectrum rather than the total flux density spectrum. A striking peculiarity of the burst was that the peak frequency remained nearly constant while the peak brightness temperature varied over 2 orders of magnitude. As an explanation, Belkora suggested the Razin effect. If Razin suppression is present, only a change in the number of nonthermal electrons is required to cause the observed change in brightness temperature. The steep low frequency slope of the observed burst spectrum gave additional support for Razin suppression. The parameters required to explain the event in terms of the Razin effect are electron density $n_e = 2 \times 10^{11} \text{ cm}^{-3}$ and magnetic field $B = 300 \text{ G}$, respectively.

The importance of Razin suppression looks very attractive, but for many microwave bursts such high densities appear unlikely. The analysis of microwave decay times, time delays between microwave and hard X-ray time profiles (Wiehl et al. 1985; Bai 1986; Melnikov 1994), and time delays between different optically thin frequencies (Melnikov & Magun 1998; Lee & Gary 2000) all typically indicate a lower plasma density. For a density $n_e = 10^{11} \text{ cm}^{-3}$, the lifetime of trapped mildly relativistic electrons due to Coulomb collisions is less than 2-3 s. Such small delays between microwaves and hard X-rays are usually observed only for short, impulsive bursts.

The main purposes of our present study are to: a) develop an analysis procedure to distinguish between the two competing effects, self-absorption and

Razin suppression, using the temporal behavior of the microwave spectrum, b) investigate which effect is dominant for a specific burst or specific time during the burst, and c) determine in what percentage of bursts each effect is important. To accomplish this, we conduct a statistical study of more than 300 microwave bursts obtained during the period 2001-2002 with the Owens Valley Solar Array (Nita, Gary & Lee 2003). For 40 events selected for their relatively simple time profiles, we perform a detailed analysis of the spectral evolution of f_{peak} . We find that the bursts divide naturally into a few distinct types with specific temporal behaviors during their rise and decay. We carry out a theoretical study of each type to show that the types correspond to different relative importance of GS self-absorption and Razin suppression.

In §4.2 we present observations and in §4.3 the results of data analysis. In §4.4 we consider the influence on f_{peak} of the temporal evolution of energetic electrons during their injection into magnetic loops for low and high plasma density, for constant and varying electron spectral index, and for the case of relatively high plasma density increasing with time. In the last section we compare empirical and calculated features of the spectral evolution and summarize our results.

4.2 Observational Data

The data for this study come from the set of events analyzed by Nita, Gary & Lee (2003), namely 412 bursts observed in microwaves with the solar-dedicated Owens Valley Solar Array (OVSA). After some upgrades (Gary & Hurford 2000) this frequency-agile interferometer array consists of 6 antennas (two 27 m dishes and four 2 m dishes). OVSA data comprise both total power from each antenna and correlated amplitudes and phases from each baseline (pair of antennas), but this study is limited to total power (integrated flux density, without spatial resolution). Because of difficulties with absolute flux calibration of the 27-m dishes due to various

effects arising from their restricted field of view, we further restrict our analysis to data from the 2-m antennas, and hence discuss only total intensity (Stokes I). The 2-m dishes have a total power sensitivity of a few solar flux units (sfu; $1 \text{ sfu} = 10^{-22} \text{ W m}^{-2} \text{ Hz}^{-1}$). The data are taken at typically 40 frequencies, distributed approximately logarithmically from 1 to 18 GHz, with 4 s time resolution. The 2-m flux calibration is based on the quiet Sun total flux density as reported by the National Oceanic and Atmospheric Administration (NOAA). See Nita, Gary & Lee (2003) for details of the calibration procedure. OVSA data are highly suitable for studies of the peak frequency evolution of GS spectra due to OVSA's relatively large number of closely spaced frequencies covering the relevant range of 1-18 GHz over which most bursts have their spectral maximum.

The 412 bursts analyzed by Nita, Gary & Lee (2003) included decimetric bursts with no clear GS component. For this study we restrict our initial selection to bursts with well defined spectral peaks in the range $f = 3 - 16 \text{ GHz}$, which are identified with GS emission. This results in a total of 338 events used in this study.

After calibration, we performed a 4-parameter fit to the burst spectrum at each time using the generic function introduced by Stähli, Gary & Hurford (1989):

$$S(f) = a_1 f^{a_2} [1 - \exp(-a_3 f^{-a_4})], \quad (4.1)$$

which yields four physically relevant parameters, the low frequency spectral index (a_2), the high frequency spectral index ($\alpha = a_4 - a_2$), the peak, or turn over frequency (f_{peak}) and the peak flux $S(f_{peak})$. This generic function has a shape similar to the GS emission spectrum obtained using the simplified formulas by Dulk & Marsh (1982). An example of such fitting is shown in Figure 4.1. In some events the low frequency part of the spectrum contains an additional low frequency, $f_{peak} \sim 1 - 2 \text{ GHz}$, spectral peak (Nita, Gary & Lee 2003). Therefore, the use of Eq.4.1 can give us an error in estimations of f_{peak} . In these cases, to avoid a possible error we limited the range of

frequencies by a reasonable value f_{min} that depends on the burst but was generally around 2-3 GHz.

In addition to our statistical study of the 338 bursts, we also performed a more detailed analysis of a much smaller subset of bursts. To avoid complexities due to overlapping spectral or temporal components, for the detailed study we selected only bursts with a single, well defined spectral peak in the range $f = 3 - 16$ GHz at the burst maximum and simple time profile with peak flux density $S_{peak} > 100$ sfu. This selection reduced the 338 bursts to a total of 40 events.

4.3 Peak Frequency Dynamics

Comparison of spectra at different times during a burst clearly shows a change of peak frequency with time for most of the bursts in our data set. In Figure 4.1 we show an example of the typical spectral evolution. In this figure, spectra at different times are overplotted on two plots, separately for the rise phase and decay phase. We can see a considerable increase of f_{peak} on the rise phase and then a decrease after the burst maximum. A remarkable feature of the spectral evolution in this example is the much faster increase of the flux at frequencies $f > f_{peak}$ than at $f < f_{peak}$, which is an indication that the source is optically thick at $f < f_{peak}$. In what follows, we use the ratio $R = \log \frac{S(f > f_{peak})}{S(f < f_{peak})}$ as an indicator of optical thickness below f_{peak} . A value of R that increases during the rise phase and decreases during the decay is indicative that the spectral turnover is due to self-absorption, while a relatively constant R indicates that frequencies on both sides of the turnover frequency are optically thin—a signature of Razin suppression. In contrast to the burst in Figure 4.1, in Figure 4.2 we show the spectral evolution of a burst with constant R throughout the rise and most of the decay. This is an excellent example of a burst for which Razin suppression would be suspected, as further indicated by the constancy of the peak frequency over most of the burst.

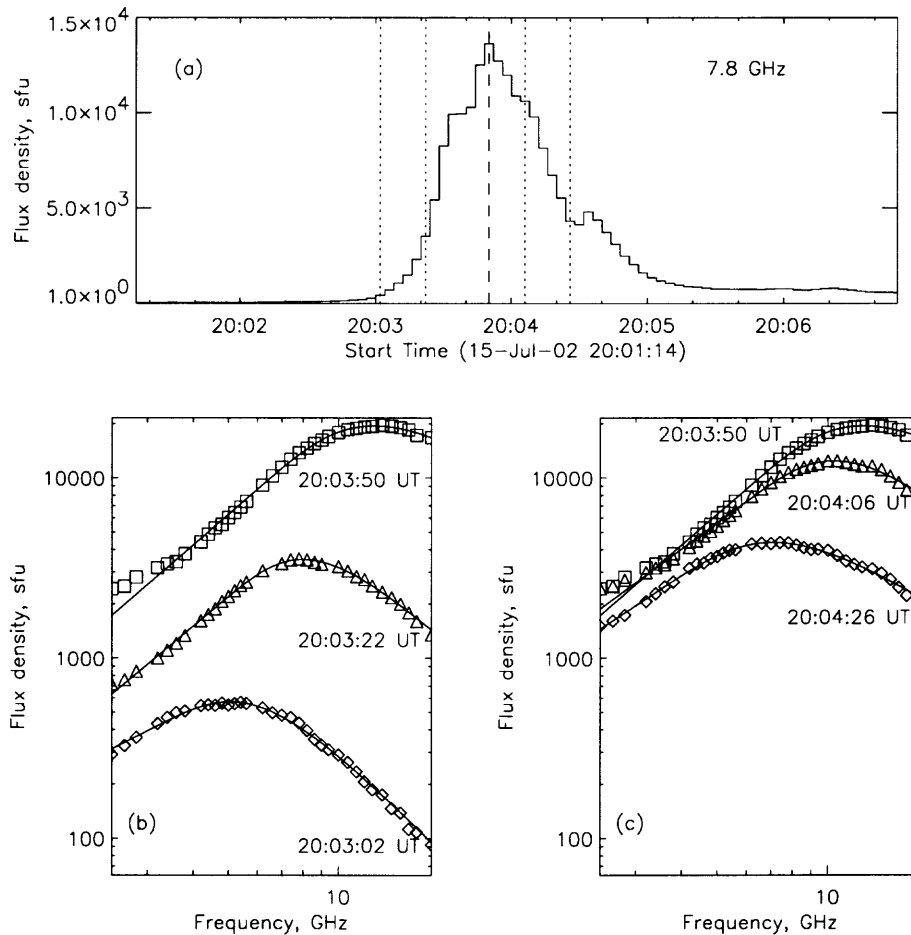


Figure 4.1 Spectral evolution of the first peak in the microwave multi-component burst of July 15, 2002, (a). Solid lines show the best fit with the generic function Eq. 4.1. An increase of the turnover frequency on the rising phase, (b), and a corresponding decrease on the decay phase, (c), is clearly seen.

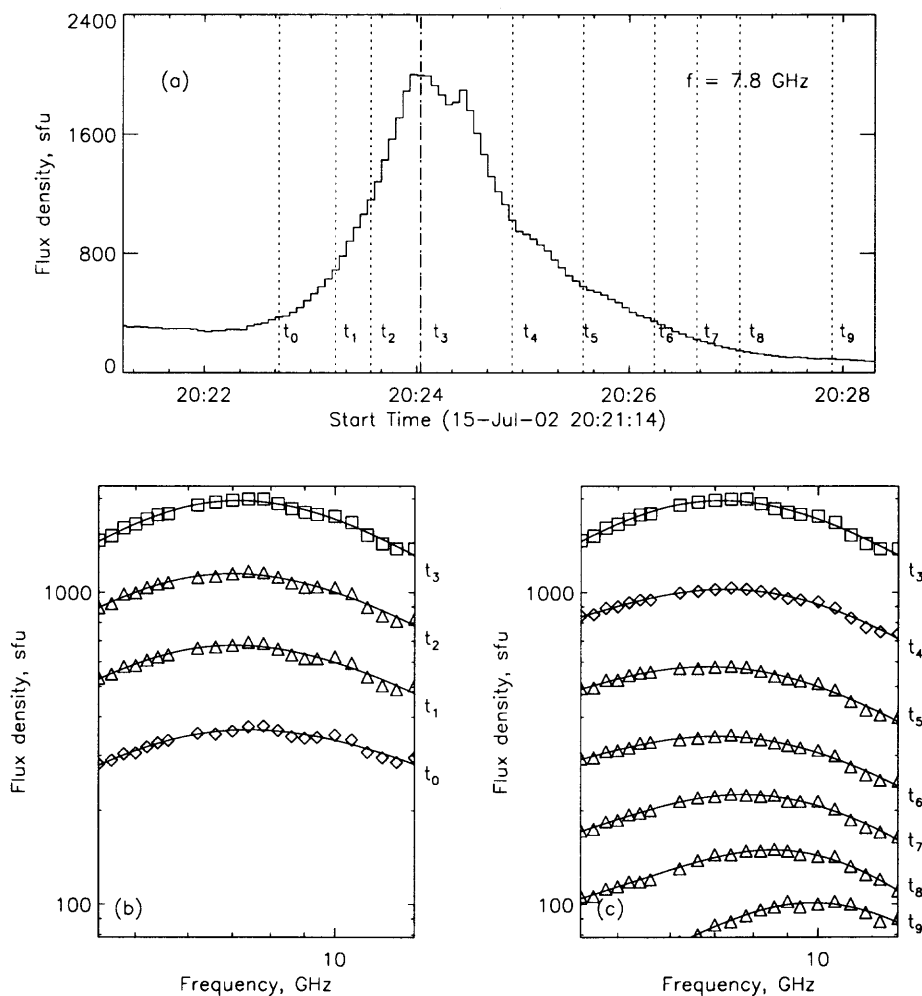


Figure 4.2 Spectral evolution as in Figure 4.1 for a secondary peak in the microwave burst of July 15, 2002, (a). Note the remarkable stability of the peak frequency during the most of the burst, (b, c), and the equal rise and fall on both sides of the peak frequency, which yields a constant R .

Time profiles for several key spectral parameters of the event shown in Figure 4.1 are represented in Figure 4.3. The three parameters S_{peak} (panel *a*), f_{peak} (panel *b*), and R (panel *c*) all show a clear, positive correlation. The high-frequency spectral index α_h in panel *d* shows a slight, but unremarkable correlation in this burst. It is an important parameter, however, as it gives a measure of the evolution of the nonthermal electron energy distribution.

To determine how common is the correlation shown in Figure 4.3*a, b*, we plot in Figure 4.4 the distribution of correlation coefficients between the peak frequency, f_{peak} , and peak flux, S_{peak} , separately for the rise and decay phases for those bursts from our dataset that had sufficiently clean rise and decay phases. The number of bursts used in Figure 4.4*a* is 202, and the number used in Figure 4.4*b* is 216.

It is clearly seen from the distributions that there is a large subset of bursts with strong positive correlation ($r > 0.5$) between peak frequency and peak flux of a burst, both on the rise phase (50%) and on the decay phase (52%). However, a similar number of bursts show a random scatter of correlations, and a minor peak in the distribution occurs near $r = -1.0$, showing a distinct anti-correlation.

Although we did not include long-duration bursts with multiple temporal components in our detailed analysis, we find it convenient to use two such bursts, shown in Figures 4.5 and 4.6, as an illustration of both types of correlation. In Figure 4.5, we see an excellent one-to-one correspondence between sub-peaks in flux density (Fig. 4.5*a*) and peak frequency (Fig. 4.5*b*) time profiles. The parameter R (Fig. 4.5*c*) also shows excellent overall correlation, showing that the spectral turnover is due to GS self-absorption over the entire lifetime of the burst. The long-duration burst in Figure 4.6, on the other hand, shows excellent one-to-one correlation only during the later stages of the burst, after 1910 UT. During the earlier stage of the burst, the peak frequency plot (Figure 4.5*b*) is essentially flat except for localized

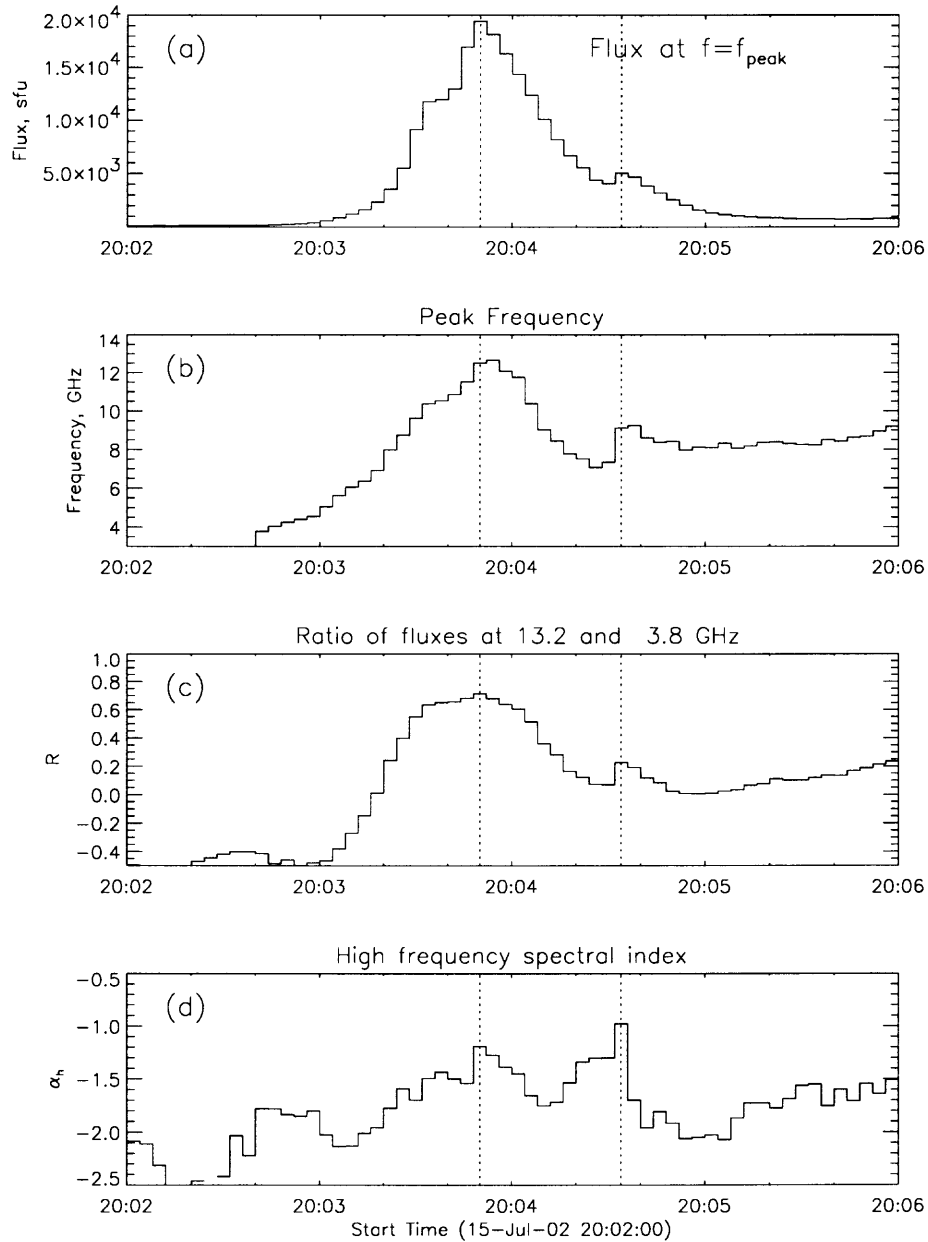


Figure 4.3 Time profiles of several key parameters of the spectral evolution of the burst shown in Figure 4.1: (a) Flux density, (b) peak frequency, (c) ratio R of fluxes at two frequencies, one (13.2 GHz) on the high-frequency side and one (3.8 GHz) on the low-frequency side of f_{peak} , and (d) the high frequency spectral index, α_h . A strong correlation is seen among the top three panels, both on the rise phase and initial part of the decay phase. The dotted vertical lines in each panel mark the peak times in a.

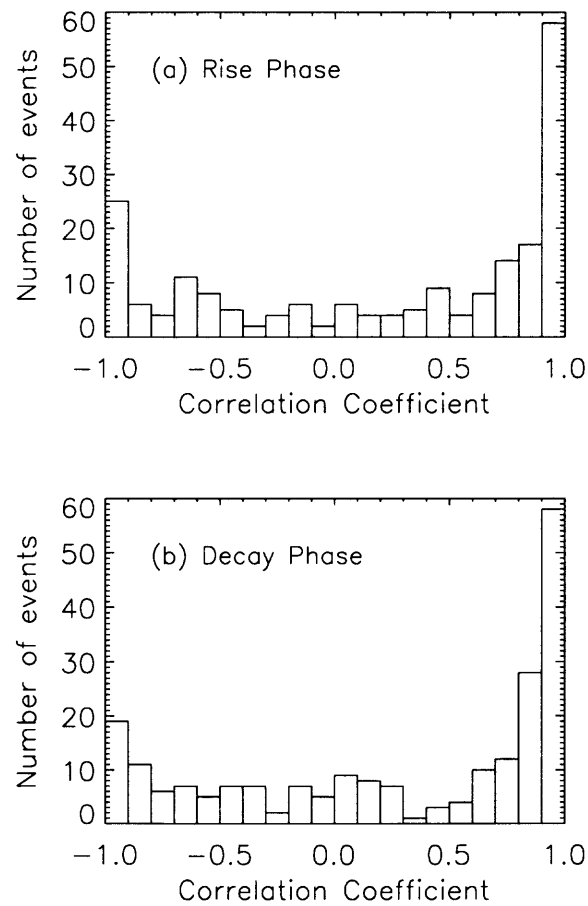


Figure 4.4 Distribution of correlation coefficients between the peak frequency f_{peak} and peak flux S_{peak} on the rise (upper panel) and decay (lower panel) phases of the bursts from our set of events.

excursions to higher frequency near a few flux density peaks (e.g. at 1906 UT, 1907.5 UT, and 1909 UT).

Qualitatively, the positive correlation between the peak frequency and the burst flux agrees well with the predictions of the simple GS model in which low frequency turnover occurs due to the self-absorption. We can show this semi-quantitatively using the simplified formulas of Dulk & Marsh (1982). For the simple case of a homogeneous radio source, the emitted spectral flux density $S(f)$, at the frequency f , is given by the radiation transfer equation in the form:

$$S(f) = \frac{2k_B T_{eff}(f)}{c^2} f^2 [1 - e^{-\tau(f)}] \times \frac{A}{R_s^2}, \quad (4.2)$$

where $k_B = 1.38 \times 10^{-16}$ erg K^{-1} and $c = 3 \times 10^{10}$ cm s^{-1} are the Boltzmann constant and velocity of light, $R_s = 1.5 \times 10^{13}$ cm is the distance from the Sun to the Earth, and A is the area of the source, in cm^2 . In general, the effective brightness temperature, $T_{eff}(f)$, and optical thickness, $\tau(f)$, are complicated functions of the electron energy and pitch-angle distributions, magnetic field strength, B , viewing angle between the directions of magnetic field and the line of sight, θ , plasma density, n_0 , and the source depth, L .

The flux $S(f)$ reaches its maximum value, S_{peak} , at the frequency $f = f_{peak}$ where $\tau(f_{peak}) \simeq 1$, so the expression $1 - e^{-\tau(f)} \simeq 0.63$. In the case where the Dulk & Marsh (1982) formulas are valid, i.e. for low plasma density and energetic electrons with an isotropic, single powerlaw energy distribution of spectral index δ , the effective temperature is given by

$$T_{eff} \simeq 2.2 \times 10^9 10^{-0.31\delta} (\sin \theta)^{-0.36-0.06\delta} \left(\frac{f}{f_B}\right)^{0.50+0.085\delta}. \quad (4.3)$$

where f_B is the gyrofrequency. After insertion of (4.3) into (4.2), we obtain

$$S_{peak} \simeq 1.9 \times 10^{-54.0-0.31\delta} (\sin \theta)^{-0.36-0.06\delta} f_B^{-0.50-0.085\delta} f_{peak}^{2.50+0.085\delta} A. \quad (4.4)$$

A positive correlation between the peak flux and peak frequency is clearly seen from Eqn. 4.4. Dulk & Marsh (1982) also give an expression for the peak frequency in

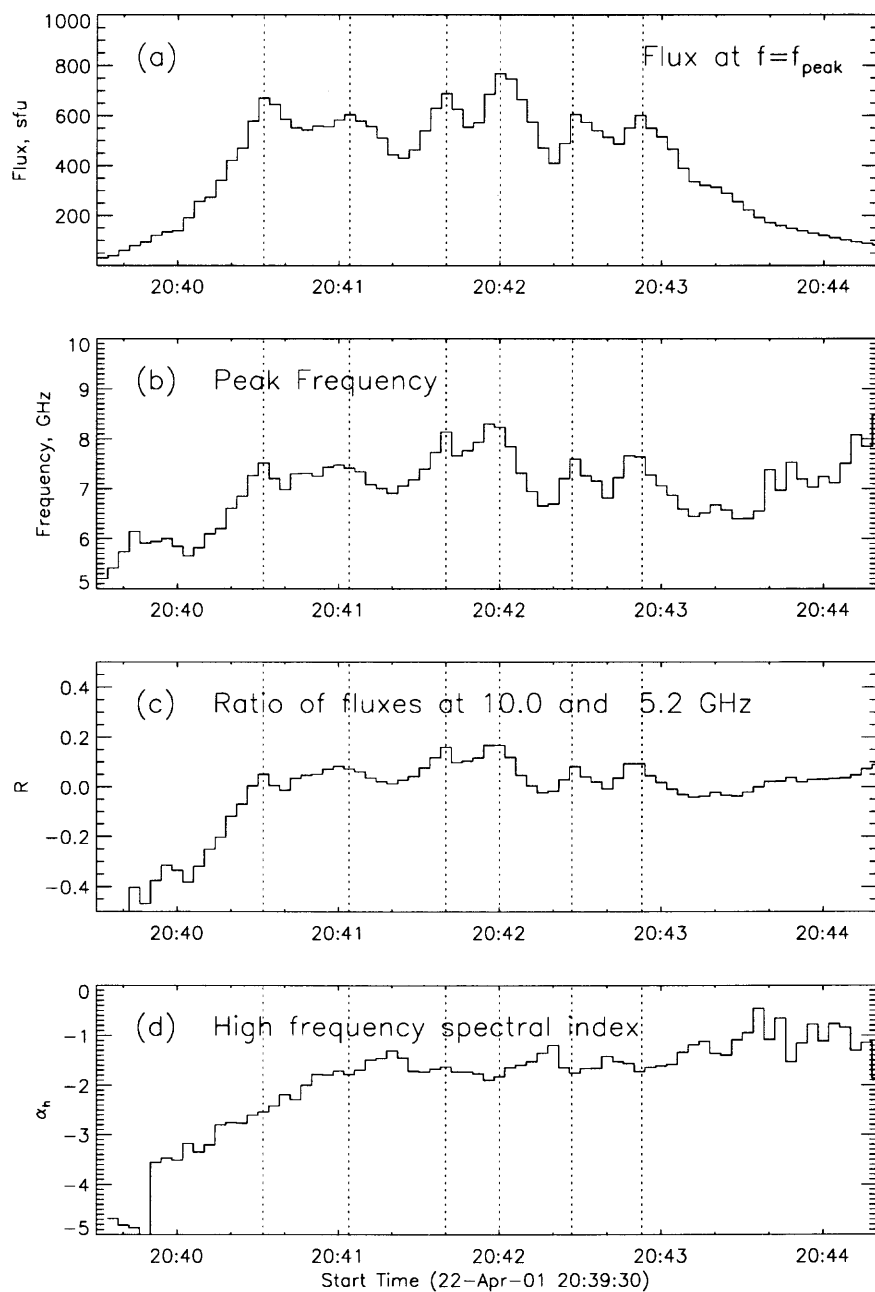


Figure 4.5 Peak frequency evolution in the multi-component burst of 2001 April 22, for the same parameters as shown in Figure 4.3.

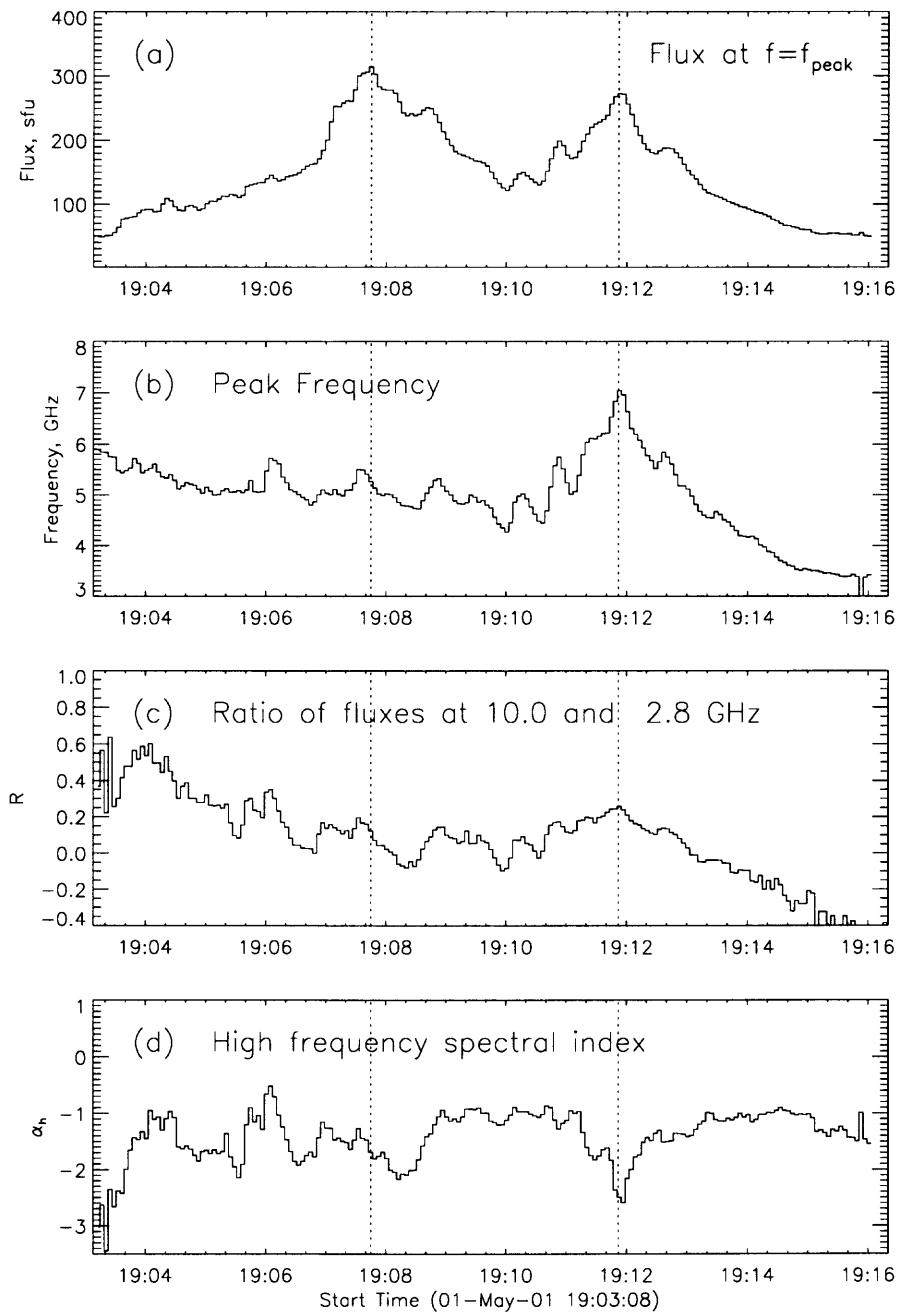


Figure 4.6 The same as on Figure 4.5, but for the event May 1, 2001.

this homogeneous model,

$$f_{peak} \simeq 2.72 \times 10^{3+0.27\delta} (\sin \theta)^{0.41+0.03\delta} B^{0.68+0.03\delta} (nL)^{0.32-0.03\delta}, \quad (4.5)$$

which depends on the number density, n , of nonthermal electrons with energies $E > 10$ keV, their spectral index, magnetic field strength, viewing angle and the source depth, L . Note that f_{peak} does not depend on the source area A . As is seen from Eqs. (4.4), (4.5), any increase or decrease of the electron column number density, nL , leads to a simultaneous increase or decrease of both the microwave flux density and the peak frequency.

Earlier we introduced a parameter, R , that serves as a measure of the difference in rate of change of flux density on either side of the spectral peak. To better quantify the choice of frequencies and the precise interpretation of R , we define:

$$R = \log \frac{S(f_2)}{S(f_1)}, \quad (4.6)$$

where $f_2 = (f_{pabs} + f_{max})/2$, $f_1 = (f_{pabs} + f_{min})/2$, f_{pabs} is the absolute maximum of $f_{peak}(t)$ during a burst, and f_{min} , f_{max} indicate the frequency range in which the burst was detected. From the GS formulas of Dulk & Marsh (1982), we expect the optically thin flux density S_{thin} (\propto emissivity), and the optically thick flux S_{thick} ($\propto T_{eff}$), to be given by

$$S_{thin} \simeq 2.94 \times 10^{-50-0.52\delta} (\sin \theta)^{-0.43+0.65\delta} \left(\frac{f_2}{f_B}\right)^{1.22-0.90\delta} B (nL) A \quad (4.7)$$

$$S_{thick} \simeq 3.0 \times 10^{-54-0.31\delta} (\sin \theta)^{-0.36-0.06\delta} \left(\frac{f_1}{f_B}\right)^{0.50+0.085\delta} f_1^2 A. \quad (4.8)$$

The expected ratio of these flux densities is then

$$\frac{S_{thin}}{S_{thick}} \simeq 10^{4-0.21\delta} (\sin \theta)^{0.71\delta-0.07} f_1^{-2} \left(\frac{f_2}{f_1}\right)^{1.22-0.90\delta} B \left(\frac{f_1}{f_B}\right)^{-0.985\delta-0.72} (nL). \quad (4.9)$$

Thus, for GS emission, R should change in proportion to nL , B , and δ in a similar way as does S_{peak} (Eq. 4.4 with 4.5). Note that Eq. 4.9 is valid only for a homogeneous

source. In the real flaring loop the source is inhomogeneous and emission at different frequencies comes from different parts of the loop. So we should use different values of B , A and, possibly, δ for S_{thin} and S_{thick} , but the general correlation of R with S_{peak} should remain.

Figures 4.3, 4.5 and 4.6 show the close correlations among R , f_{peak} , and S_{peak} for three events. We have checked the relationship between R and f_{peak} for all the events from our sample and found a strong correlation ($r > 0.5$), for 76% of events in the rise phase and for 70% of events in the decay phase. Only for 13% of events on the rising phase and 17% on the decay phase does the correlation between R and f_{peak} become negative. Therefore, in general, our preliminary statistical results confirm the important role of self-absorption in the formation of the low frequency turnover for the majority of microwave bursts under study.

However, the early part of the burst in Figure 4.6 shows that this good correlation may be absent in some cases. In general, bursts show many different time behaviors and different amplitudes of f_{peak} variations during a burst. We can see in Figure 4.4 that there is small but non-negligible percentage of bursts showing strong ($r < -0.5$) negative correlation (27% and 22% of all bursts for the rising and decay phases, respectively), as well as very poor or no correlation, $|r| < 0.5$ (23% and 26% of bursts).

The multiple bursts in Figures 4.5 and 4.6 can also serve as examples of some unusual spectral behaviors that hardly can be understood using above simplified considerations. A remarkable feature of the burst in Figure 4.5 is the significant increase of both f_{peak} and R in the late decay phase (after 20:43:20 UT), while S_{peak} continues to decrease by a factor of several. The burst in Figure 4.6 consists of two major components with a similar change in amplitude, but the first component of the burst has a much smaller overall f_{peak} variation than the second component. The

trend in f_{peak} for the first component starts from near 6 GHz and slowly decreases throughout the rise and decay phase.

4.3.1 Magnitude of Peak Frequency Variations

To study the quantitative change in peak frequency Δf_{peak} during the rise and decay phases, we selected only bursts with relatively simple time profiles and well defined peaks. Figure 4.7a shows the distribution of Δf_{peak} during the time over which the flux density increases from 25% to 100% of its maximum value, while Figure 4.7b shows the same during the decay to 25% of maximum.

The range of Δf_{peak} variations is quite large, from -0.5 to 3.8 GHz for the rise phase and from -6.5 to 2.6 GHz for the decay phase. Almost all the events (84%) on the rise phase have positive values of Δf_{peak} , and most of events (64%) on the decay phase have negative Δf_{peak} as expected. Since we might expect larger shifts for larger f_{peak} , it is useful to replot the distributions normalized by peak frequency $\Delta f_{peak}/f_{peak}$ as shown in Figure 4.8. An interesting feature of the distributions is the relatively high percentage of events with small frequency shifts ($-0.1 < \Delta f_{peak}/f_{peak} < 0.1$): 36% and 30% for the rising and decay phases respectively. Note, however, that this is still a much smaller percentage than found by Stähli, Gary & Hurford (1989). Another interesting feature is unexpectedly high percentage of events with positive shifts on the decay phase, 44%, which is not explained by the GS self-absorption model.

For the following analysis we will divide the events into three groups: those with high ($|\Delta f_{peak}/f_{peak}| \geq 0.3$), moderate ($0.1 \leq |\Delta f_{peak}/f_{peak}| < 0.3$), and low ($|\Delta f_{peak}/f_{peak}| < 0.1$) relative peak frequency shifts and discuss them in detail below.

4.3.2 Peak Frequency Evolution on the Rising Phase of Bursts

4.3.2.1 Large Peak Frequency Shifts

In Figure 4.9 we show the correlation between f_{peak} and S_{peak} on the rising phase of the 7 events with the highest relative

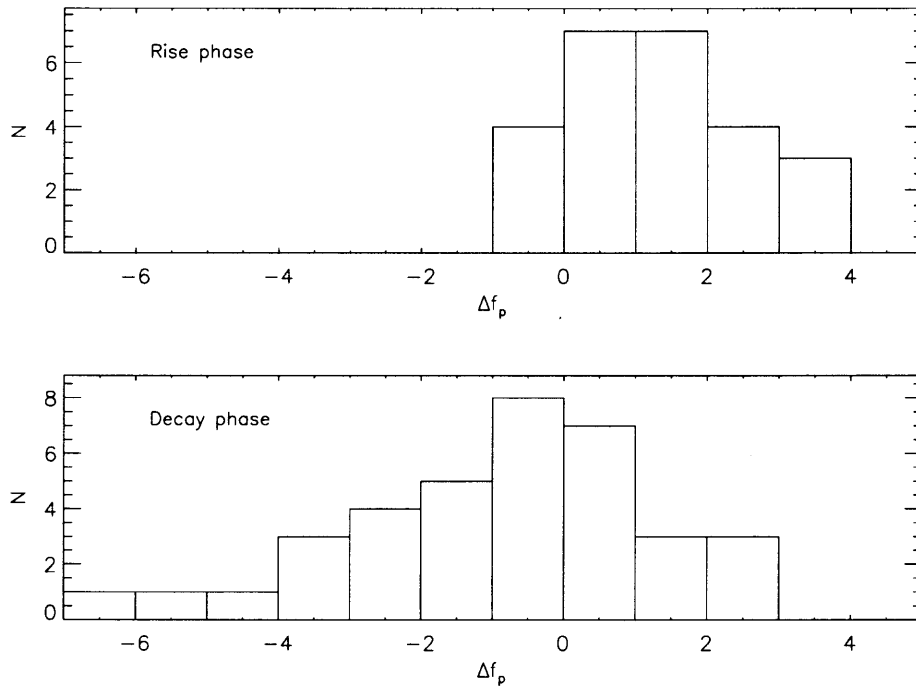


Figure 4.7 The distributions of Δf_{peak} (a) on the rise and (b) decay phases. The corresponding flux density increase (decrease) is from (to) 25% of its maximum value. The total number of bursts used in the distributions is 25 in a and 36 in b.

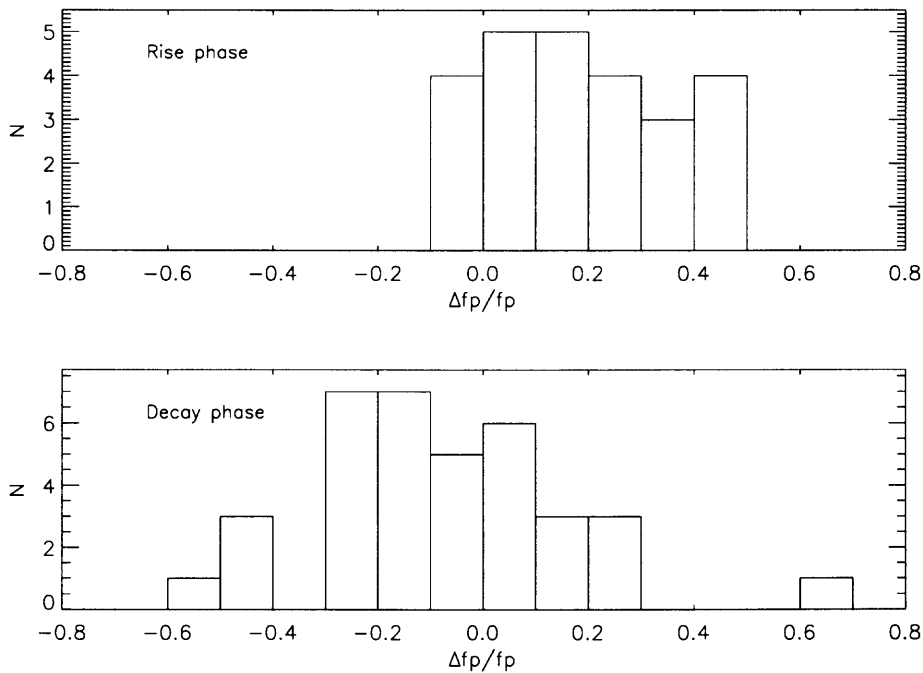


Figure 4.8 The same as in Figure 4.7, but normalized by the peak frequency $\Delta f_{peak}/f_{peak}$. Here f_{peak} is taken at the peak time of $S_{peak}(t)$.

Table 4.1. Regression coefficients for events with $\Delta f_{peak}/f_{peak} > 0.3$.

Event	$\beta(f_{peak}, S_{peak})$	$\beta(f_{peak}, S_2)$	$\beta(f_{peak}, S_1)$
2001 Apr 22	0.23	0.14	0.30
2001 Oct 19	0.27	0.17	0.31
2001 Oct 22	0.21	0.18	0.27
2001 Nov 04	0.26	0.20	0.34
2001 Nov 22	0.34	0.27	0.66
2002 Jul 15	0.26	0.17	0.43
2002 Dec 04	0.32	0.22	0.54
Mean	0.27	0.19	0.41

peak frequency shifts, $\Delta f_{peak}/f_{peak} > 0.3$). The straight lines are the best linear fits (in logarithmic scale) near the peak of the bursts. Generally, we can see that the dependence is a power law

$$f_{peak} \propto S_{peak}^{\beta} \quad (4.10)$$

with the index β varying from event to event. The values of β for each event are listed in Table 4.1. As we can see the mean value of β is 0.27.

For comparison, in Table 4.1 we show also the power law indices β_1 and β_2 obtained for the fluxes at the previously defined frequencies f_1 and f_2 (see Eq. 4.6), below and above the peak. The mean values are $\beta_1 = 0.41$ and $\beta_2 = 0.19$. We can understand the differences between β , β_1 and β_2 in the frame of self-absorption. Indeed, the value of β_2 is minimal, and β_1 is maximal, since in the optically thin regime the GS flux variations are expected to be much greater than in the optically thick regime under variations of the parameters like n , L , δ or B (see Eq. 4.7, 4.8). The value of β falls between these limits, because flux density S_{peak} is from a partly optically thick, partly thin source with optical depth $\tau \simeq 1$.

Quantitatively the value of β also corresponds well with Eq. 4.4 under the assumption that the area A , spectral index δ and magnetic field B do not change

during the rising phase of these bursts. For electron spectral index $\delta = 3.0 - 5.0$, the theoretical value $\tilde{\beta} = 1/(2.50 + 0.085\delta) = 0.34 - 0.36$ is slightly greater than β , giving a mean difference $\tilde{\beta} - \beta = 0.08$. This systematic reduction in β is likely due to a change in one or more of the other parameters on which S_{peak} depends (Eq. 4.4).

Let us examine the required changes quantitatively. First, an increase in source area A during the rise will reduce β . It follows from Eqs. 4.4 and 4.10 that

$$\frac{A}{A_0} = \left(\frac{S}{S_0} \right)_{peak}^{(\tilde{\beta}-\beta)/\tilde{\beta}}, \quad (4.11)$$

where index 0 indicates the value at some initial time. To obtain the value $\tilde{\beta} - \beta = 0.08$ due solely to a change in source area, A should increase by a factor ~ 1.4 during a factor 4 increase in peak flux.

Second, a decrease of electron spectral index during the rise phase will also decrease β . In this case:

$$\Delta\delta = \frac{1 - \beta/\tilde{\beta}}{0.31 - 0.085k} \log\left(\frac{S}{S_0}\right)_{peak}, \quad (4.12)$$

where $\Delta\delta = \delta - \delta_0$ and $k = \log(f_{peak}/f_B)$. Here we drop the term with $\sin\theta$ because its influence is very small—with all reasonable δ it differs from unity by less than 1% for $\theta > 60^\circ$. For $k = 1.0$ (10th harmonic of the gyrofrequency) and a change in flux density $S/S_0 = 4$, a decrease of electron spectral index $\Delta\delta = 0.51 - 0.61$ is needed for $\beta - \tilde{\beta} = 0.08$. This value of $\Delta\delta$ seems reasonable, and a hardening of the electron energy spectrum to such an extent on the rise phase of bursts is a quite common from studies of hard X-ray (Dulk, Kiplinger, & Winglee 1992) and microwave spectral dynamics (Melnikov & Magun 1998).

Finally from Eq.4.4, a decrease in magnetic field will also reduce β . In this case:

$$\frac{B_0}{B} = \left(\frac{S}{S_0} \right)_{peak}^{(\tilde{\beta}-\beta)/(1-2\tilde{\beta})}, \quad (4.13)$$

where B_0 is the magnetic field strength at the initial time. In this case, to explain the difference $\tilde{\beta} - \beta = 0.08$ we need the magnetic field decrease of $B_0/B = 1.45$ for a

factor of 4 change in peak flux density. Such a decrease of B can occur, for instance, if the brightness center of the source shifts to the region of smaller magnetic field. For the case of a single magnetic loop, this implies a shift from the footpoint region to the looptop. Such a shift has been observed with spatial resolution by Nobeyama Radioheliograph in a number of cases (Melnikov et al. 2003).

So we see that an increase of source area, a hardening of the electron spectrum, or a decrease in B during the rise phase of a burst all act to decrease the index β shown in Figure 4.9 and Eq. 4.10. Any of these changes may be reasonably expected, and the actual decrease in slope is likely a combination of these effects. With our dataset, we cannot evaluate whether changes in area or magnetic field plays the main role, because we do not have observations with the necessary spatial resolution. However, it appears that for at least 5 of the 7 bursts shown in Figure 4.9 the reduction of β is not due to a flattening of the electron spectral index, since their high frequency microwave spectral slope α_h was instead steepening on the rising phase. An exception is the event 2002 Jul 15, for which α_h increased from -2.0 to -1.2 .

4.3.2.2 Moderate Peak Frequency Shifts Investigating the 9 bursts that show moderate $\Delta f_{peak}/f_{peak} < 0.3$, we find a common signature of clear spectral flattening over time at frequencies $f > f_{peak}$ during the rise phase. Two examples are shown in Figures 4.10 and 4.11. In the previous section we showed that the electron spectral flattening, which is reflected in the increase of α_h , should in principle reduce the frequency shift of S_{peak} (decrease β). However, this is not the only effect that can give small observed values of $\Delta f_{peak}/f_{peak}$. Our comparative analysis of the flux and peak frequency time profiles show that the bursts can be divided into two subsets according to the temporal behavior of f_{peak} .

The first subset is characterized by relatively high and stable values of the peak frequency in the very beginning of the rising phase. The peak frequency starts to increase only after some delay relative to the flux increase, and peaks simultaneously (within the 4 s time resolution of OVSA) with the flux maximum. An example of such behavior is shown in Figure 4.10*a, b*. Here f_{peak} maintains a relatively high and constant value during the entire burst. Only near the very peak does it slightly increase, with $\Delta f_{peak}/f_{peak} = 0.21$. The simple GS model cannot explain the relative constancy of f_{peak} during such a large change in S_{peak} , except by including the effects of relatively strong Razin suppression. We will consider this effect in detail in Section 4 of our paper.

The second subset of events in this category is characterized by f_{peak} reaching its maximum value prior to the peak time of S_{peak} , as shown in Figure 4.11. For these events, the peak frequency increases with a regular rate in the beginning of a burst, but then decreases prior to and throughout the peak of the burst. Note that the behavior of R in Figure 4.11*d* shows a similar time delay. Such time delays also occur for events with small $\Delta f_{peak}/f_{peak}$ discussed in the next section. As a whole we found 10 events out of 25 where such time delays occur, and all of them show a significant increase in α_h . In Figure 4.11, for example, the change in microwave spectral index was $\Delta\alpha_h \geq +1$ for a factor of 4 increase in flux density.

On the other hand, the maximum value for f_{peak} may be delayed relative to the flux density maximum, as can be seen by careful attention to the burst in Figure 4.3 (both for the main and later minor peak). Note that in this case α_h also behaves oppositely, showing a significant steepening after the burst maximum.

We conclude that the flattening or steepening of the electron energy spectrum can affect the evolution of f_{peak} to such an extent as to cause these differences in timing. In Figure 4.12 we show the results of a simulation of the peak frequency evolution for the gaussian time profile of S_{peak} and for the electron spectral flattening

or steepening similar to that suggested by the observations. We used the relation $\alpha_h = 0.90\delta - 1.22$ from Dulk & Marsh (1982), for three different linear variations in electron spectral index, $\Delta\delta = -1, -0.5, +0.5$. These correspond to microwave slope variations of $\Delta\alpha_h = +0.9, +0.45, -0.45$. It is clearly seen that hardening or softening of the electron spectrum affects the time of maximum of f_{peak} in the way indicated by the observations.

4.3.2.3 Small Peak Frequency Shifts A total of 8 bursts show small relative peak frequency shifts, $-0.1 < \Delta f_{peak}/f_{peak} < 0.1$, on their rise phase. Of these, 4 show complex behavior. An example is shown in Figure 4.13, where a burst with a simple flux density profile nevertheless displays a complicated shift of f_{peak} , decreasing rapidly in the beginning before showing a more normal behavior through the peak. This may be a result of some previous burst activity or a radical source shift from a region of strong magnetic field to the one with weak magnetic field.

The remaining 4 bursts with small $\Delta f_{peak}/f_{peak}$ are characterized by a nearly constant f_{peak} right through the flux density peak, while S_{peak} first increases and then decreases by a factor of several. Examples of such events are shown in Figures 4.14 and 4.15. The constancy of the high frequency spectral index in both bursts indicates a constant electron spectral index δ , so it cannot influence the f_{peak} behavior. These bursts are relatively long and have smooth, gradual profiles. In fact, both bursts are secondary components of earlier, strong multi-component bursts. We can see in both events that the R is nearly constant as well, indicating that the flux density increases and decreases almost with equal rate both at low ($f < f_{peak}$) and high ($f > f_{peak}$) frequencies. As we mentioned earlier, this is a clear signature of Razin suppression, which will be investigated in more detail shortly.

Table 4.2. Regression coefficients for events with $\Delta f_{peak}/f_{peak} < -0.4$

Event	$\beta(f_{peak}, S_{peak})$	$\beta(f_{peak}, S_{thin})$	$\beta(f_{peak}, S_{thick})$
2001.08.30	0.80	0.45	> 0.78
2001.08.31	0.55	0.39	> 0.55
2001.10.22	0.39	0.32	> 0.52
2002.08.28	0.53	0.27	> 0.42
Mean	0.57	0.36	> 0.57

4.3.3 Peak Frequency Evolution on the Decay Phase of Bursts

In general, peak frequency evolution on the decay phase considerably differs from the evolution on the rising phase. The powerlaw dependence of f_{peak} on S_{peak} seen in the rise phase is observed typically only in the beginning of the decay phase. In the late decay phase, the opposite dependence (i.e. a continued increase in f_{peak}) is seen for a significant fraction of events.

4.3.3.1 Large Negative Frequency Shifts Of the 36 bursts that we could study in the decay phase, there are 4 events with large negative relative frequency shifts, $\Delta f_{peak}/f_{peak} = -0.4$ to -0.6 . In Figure 4.16 we show the relationship between f_{peak} and S_{peak} for these events. The straight lines are the best linear fits (in logarithmic scale) near the peak of the bursts. This dependence can be described by the same power law expression as Eq.4.10. The values of β for each of the 4 events are listed in Table 4.2. From the table we can see remarkably high values of slope β (average $\beta = 0.57$) relative to the value of $\beta = \tilde{\beta} \simeq 0.35$ expected from Eq. 4.4, much higher than the highest values of β found during the rising phase of bursts (see Table 4.1).

Such a strong decrease of f_{peak} on the decay phase can be explained by one or more of the effects that we discussed earlier: increase of the source area A , flattening of the electron energy spectrum (decrease of δ), or decrease in magnetic field B . To

explain the extent of the difference $\tilde{\beta} - \beta$ that we see in these events would require A to increase 2.7 times, δ to decrease by 1.6, or B to decrease by 2.6 times for a factor of 4 decrease in S_{peak} . A combination of two or more effects would reduce the amount of change necessary for each.

Again, we cannot investigate the change of the magnetic field and area without spatially resolved observations, but we can use the observed microwave spectral index α_h to investigate δ . First of all, we have found that α_h does flatten on the decay phase of the bursts, giving $\Delta\alpha_h = 1.8, 1.3, 1.3,$ and 0.6 for the events 2001 Aug 30, 2001 Aug 31, 2001 Oct 22, and 2002 Aug 28, respectively. These correspond to $\Delta\delta = 2.0, 1.4, 1.4, 0.7,$ respectively. These spectral index variations can explain a considerable part of the difference $\tilde{\beta} - \beta$, but not all of it. In our opinion, some of the enhanced decrease of f_{peak} could be ascribed to a magnetic field decrease in the radio source, as discussed earlier. Again we refer to direct measurements with spatial resolution indicating the brightness centroid may shift from the footpoints to the looptop during the decay phase, where the magnetic field is weaker (Melnikov et al. 2003).

A plot of the time profiles of our four parameters for one of the bursts in this category is shown in Figure 4.13, where our focus is now on the decaying portion after 2241 UT. We can clearly see the strong decrease of f_{peak} and R on the initial part of the decay phase, which is accompanied by a flattening of the high frequency spectral slope through the peak of the burst. We conclude that GS self-absorption can explain all 4 of the bursts with large negative peak frequency shifts when other effects are included.

4.3.3.2 Moderate Negative Frequency Shifts A total of 14 events show moderate relative shifts ($-0.3 < \Delta f_{peak}/f_{peak} < -0.1$). Six of these are plotted in Figure 4.17 and listed in Table 4.3. These bursts have mean value $\beta \simeq 0.4$ that

Table 4.3. Regression coefficients for events with $-0.3 < \Delta f_{peak}/f_{peak} < -0.1$.

Event	$\beta(f_{peak}, S_{peak})$	$\beta(f_{peak}, S_{thin})$	$\beta(f_{peak}, S_{thick})$
2001.08.25	0.95	0.52	1.97
2001.12.28	0.35	0.19	0.65
2001.07.20	0.21	0.16	0.38
2001.07.26	0.27	0.20	0.56
2002.08.18	0.27	0.20	0.43
2002.10.31	0.38	0.20	> 0.7
Mean	0.40	0.24	> 0.8

is closer to the theoretical expectations. The detailed analysis shows that in some cases the moderate values of $\Delta f_{peak}/f_{peak}$ are actually large-shift events (e.g. event 1 in Figure 4.17) whose overall slope is moderated due to a change of the evolution from an initial step decrease to a constant or increasing value of f_{peak} on the time interval over which the slope is measured. Such a change in slope during the decay is quite typical, as one can see from all 6 bursts in Figure 4.17). In fact, in only 4 of the 14 events did the peak frequency decrease monotonically. In the other 10 events the peak frequency became constant or started to increase before S_{peak} had dropped by an order of magnitude. We will discuss these flat or increasing frequency shifts on the decay shortly.

4.3.3.3 Small Frequency Shifts Ten events show small relative frequency shifts on the decay, in the range $-0.1 < \Delta f_{peak}/f_{peak} < 0.1$. Half of these bursts (5 of 10) are explained by a similar change of slope of f_{peak} vs S_{peak} that we saw in Fig. 4.17, from an initial decrease to a later increase. In the other 5 events we observe small, gradual monotonic shifts or even remarkably flat values of f_{peak} on the decay phase similar to what we have already discussed for the rising phase. The examples of such a behavior can be seen in Figures 4.14 and 4.15. For 7 of these 10 events the

peak frequency became constant or started to increase before S_{peak} dropped by an order of magnitude (see Figure 4.16). Figure 4.2b, c displays instantaneous spectra at different moments of time for one of the events. Comparison of this type of spectral evolution with the type shown in Figure 4.1 demonstrates strong differences between them. Indeed, in this event the flux at all frequencies, including $f > f_{peak}$ and $f < f_{peak}$, changes in parallel so that the turnover frequency shows no visible change during the main part of the burst.

4.3.3.4 Positive Frequency Shifts Only a small percentage of bursts ($\sim 10\%$) maintain the behavior expected for pure GS self-absorption, i.e. a monotonic decrease in peak frequency during the entire decay phase (defined as lasting from the time of peak flux to the point where S_{peak} drops by a factor of 10). Examples of these relatively rare bursts are shown in Figure 4.6 and Figure 4.16 (event 4).

On the other hand, a large percentage (25 of 36 events, i.e. $\sim 70\%$) display a considerable *increase* of f_{peak} starting at some point during the decay phase. As we have already mentioned in sections 3.3.1-3.3.3, in most cases the increase begins after some decrease of the burst flux, often by a factor of 2-3 and sometimes by a larger factor. The characteristic time delay of the beginning of the peak frequency increase relative to burst maximum is 2 minutes. However, the delay varies considerably from event to event.

In several events the increase of f_{peak} begins much earlier, just after the intensity peak and before S_{peak} drops by more than a factor of 2. For example, in the event shown in Figure 4.18 the strong increase of f_{peak} (from 5.6 up to 7.7 GHz) occurs on the gradual decay phase of the last peak. It begins only ~ 30 s after the flux maximum, when S_{peak} has decreased less than half of its maximum value. It is interesting that the increase of f_{peak} is accompanied by the continuous flattening of the high frequency spectral slope (α_h increases from -2.4 to -0.9) which starts

just in the beginning of the decay phase. On the contrary, from other events and from our simple GS model (see section 3.2.1) we know that such a flattening on the decay phase should actually enhance the rate of decrease of f_{peak} . In §4 we show that this type of peak frequency evolution can be explained by Razin suppression that increases with time due to the hardening of the electron energy spectrum in the source.

In 10 of the 25 events showing an increase in f_{peak} , the delay in the f_{peak} increase relative to the burst maximum varies from 2 to 8 minutes. These events are usually long lasting gradual bursts with relatively low peak frequency, $f_{peak} \lesssim 7$ GHz, prior to the increase (see examples in Figures 4.14, and 4.15, 4.2). In Figure 4.15 one can clearly see the considerable increase of f_{peak} and ratio R on the late decay phase, starting from 20:26 UT. The increase of R means that the flux decrease at low frequency $f_1 = 4.6$ GHz $< f_{peak}$ goes faster than at high frequency $f_1 = 11.2$ GHz $> f_{peak}$. The faster flux decrease at lower frequencies (steepening of the spectrum at $f < f_{peak}$) after moment t_6 is easily seen in Figure 4.2c. Note that the shape of the microwave spectrum during this increase remains the typical GS spectrum with a well pronounced spectral peak. This is true also for other events with an increase in f_{peak} .

We have examined possible reasons for an increase in f_{peak} in the late decay phase, such as thermal GS emission, or the required variations in parameters (decrease in A , or increase in B), and again find that the most plausible explanation is an increase in density in the decay phase, which increases the effect of Razin suppression with time. An analysis of this possibility will be given in the next section.

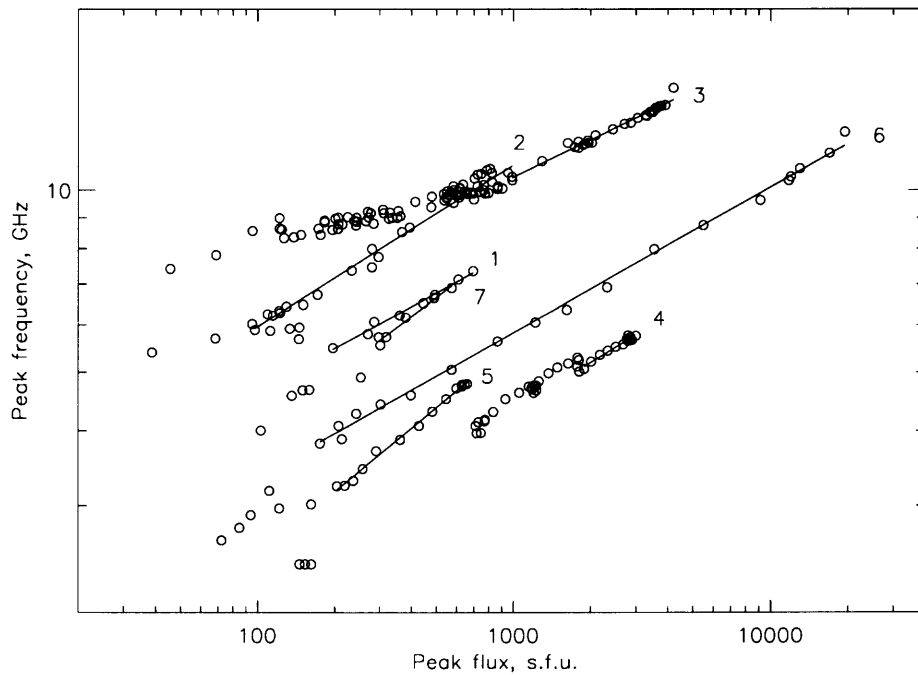


Figure 4.9 Peak frequency vs. peak flux density on the rise phase of 7 events. The straight lines are the best linear fits (in logarithmic scale) near the peak of the bursts. The numbers indicate the events: 1–2001 Apr 22, 2–2001 Oct 19, 3–2001 Oct 22, 4–2001 Nov 04, 5–2001 Nov 22, 6–2002 Jul 15, 7–2002 Dec 04.

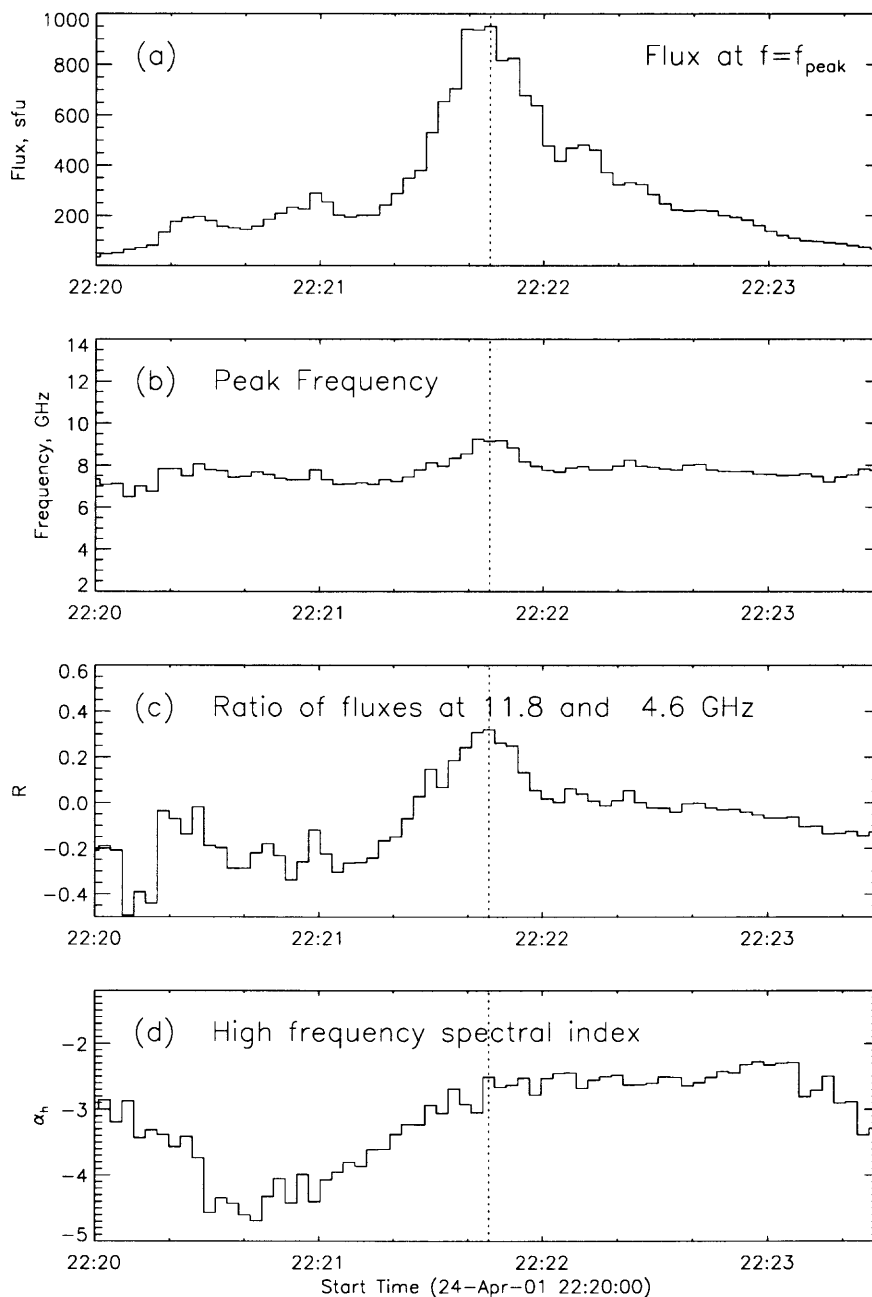


Figure 4.10 Time profiles as in Figure 4.3 for the burst of 2001 April 24. The peak frequency in *b* remains high and nearly constant except near the main peak in *a*. The ratio R in *c* also becomes high and constant during the decay. Note that the spectral index α_h in *d* increases all during the rise phase and is constant in most of the decay phase.

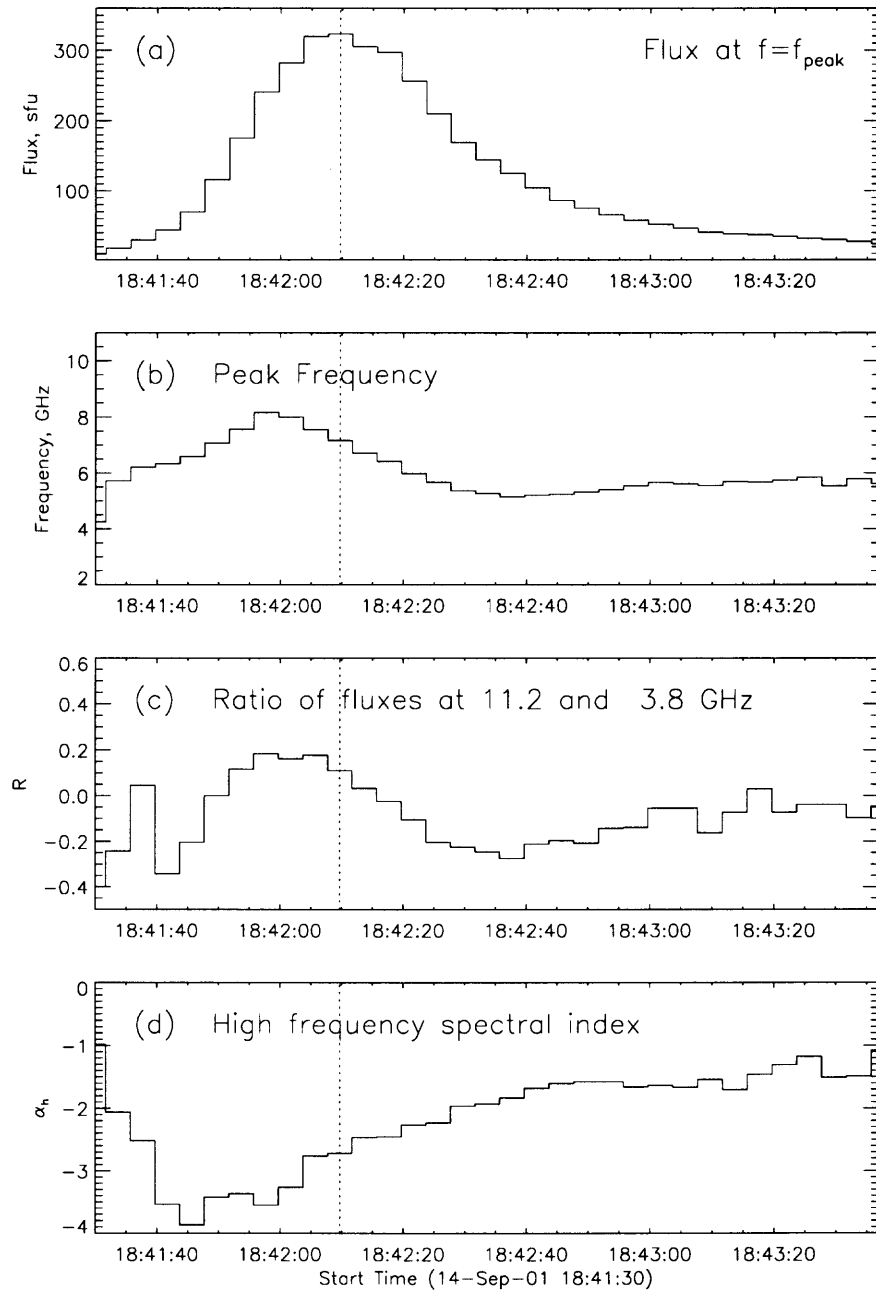


Figure 4.11 Time profiles as in Figure 4.3 for the bursts of 2001 Sep 14. This example shows a time delay between f_{peak} in *b* and S_{peak} in *a*. Note also that on the decay f_{peak} first decreases and then slightly increases. The α_h in *d* increases throughout the burst.

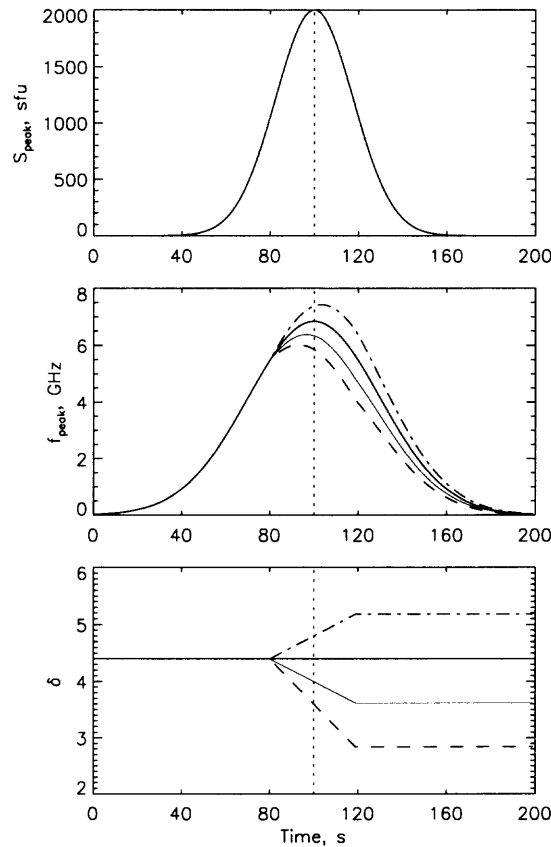


Figure 4.12 Simulation of the spectral evolution for a gaussian flux density profile (a) under the influence of hardening or softening of the electron spectrum, showing in b the leading or lagging of the time of maximum of f_{peak} . The assumed electron spectral index evolution is shown in c: solid line, $\delta = const$; dashed line, $\Delta\delta = -0.5$; dotted line, $\Delta\delta = -1.0$; dot-dashed line, $\Delta\delta = +0.5$. The peak frequency time profile leads the flux maximum if the electron spectrum flattens, and it lags if the electron spectrum steepens.

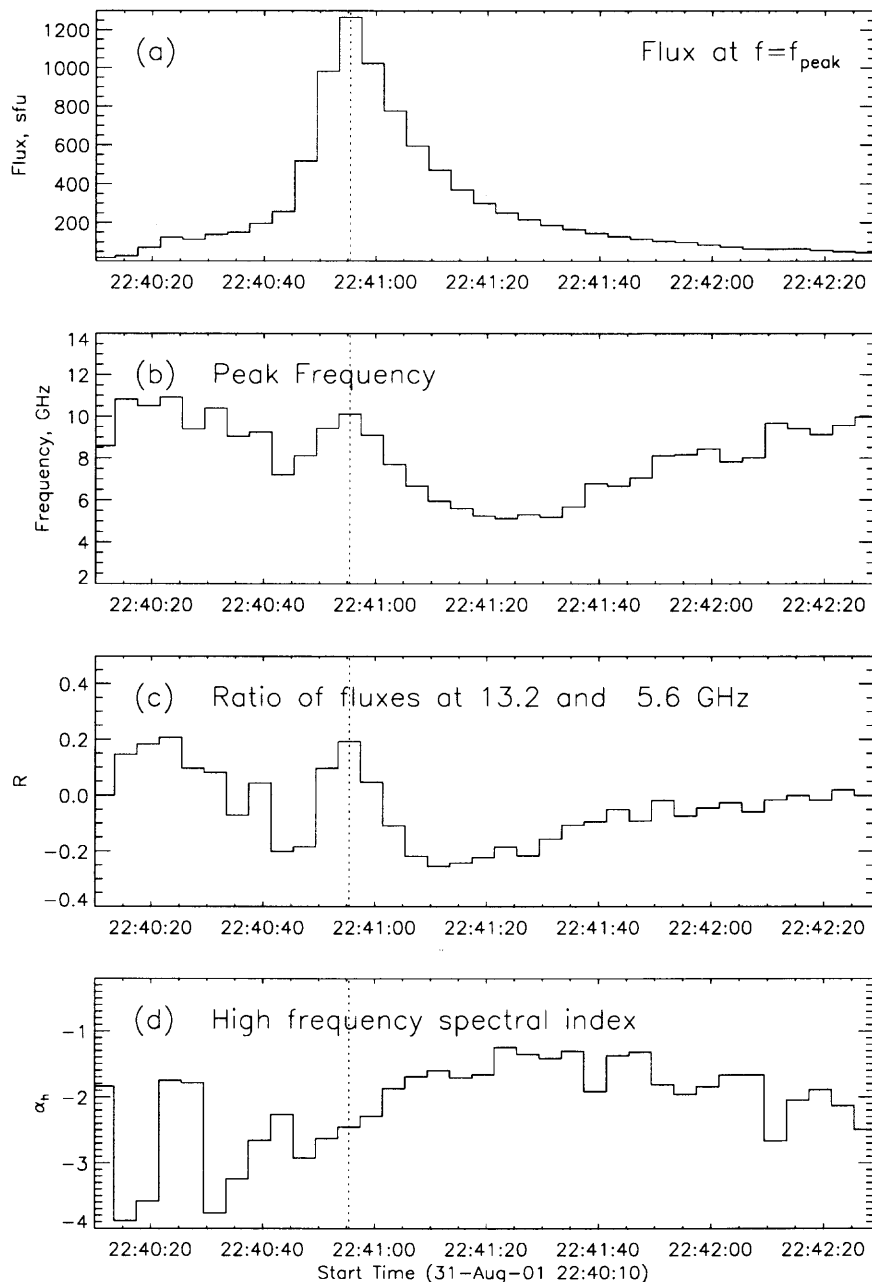


Figure 4.13 Time profiles as in Fig. 4.3 for the burst of 2001 August 31. This example shows a rather complex time profile for f_{peak} , with a strong decrease of f_{peak} and R in the initial rise phase followed by more normal behavior. On the late decay phase, there is also a strong subsequent increase of the peak frequency and flux ratio. Note that for the ratio R the end of decrease and the beginning of the increase occur earlier than for the peak frequency. The high frequency spectral slope flattens during all the main part of the burst, and keeps almost constant on the late decay phase.

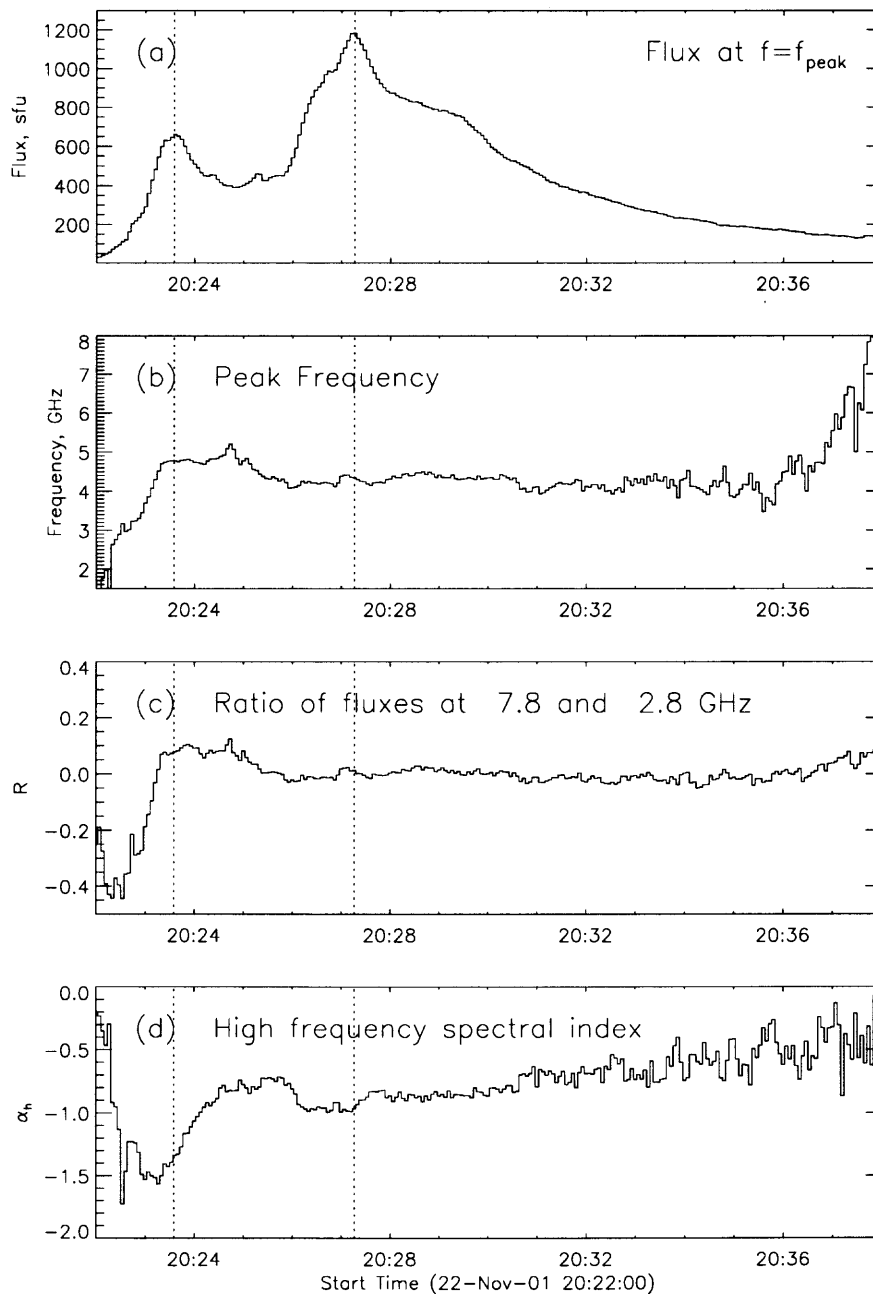


Figure 4.14 Time profiles as in Fig. 4.3 for the second major peak of the burst of 2001 Nov 22. The turnover frequency in *b* is remarkably constant during the main part of the rise and decay. The same is true for the ratio *R* in *c*. On the late decay phase the peak frequency starts to increase.

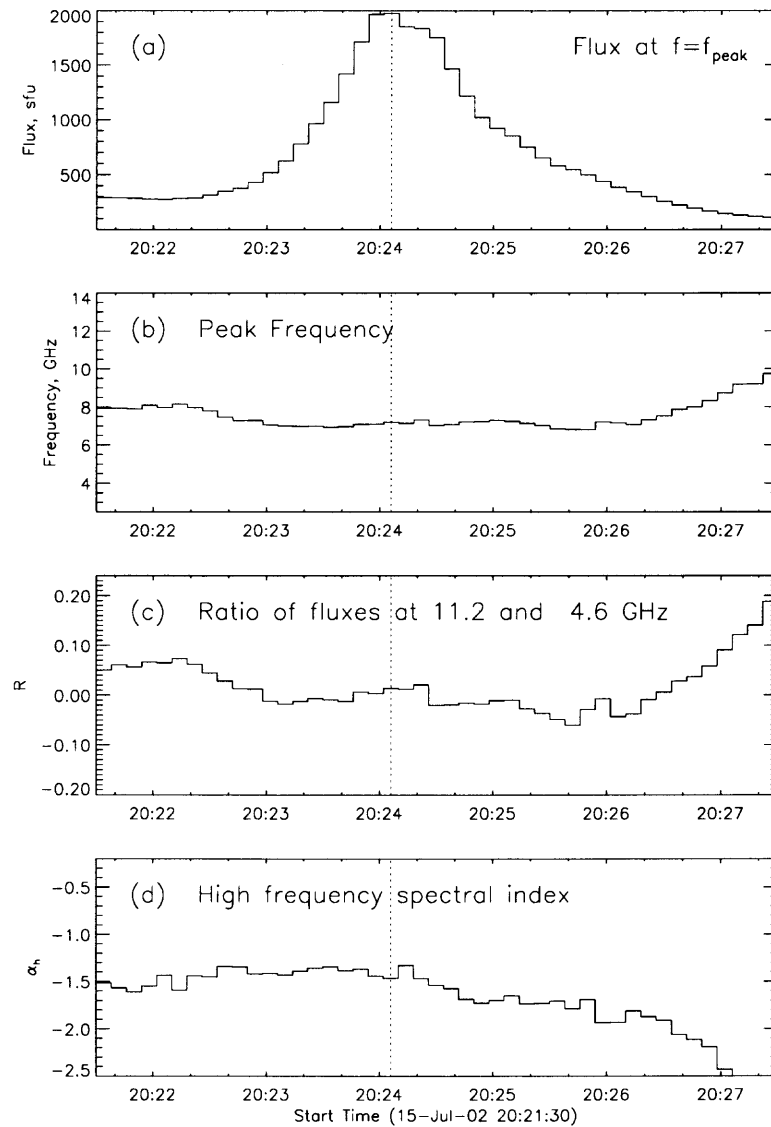


Figure 4.15 Time profiles as in Fig. 4.3 for the burst of 2002 Jul 15. The turnover frequency in *b* is remarkably constant during the entire rise and decay of the second major peak of the burst. The same is true for the ratio R in *c*. Note also the gradual increase of f_{peak} and R after 2026 UT, while S_{peak} decreases gradually more than a factor of 4. The spectral evolution of this burst is shown in Fig. 4.2.

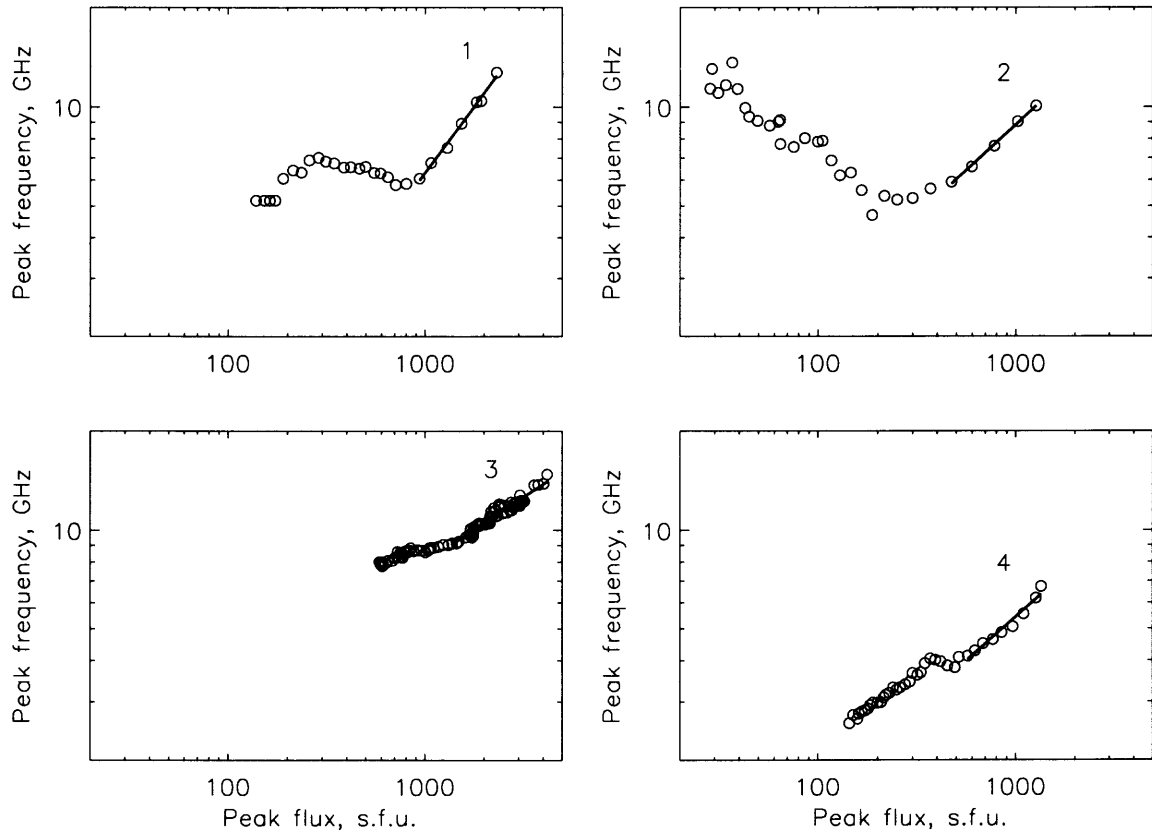


Figure 4.16 The relationship between the peak frequency, f_{peak} , and peak flux density, $S_{peak} = S(f_{peak})$ on the decay phase of 4 events with the highest values of $\Delta f_{peak}/f_{peak}$. The straight lines are the best linear fits (in logarithmic scale) near the peak of the bursts. The numbers indicate the events: 1 - 2001.08.30, 2 - 2001.08.31, 3 - 2001.10.22, 4 - 2002.08.28.

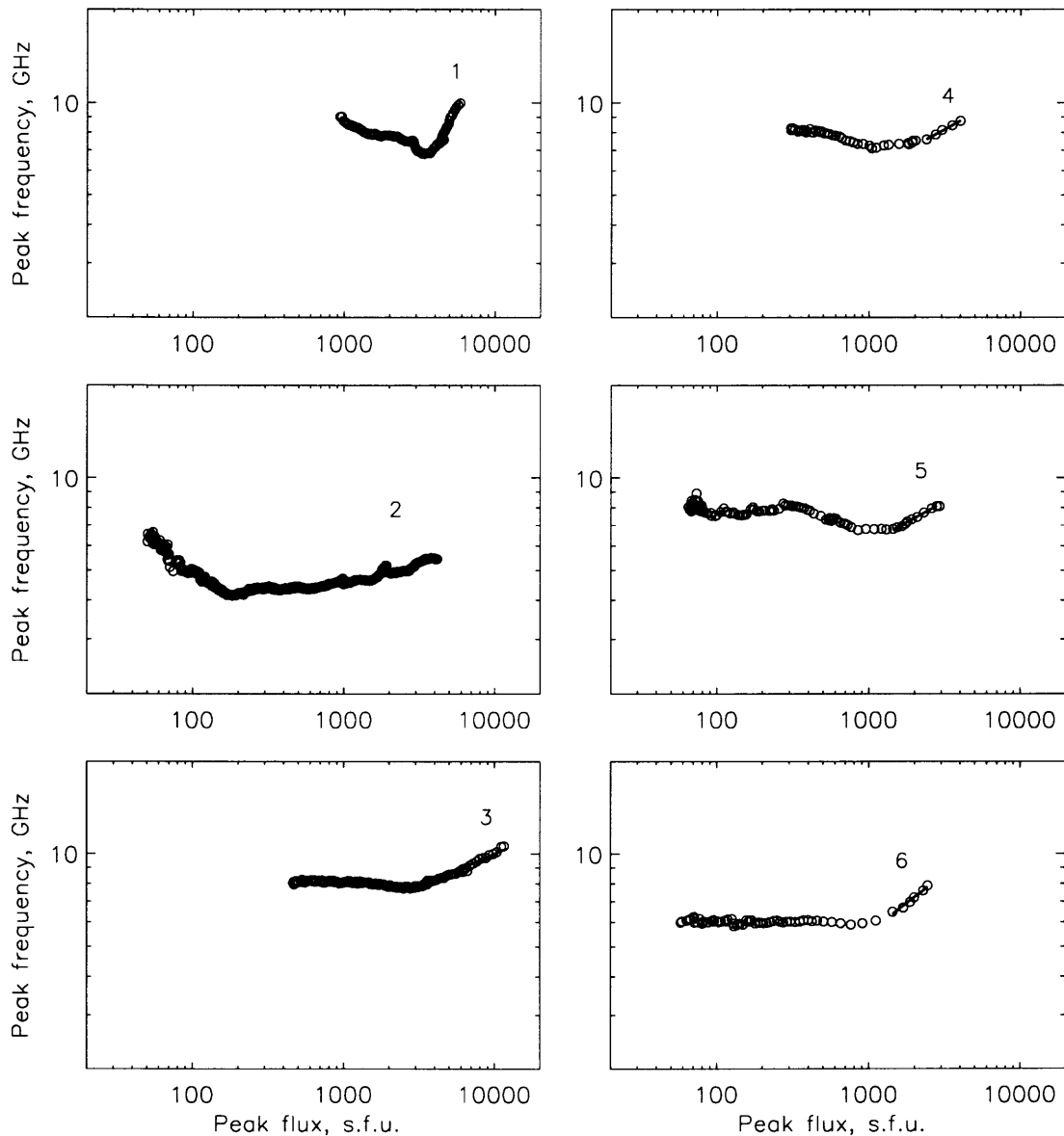


Figure 4.17 The relationship between the peak frequency, f_{peak} , and peak flux density, $S_{peak} = S(f_{peak})$ on the decay phase of 6 events with the moderate values of $\Delta f_{peak}/f_{peak}$ ($-0.3 < \Delta f_{peak}/f_{peak} < -0.1$). The straight lines are the best linear fits (in logarithmic scale) near the peak of the bursts. The numbers indicate the events: 1 - 2001.08.25, 2 - 2001.12.28, 3 - 2002.07.20, 4 - 2002.07.26, 5 - 2002.08.18, 6 - 2002.010.31. A change of the dependence slope on the late stage of decay is well seen for all the events.

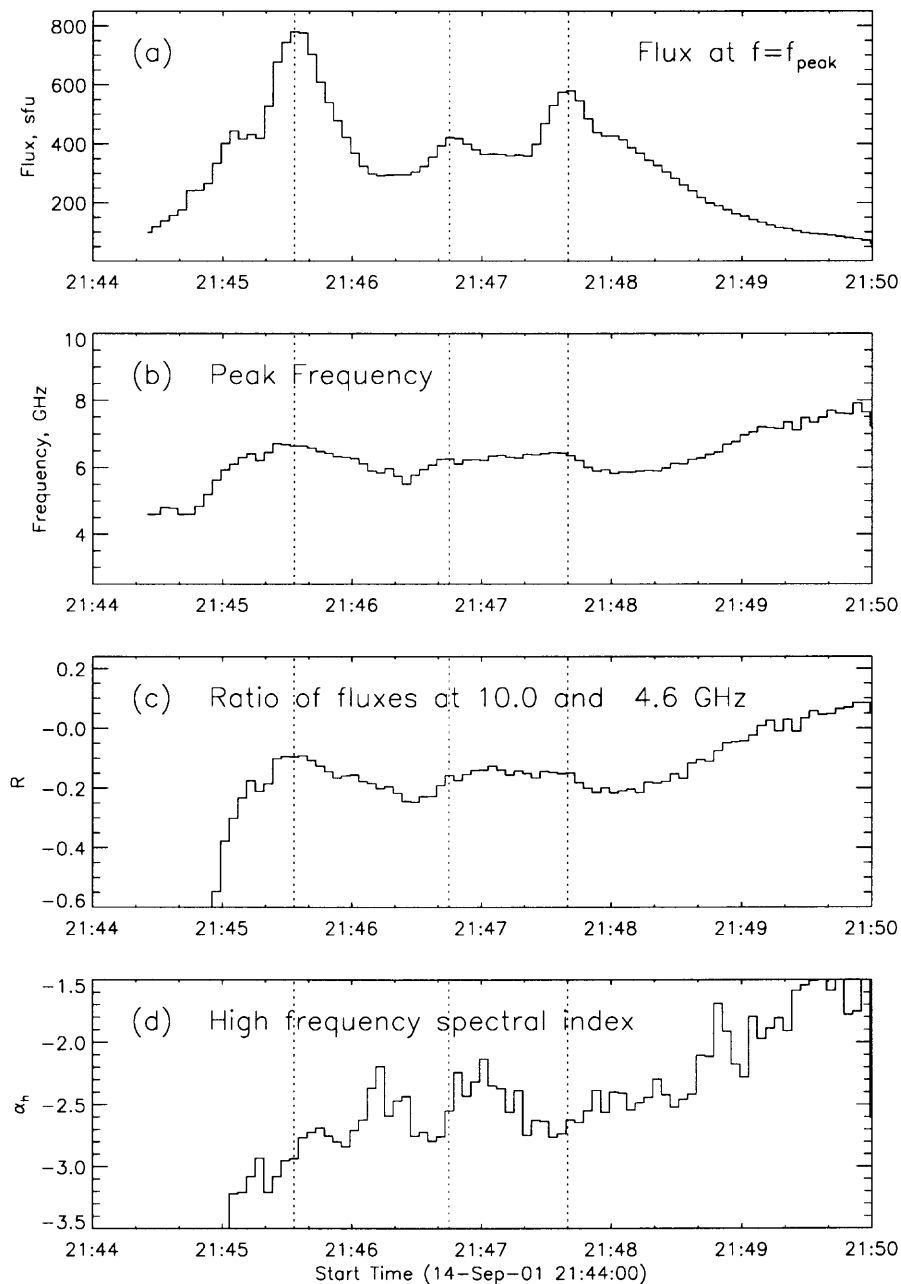


Figure 4.18 Time profiles of the microwave burst of September 14, 2001. Strong increase of f_{peak} and R on the gradual decay phase of the last peak is accompanied by continuous flattening of the high frequency spectral slope (increase of α_h).

4.4 Discussion and Model Simulations

We showed earlier that in a majority of bursts the peak frequency shifts are well correlated with flux density (at least near the maximum of the burst), as expected if the spectral turnover is due to GS self-absorption. We also showed that other effects such as evolution of the electron energy distribution can act in concert with GS self-absorption to account for some other peculiarities of spectral dynamics (e.g. time delays between f_{peak} and S_{peak}).

However, GS self-absorption cannot explain behavior found in a significant number of events including: 1) slight variations or even constancy of the peak frequency even when the burst intensity changes by an order of magnitude or more, or 2) a remarkable shift of the peak frequency to higher frequencies starting in the middle or late decay phase. A common feature that seems associated with the above behavior is a relatively low maximum value for f_{peak} . In some events f_{peak} can be as small as 3 GHz, which indicates a relatively weak magnetic field in the radio source. In this section we will examine Razin suppression as a mechanism to explain each of these properties.

4.4.1 Gyrosynchrotron Spectrum Formation

The idealized GS spectrum has a single peak at $f = f_{peak}$ whose low frequency turnover is either due to GS self-absorption (Twiss 1954) or due to Razin suppression (Razin 1960 a,b). In the GS self-absorption case, the peak frequency occurs near optical depth unity:

$$\tau(f_{peak}) = \kappa_f L \sim 1, \quad (4.14)$$

where κ_f is the absorption coefficient, and L is the source thickness. In the case of Razin suppression (for classical synchrotron emission) the low frequency turnover is defined by the Razin frequency:

$$f_R = \frac{2f_p^2}{3f_B}, \quad (4.15)$$

where f_p and f_B are the plasma frequency and gyrofrequency, respectively. So it is proportional to the ratio of plasma number density to magnetic field strength. High ambient density and/or low magnetic field strength act to raise f_R .

In this section, we carry out numerical simulations of peak frequency dynamics using the exact formalism for the GS emissivity and absorption coefficient (Ramaty 1969; Ramaty 1994). Electrons in the source are assumed to have a power law distribution and be distributed isotropically. The time profile of nonthermal electrons is chosen to have a Gaussian shape with effective duration and maximum time defined by the values t_0 and t_m , respectively:

$$n(E, t) = k \exp\left[-\frac{(t - t_m)^2}{t_0^2}\right] E^{-\delta}, \quad (4.16)$$

where E is the electron energy in MeV in the range (0.01-500)MeV, δ is electron spectral index, and k is a constant factor. We consider cases with low and high plasma density, with constant and varying electron energy power law index, and a case in which the plasma density increases with time. To show the pure effect on the microwave spectral dynamics and for simplicity, the magnetic field and plasma density are assumed to be homogeneous in the microwave source.

4.4.2 Influence of Self-Absorption

Figure 4.19 displays the spectral evolution of GS emission in a low density plasma, for parameters such that the low frequency turnover is entirely determined by GS self-absorption and Razin suppression is almost negligible at $f \geq 2$ GHz. The increase of GS intensity on the rise phase occurs due to the increase in number of energetic electrons and leads to the corresponding increase of f_{peak} (panels *a* and *d*). On the decay phase, the behavior is symmetrical. Note the low initial value (f_{peak} can be as low as 1.2 GHz) and large range of peak frequency variations: f_{peak} changes by a factor of 2 when S_{peak} changes by an order of magnitude. Note also a strong change (two orders of magnitude) in the ratio of fluxes at high $f_2 > f_{peak}$ and low $f_1 < f_{peak}$

frequencies (defined after Eq. 4.6), which occurs due to very small variation of the flux at f_1 where the source is optically thick. Panel *c* shows the dependence of the peak frequency on the peak flux as in Figure 4.9. The dependence is roughly a power law, $f_{peak} \propto S_{peak}^\beta$ with $\beta = 0.34$, practically the same value that we obtained in §3 using the simplified formulas for GS emission by Dulk & Marsh (1982).

This behavior looks similar to the f_{peak} and R evolution during the first peak of the event in Figure 4.1.

4.4.3 Influence of High Plasma Density: Razin Effect

When the ratio of plasma density to magnetic field in a source is large (the plasma parameter $Y = f_p/f_B \gg 1$), the GS spectrum experiences a strong influence of the ambient medium. For relativistic electrons, this effect is known as Razin suppression, and modifies the spectrum to produce a) an exponential decrease of the emissivity and absorption coefficient at low frequencies, $f < f_R$ (Razin 1960 a, b) considerable flattening of the original synchrotron power law spectrum, $F_f \sim f^{-\alpha}$, at higher frequencies (Razin 1960b).

The physical meaning of the medium influence can be understood from the simple consideration of Lienard-Wiechert potentials \mathbf{A} and ϕ in a medium with index of refraction $n < 1$ (Ginzburg 1953):

$$\mathbf{A}(t) = \left[\frac{ev}{c(R - n\mathbf{R} \cdot \mathbf{v}/c)} \right]_{t - n\frac{R}{c}} \quad (4.17)$$

$$\phi(t) = \left[\frac{e}{n^2(R - n\mathbf{R} \cdot \mathbf{v}/c)} \right]_{t - n\frac{R}{c}}, \quad (4.18)$$

where e is the electron charge, and \mathbf{R} is the radius-vector of the electron moving with velocity \mathbf{v} taken at the retarded time $t' = t - nR/c$. It follows from Eq. 4.17, 4.18 that the emissivity of a single electron depends strongly on the ratio of the electron velocity v to the wave phase velocity $v_{ph} = c/n$. In vacuo, $n = 1$ and therefore the effectiveness of emission is very high when the electron velocity is close to the speed of light c , since the denominator in Eq. 4.17, 4.18 tends to 0. In a plasma, $n < 1$

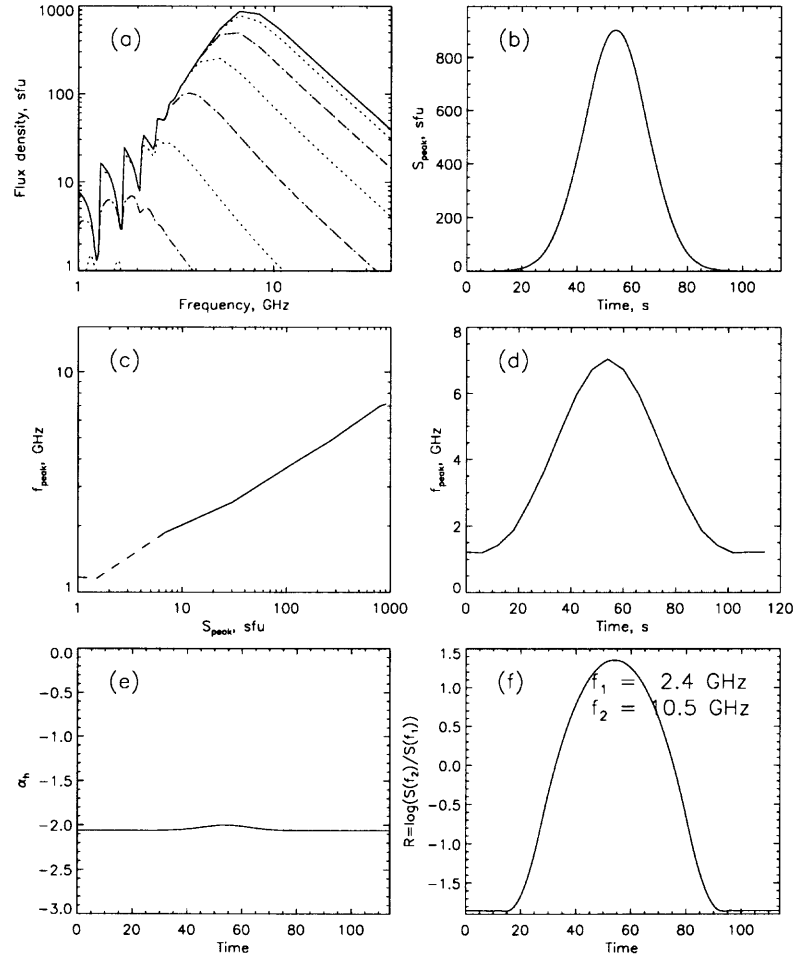


Figure 4.19 Spectral evolution of GS emission in a low density plasma ($n_0 = 5 \times 10^9 \text{ cm}^{-3}$, $B = 150 \text{ G}$, $t_m = 54 \text{ s}$, $t_0 = 12 \text{ s}$, $\delta = 4.0$, $L = 10^9 \text{ cm}$, $\phi = 17''$, $k = 10^4$). For these parameters, the low frequency turnover is determined by GS self-absorption. Panel (a): Flux density spectrum at different times on the rising (dotted lines) and decay (dashed lines) phases. Panel (b): Peak flux time profile $S_{peak} = S(f_{peak})$. Panel (c): Dependence of the peak frequency on the peak flux on a log scale (solid and dashed lines for the rise and decay, respectively). Panel (d): Peak frequency evolution. Panel (e): High frequency spectral index evolution. Spectral index is defined by fitting of a calculated spectrum (panel a) at frequencies $f > f_2$, $f_2 = 1.5f_{pabs}$ (see Eq. 4.6). Panel (f): Evolution of logarithm of the flux ratio R at $f_2 > f_{peak}$ and $f_1 < f_{peak}$.

and the denominator can never be very close to 0, even if $v \simeq c$. So a relativistic electron has an emission efficiency comparable with a nonrelativistic one, i.e. much lower than in vacuo. This causes a strong suppression of radiation in the plasma, especially at lower frequencies since in plasma $n \simeq 1 - f_p^2/f^2$. The Razin effect is predominantly a relativistic effect. As follows from Eqs. 4.17 and 4.18, the strong influence of the refraction coefficient n is only possible if the electron velocity v is close to the speed of light c .

Figure 4.20 shows the spectral evolution of GS emission for relatively high plasma density $n_0 = 5 \times 10^{10} \text{ cm}^{-3}$. The other parameters in the source are same as in Figure 4.19. In the beginning of the rise phase and during the late decay phase the radio source is optically thin at low frequencies due to the Razin effect. Due to the high ratio of n_0/B , the values of f_{peak} are quite high, $\sim 5 \text{ GHz}$. Although the flux density is changing, the peak frequency remains nearly constant during these periods. The low and high frequency fluxes change nearly at the same rate leading to $R = const$. However, near the maximum of S_{peak} , when the column density of nonthermal particles becomes high enough, the source becomes optically thick at $f \leq f_{peak}$, despite the Razin suppression, and the spectral evolution of f_{peak} follows the familiar behavior where the self-absorption plays main role. Note, however, the small range of this peak frequency variation, only about $\sim 30\%$ for an order of magnitude change in S_{peak} . The variation of R (< 0.5 order of magnitude) is also considerably smaller than in the case of pure self-absorption (Figure 4.19). The slope of f_{peak} vs. S_{peak} is much flatter than in the absence of the Razin suppression, with $\beta < 0.17$. This is comparable to the values of β found for the events with moderate $\Delta f_{peak}/f_{peak}$ (see Section 3). It is clear that for smaller k (defining the number density of energetic electrons, Eq. 4.16) the amplitude of the f_{peak} variation and the value of β will decrease. With sufficiently small k , we get no visible change at all in f_{peak} . Another remarkable feature of the case with high plasma density (high

level of Razin suppression) is a flatter microwave high frequency spectral slope at $f > f_{peak}$. It follows from Figure 4.19e and Figure 4.20e that the difference in the spectral indices is 0.5.

The spectral evolution shown in Figure 4.20 looks very similar to the f_{peak} evolution in Figure 4.10. Bursts with this spectral evolution indicate the presence of considerable Razin suppression, and serve as a diagnostic of high plasma density to magnetic field ratio in flaring loops.

4.4.4 Razin Effect and Electron Power Law Index

Note that Eq. 4.15 is derived only for emission from a single relativistic electron. For mildly relativistic electrons the position of the low frequency turnover depends on their energy: the higher the energy, the higher f_R becomes. The real situation is even more complicated since the electrons have some distribution over energy. The resulting f_{peak} of an actual spectrum is thus defined by some effective mean energy. We expect a higher f_{peak} for flatter electron spectra (lower δ). To quantify these expectations, one must perform numerical simulations, which we do in Figure 4.21. We choose very low density of nonthermal electrons to avoid the influence of GS self-absorption. The figures shows the dependencies of f_{peak} on the plasma density for different values of $\delta = 3$ to 5 and magnetic field. It is clear from the figures that the dependence becomes considerably steeper for the weaker magnetic fields as well as for the smaller electron spectral index. We can see a strong difference in f_{peak} for different δ . For example, f_{peak} increases from $\simeq 7$ to $\simeq 20$ GHz if δ decreases from 5 to 3 under conditions when $B=150$ G and $n_0 = 10^{11} \text{ cm}^{-3}$. The corresponding value of the Razin frequency is $f_R \simeq 13$ GHz. So the variation is remarkable.

Armed with this understanding of the effect of spectral hardening on Razin suppression, we show in Figure 4.22 the spectral evolution when both are present. We assume a linear change of δ from 5 to 3 during the burst. To show the pure

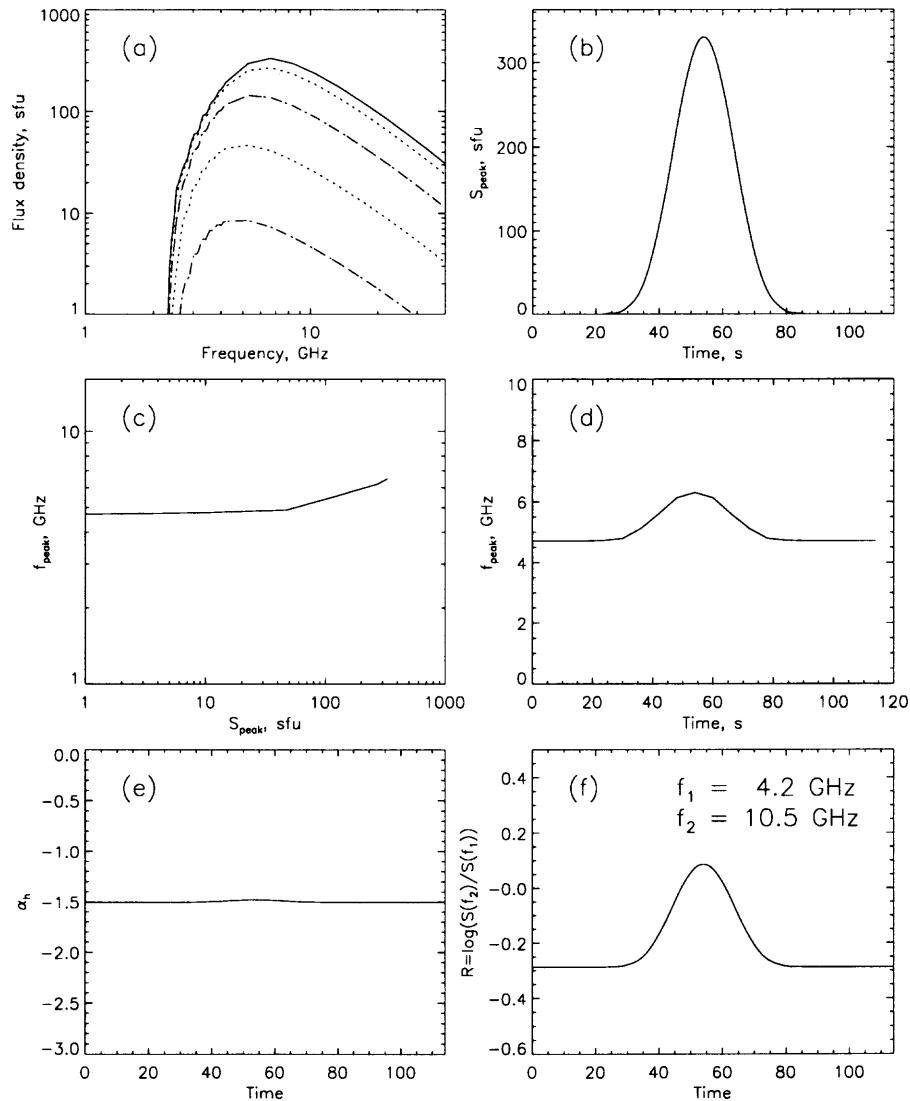


Figure 4.20 Spectral evolution of GS emission in the presence of high density plasma: $n_0 = 5 \times 10^{10} \text{ cm}^{-3}$. The other parameters are same as in Figure 4.19. The low frequency turnover is determined by two effects: 1) by the Razin suppression on the initial rising phase and late decay phase, and 2) by the self-absorption near the maximum of the simulated burst. Note the high initial value and small range of the peak frequency and R variations.

effect, here we have chosen the number density of energetic electrons sufficiently low so that GS self-absorption is never important, even near the burst maximum. As expected, the peak frequency increases throughout the rising and decay phases while the electron energy spectrum continuously hardens (panel d). While δ changes from 5 to 3, the peak frequency increases from 3.5 up to 8 GHz. The steepest increase of f_{peak} occurs in the late decay phase, where the electron spectrum is most hard. Note also the considerable increase of the flux ratio during all the burst: almost an order of magnitude (panel f). This happens since at both frequencies, f_1 and f_2 , the source is optically thin. Therefore, due to the electron spectral hardening the flux at low frequency increases slower on the rise phase of the burst and decreases faster on the decay phase.

Finally, in Figure 4.23 we add the effect of GS self-absorption by increasing of the number density of energetic electrons by 10 times with respect to the case shown in Figure 4.22. As we saw earlier, the behavior is modified near the peak of the burst due to a temporary increase of the optical thickness of the GS source. At other times, Razin suppression is dominant in defining the spectral peak. Note that the f_{peak} and R on the decay phase (panels c-f) are always higher than on the rising phase similar to the observed behavior described in Section 3.3.4, in particular, to the f_{peak} and R evolution in Figure 4.18, the last peak after 21:47:40 UT.

4.4.5 Plasma Density Increase on the Late Decay Phase

An energy release of sufficient magnitude in a flaring loop will be accompanied by chromospheric evaporation, which will increase the plasma density inside the loop over time. As we have shown in Figure 4.21, such an increase, if it is great enough, may produce a gradual increase of f_{peak} in the middle or late decay phase as the Razin effect becomes dominant.

A simulation of this process is shown in Figure 4.24. We suppose that the plasma density in the loop starts to increase at the burst maximum and increases throughout the decay phase. Near the burst maximum, the dominant low frequency turnover mechanism is GS self-absorption, but on the late decay phase the Razin effect dominates. This is shown by the fact that the flux at low and high frequencies changes almost at the same rate (see panel *a*, dashed lines). On panels *c* and *d* one can see that just after the flux maximum the peak frequency decreases more slowly than on the rising phase ($\beta = 0.02$) and then starts to increase. To get a 2 GHz increase of f_{peak} as shown on the panel *d*, we need only 50% plasma density enhancement. It is interesting to note that the high frequency spectral index also increases (spectrum flattens) with the plasma density increase on the decay phase (panel *e*). This occurs due to the already mentioned effect of the medium at high frequencies, $f > f_{peak}$ (Razin 1960b).

We should say that a similar f_{peak} increase occurs if the magnetic field in the radio source gradually decreases on the late decay phase. To get the same enhancement of f_{peak} , we need only 25% decrease of the magnetic field strength. In principle this can happen as newly reconnected loops appear at higher levels in the corona during continuous energy release and particle acceleration in the helmet coronal structures.

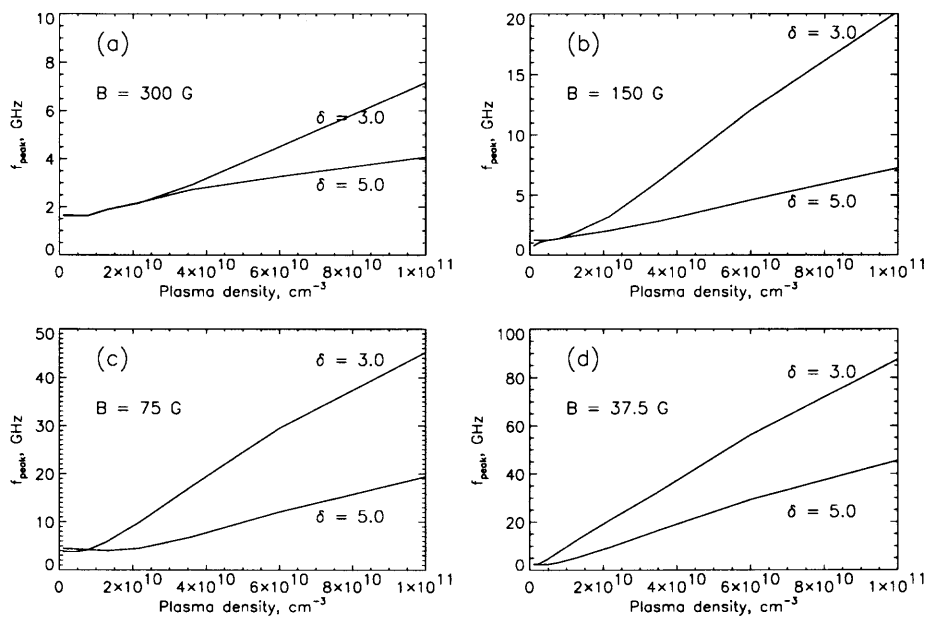


Figure 4.21 Dependence of the GS peak frequency on plasma density, magnetic field and electron energy index δ . The peak frequency defined by the Razin effect is considerably larger for a harder electron energy spectrum.

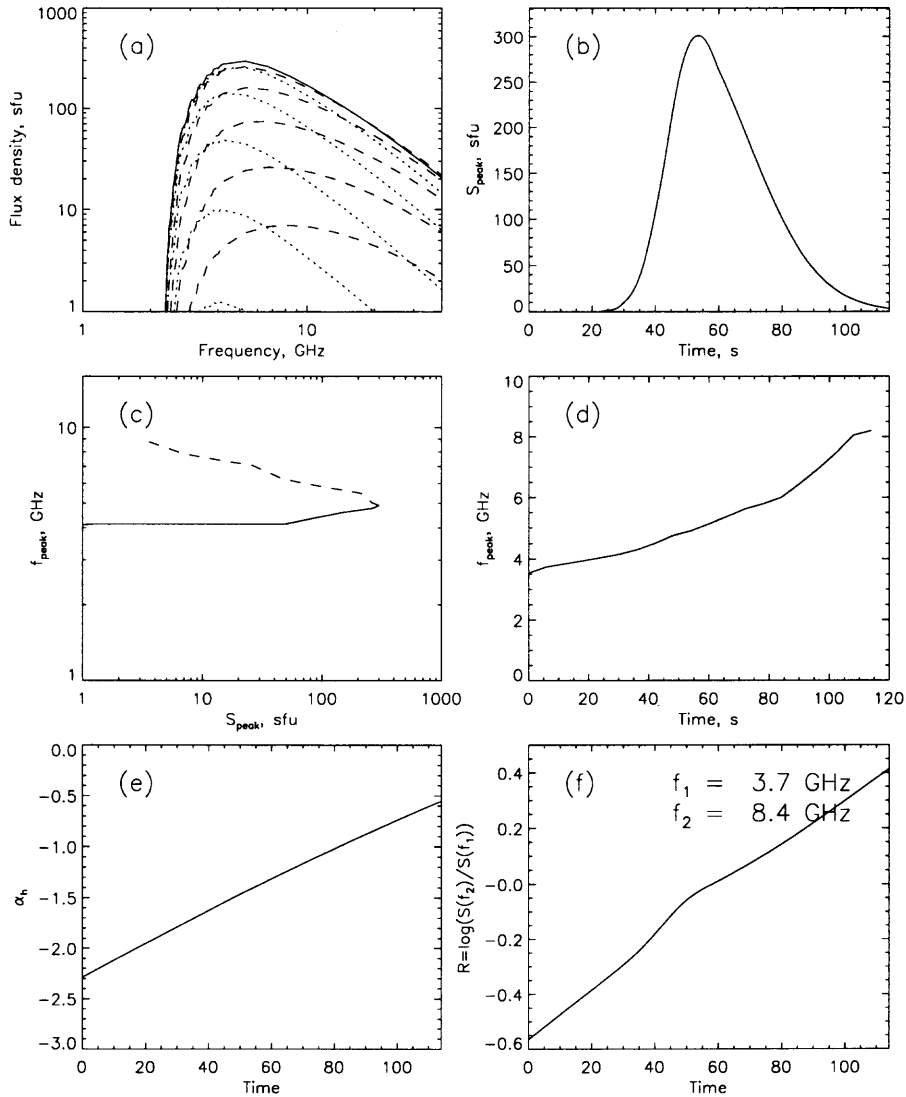


Figure 4.22 Spectral evolution of GS emission in the presence of high density plasma and continuous electron spectrum hardening, $\delta = 4.0 - (t - t_{max})/t_{max}$. The other parameters are the same as in Figure 4.20 except $k = 10^3$ and $\phi = 45''$. Note the continuous increase of f_{peak} and R on the rise and decay phases. On panels (a) and (c) solid line is for the rising phase and dashed line for the decay phase.

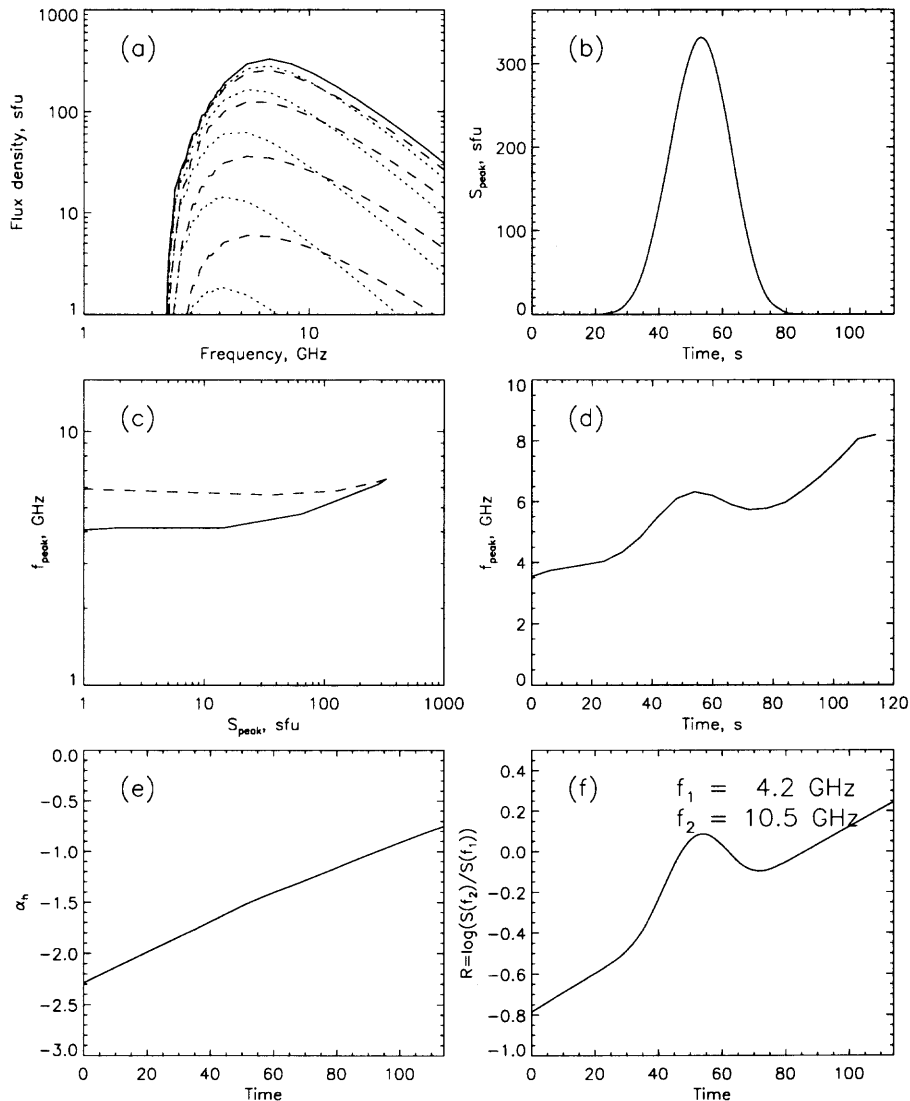


Figure 4.23 Spectral evolution of GS emission in the presence of high density plasma and electron spectral hardening, $\delta = 4.0 - (t - t_{max})/t_{max}$. The other parameters are the same as in Figure 4.20. The increase and decrease of f_{peak} and R in the main part of the emission peak is due to GS self-absorption. A new increase of the peak frequency and the flux ratio with time is clearly seen on the decay phase when the source becomes optically thin at low frequencies and the Razin suppression becomes dominant in defining the spectral peak.

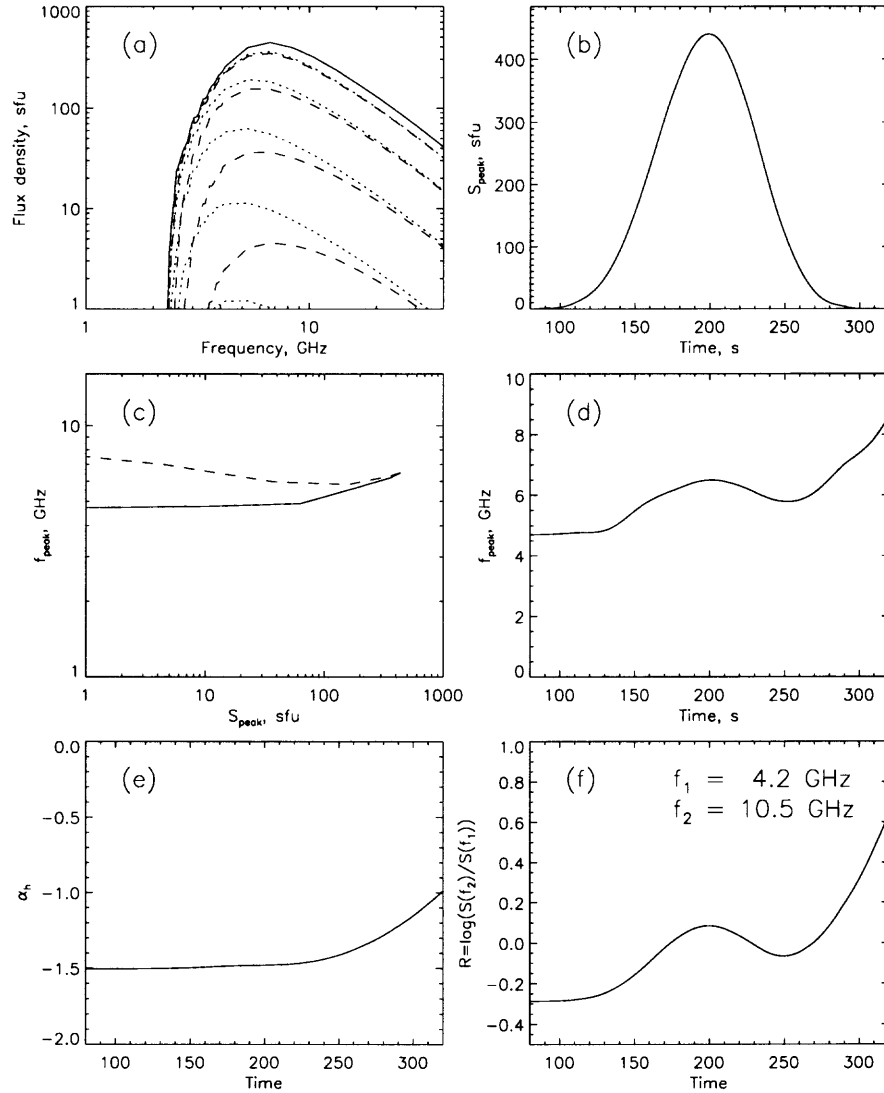


Figure 4.24 Spectral evolution of GS emission in the case of plasma density increase on the decay phase: $n(t) = n_0[1 + 2(t - t_m)^2/t_m^2]$, where $n_0 = 5 \times 10^{10} \text{ cm}^{-3}$, $t_m = 200$ s. The other parameters are the same as in Figure 4.20, except $\phi = 20''$. The increase of f_{peak} , R and α_h on the late decay phase is completely due to the influence of high plasma density (Razin effect).

4.5 Conclusion

Dynamical changes in the peak frequency of the GS spectrum of intense microwave bursts have been analyzed using data on more than 300 bursts obtained in 2001-2002 with OVSA. We find that the dynamical changes show a few distinct behaviors, which we have interpreted in terms of two competing effects: a) GS self-absorption and b) Razin suppression.

Observationally, we find that for a majority of simple bursts the peak frequency is very well correlated with the intensity of microwave bursts, at least near the burst maximum. The peak frequency increases on the rise phase in $\sim 84\%$ of bursts in our sample, and decreases on the decay phase in $\sim 64\%$ of bursts, in qualitative agreement with GS self-absorption as the origin of the low frequency turnover of the spectrum. For some bursts of this type, however, we find a faster than expected decrease of f_{peak} on the decay phase. This behavior is correlated with flattening of the high-frequency slope (increasing α_h) of the microwave spectrum, which is indicative of hardening of the electron energy distribution. The presence in many bursts of a positive or negative time difference between the maxima of f_{peak} and S_{peak} time profiles is also shown to be due to GS self-absorption under evolution (usually hardening but sometimes softening) of the electron spectral index.

However, we also find that for $\sim 30\text{-}36\%$ of bursts the peak frequency increase near the burst maximum is much smaller than expected or even may be entirely absent. Typically in these bursts f_{peak} starts at a rather high frequency in the very beginning of the burst and remains almost constant during a considerable (factor of ~ 10) increase and decrease of the burst intensity. We explain this temporal behavior as follows: In the beginning of the rise phase and during the late decay phase the radio source is optically thin at low frequencies due to the Razin effect. But briefly, near the maximum, when the column density of nonthermal particles becomes high enough, the source becomes nearly optically thick at $f \leq f_{peak}$, despite of the Razin

suppression, and the spectral evolution of f_{peak} takes on the characteristics for GS self-absorption.

About 70% of bursts show a gradual increase in f_{peak} starting at some point in the decay phase. We show that this behavior can easily be explained by Razin suppression together with either hardening of the high energy electron spectrum or an increase in Razin parameter (due to an increase in plasma density or a decrease in magnetic field strength in the microwave source). Again, the evidence for electron spectral hardening comes directly from the observed flattening of the microwave high frequency spectral slope. An increase in f_{peak} in the late phase that is unaccompanied by microwave spectral flattening may thus be a direct signature of chromospheric evaporation and/or evolution of the source to greater heights where the magnetic field strength is lower.

Using numerical calculations from GS theory, including the effect of the medium, we have confirmed that the wide range of evolutionary behavior can be interpreted as an interplay between GS self-absorption and Razin suppression. In Figure 4.25 we show a schematic representation summarizing our theoretical predictions. The time profiles of f_{peak} are shown in each panel for three cases: 1) GS self-absorption is dominant throughout the burst (solid lines), 2) Razin suppression is dominant in the beginning and end of the burst, while GS self-absorption is important near the burst maximum (dot-dashed lines), 3) the Razin suppression is dominant throughout the burst (dashed lines). These three cases correspond to increasing values of parameter $Y = f_p/f_B$ from very low to moderate to high. Fig. 4.25a shows the case when other parameters are held constant; Fig. 4.25b for the case of continuous hardening of the electron spectrum, which can be recognized from the evolution of α_h ; and Fig. 4.25c for the case when the electron spectrum is stable but the parameter $Y = f_p/f_B$ increases on the decay phase of the burst.

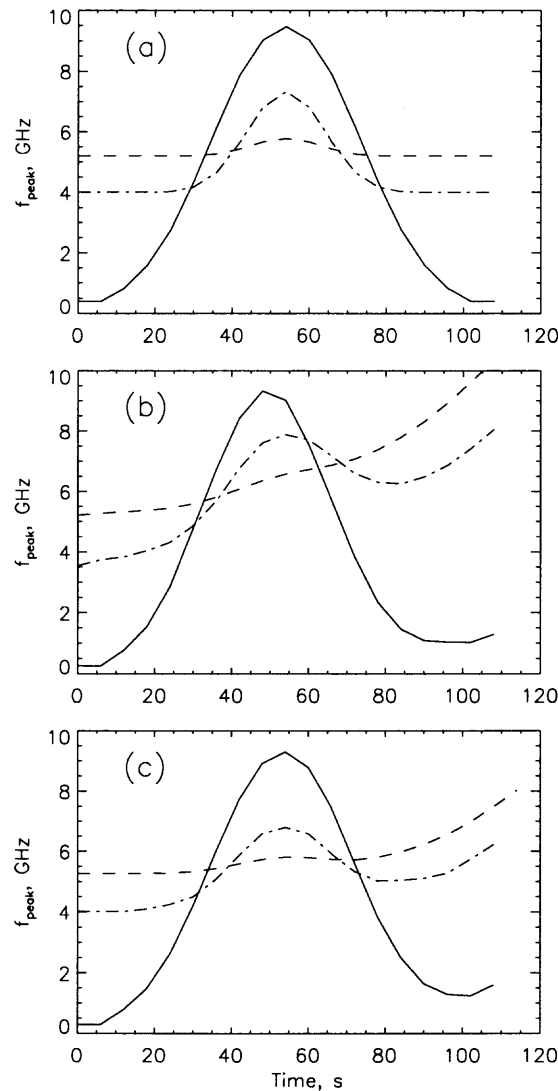


Figure 4.25 Schematic representation of characteristic time profiles of the peak frequency expected from GS theory. The three curves in each panel are (solid line) self-absorption dominant throughout a burst, (dot-dashed line) Razin suppression dominant in the beginning and end of a burst, but self-absorption important near the burst maximum, and (dashed line) Razin suppression dominant throughout a burst. The panels show three cases: *a*) electron spectral index is constant, *b*) continuous hardening of the electron spectrum, *c*) stable electron index but Razin suppression (as expressed by $Y = f_p/f_B$) increases on the decay phase.

Applying these theoretical predictions to our observational findings, we can say that Razin suppression plays an important role in the spectral dynamics of more than 70% of bursts, at least on their decay phase. For the Razin effect to be important for a relatively large number of bursts (with average $f_{peak} \sim 6$ GHz), we require that the magnetic field in the source be relatively weak (100-300 G for a corresponding plasma density $(1 - 10) \times 10^{10} \text{ cm}^{-3}$) (see Figure 4.21). Now that we have shown how to recognize the presence of Razin suppression from the dynamical changes in f_{peak} and R during a burst, the changes in f_{peak} can be used quantitatively as a further constraint on the evolution of plasma parameters, especially ambient density and magnetic field strength. Together, the combination of spectral measures (1) temporal evolution of f_{peak} , (2) R , the logarithm of the ratio of flux densities above and below f_{peak} , and (3) the high-frequency slope α_h , relative to the flux density at spectral maximum, S_{peak} provide a new, valuable diagnostic for microwave bursts of GS origin.

To be of greatest diagnostic power, the spectral dynamics should be measured in brightness temperature, i.e. using spatially resolved spectra. This requires simultaneous spatial and spectral resolution over a wide band of frequencies. The work of Belkora (1997) is the only published example that showed Razin suppression in a brightness temperature spectrum. Such observations will be possible routinely with a new generation radio facility, the Frequency Agile Solar Radiotelescope (FASR), now being designed. For more comprehensive application of these new diagnostics to flaring loops, such microwave data should be analyzed in combination with diagnostics from EUV, X-ray and gamma-ray data.

CHAPTER 5

NONTHERMAL ELECTRONS IN SOLAR FLARES DERIVED FROM MICROWAVE SPECTRA

5.1 Introduction

The energetics of nonthermal electrons in solar flares is one of the major interests in studies of particle acceleration. The observed hard X ray (HXR) flux is related to the energy deposition rate under the thick target bremsstrahlung model (Brown 1982), and when integrated over time yields the total energy content. Lin & Hudson (1971, 1976) analyzed HXR observations of the August 1972 series of large flares from ESRO TD-1 and OSO-7 spacecraft and estimated that the total energy in ≥ 20 keV electrons ranged from 1.5×10^{30} to 1.1×10^{32} ergs. Brown & Hoyng (1975) analyzed the large X-ray burst of 1972 August 4 and deduced that 3.5×10^{39} electrons were produced above 25 keV, with a total integrated energy of 2.0×10^{32} erg. Most recently, the X4.8 flare of 2002 July 23 has been carefully analyzed with the very high resolution spectra obtained with the NASA *Reuven Ramaty High Energy Solar Spectroscopic Imager (RHESSI)*. Lin et al. (2003) found the energy deposited by ≥ 10 keV electrons in the rise phase reached $\sim 4 \times 10^{32}$ ergs if interpreted as solely due to nonthermal electrons, while Holman et al. (2003) obtained a smaller estimate of $\sim 2 \times 10^{31}$ ergs when the presence of a hot thermal plasma was taken into account. Since these energies amount to a significant fraction of the total energy ($\geq 10^{32} - 10^{33}$ ergs) released in large solar flares, the acceleration of nonthermal electrons is seen to be energetically important (Lin & Hudson 1971, 1976). The large number of nonthermal electrons also places a strong constraint on theories of particle acceleration, because the inferred total number actually exceeds that of background thermal particles in a typical flare loop (Miller et al. 1997).

While the HXR flux gives the nonthermal energy deposition rate, microwaves provide the instantaneous number of nonthermal electrons producing gyrosyn-

chrotron emission, and thus radio observations play a complementary role to the HXR in diagnostics of nonthermal electrons. Gary (1985) analyzed 9 solar flares with microwave flux greater than 500 sfu as measured with the Berne radiometer at 3–35 GHz. The number of nonthermal electrons in these events ranged from 4×10^{33} to 1×10^{39} . When these numbers were compared with those deduced from HXR data from the Hard X-Ray Burst Spectrometer (HXRBS), they could be made to agree so long as sufficiently low magnetic field strengths were chosen. Lee, Gary & Zirin (1994) modelled magnetic loops to reproduce the microwave spectra from four X-class flares and deduced a total number of ≥ 10 keV electrons in the range $7 \times 10^{35} - 3 \times 10^{38}$. Although neither study gave the corresponding total energy, a rough estimate gives 6×10^{25} to 2×10^{31} ergs if we conservatively assume that the mean energy of individual electrons is ~ 10 keV. These microwave-based results suggest that the nonthermal electron energy may be distributed over a much wider range than previously found with HXR observations.

In several statistical studies of HXR and microwave data, it is common to present frequency distributions that bin the number of bursts according to measured parameters. As well documented in comprehensive studies, analysis of both HXR (Crosby, Aschwanden & Dennis 1993) and microwave (Nita et al. 2002) observations reveal that such frequency distributions commonly show a power law form with power-law index typically lying between -1.5 and -2.0 . In particular, Crosby, Aschwanden & Dennis (1993) showed that not only were the observed parameters of HXR fluxes and burst durations distributed in a power law, but that the total energy derived from them also forms a power-law distribution, but with somewhat lower index -1.53 . Their results were found to be consistent with both the stochastic exponential energy build up model (Rosner & Vaiana 1978) and the avalanche model under the principle of self-organized criticality (Lu et al. 1993). In the former case, the slope of the frequency distribution can tell the ratio of the energy build up time

to flare interval, while in the latter case, it may constrain the threshold for magnetic reconnection used in the simulation of avalanche models.

In this paper we derive statistics on total nonthermal electron numbers and integrated energy produced in solar flares, using microwave total power spectral data of a large number of bursts obtained with OVSA (Chapter 3). Such diagnostics require that we be able to distinguish optically thick and optically thin fluxes so that we can choose an observed flux that is appropriate for the derivation of the desired physical quantity under the gyrosynchrotron radiation mechanism. We utilize our unique spectral coverage, which allows us to use the directly measured peak frequency and the optically thin spectral slope in deriving the column density and the electron power-law index, respectively. We also utilize independent statistics of microwave source areas inferred from NoRH data, to complement the non-imaging spectral data from the above-mentioned OVSA database.

In §5.2 we give an overview of the OVSA data and outline the analysis strategy. In §5.3 we use NoRH data to give the statistical relationship between the flux density distribution and the brightness temperature distribution. In §5.4 we combine the OVSA and NoRH results to deduce the statistical distribution of physical parameters, and we discuss related issues in §5.5.

5.2 Data and Strategy

The main data set used in this study was obtained from the 412 flares observed with OVSA during 2001-2002. OVSA is a solar-dedicated interferometer array consisting of two 27-m dishes and four 2-m dishes, observing from 16:00-24:00 UT daily (Hurford, Read & Zirin 1984). Although the main purpose of the instrument is to provide interferometric data, in order to study such a large number of bursts we restrict ourselves to total power (integrated flux density) data without spatial resolution. Because of difficulties with the 27-m dishes due to various effects arising

from their restricted field of view, we further restrict our analysis to data from the 2-m antennas, which measure only total intensity (Stokes I). Details of the instrument, data calibration, and description of the dataset are given in Chapter 3.

One of the puzzling findings in Chapter 3 was that the cm radio emissions show an apparent frequency-dependent flux density limit that increases with the square of the frequency on a frequency-flux density plot, whereas the dm emissions (see Chapter 3) do not follow the behavior. On one hand, this characteristic has been used as a criterion for distinguishing the radiation mechanism. Namely the events with spectral maximum above 3 GHz and showing the frequency-dependent limit share similar spectral and temporal behaviors and are due to a common mechanism, gyrosynchrotron radiation. On the other hand, this finding also brings to our attention the implications of this frequency-dependent flux limit for the flare parameter distribution. We reproduce this result of Chapter 3 in a slightly different form in Figure 5.1, where the peak frequencies are plotted against peak flux scaled by ν^2 . It is obvious that the cm events do not cross the vertical limit (dotted line), which we empirically set at ~ 300 sfu/GHz². The dotted horizontal line represents the dm frequency limit of 2.6 GHz discussed further in Chapter 3. No event has been recorded in OVSA data whose peak flux density falls outside of these two empirical limits. We do not consider this frequency-independent limit in S_ν/ν^2 as an artifact, because no instrumental sensitivity threshold with such particular frequency dependence is known. We also note that the limit pertains only to the peak fluxes and peak frequencies. Fluxes of individual bursts can exceed this limit at some frequencies, but do not exceed it at their peak frequency.

As to why there should be such a limit in microwave flux, we propose a simple idea that S_ν/ν^2 is somehow related to a sort of maximum energy in nonthermal electrons that a solar flare can produce. According to the Rayleigh-Jeans law, the observed flux is given by the source solid angle, Ω , or its area, A and effective

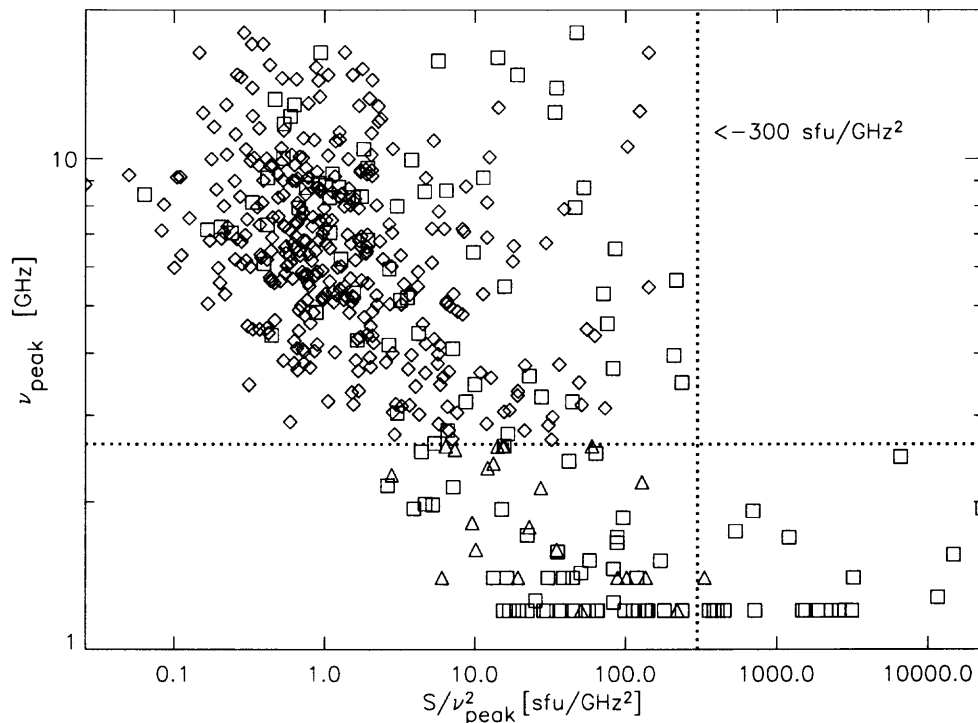


Figure 5.1 The distribution of peak flux density divided by the square of peak frequency. All cm bursts, (C-diamonds, CD-squares), and almost all D-type bursts (triangles), have the same limit of this ratio that we empirically set at ~ 300 sfu/GHz², represented by the dotted vertical line. The dotted horizontal line represents the dm frequency limit of 2.6 GHz. No event has been recorded in OVSA data above these two empirical limits. The lack of events in the left-down corner of the plot is just an artifact due to the 1 sfu frequency-independent sensitivity limit of OVSA.

temperature T_{eff} as:

$$\frac{S_\nu}{\nu^2} = \frac{2k}{c^2} T_{\text{eff}} \Omega = \frac{2k}{r^2 c^2} T_{\text{eff}} A \quad (5.1)$$

where k is the Boltzmann constant, c is the speed of light, and $r = 1$ AU is the distance from the source to the observer. The empirical limit we found now becomes a limit of the product of A and T_{eff} . Note that for optically thin emission T_{eff} should be replaced by the brightness temperature, $T_b = T_{\text{eff}}[1 - \exp(-\tau)]$, but since we are talking about upper limits, we tacitly assume that the emission is optically thick. Note that the quantity on the right hand side, aside from some constants, is $kT_{\text{eff}}A$, which has dimensions of energy per unit column density. We may even expect an association with the column density, because these quantities are measured at the peak frequency, which is mainly determined by the column density (see §5.4.2). In this sense, we may naively interpret S_ν/ν^2 as a quantity representing an energy content, and it may be presumed that the energy content per flare has a typical upper limit. It should be noted, however, that the limit in Figure 5.1 is empirical, not fundamental, and a rare event may occur that exceeds the limit.

Since the source area has an obvious practical upper limit, namely, the largest active region size, we tentatively estimate this limit from the maximum value of S_ν/ν^2 . For convenience, we introduce dimensionless parameters such as,

$$\nu_{10} = \frac{\nu}{10\text{GHz}}, \quad S_4 = \frac{S}{10^4\text{sfu}}, \quad T_9 = \frac{T_{\text{eff}}}{10^9\text{K}}$$

into (5.1), and then find that the angular source diameter, $D = 2\sqrt{\Omega/\pi}$, will be expressed as

$$D = 0.7' \frac{1}{\nu_{10}} \sqrt{\frac{S_4}{T_9}}. \quad (5.2)$$

The empirical limit we found implies a limit of the radio source size scaled by the effective temperature:

$$D\sqrt{T_9}\Big|_{\text{max}} \simeq 1.2'. \quad (5.3)$$

This result suggests that in the case of an effective temperature of 10^9K , a reasonable temperature for gyrosynchrotron emission (Dulk & Marsh 1982), the associated source size becomes $1.2'$, which is also a reasonable value compared with the typical size of an active region. A one order of magnitude smaller effective temperature would require a larger source size by a factor of about 3 in order to maintain the same limit. For comparison, we examined the list of flares observed by the Nobeyama Radioheliograph (NoRH) and found that their largest reported source size at 17 GHz is $1.37'$. We use the NoRH results further in the next section.

Although the above assumption of the constant effective temperature provides a means for simple estimate for the limiting source size, we should more realistically consider the variations of A and T_{eff} from flare to flare. Under gyrosynchrotron emission, T_{eff} is a complicated function of the nonthermal electron distribution and the magnetic field strength, and is frequency dependent (Ramaty 1969). In the optically thick regime, T_{eff} is related to the mean energy of the nonthermal electrons, alternatively called effective temperature by Dulk & Marsh (1982), and using the optically thick microwave spectrum we can explore the corresponding electron energy and magnetic field. In the optically-thin regime, we must instead consider the brightness temperature T_b , which is determined by the total emissivity and cannot be identified with a mean temperature. The optically thin spectral slope, however, becomes important in the optically thin regime, and can be directly related to the electron distribution in phase space (Dulk & Marsh 1982).

The strategy adopted in this paper is as follows: (1) The electrons are assumed to have an isotropic pitch angle distribution and a single power law energy distribution. Thus, the spectral slope at optically thin frequencies can be used to directly determine the electron power law index without other assumptions. (2) We make use of NoRH data in the next section, which provides flux density, area, and brightness temperature through imaging observations, to determine an empirical relationship

between brightness temperature and flux density, which we assume to be statistically valid for flares in general. We then apply the empirical relationship to the OVSA dataset in order to separate T_b from the observed S_ν . (3) Knowing the brightness temperature and the electron power-law index, we can statistically determine the magnetic field. We thus obtain the statistical distributions of the entire set of parameters involved with gyrosynchrotron radiation.

5.3 The Relationship between Flux and Brightness Temperature Inferred from NoRH Data

We use the flare list obtained with the NoRH, which at the time contained 383 flares with peak fluxes at 17 GHz above 10 sfu, observed by NoRH since 1992. The flare list gives flux densities, source sizes as a ratio of flare area to beam area, and equivalent brightness temperatures. To convert the area ratio to area, we assumed a beam size of 20'' at 17 GHz.

Although the database provides such quantities as the flux density, brightness temperature and area for events observed at 17 or 34 GHz, it is, however, not as simple as finding the statistical correlation between any two desired quantities. While the quantity presented in Figure 5.1 is the spectrally determined peak flux density (i.e. at optical depth $\tau \simeq 1$), the 17 and 34 GHz fluxes in NoRH data are in many cases due to optically thin radiation. As we noted earlier, the optically thin T_b is highly sensitive to frequency and its magnitude does not imply a mean energy. On the other hand the area of the optically thin source is independent of frequency, so the diagnostics are valid even though the burst may consist of multiple sources and may be inhomogeneous to some extent. For this reason we use the NoRH data to define the distribution of source size A vs. S_ν and take the peak T_b as a quantity to be derived.

We look for power law relationships among the three relevant quantities in Equation (5.1):

$$y \equiv \frac{S_\nu}{\nu^2}, \quad A \sim y^\alpha, \quad T \sim y^{1-\alpha}. \quad (5.4)$$

Thus we want to determine the value of α , which can be determined in the case of the NoRH database by simply correlating the flux density and the area listed in that database. However, in order to apply it to the OVSA dataset, we must first check for consistency between the two.

We postulate that the flux density, area, and brightness temperature all separately follow power law distributions and define the distribution functions of these quantities as

$$\Phi_y(y) \sim y^{-\gamma}, \quad \phi_A(A) \sim A^{-\beta}, \quad \psi_T(T) \sim T^{-l}, \quad (5.5)$$

respectively, where γ , β , and l are completely general indexes to be related to α . From the conservation of total numbers, using equations 5.4 and 5.5 we get

$$\phi_A(A) = \left(\frac{dy}{dA} \right) \Phi_y(y) \sim A^{-(1+\frac{\gamma-1}{\alpha})} \quad (5.6)$$

and

$$\psi_T(T) = \left(\frac{dy}{dT} \right) \Phi_y(y) \sim T^{-\frac{\gamma-\alpha}{1-\alpha}}. \quad (5.7)$$

Comparing Equations (5.5)–(5.7), we get the following relations for the indexes:

$$\alpha = (\gamma - 1)/(\beta - 1) \quad \text{and} \quad l = (\gamma - \alpha)/(1 - \alpha). \quad (5.8)$$

These relations allow us to compute two of the above indexes, given the other two. One of the indexes, γ can be obtained directly from the OVSA dataset by fitting a power law to the number distribution versus $S_{\text{peak}}/\nu_{\text{peak}}^2$, as shown in Figure 5.2. From the figure we see that the flux distribution is indeed fit well with a single power law, of index $\gamma = 1.56 \pm 0.04$. However, at least one other index is needed, and for that we require spatially resolved observations.

It is straight-forward to check that the NoRH database of 383 flares with peak fluxes at 17 GHz above 10 sfu agrees with this distribution. Figure 5.3a displays the $S_{\text{peak}}/\nu_{\text{peak}}^2$ distribution of this data set. Although all observations were at a single, generally optically thin frequency, 17 GHz, rather than the spectral peak frequency as for the OVSA data, nevertheless the power-law index of the distribution, 1.63 ± 0.07 is in excellent agreement with the OVSA value.

We also estimate the power-law index of the source size distribution, available from the same NoRH dataset. Although this dataset gives the distribution of the source sizes at 17 GHz, we assume that only the normalization constant, not the slope itself, may be affected by this restriction. This is reasonable because, as we mentioned earlier, the source size becomes independent of frequency for optically thin emission. From Figure 5.3b we estimate that the power-law index of the source size distribution is $\beta = 2.57 \pm 0.23$. Inserting these values into equation 5.8, we get $\alpha = 0.40 \pm 0.07$ and $l = 2.04 \pm 0.22$. To test the consistency of our assumptions, we plot in 5.3c the observed distribution of NoRH brightness temperatures. The power-law index of the observed distribution, 1.65 ± 0.09 , agrees with the derived value $l = 2.04 \pm 0.22$ within about 2σ . Figure 5.3d provides a direct estimate of the power law index of the area- $S_{\text{peak}}/\nu_{\text{peak}}^2$ dependence. The measured value, 0.32 ± 0.2 , although it has a large uncertainty due to the scatter of the data points, is consistent with $\alpha = 0.40 \pm 0.07$ that we derived above. We conclude that it is statistically valid to consider the distribution of bursts versus flux density as a product of two other power law distributions of source area A and effective temperature T_{eff} . We therefore take the area and temperature distributions according to Equation (5.4) to be

$$A \sim \left(\frac{S_{\nu}}{\nu^2}\right)^{0.4}, \quad T \sim \left(\frac{S_{\nu}}{\nu^2}\right)^{0.6}. \quad (5.9)$$

5.4 Analysis of the OVSA Data

In this section we use the statistical relationship between flux and effective temperature given in Equation (5.9) to derive parameters of flare electrons such as the power law index of the energy distribution, the total number, and total energy of nonthermal electrons. We have already selected only events that are likely due to gyrosynchrotron emission. For convenience, we use Dulk & Marsh's (1982) simplified expressions for gyrosynchrotron radiation from electrons above 10 keV with isotropic pitch angles, with energy distribution

$$n(E) = N(\delta - 1)E_0^{\delta-1} E^{-\delta}. \quad (5.10)$$

Dulk & Marsh (1982) give simplified expressions for nonthermal gyrosynchrotron radiation for the x -mode and for $2 \leq \delta \leq 7$, $\theta \geq 20^\circ$ and $\nu/\nu_B \geq 10$ where the cyclotron frequency $\nu_B = 2.8 \times 10^6 B$ is in Hz, magnetic field B is in gauss, and N is the electron number per unit volume in cm^{-3} . Within the range of validity of the Dulk & Marsh formulae, we will determine the statistical distribution of *the total number and the corresponding total energy* of nonthermal electrons in the solar bursts in our sample.

5.4.1 Electron Power-law Index

The electron power law-index δ can be directly determined from the observed spectral index of gyrosynchrotron radiation, since the spectral index of the optically thin microwave radiation is determined by the emissivity, η_ν . According to the Dulk & Marsh (1982) simplified expression, the microwave emissivity is given by

$$S_\nu^{\text{thin}} \sim \eta_\nu \sim \nu^{1.22-0.90\delta}. \quad (5.11)$$

We can thus determine the electron power-law index δ from the measured optically thin spectral index q by $\delta = (q + 1.22)/0.9$ without any further assumption.

In Figure 5.4 we plot the resulting distribution of the electron power-law index for three groups of microwave bursts. In the left panel, the groups are divided

according to the peak flux density. The darker gray, medium gray, and lighter gray areas show all data with $10 \leq S_{\nu}^{\text{peak}} \leq 300$ sfu, $300 \leq S_{\nu}^{\text{peak}} \leq 3000$ sfu, and ≥ 3000 sfu, respectively. The maximum population is found near $\delta \approx 4.0$ with a trend that weaker events show a wider distribution extending to higher index and stronger events show a more confined and harder distribution at $2 < \delta < 4$. The trend of stronger events having harder index is more obvious when we plot the distributions in groups divided according to the scaled flux, y , as shown in the right panel of Figure 5.4. The scaled flux plot is especially significant since by dividing the flux density by ν^2 we remove most of the frequency dependence of the distribution, as shown in Fig.5.1. Hence, the tendency for stronger events to have a harder spectrum is independent of the tendency of stronger events to have a high peak frequency. Note that the result shown in Figure 5.4 has also been seen in studies of HXR spectral index. Dennis (1985) shows that the distribution of HXR spectral index at a given peak count rate also gets narrower with increasing count rate with a trend toward harder X-ray spectrum at higher total count rate.

From this point on, we restrict our investigation to events with $y > 0.5$, which are those obeying the power-law distribution in Fig.5.2. We exclude the events with $\delta \leq 2$ for which the mean energy diverges (see below, eq.[14]), and further limit ourselves to events with $\delta < 6$ to ensure that we do not include events that may be thermal in nature. Originally we start with 770 bursts (temporal components) from 412 flares, and after applying these criteria the final dataset contains 588 bursts.

5.4.2 Total Number and Total Energy

To determine the total number or energy, we must separate the contributions of brightness temperature and area to the observed peak flux and peak frequency. For this, our analysis will rely on our earlier result that, statistically, there is a power law relationship between the flux and T_{eff} and the flux and area, so that we can separate

these two contributions. Although such a relationship may not apply to individual events, we expect that it can serve as a means to derive statistical properties. Based on the result given in the previous section, we assume

$$T_{\text{B,peak}} = 7 \times 10^8 \text{K} \left(\frac{S_{4,\text{peak}}}{\nu_{10,\text{peak}}^2} \right)^{0.60}. \quad (5.12)$$

This *assumed* brightness temperature is then compared with theoretical effective temperature (the brightness temperature in the optically thick regime), which is given by Dulk & Marsh (1982) as

$$T_{\text{eff}} \approx 2.2 \times 10^9 10^{-0.31\delta} |\sin \theta|^{-0.36-0.06\delta} \left(\frac{\nu}{\nu_B} \right)^{0.50+0.085\delta}. \quad (5.13)$$

By equating (5.13) with (5.12), we obtain the magnetic field B . The viewing angle θ is another unknown, but we use quantities averaged over the range 20° – 70° centered on 45° . Our justification is that optically thick microwaves are emitted from electrons occupying an entire flaring loop, in which case the magnetic field vector spans a wide range of viewing angle.

Finally, we make use of the peak frequency, which is largely determined by the column density NL along the line of sight. Dulk & Marsh (1982) give a simplified expression for the peak frequency as

$$\nu_{\text{peak}} \approx 2.72 \times 10^3 10^{0.27\delta} |\sin \theta|^{0.41+0.03\delta} B^{0.68+0.03\delta} (NL)^{0.32-0.03\delta}. \quad (5.14)$$

We derive NL from this equation using the measured ν_{peak} and the above-determined magnetic field B . We then combine NL with the source area $\Omega = A/1\text{AU}^2$ determined by using (5.13) in (5.1), to obtain the total number of nonthermal electrons $N_{\text{tot}} = (NL)A$.

We plot the frequency distribution of bursts versus N_{tot} in Figure 5.5*a, b*. Fig.5.5*a* shows the distribution of N_{tot} for a cutoff energy of 10 keV, which obeys a power law over the range from $\sim 10^{33}$ to $\sim 6 \times 10^{42}$ electrons, with index -1.15 ± 0.02 . Fig.5.5*a* is the result for a cutoff energy of 100 keV, mainly to see the effect of the

low energy bound on the nonthermal energy content. In the latter case, the N_{tot} distribution is a steeper power law with index -1.23 ± 0.02 , reaching a maximum of $\sim 3 \times 10^{38}$. The slope changes only a little with an order of magnitude change of E_0 .

The total energy of the nonthermal electrons may then be determined by multiplying the number N_{tot} by the mean energy $\langle E \rangle$ of the distribution:

$$E_{\text{tot}} \equiv N_{\text{tot}} \langle E \rangle. \quad (5.15)$$

Since we assume a power law electron energy distribution, the mean energy of individual electrons is defined as:

$$\langle E \rangle = \frac{\int_{E_0}^{\infty} E n(E) dE}{\int_{E_0}^{\infty} n(E) dE} = \frac{\delta - 1}{\delta - 2} E_0 \quad (5.16)$$

where E_0 is the low cutoff energy. Because of the power-law nature, the mean energy $\langle E \rangle$ from all flares with $2 < \delta < 6$ are closely clustered near E_0 . Thus the distribution of total energy, despite its nominal dependence on δ , is largely determined by variations in N_{tot} from flare to flare.

Figure 5.5*c, d* show the frequency distribution of bursts versus total energy of nonthermal electrons again for the two values of E_0 . Again the distributions follow a power law, with nearly identical slopes as for the N_{tot} distributions. For $E_0 = 10$ keV (Fig.5.5*c*), the index is -1.18 ± 0.026 over energies from $\sim 10^{25}$ erg to $\sim 10^{33}$ erg. For $E_0 = 100$ keV (Fig.5.5*d*), the distribution reaches a maximum of 3×10^{31} erg with index -1.24 ± 0.02 .

In comparison, Crosby et al. (1993) showed that total energies in electrons above 25 keV as derived from HXR data show a power law index -1.53 ± 0.02 within the range: 10^{28} erg $\lesssim E_{\text{tot}} \lesssim 10^{32}$ erg. Our result, when converted to $E_0 = 25$ keV, is a rather flatter power law with index -1.21 ± 0.02 within the range: 10^{23} erg $\lesssim E_{\text{tot}} \lesssim 10^{33}$ erg. Our microwave-based energy range is therefore similar to their HXR-based range. Especially, the upper limit of the energy distribution agrees within an order of magnitude ($E_{\text{tot}}^{\mu} \lesssim 10^{33}$ erg vs. $E_{\text{tot}}^X \lesssim 10^{32}$ erg). However, we note

a some distinctions: The microwave-derived distribution is less steep ($\Gamma_\mu \approx -1.21$ vs. $\Gamma_X \approx -1.53$), and extends to much lower limit ($E_{\text{tot}}^\mu \gtrsim 10^{25}$ erg vs. $E_{\text{tot}}^X \gtrsim 10^{28}$ erg). The latter could be due to the greater sensitivity of microwave observations to nonthermal electrons compared to HXR observations. Our distributions shown in Figure 5.5 may include weaker events ($\lesssim 10^{29}$ ergs) that were not detected in previous HXR observations. The origin of the differing power law index is not clear and requires more study. As a preliminary speculation, we consider that it may result from an intrinsic difference between HXR and microwave emitting electrons (i.e., precipitating vs. trapped populations, respectively, Lee 2003). It may also be affected by the greater sensitivity of the microwaves to weaker events.

5.4.3 Derived Total Energy vs. Directly Measured Parameters

In Figure 5.6 we correlate the derived total energy with the directly observed parameters: the spectral index, peak frequency and peak flux, in order to know which parameter is best correlated with the energy content of nonthermal electrons. We plot the data points as dots, again for the two cases $E_0 = 10$ keV (top panels) and $E_0 = 100$ keV (bottom panels). The line in each panel represents a linear fit to the data, and the number written in the upper part of each panel is the slope of the fit.

In the upper row, first panel, we see a trend that the derived total energy has some correlation with δ in the sense that a softer event has a higher total energy. This is because softer events have electrons mostly confined to low energies, say 10–100 keV, that dominate the total energy content. When a higher cutoff energy is used (lower row, first panel), the correlation with δ nearly disappears. Since the microwaves come mainly from higher energy electrons, we conclude that statistically there is no particular value of δ preferred during flare acceleration.

The second column shows the correlation between the total energy and the peak frequency of the microwave spectrum. The peak frequency generally increases with the column density of nonthermal electrons and magnetic field strength. The absence of good correlation in the second columns, independent of E_0 , implies that both the column density and magnetic field strength may not be an important factor in governing the total nonthermal energy produced in solar flares.

Finally, in the third column, we find a good correlation of the derived total energy with the scaled peak flux density, $y = S_\nu/\nu^2$, as shown. As we raise E_0 to higher values, the correlation becomes even stronger. In the lower row, third panel, we find that E_{tot} integrated above 100 keV is well approximated by $(24.29 \pm 0.05)y^{2.69 \pm 0.06}$ ergs.

To keep our interpretation of the scaled flux (§5.2), it is likely that the strength of a flare is not simply a matter of efficiency of particle acceleration per volume, but how wide area the particle acceleration takes place is also important.

5.5 Discussion

5.5.1 Our Diagnostic Procedure

One of key assumptions used in this microwave study is that the peak brightness temperature has a power-law relationship with the scaled flux, $y = S_\nu/\nu^2$ (Eq. [5.12]). We needed this assumption in order to determine the statistical distribution of area and magnetic field, which in turn are needed together with the observed peak frequency of the microwave spectrum in order to estimate the number and energy of electrons producing the gyrosynchrotron emission. We adapted an empirical relationship found from NoRH data for this purpose. We emphasize that the findings in this paper pertain to statistical properties of events, and are not necessarily followed by individual events. The derived relations are $T_{\text{eff}} \sim (S_\nu/\nu^2)^{0.6}$

and $A \sim (S_\nu/\nu^2)^{0.4}$, which are statistically valid for events with $y > 0.5$, where the distribution (Fig.5.2) is well approximated by a power law.

Another important assumption is that the observed gyrosynchrotron emission is entirely due to nonthermal electrons in a single power-law energy distribution, specified by index δ , that extends from a low energy cutoff up to infinite energy. Such a distribution allows the simplified expressions for nonthermal gyrosynchrotron radiation by Dulk & Marsh (1982) to be employed, and so makes possible a statistical study of our large database of 588 burst components. Compared to the more general case of a double power-law energy distribution (e.g., Dulk, Kiplinger, & Winglee 1992), our approach will yield a result that corresponds typically to the higher-energy slope above the break. A more serious shortcoming is the case where thermal and nonthermal populations may coexist. This issue has been explored with hard X ray observations by Holman & Benka (1992), who pointed out the number of electrons required to reproduce a given radiation could be overestimated if the thermal component is not counted. Most recently, the energy of nonthermal electrons estimated for the rise phase of the 2002 July 23 flare differs by a factor of ~ 20 depending on whether the thermal component is assumed to exist Holman et al. (2003) or not (Lin et al. 2003). To avoid or reduce this ambiguity associated with the thermal population, we have confined our investigation to the events with $2 < \delta < 6$, namely the events that can more obviously be identified with nonthermal gyrosynchrotron spectrum.

5.5.2 Upper Limit in the Nonthermal Energy Distribution

The present result for the upper limit in the distribution of total energy ($\sim 10^{33}$ ergs for $E_0 = 25$ keV) is within an order of magnitude the previously known energy from HXR: $\sim 10^{32}$ erg above 25 keV for the 1972 August series flares (Lin & Hudson 1971, 1976) or $\sim 4 \times 10^{32}$ erg for the 2002 July 23 flare (Lin et al. 2003). This is somewhat

contrary to our expectation that the energy from HXR diagnostics is obtained by integrating the observed flux over the flare duration, and would thus be higher than inferred from our microwave diagnostic, which pertains to the instantaneous energy at the peak time. By chance, we might have both results comparable to each other if a flare is so impulsive that the energy deposition rate is mostly confined to the peak time. Another simple resolution can be argued based on the fact that microwaves represent electrons trapped in the corona while HXRs are due to the precipitating electrons. The numbers can differ by a finite ratio depending on the mirror ratio and pitch angles (see, for a review, Lee 2003). Suppose that 10% of the accelerated electrons precipitate into the chromosphere to emit thick target bremsstrahlung at the footpoints while the other 90% remain in the corona to emit microwaves. The factor of ten difference could then be explained. However, our results are based on a number of assumptions that, while statistically justified for the population as a whole, may become suspect when extrapolated to the largest events. Therefore, the discrepancy in numbers and energy may not be significant. To improve the comparison, we will need spatially resolved observations with measured brightness temperatures. A more careful analysis may also be needed that takes into account the acceleration and loss time scales (Lin & Hudson 1971) or conversion of the microwave flux to nonthermal energy production rate (Gary 1985).

5.5.3 Statistical Properties of Flare Parameters

The total nonthermal energy that we derived in the present study obeys a power law with index ~ -1.2 , which is considerably flatter than the corresponding result (~ -1.53) obtained with the HXRBS/SMM data (Crosby et al. 1993). We do not have a clear explanation for the difference, also it may be due in part to the differences in the ratio of the trapped electrons to the precipitating electrons discussed above, so that the microwave diagnostic may systematically extend the distribution to

higher energies, leading to a shallower slope. Alternatively, the difference may have something to do with the weighting of the microwaves to electrons of higher energies than for the HXR emission. However, we consider our power law measurement to be robust, in the sense that the law holds over a wide energy range, and only weakly depends on the low energy bound E_0 .

We note, however, that a power-law index near -1.8 is found for directly observed microwave fluxes. At radio wavelengths, monochromatic flux at a fixed frequency (Akabane 1956) or the maximum flux distribution at the peak frequency (Chapter 3) shows such a power law index around -1.7 , and the scaled flux, S_ν/ν^2 , in the present study shows a power-law index around -1.6 . A series of flare parameter studies based on the same HXR data set (HXRBS/SMM) presented slightly differing slopes depending on the selection criterion (Crosby et al. 1993). Also a relatively low slope was found for a derived quantity such as total energy in HXR emitting electrons, which is derived after multiplication of energy deposition rate and duration, each of which has its own distribution. In the present case, the mean energy and area showed much steeper distributions with index -3.6 ± 0.34 and -2.57 ± 0.23 , respectively. Presumably the (much steeper) distributions of these auxiliary parameters such as mean energy and area play a role in shaping the resulting distribution of total electron energy. Therefore, a more careful determination of these parameters could be important to establish the universality of the power-law distribution of major flare parameters (cf. Wheatland & Sturrock 1996).

5.5.4 Electron Acceleration

We finally discuss our result for the electron power-law index δ as a potentially important issue in electron acceleration. We found that the strong events ($y > 30$) tend to show a hard spectrum with a relatively narrow range of δ , whereas weaker events ($y < 3$) appear in a much wider range (Fig.5.4). There are, in fact, a few

HXR studies that presented HXR spectral index distributions consistent with this result. On the other hand, our finally derived total energy (integrated above 100 keV) shows no good correlation with δ (Fig.5.6). The latter is a result confining our investigation to moderately harder events $2 < \delta < 6$ in which case the numbers of strong ($y > 30$), moderate ($y < 30$) and weak ($y < 3$) events distribute more uniformly with δ . Contrary to our naive speculation that softer events would have less nonthermal energy, **they** can have a large total number of electrons within a relatively low energy range (say 10–100 keV) and, as a result, can have a total energy as large as another event with harder, but fewer electrons. With the present result alone, there seems to be no preferred value of δ for strong flares in terms of total nonthermal electrons.

We briefly compare this result to the stochastic electron acceleration model by Hamilton & Petrosian (1991) which predicts a detailed shape of the electron energy distribution in phase space, $n(E)$ in our notation. The model shows that $n(E)$ at the peak time is not necessarily in single power law, although under our assumption we nevertheless approximate it as one. But we can at least expect that this acceleration mechanism can produce δ in the wide range that we find, with no apparent effect on the total energy content. We repeat that δ inferred from HXR and microwaves may represent properties of $n(E)$ in differing energy ranges. Because the electron distribution at relatively low energies (10–100 keV) tends to be strongly influenced by Coulomb collisions whereas at high energies ($\gtrsim 200$ keV) it is largely determined by the accelerator, our result from microwaves may better reflect the accelerator properties. In that case, our result that E_{tot} is insensitive to δ could be a property associated with the acceleration process.

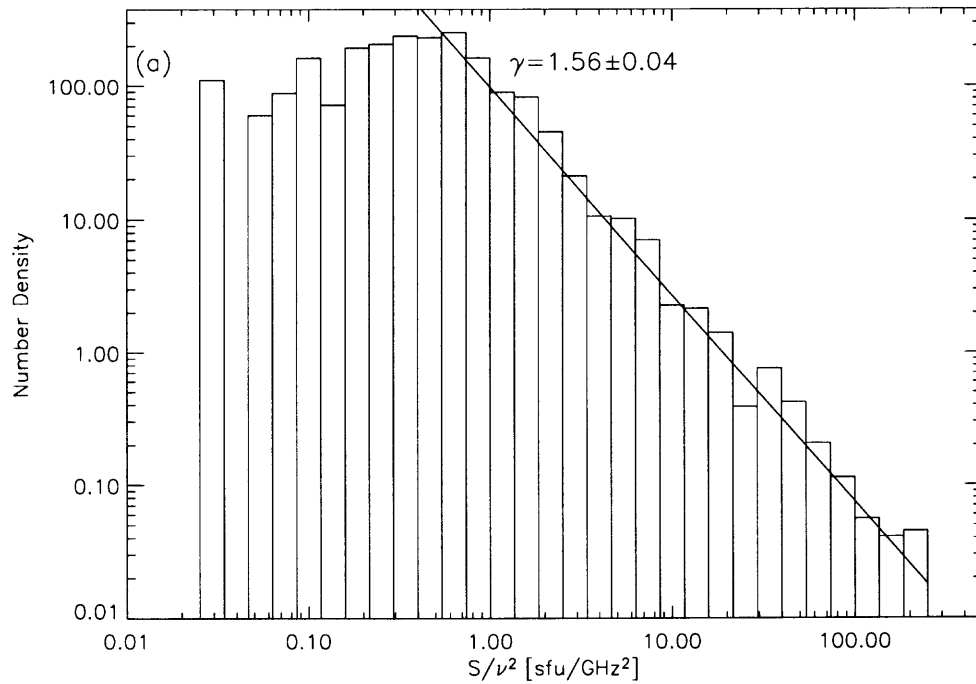


Figure 5.2 The S_{peak}/ν_{peak}^2 distribution from OVSA data above 2.6 GHz. The power-law index of this distribution is 1.56 ± 0.04 the same as, within the statistical limits, the one derived from NoRH observations at a single frequency.

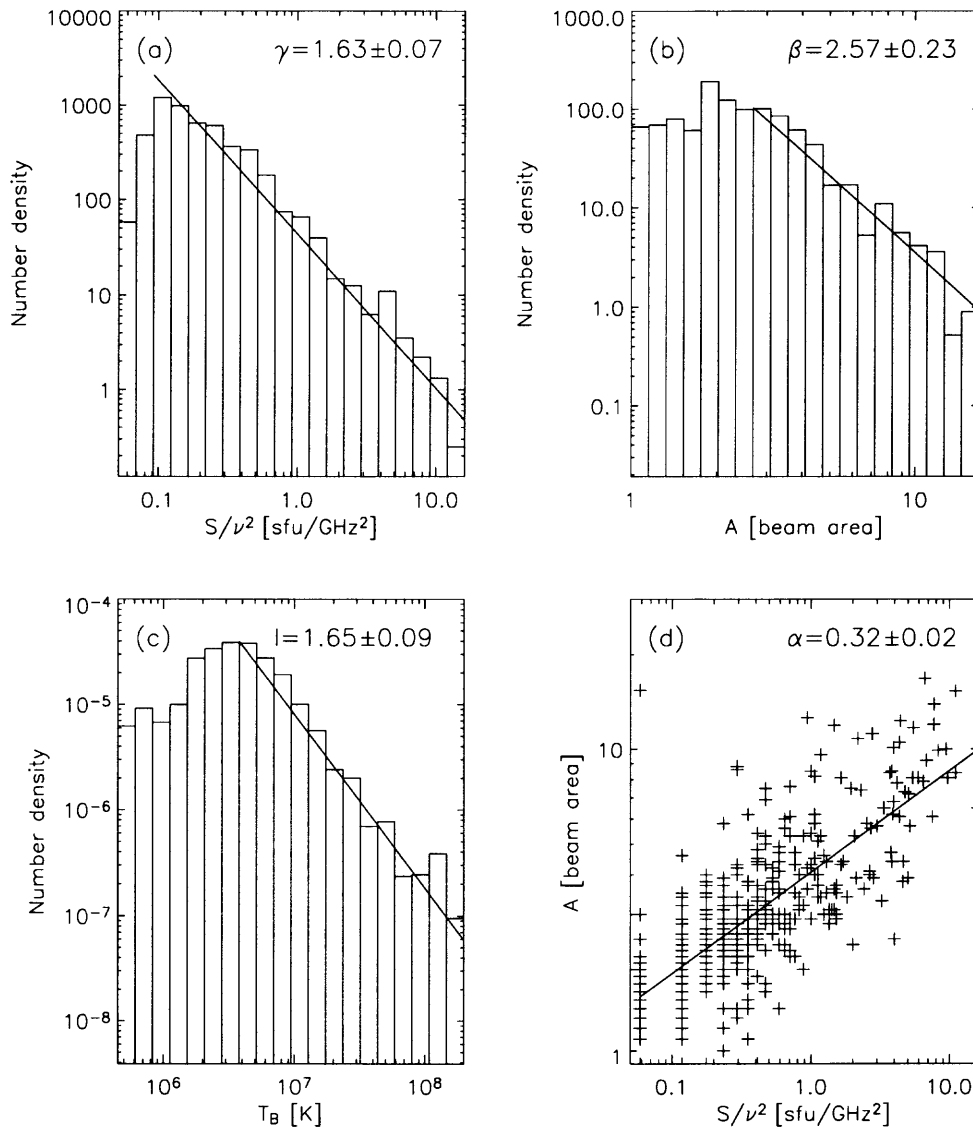


Figure 5.3 (a) The S_{peak}/ν_{peak}^2 distribution from NoRH data at 17 GHz. A power-law index of 1.63 ± 0.07 is found. (b) Source area distribution from NoRH. Area is expressed in units of NoRH beam area, which is about $20''$ at 17 GHz. The tail of the distribution obeys a power-law with an index of 2.57 ± 0.23 . (c) Brightness temperature distribution from NoRH. The power-law index of this distribution is 1.65 ± 0.09 . (d) The correlation plot of source area and S_{peak}/ν_{peak}^2 at 17 GHz from NoRH data. The distribution is best fitted by a power-law with an index of 0.32 ± 0.02 .

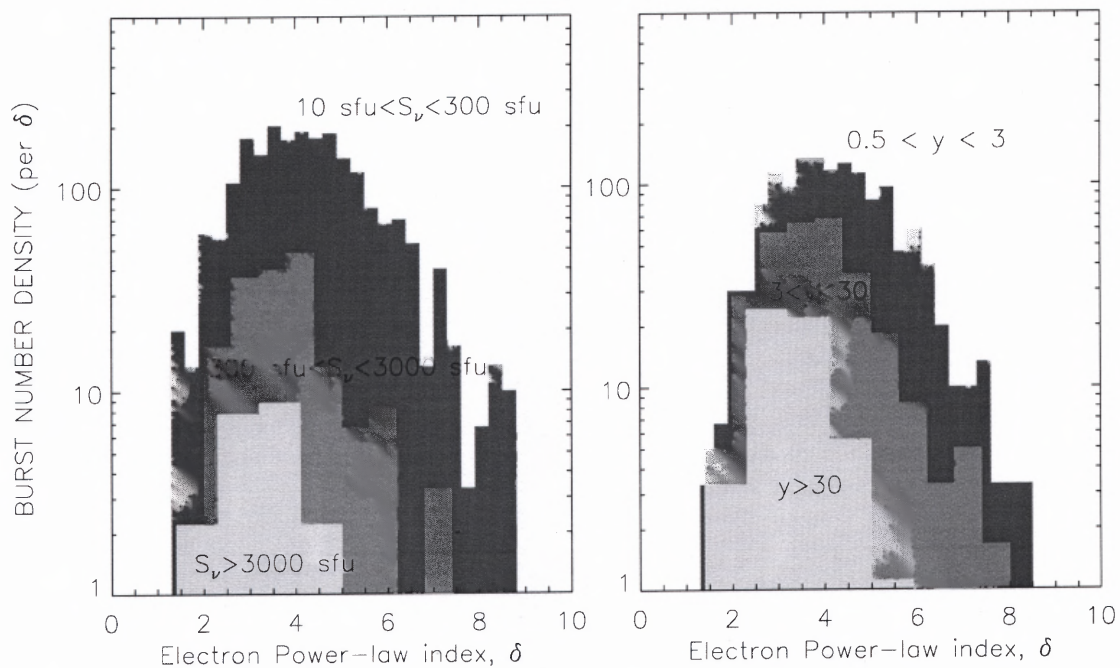


Figure 5.4 Distribution of the electron power-law index derived from the optically-thin spectral slopes of the OVSA spectra. These index distributions are shown at three different groups according to the flux (left panel) and according to the scaled flux, $y \equiv S_\nu/\nu^2$ (right panel).

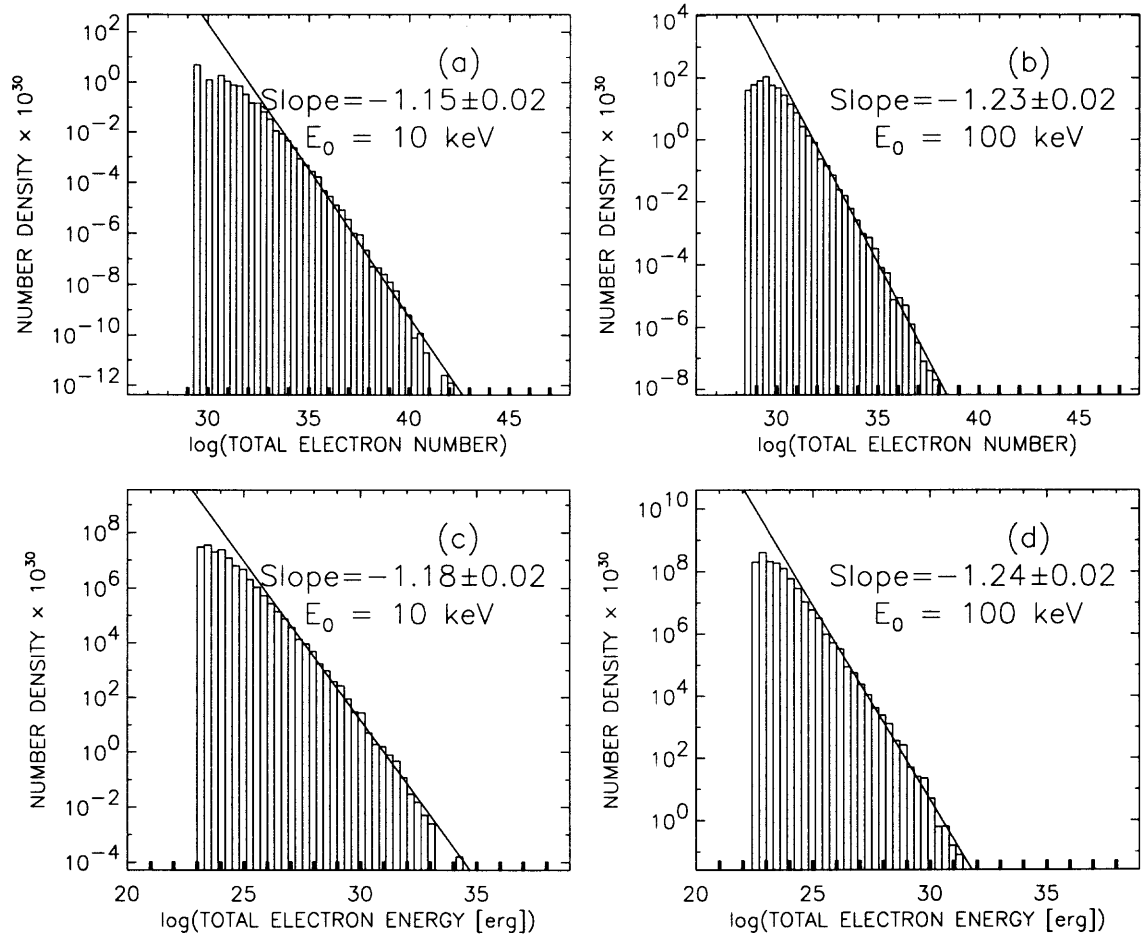


Figure 5.5 The total number (upper panels) and total energy (lower panels) distributions of nonthermal electrons derived from the OVSA microwave spectra. The slope of a power-law fit (lines) to the distribution and the lower bound energy E_0 used for integration are specified in each panel.

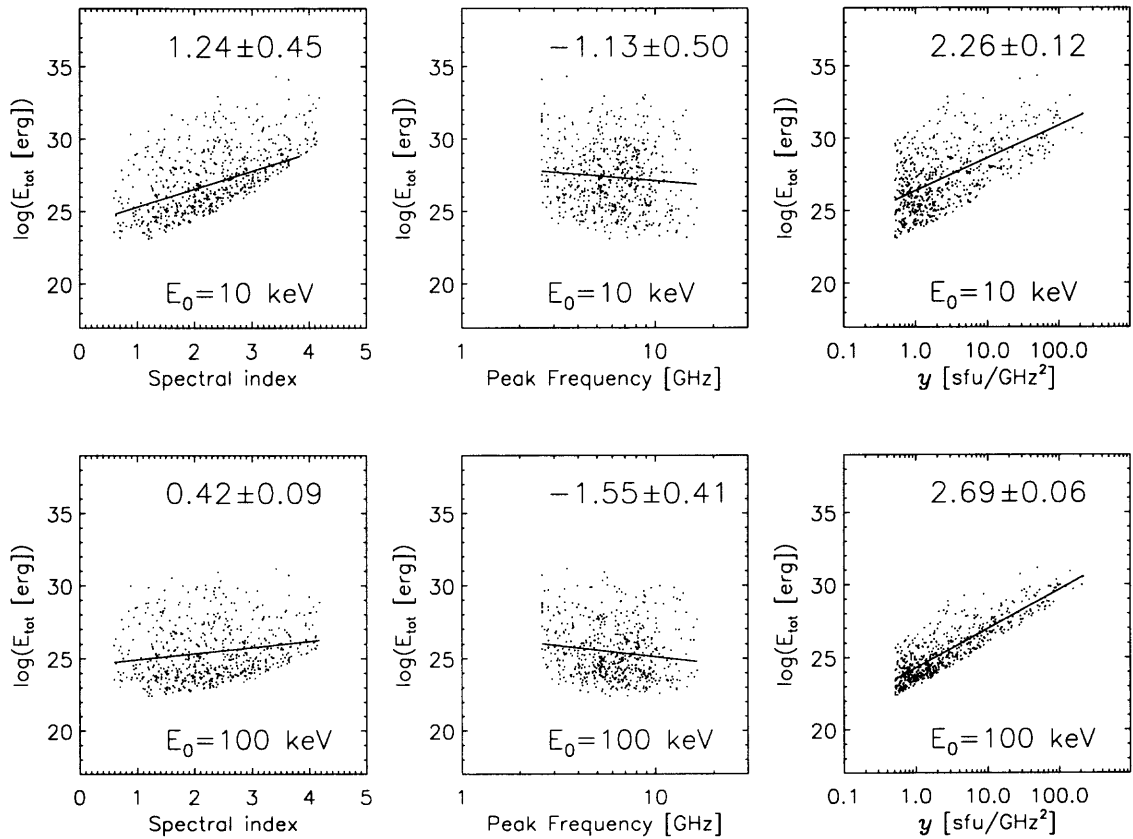


Figure 5.6 Derived total energy vs. directly observed flare parameters. In the top panels, total energies integrated above $E_0 = 10 \text{ keV}$ are used, and in the bottom panels, those integrated above $E_0 = 100 \text{ keV}$ are used for correlation with other parameters. From the left to right columns we show scatter plots of spectral index, peak frequency, and the scaled peaked flux, y , respectively, against the total energy, E_{tot} . The line in each panel represents a linear fit to the data and the slope of the fit is specified.

CHAPTER 6

DECIMETRIC SPIKE BURSTS VERSUS MICROWAVE CONTINUUM

6.1 Introduction

Millisecond solar radio spikes represent an interesting class of solar radio emission associated with flares. The spikes usually form a cluster of short-duration narrow-band pulses on the dynamic spectrum covering a range of about a few hundreds MHz and lasting about a few minutes. This type of radio emission was initially interpreted as a signature of highly fragmented energy release in flares (Benz 1985). This idea had been one of the main “drivers” of the extensive observational (Benz, Zlobec, & Jaeggi 1982; Karlický 1984; Messerotti, Nonino, & Zlobec 1985; Stähli & Magun 1986; Benz & Güdel 1987; Güdel 1990; Gary, Hurford, & Flees 1991; Güdel, Aschwanden, & Benz 1991; Csillaghy & Benz 1993; Altyntsev et al. 1995, 1996; Karlický, Sobotka, & Jiricka 1996; Zlobec & Karlický 1998; Messmer & Benz 2000; Wang, Yan, & Fu 2002) and theoretical (Stepanov 1978; Kuijpers, van der Post, & Slottje 1981; Sharma, Vlahos, & Papadopoulos 1982; Sharma & Vlahos 1984; Li 1986; Winglee & Dulk 1986; Li 1987; Winglee, Dulk, & Pritchett 1988; Aschwanden 1990; Fleishman 1994; Fleishman & Yastrebov 1994b; Ledenev 1998; Stupp 2000; Bárta & Karlický 2001; Vlasov, Kuznetsov, & Altyntsev 2002) studies of the subject.

However, the integrated spike flux was found to be delayed by 2 – 5 s in respect to simultaneous hard X-ray (HXR) peaks (Aschwanden & Güdel 1992). This discovery is entirely inconsistent with the interpretation of the radio spikes as tracers of the primary energy release. Such a delay can be consistently explained in terms of spectral hardening of the respective fast electrons trapped in a coronal magnetic loop (Fleishman & Melnikov 1998). This model associates the appearance of the spikes with a secondary fragmentation of the radio source (related, e.g., to the local inhomogeneities of the magnetic field).

Another important driver for the spike study is the strong diagnostic potential of the spikes related, e.g., to their extremely narrow bandwidth and short duration (Benz 1986). As a result, many important properties of the spikes have been established from the analysis of observations, leading to the development of many models. Currently, the most detailed comparison of the observed spike properties with various theoretical models is done in a recent review paper (Fleishman & Melnikov 1998). It was shown that the complete list of the spike properties can be interpreted within electron cyclotron maser (ECM) emission produced by fast electrons (with $E_{kin} \sim 10 - 100 \text{ keV}$) with a power-law momentum and anisotropic (loss-cone) pitch-angle distributions. The source of a spike cluster is shown to be a loop with more or less strong local inhomogeneities forming some local traps, where the pitch-angle anisotropy is stronger than on average and provides strong local wave amplification due to negative gyro-synchrotron absorption. Thus, each local trap forms a site where a single spike is generated.

The model has since been developed further to account for some specific spike properties. For example, quasi-linear saturation of ECM (Fleishman & Arzner 2000) was shown to provide spike time profiles with a gaussian rise phase and exponential decay phase in agreement with spike observations (Güdel & Benz 1990; Fleishman & Melnikov 1998; Mészárosová et al. 2002). Non-integer harmonic ratios of the spikes (Krucker & Benz 1994) were interpreted as a result of an ECM line splitting due to source inhomogeneity (Fleishman & Platonov 1999; Platonov & Fleishman 2001).

Nevertheless, in spite of success of current models based on the ECM mechanism, the interpretation remains rather indirect, thus, more direct evidence for ECM operation in the spike bursts is strongly required.

According to ECM theory (Sharma et al. 1982; Sharma & Vlahos 1984; Li 1986; Winglee & Dulk 1986; Li 1987; Aschwanden 1990; Fleishman & Yastrebov 1994a; Fleishman & Melnikov 1998; Stupp 2000) this mechanism is effective if

1. gyro-frequency to plasma frequency ratio is sufficiently large,

$$\omega_{Be}/\omega_{pe} \gtrsim 1, \quad (6.1)$$

2. the distribution function of fast electrons over momentum is sufficiently hard in the range of tens to hundreds keV,
3. the pitch-angle distribution of fast electrons is anisotropic (say, of loss-cone type).

There are various scenarios of ECM operation in solar flares. One of the widely accepted ideas assumes that the main population of fast electrons trapped in a loop is isotropic, while a minor fraction of the electrons just reflected up at the foot-points forms the loss-cone distribution providing the cyclotron instability. Therefore, these models predict that the spikes are generated in a restricted area around the foot-points.

We envision another possibility. If the main electron distribution has an anisotropic pitch-angle distribution (close to marginal stability state) then fluctuations of the angular distribution can provide ECM emission at any location through the entire loop. This model allows spikes to be generated at any height. Moreover, the overall anisotropy will substantially affect the accompanying incoherent gyrosynchrotron emission (Fleishman & Melnikov 2003), which can be tested observationally.

In particular, the model developed by Fleishman & Melnikov (1998) assumes that the spikes are generated by a population of fast electrons accumulated in a magnetic loop due to formation of small-scale traps by inhomogeneities of the magnetic field. Gyrosynchrotron continuum bursts are known to be produced by trapped electrons as well (with characteristic electron energies from hundreds of keV to a few MeV).

Thus, the microwave continuum and simultaneous spike bursts should be related to each other. Since the properties of the gyrosynchrotron emission and

its relation to the source parameters and fast electron distribution are well-known, we expect that analysis of some important correlations between spike bursts and gyrosynchrotron bursts might be rather informative to the study of solar radio spikes.

The study of spike cluster to microwave continuum correlations performed in this paper is similar to some extent to that done by Aschwanden & Güdel (1992), who considered the correlations between spike clusters and HXR emission. Unlike that study, however, we pay a particular attention to the spectral properties of the microwave bursts (rather than flux-to-flux correlations only) and their association to energetic and pitch-angle distributions of the trapped fast electrons.

While both HXR and microwave emissions are produced by accelerated electrons with incoherent emission mechanisms, we emphasize that the study of spike-to-microwave correlations is not a simple repetition of the previous spike-to-HXR study for a few reasons. HXRs are produced mainly by precipitating electrons, while gyrosynchrotron emission is by trapped electrons. Thus, these are different (while related) populations of accelerated electrons. Also, the characteristic energies of radiating electrons are different for these two emission types. And finally, the gyrosynchrotron emission is sensitive to the coronal magnetic field and plasma density, unlike HXR.

We found that all of the conditions required for ECM generation are fulfilled in the analyzed spike events, which is strong evidence that the spikes are produced by the ECM mechanism. Thus, the spike emission can be further used for more reliable diagnostics of the source parameters. In particular, we conclude that the spike clusters are associated with the flares that have the largest magnetic field (more specifically, the largest ω_{Be}/ω_{pe} ratio).

The paper is arranged as follows. Section 2 discusses briefly the observations and the selection criteria. Section 3 considers the theoretical concepts to be checked

against the observations. Section 4 analyzes in some detail a few spike events recorded by Owens Valley Solar Array (OVSA) during 2001. Finally, the results are discussed in Section 5.

6.2 Observations

The Owens Valley Solar Array (OVSA), (Hurford, Read, & Zirin 1984; Gary & Hurford 1994), observes in the frequency range 1 – 18 GHz, typically with 40 frequency channels. The standard temporal resolution is 4 s for the total intensity and 8 s for the circular polarization. The temporal resolution is obviously insufficient to resolve any single spike, since the typical spike duration is of the order of 10 *ms* or less in the frequency range 1 – 3 GHz (Güdel & Benz 1990; Mészárosová et al. 2002; Wang et al. 2002). Nevertheless, an averaged flux of a dense spike cluster can be observed with the OVSA resolution. The results we describe here pertain to average properties of such spike clusters. In particular, the average spike flux densities likely relate more closely to the spike occurrence rate than to individual spike flux densities (Aschwanden & Güdel 1992).

For the detailed analysis we selected a few events demonstrating fluctuating low-frequency (1 – 3.4 GHz) emission with time scales much less than the time scales of the simultaneous microwave continuum. Only the events with narrow-band decimetric structures and without any indication of drifting structures (such as could be related to type III bursts) were selected. Also, we did not include the events with very few decimetric peaks, since no quantitative analysis was possible for those cases. Finally, we selected six events (from about ten spike events recorded for the entire year 2001). Five of them were observed with the standard 4/8 s time resolution, while the sixth was with 2 s time resolution without polarization measurements.

6.3 Theoretical Background

In essence, ECM is a kind of gyrosynchrotron emission in the conditions where the respective absorption coefficient is negative, providing wave amplification instead of absorption. Respectively, the usual solution for the radiation intensity applies for this case (for a uniform source):

$$J_{\sigma}(\omega, \theta) = \frac{j_{\sigma}(\omega, \theta)}{\kappa_{\sigma}(\omega, \theta)}(1 - e^{-\tau_{\sigma}}) \quad (6.2)$$

where $\tau_{\sigma} = \kappa_{\sigma}L$ is the optical depth of the source for either ordinary ($\sigma = 1$) or extraordinary ($\sigma = -1$) modes of radiation, L is the source size along the line of sight, $j_{\sigma}(\omega, \theta)$, $\kappa_{\sigma}(\omega, \theta)$ are the emissivity and absorption coefficient of the gyrosynchrotron emission at frequency ω and viewing angle θ .

If the optical depth $|\tau|$ is large in value and positive, we arrive at the standard optically thick gyrosynchrotron emission, with the intensity

$$J_{\sigma}^{thick}(\omega, \theta) = \frac{j_{\sigma}(\omega, \theta)}{\kappa_{\sigma}(\omega, \theta)}, \quad (6.3)$$

whose spectral behavior does not depend noticeably on the electron spectral index.

However, if the absorption coefficient is negative for some restricted range of the frequency and viewing angle for any wave-mode, the amplification of the respective waves occurs according to Eq. (6.2), which reduces to

$$J_{\sigma}^{ECM}(\omega, \theta) = \frac{j_{\sigma}(\omega, \theta)}{|\kappa_{\sigma}(\omega, \theta)|} e^{|\tau_{\sigma}|} \quad (6.4)$$

if $|\tau_{\sigma}| \gg 1$ for this case (in the linear approximation).

From these two equations it becomes very clear what kind of correlation should exist in observations when we compare ECM emission with the standard gyrosynchrotron emission. The ratio of the two becomes

$$J_{\sigma}^{ECM}(\omega_1, \theta) / J_{\sigma}^{thick}(\omega_2, \theta) = \frac{j_{\sigma}(\omega_1, \theta) / |\kappa_{\sigma}(\omega_1, \theta)|}{j_{\sigma}(\omega_2, \theta) / \kappa_{\sigma}(\omega_2, \theta)} e^{|\tau_{\sigma}|}, \quad (6.5)$$

where ω_1 is the (low) frequency at which ECM emission is generated, ω_2 is a (higher) frequency at which the gyrosynchrotron source is optically thick, and $|\tau_{\sigma}|$ is the

optical depth of the ECM emission. The ratio depends primarily on the exponential factor $e^{|\tau_\sigma|}$ while the pre-exponential factor has much weaker dependence on the distribution function of fast electrons (Fleishman & Melnikov 2003). Thus, the logarithm of the ratio (6.5) is linearly related to the optical depth $|\tau_\sigma|$, which in turn depends substantially on the distribution function of fast electrons.

More specifically (Fleishman & Yastrebov 1994a; Fleishman & Melnikov 1998), the negative absorption coefficient (and $|\tau_\sigma|$ respectively) increases in value as the hardness of the electron momentum spectrum and pitch-angle anisotropy (namely, the angular gradient) of the loss-cone distribution increase. On the other hand, the hardness and the pitch-angle distribution specify the optically thin spectral index of the incoherent gyrosynchrotron radiation (Ramaty 1969; Fleishman & Melnikov 2003).

The calculations of the standard gyrosynchrotron emission produced by anisotropic pitch-angle distributions of fast electrons with a power-law momentum distribution (Fleishman & Melnikov 2003) show that the optically thin spectral index (α_h) of the gyrosynchrotron radiation depends substantially on the viewing angle at which the gyrosynchrotron source is observed with respect to the magnetic field. For the quasi-transverse case, the spectral index is specified primarily by the spectral index δ of the fast electron distribution over momentum, so that harder electron distributions produce flatter gyrosynchrotron spectra in the optically thin region. However, for the quasi-parallel case (Fleishman & Melnikov 2003), the spectral index α_h is specified mainly by the pitch-angle anisotropy of fast electrons in such a way that more anisotropic distributions produce softer optically thin gyrosynchrotron spectra (larger α_h).

Thus, combining the predictions of the ECM and gyrosynchrotron theories, we can expect two different types of correlation between $|\tau_\sigma|$ and α_h . If we observe the microwave source at a quasi-transverse direction, then the larger optical depth $|\tau_\sigma|$

should correspond to a flatter gyrosynchrotron spectrum in the optically thin region, while for the quasi-parallel case the larger optical depth $|\tau_\sigma|$ should correspond to a steeper gyrosynchrotron spectrum.

6.4 Data Analysis

Aschwanden & Güdel (1992) considered correlations between decimetric spike rate, integrated over some frequency range, and HXR emission. In particular, they found that some X-ray peaks are tightly correlated with the averaged spike flux density, while others are entirely uncorrelated. This was interpreted (but not proven) as a result of particle acceleration in different loops with only part (one) of them satisfying the specific conditions for the spike generation. Another important finding is a considerable time delay (of 2 – 5 s) of the averaged spike flux in respect to HXR peaks.

Accordingly, we performed some studies similar (and complementary) to those by Aschwanden & Güdel (1992), but we paid more attention to the role of gyrosynchrotron spectral evolution based on the theoretical concepts discussed briefly in Section 3.

First of all, we address the question if there are any indications that the ratio of frequencies (6.1) is systematically larger for bursts producing the spike clusters than on average for all radio bursts. For this purpose we study the low-frequency part of the microwave continuum bursts. It is well-known (Bastian, Benz, & Gary 1998; Fleishman & Melnikov 2003) that the slope (α_l) of the low-frequency gyrosynchrotron emission depends on the gyro-frequency to plasma frequency ratio due to the Razin effect. While the expected low-frequency spectral indices for the gyrosynchrotron optical depth is $\alpha_l < 3$, the Razin effect can increase the values to the range $\alpha_l > 3$ if $\omega_{Be}/\omega_{pe} < 0.3$.

Figure 6.1 displays the distribution of the low-frequency spectral indices α_l separately for the spike-producing bursts and all other gyrosynchrotron bursts. It is remarkable that the overall distribution has a significant tail in the range $\alpha_l > 3$, while the spike-producing bursts display the spectral indices lying entirely in the range $\alpha_l < 2.5$. Thus, no indication of the Razin-effect operating in the spike-producing bursts is present, hence, we can conclude the condition (6.1) is fulfilled for these events.

Below we analyze in more detail the six events with dense spike clusters in the range 1.2 – 3.4 GHz, recorded by OVSA during 2001.

6.4.1 25-mar-01 event

The event lasted about 8 min, Figure 6.2a, the microwave continuum burst produced a flux density up to 50 sfu, while the decimetric flux density exceeded 150 sfu. The power and polarization spectra, averaged over the entire burst duration, are shown in Figure 6.2b, c. The microwave burst displays a remarkably strong degree of polarization at the high (optically thin) frequencies. A few important conclusions can be derived from the polarization plot. First, the microwave source is reasonably uniform, otherwise, the degree of polarization might not have been so strong. Second, we look at the source at a direction quasi-parallel to the magnetic field, since at a quasi-transverse direction even a uniform source would produce a weak or moderate degree of polarization. Third, the dominant sense of circular polarization (L) for the spikes is that expected for optically thin gyrosynchrotron emission (X-mode) and opposite to that of optically thick emission (typically, O-mode). Thus, the spikes are preferentially X-mode polarized (within the simplest geometry). We have to emphasize that we discuss here an averaged degree of polarization of the entire spike cluster, while the instantaneous degree of polarization varies with time and can be as large as 100%. The sense of spike polarization also changes with time. Moreover, the

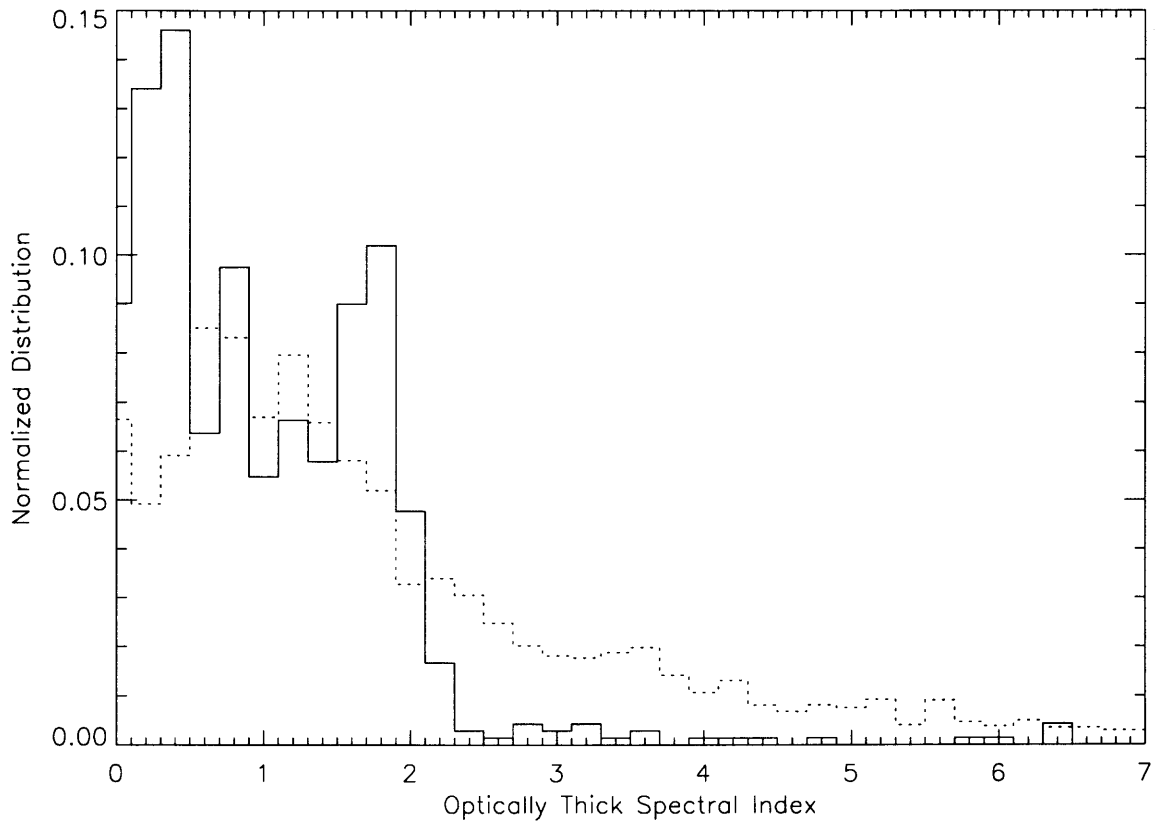


Figure 6.1 Distribution of optically thick spectral index of 6 spike-producing bursts (solid line) and the equivalent distribution obtained for 125 gyrosynchrotron bursts above 60 sfu observed by OVSA during 2001 (dashed line).

preferential sense of spike polarization depends on frequency: lower-frequency spikes (1.2 – 2 GHz) are mainly L-polarized, while higher-frequency spikes (2 – 3.4 GHz) are mainly R-polarized.

Let us proceed to examine correlations between spike emission and microwave continuum. Figure 6.3a displays a very good correlation between averaged spike flux and microwave light curve. This finding is similar to that found for HXR bursts accompanied by spike clusters: some HXR peaks are tightly correlated with the spike rate (Aschwanden & Güdel 1992). Aschwanden & Güdel (1992) found that the averaged spike flux is delayed by 2 – 5 s with respect to the simultaneous HXR peak, which was further interpreted as a result of trapping and consequent spectral evolution of spike-generating fast electrons (Fleishman & Melnikov 1998), while the HXR peak is caused mainly by precipitating electrons.

Figure 6.3b displays the dependence of the cross-correlation coefficient between the spike flux density integrated over the low-frequency band and the gyrosynchrotron flux density at a selected (optically thick) frequency as a function of the respective time lag. The respective spline fit (solid curve) has a maximum at $\Delta t \approx 2.5$ s, accordingly, the *optically thick* gyrosynchrotron emission is delayed by 2.5 s with respect to spike emission. Indeed, the delay value is frequency dependent in agreement with the property of the microwave bursts (Melnikov & Magun 1998), but the sign is stable. Since both types of radio emission are produced by trapped electrons, the delay can be easily interpreted if the spike emission is produced by fast electrons of lower energy than the gyrosynchrotron emission, because the characteristic lifetime of the trapped electrons increases with the electron energy.

The theory described in Section 3 predicts a correlation between the (negative) optical depth in the spike frequency range and the gyrosynchrotron spectral index α_h in the optically thin range. To study this correlation we plot in Figure 6.3c the quantity $\log(F_{thick}/F_{spike})$ versus high-frequency microwave spectral index α_h , where

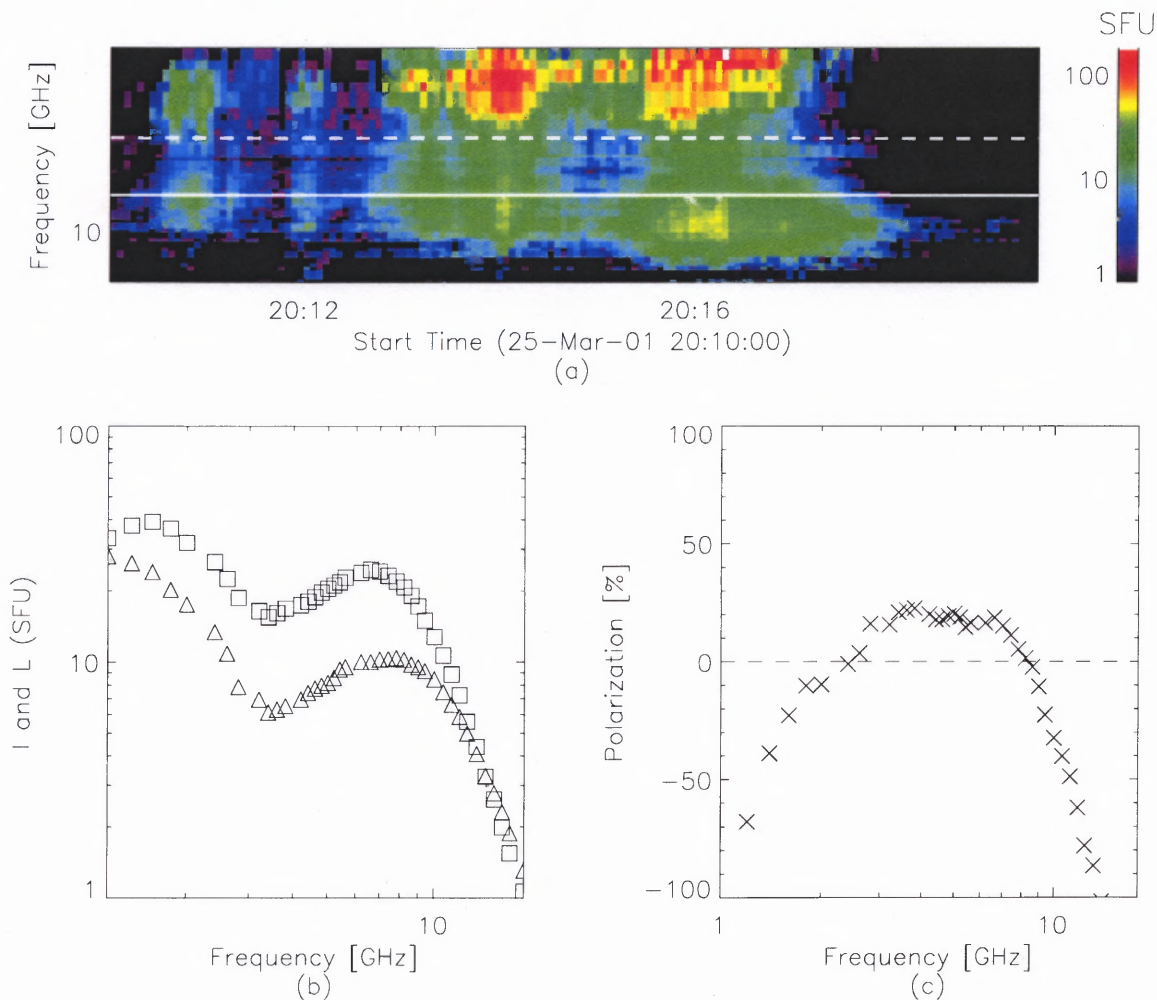


Figure 6.2 March 25, 2001: (a)-Dynamic spectrum recorded by OVSA at 40 frequencies between 1.2 and 18 GHz at 4 s time resolution. The solid line, 6.6 GHz, and the dashed line, 3.4 GHz, represent the optically thick frequency and, respectively, the upper integration limit of the spiky emission used to obtain the results displayed in Fig.6.3. (b)-The time averaged total power emission (squares) and Left-hand polarization data (triangles) for the same segment of time as in (a). (c)-The averaged polarization spectrum computed using the magnitudes displayed in (b).

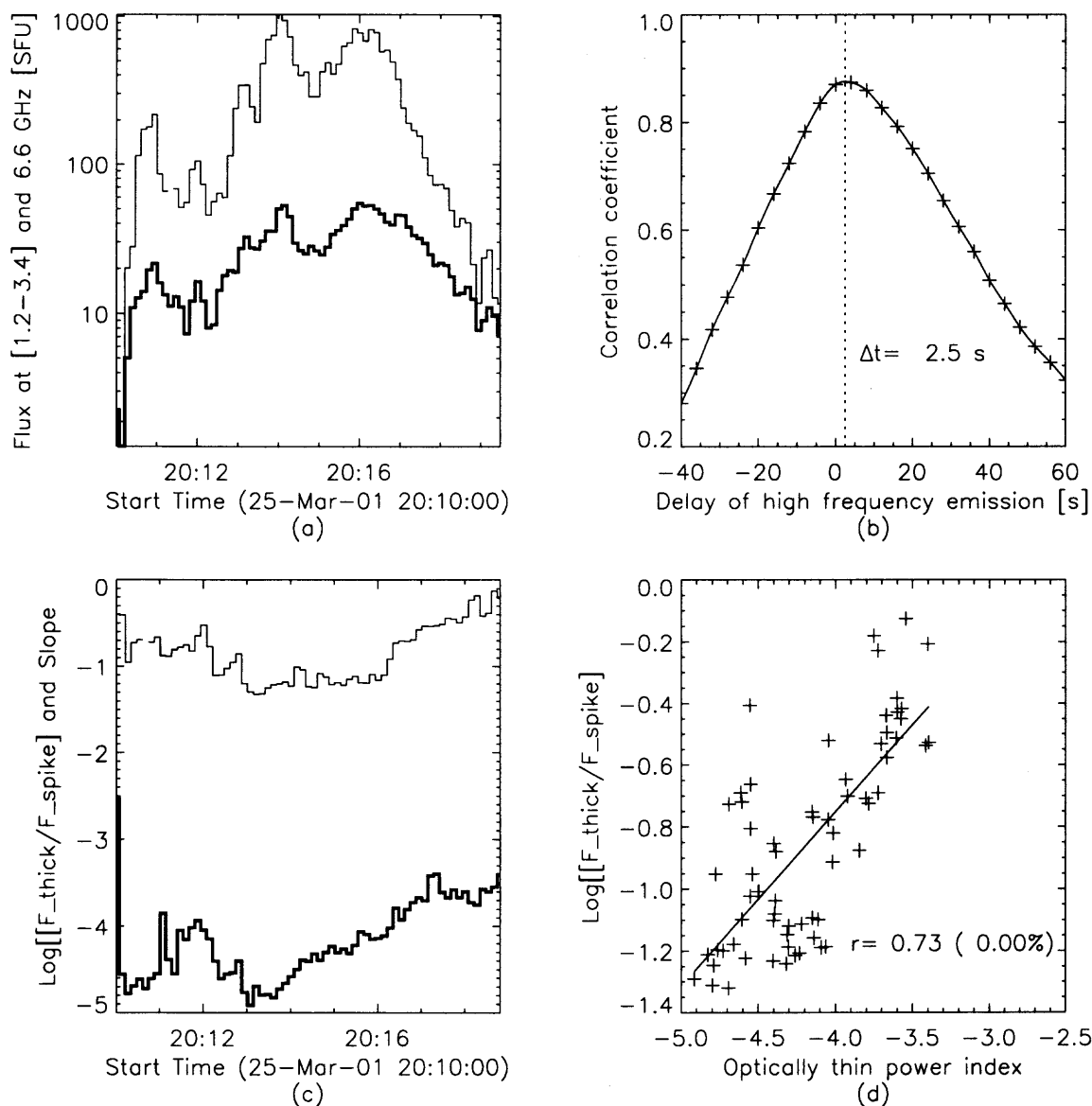


Figure 6.3 March 25, 2001: (a)-Integrated spiky emission over [1.2 – 3.4] GHz (thin line) and the optically thick gyrosynchrotron emission at 6.6 GHz, (thick line). (b)- The linear correlation coefficient (symbols) between the magnitudes displayed in (a) for different time lags. A delay of 2.5 seconds of the high-frequency emission relative to the integrated low-frequency emission has been estimated using a spline interpolation (solid line). (c)- The natural logarithm of the ratio between optically thick and integrated spiky emissions (thin line) and the optically thin spectral index (thick line). (d) The correlation plot of the magnitudes displayed in (c). A linear correlation coefficient of +0.73 has been found. The probability for such a correlation coefficient to be the result of a random distribution is 0% to two decimal places.

F_{thick} is the gyrosynchrotron flux density at an optically thick frequency, namely $f = 6.6$ GHz, and F_{spike} is the spike flux density integrated from 1.2 GHz to 3.4 GHz. The respective correlation coefficient is remarkably large, $R = 0.73$. The positive slope of the regression means that spikes are preferentially generated when the optically thin gyrosynchrotron emission displays the softest spectrum, which (for the quasi-parallel viewing angle) corresponds to the most anisotropic pitch-angle distributions of the fast electrons.

6.4.2 24-aug-01 event

The event shown in Figure 6.4a is generally similar to the previous one but one order of magnitude stronger: the microwave peak flux is about 400 *sfu*, while the spike peak flux density is about 1500 *sfu*. The total and polarized flux density (Figure 6.4b) give rise to the averaged polarization spectrum shown in Figure 6.4c. The degree of polarization is exceedingly strong at the high (optically thin) frequencies, which is evidence for the quasi-parallel viewing angle of the gyrosynchrotron source. It is interesting that the sense of polarization in the optically thick region is the same as in the optically thin region, which can be naturally interpreted as an effect of pitch-angle anisotropy of the radiating fast electrons (Fleishman & Melnikov 2003). The spikes are mainly polarized with the same sense, thus, we again arrive at the conclusion of the preferential X-mode polarization of the spikes.

The averaged spike and microwave fluxes display a significant correlation (Figure 6.5a) with the correlation coefficient $R = 0.72$. The microwave emission is delayed by about 9.6 s with respect to the spike emission (Figure 6.5b), which again is expected due to the energy dependent lifetime of the trapped fast electrons.

The logarithm of the ratio of the optically thick gyrosynchrotron flux density to the averaged spike flux density (Figure 6.5c) displays an especially tight correlation with the high-frequency microwave spectral index (Figure 6.5e) during a 3

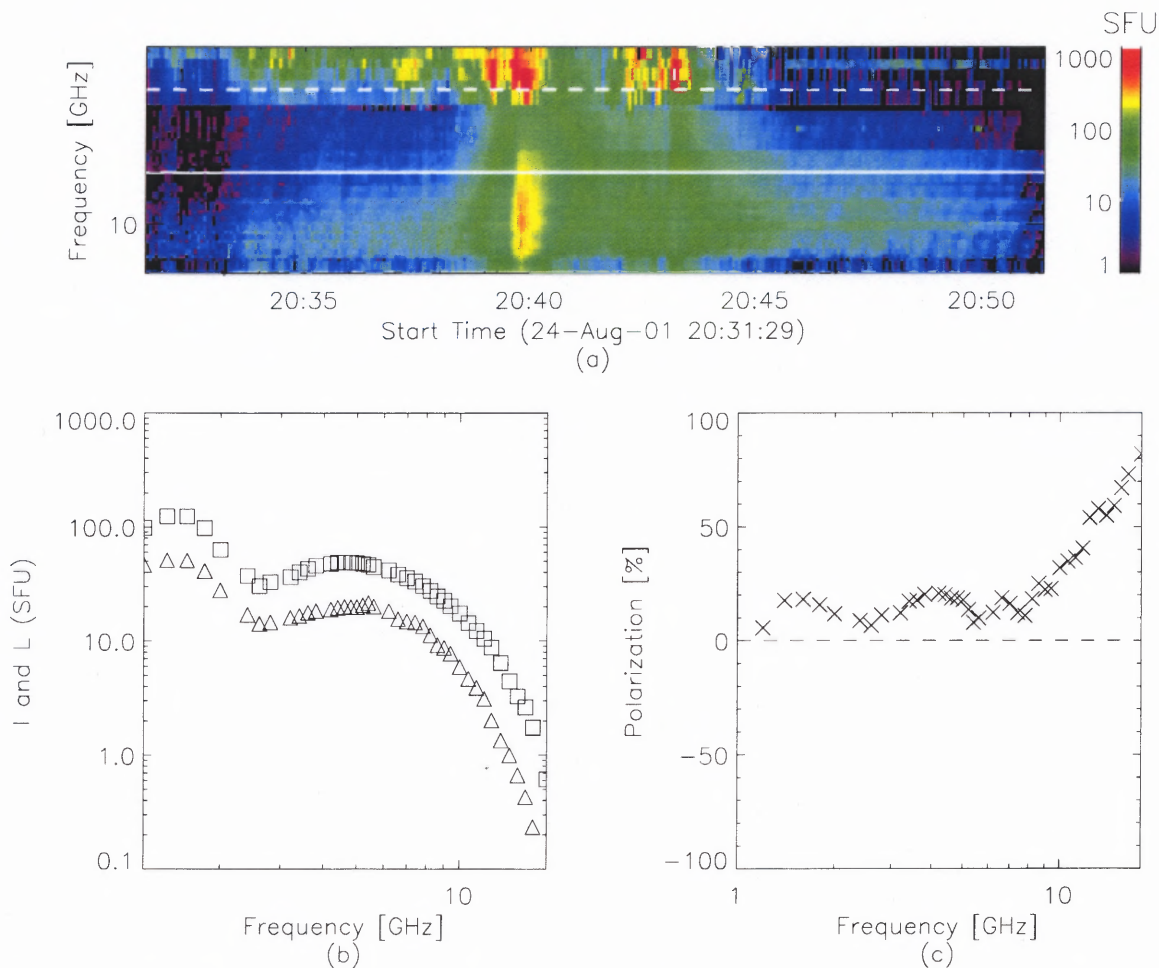


Figure 6.4 August 24, 2001: (a)-Dynamic spectrum recorded by OVSA at 40 frequencies between 1.2 and 18 GHz at 4 s time resolution. The solid line, 5.4 GHz, and the dashed line, 2.0 GHz, represent the optically thick frequency and, respectively, the upper integration limit of the spiky emission used to obtain the results displayed in Fig.6.5. (b)-The time averaged total power emission (squares) and Left-hand polarization data (triangles) for the same segment of time as in (a). (c)-The averaged polarization spectrum computed using the magnitudes displayed in (b).

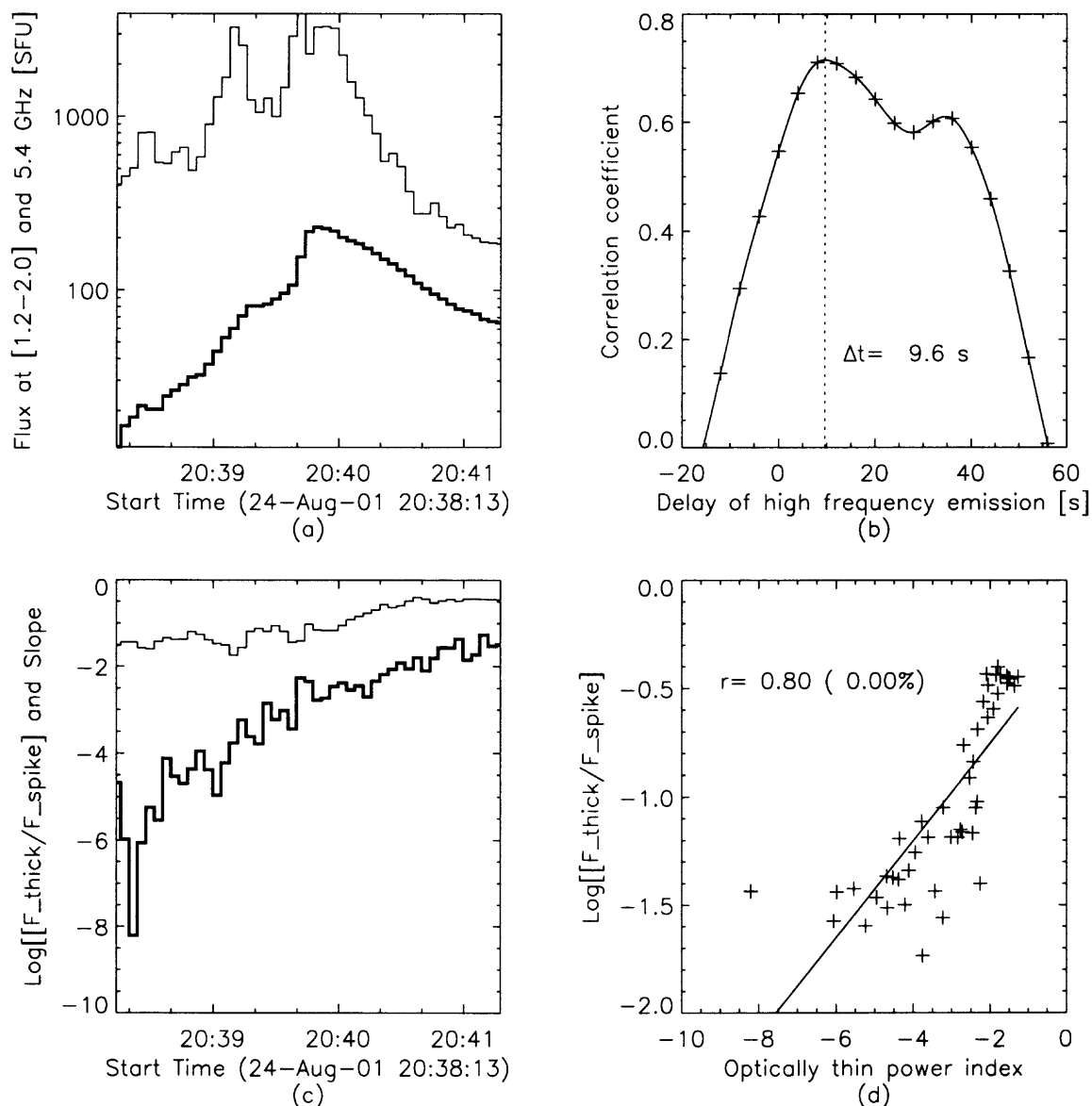


Figure 6.5 August 24, 2001: (a)-Integrated spiky emission over [1.2 – 2.0] GHz (thin line) and the optically thick gyrosynchrotron emission at 5.4 GHz, (thick line). (b)- The linear correlation coefficient (symbols) between the magnitudes displayed in (a) for different time lags. A delay of 9.6 seconds for the high-frequency emission relative to the integrated low-frequency emission has been estimated using a spline interpolation (solid line). (c)- The natural logarithm of the ratio between optically thick and integrated spiky emissions (thin line) and the optically thin spectral index (thick line). (d) The correlation plot of the magnitudes displayed in (c). A linear correlation coefficient of +0.80 has been found. The probability for such a correlation coefficient to be the result of a random distribution is again 0%.

min interval of the burst (from 20:38:10 to 20:41:20 UT), when a reliable spectral index data is available. Thus, we again conclude that the spikes are mainly generated during the softest microwave spectra. For the quasi-parallel case, softer spectra indicate more anisotropic pitch-angle distributions of the fast electrons, hence, the spikes are produced most efficiently when the pitch-angle distribution of the trapped fast electrons is the most anisotropic.

6.4.3 30-aug-01 event

The event lasted about 10 min (Figure 6.6a), but only the main phase (from 17:49:30 to 17:53:00) allows for the quantitative analysis requiring data of sufficiently high flux density. The peak flux densities of both microwave and spike emissions exceed 200 sfu in this event. The spikes display clustering on the frequency domain; we analyze here the properties of the spike flux integrated over the entire range from 1.2 GHz to 3.2 GHz. The average total and polarized spectrum (Figure 6.6b) provide us with the polarization spectrum (Figure 6.6c). The very large degree of polarization in the optically thin range allows us to derive that the microwave source is observed at a direction quasi-parallel to the magnetic field similar to the previous two cases. The sense of polarization of the spike clusters is the same as that of the optically thin gyrosynchrotron emission, once again suggesting the preferential X-mode polarization of spikes.

The first microwave peak is well correlated with the integrated spike flux, while the second one displays a much weaker correlation, similar the findings of the spike-HXR correlation study (Aschwanden & Güdel 1992). For this reason, the flux-to-flux correlation is not quite so strong ($R = 0.66$) for the entire analyzed time segment (Figure 6.7a). The dependence of the correlation coefficient of the time lag (Figure 6.6b) shows that the microwave emission is delayed only slightly, if at all, with respect to spike emission.

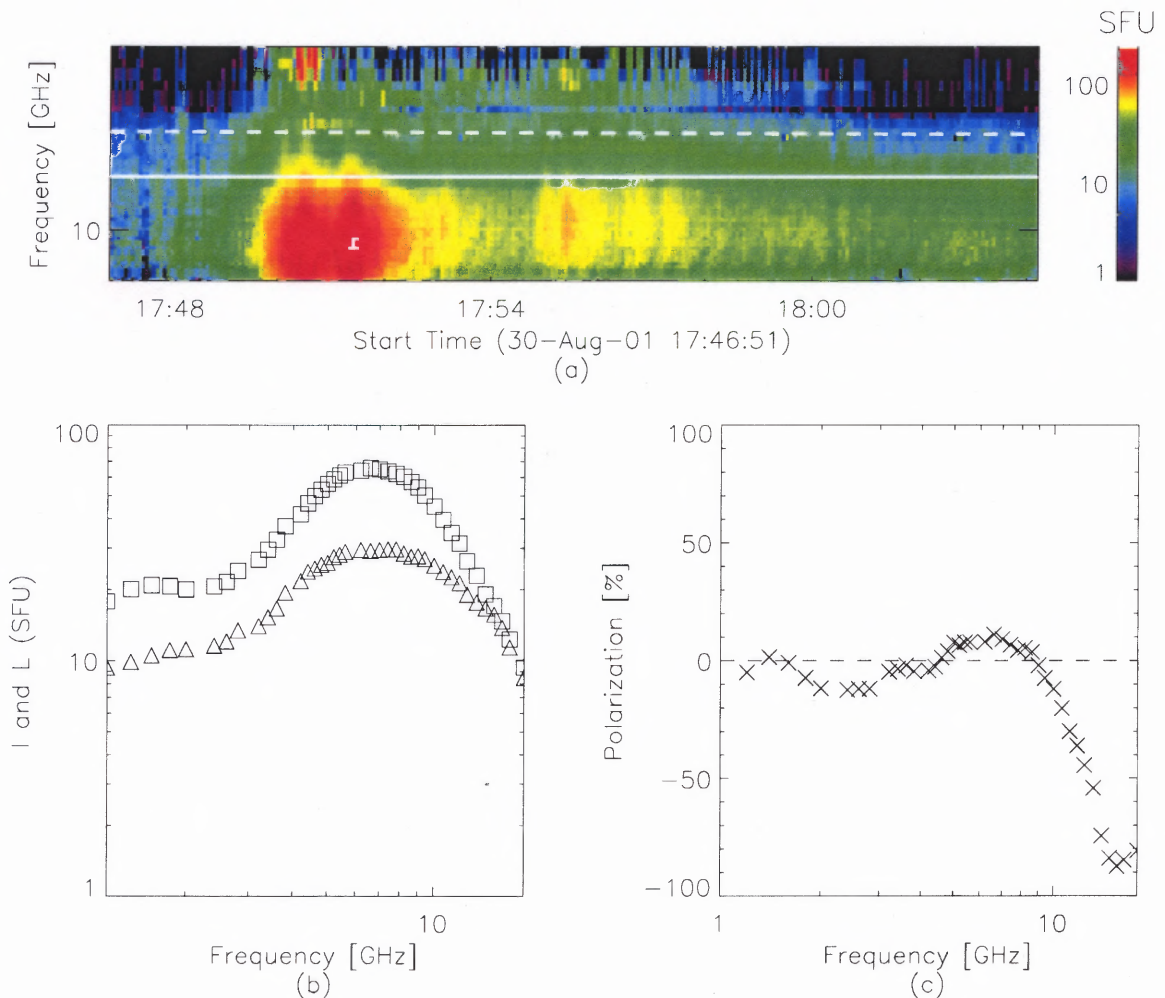


Figure 6.6 August 30, 2001: (a)-Dynamic spectrum recorded by OVSA at 40 frequencies between 1.2 and 18 GHz at 4 s time resolution. The solid line, 5.4 GHz, and the dashed line, 3.2 GHz, represent the optically thick frequency and, respectively, the upper integration limit of the spiky emission used to obtain the results displayed in Fig.6.7. (b)-The time averaged total power emission (squares) and Left-hand polarization data (triangles) for the same segment of time as in (a). (c)-The averaged polarization spectrum computed using the magnitudes displayed in (b).

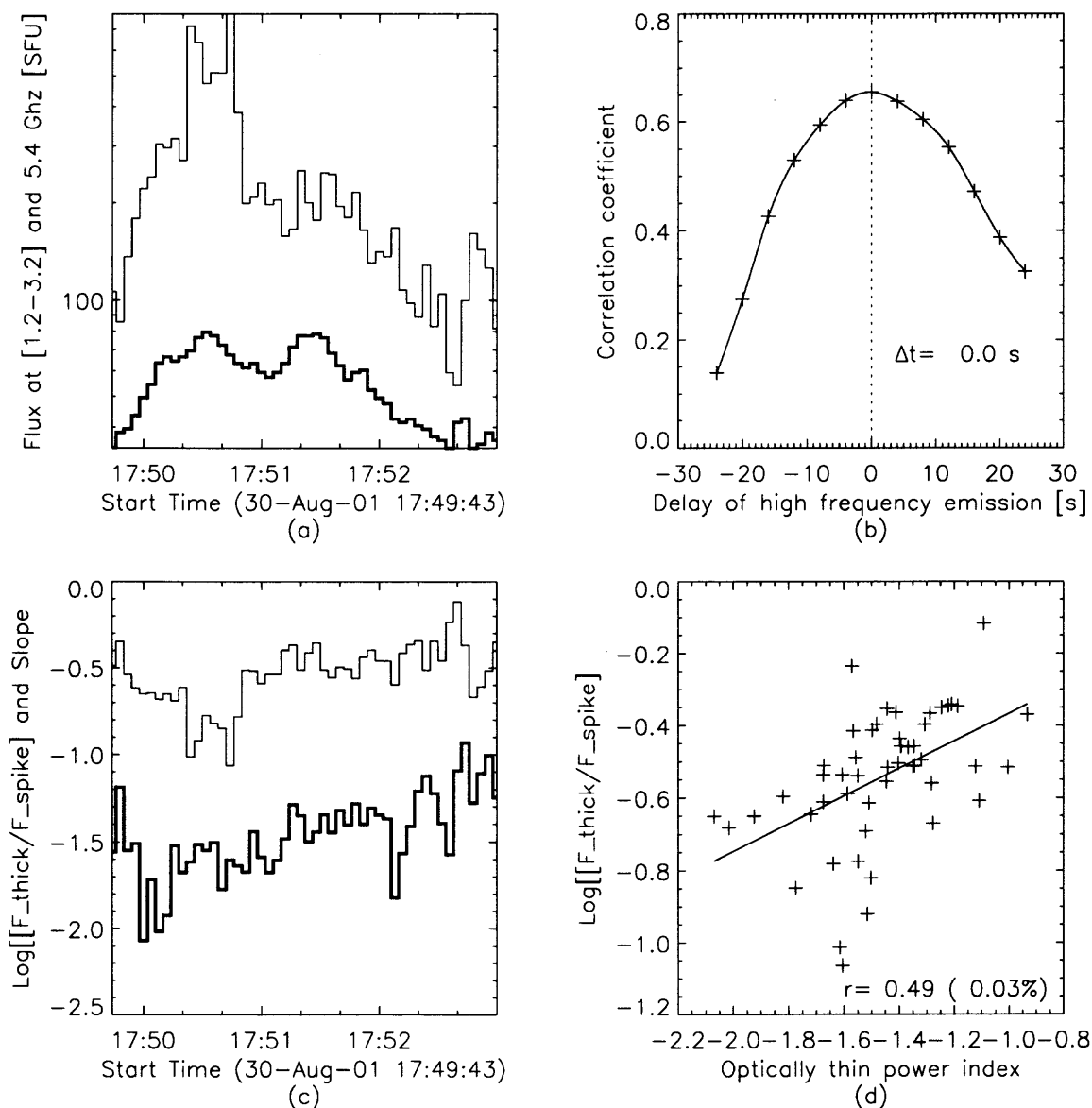


Figure 6.7 August 30, 2001: (a)-Integrated spiky emission over [1.2–3.2] GHz (thin line) and the optically thick gyrosynchrotron emission at 5.4 GHz, (thick line). (b)-The linear correlation coefficient (symbols) between the magnitudes displayed in (a) for different time lags. Practically no delay between high-frequency emission and the integrated low-frequency emission has been found in this case. (c)- The natural logarithm of the ratio between optically thick and integrated spiky emissions (thin line) and the optically thin spectral index (thick line). (d) The correlation plot of the magnitudes displayed in (c). A linear correlation coefficient of +0.49 has been found. The probability for such a correlation coefficient to be the result of a random distribution is about 0.03%.

The correlation between $\log(F_{thick}/F_{spike})$ and α_h remains significant, at $R = 0.49$, but is less than in two previous cases. Nevertheless, the general conclusion is the same for all three analyzed events demonstrating strong polarization of the optically thin gyrosynchrotron emission: the spikes are generated most efficiently when the gyrosynchrotron emission displays the softest spectra.

6.4.4 05-oct-01 event

The spikes in this event lasted about 6 min, Figure 6.8a. This is the weakest of the analyzed events, the peak flux density of both microwave and spike bursts being below 100 sfu (Fig.6.8b).

The total and polarized flux data are reliable at $f < 10$ GHz (Figure 6.8b), above which the flux density becomes too low. The polarization spectrum displays a moderate degree of polarization ($P < 50\%$) in the optically thin region (Figure 6.8c). In essence, there are a few possibilities to provide such a moderate polarization of the gyrosynchrotron emission (e.g., a single source observed at a quasi-transverse direction, superposition of two quasi-parallel sources with opposite directions of the magnetic field, or a more complicated non-uniform source).

We, however, adopt the simplest model—a single gyrosynchrotron source—as we did for the three previous events. In this case the source is observed at a quasi-transverse direction (to avoid very strong high-frequency polarization). One can note that the spikes above 1.6 GHz are polarized oppositely to the optically thin gyrosynchrotron emission, while below 1.6 GHz they have the same sense of polarization.

The averaged spike and microwave fluxes display a rather small correlation coefficient, $R = 0.13$, Figure 6.9b, although there is some indication that the microwave emission is delayed by 5.9 s with respect to the spike emission (Figure 6.9b). Nevertheless, the quantities $\log(F_{thick}/F_{spike})$ and α_h reveal a significant

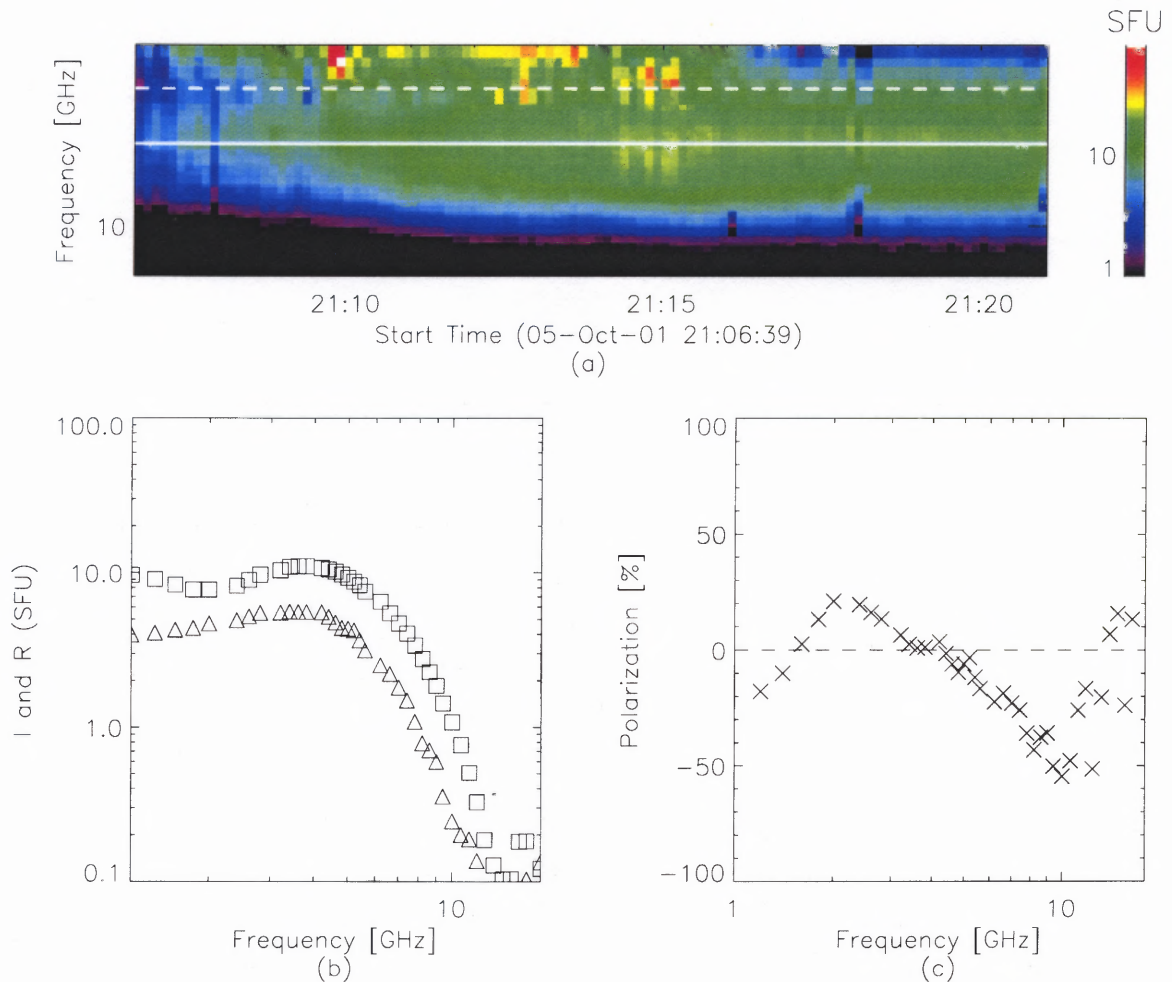


Figure 6.8 October 5, 2001: (a)-Dynamic spectrum recorded by OVSA at 40 frequencies between 1.2 and 18 GHz at 8 s time resolution. The solid line, 3.8 GHz, and the dashed line, 2.0 GHz, represent the optically thick frequency and, respectively, the upper integration limit of the spiky emission used to obtain the results displayed in Fig.6.9. (b)-The time averaged total power emission (squares) and Right-hand polarization data (triangles) for the same segment of time as in (a). (c)-The averaged polarization spectrum computed using the magnitudes displayed in (b). Only the polarization spectrum below 10 GHz is reliable due to a very weak emission above this frequency, as it can be seen in (b).

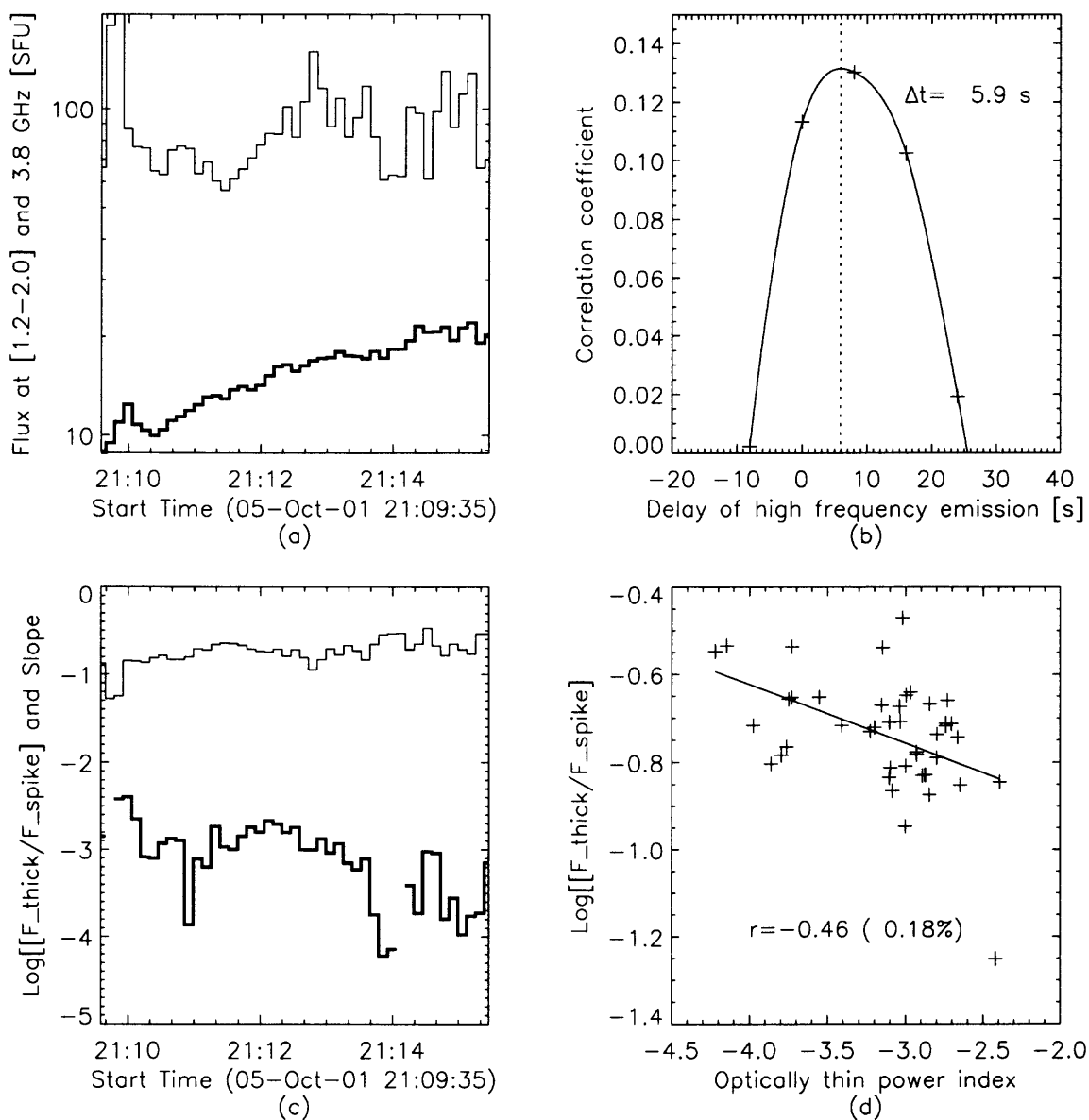


Figure 6.9 October 5, 2001: (a)-Integrated spiky emission over [1.2 – 2.0] GHz (thin line) and the optically thick gyrosynchrotron emission at 3.8 GHz, (thick line). (b)- The linear correlation coefficient (symbols) between the magnitudes displayed in (a) for different time lags. A delay of 5.9 seconds of the high-frequency emission relative to the integrated low-frequency emission has been estimated using a spline interpolation (solid line). (c)- The natural logarithm of the ratio between optically thick and integrated spiky emissions (thin line) and the optically thin spectral index (thick line). (d) The correlation plot of the magnitudes displayed in (c). A linear correlation coefficient of -0.46 has been found. The probability for such a correlation coefficient to be the result of a random distribution is about 0.18%.

negative correlation, $R = -0.46$ (Figure 6.9d) implying a physical relation between these two emission types. The negative slope of the regression means that the spikes are generated most efficiently when the gyrosynchrotron emission displays the hardest spectra, in contrast to the case of the three previous bursts.

For the quasi-transverse viewing angles the high-frequency slope is related primarily to the hardness of the fast electron momentum distribution. We, thus, conclude that the spikes are generated when the fast electrons have the hardest spectrum. A similar property was noted in the spike-HXR correlation study (Aschwanden & Güdel 1992).

6.4.5 02-apr-01 event

This event (Figure 6.10a) is exceptionally strong. The microwave peak exceeded 1000 sfu, while the spike flux exceeded $3 \cdot 10^4$ sfu. The event lasted more than half an hour and produced a few spike clusters. We analyze them all together, which provides a very long time series that improves the statistical significance of the results.

The polarization of the optically thin gyrosynchrotron emission (Figure 6.11c) is moderate ($P < 60\%$), which is interpreted here (as the simplest assumption) as an effect of quasi-transverse viewing angle of the gyrosynchrotron source. The polarization of spike clusters is rather strong, $P \sim 70 - 90\%$ on average, the sense of polarization is the same as for optically thin gyrosynchrotron emission. Thus, the spikes are preferentially X-mode polarized.

The microwave and integrated spike fluxes are remarkably uncorrelated (Figure 6.11a, b), at least on average (while some “tracks” can be noted in the plot). Accordingly, no delay between these two types of emission can be found reliably for this event.

However, if the spikes are produced by the ECM mechanism, the correlation between $\log(F_{thick}/F_{spike})$ and α_h must exist. Figure 6.11e, f displays this remarkable

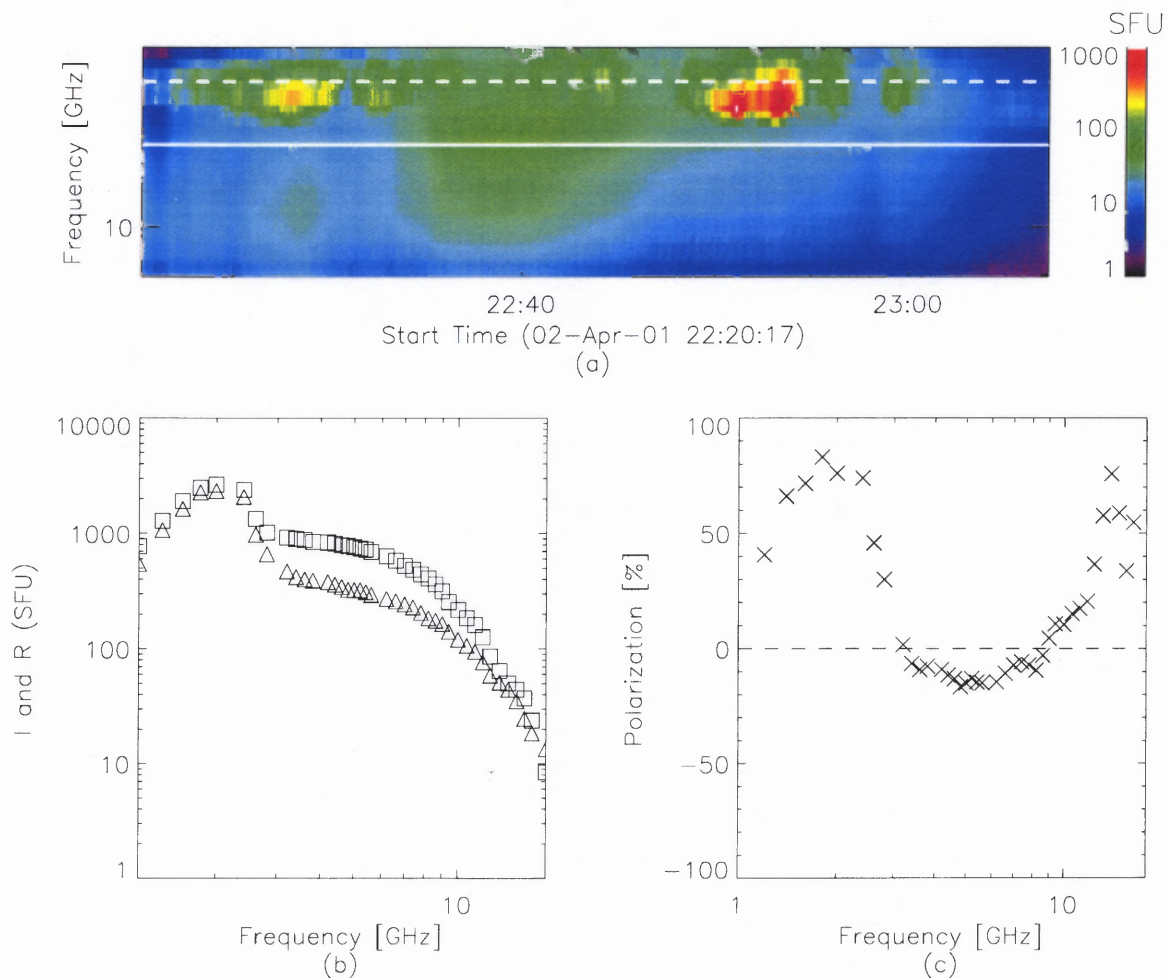


Figure 6.10 April 2, 2001: (a)-Dynamic spectrum recorded by OVSA at 40 frequencies between 1.2 and 18 GHz and 4 s time resolution. The solid line, 3.8 GHz, and the dashed line, 1.8 GHz, represent the optically thick frequency and, respectively, the upper integration limit of the spiky emission used to obtain the results displayed in Fig.6.11. (b)-The time averaged total power emission (squares) and Right-hand polarization data (triangles) for the same segment of time as in (a). (c)-The averaged polarization spectrum computed using the magnitudes displayed in (b).

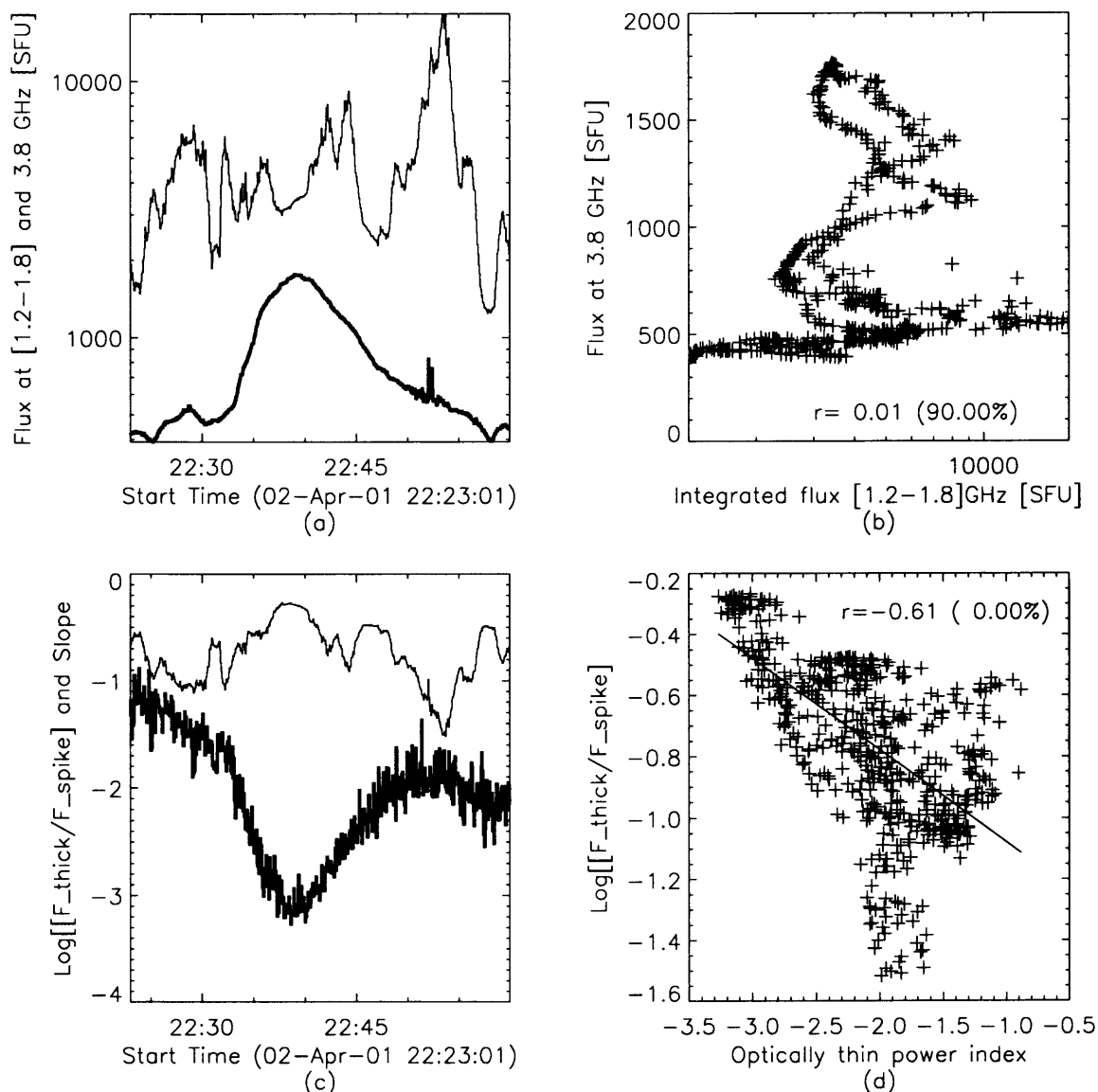


Figure 6.11 April 2, 2001: (a)-Integrated spiky emission over [1.2 – 1.8] GHz (thin line) and the optically thick gyrosynchrotron emission at 3.8 GHz, (thick line). (b)- The correlation plot of the magnitudes displayed in (a). No reliable delay could be found. For the case shown (no time lag) there is practically no linear correlation ($r = 0.01$ corresponding to a 90% probability of a random distribution). (c)- The natural logarithm of the ratio between optically thick and integrated spiky emissions (thin line) and the optically thin spectral index (thick line). (d) The correlation plot of the magnitudes displayed in (c). A linear correlation coefficient of -0.61 has been found. The probability for such a correlation coefficient to be the result of a random distribution is 0% to two decimal places.

correlation ($R = -0.61$) related to the entire duration of the event (more than half an hour!). The spikes are again generated when the gyrosynchrotron emission displays the hardest spectra, which, for the quasi-transverse case, corresponds to the hardest spectra of the fast electrons.

6.4.6 19-oct-01 event

This is one of the strongest events (Figure 6.12) recorded on 2001: the microwave peak exceeded 5000 sfu, while the spike flux exceeded $3 \cdot 10^4$ sfu (6.13a). The event was observed with a time resolution of 2 s, and we analyzed the period during the first peak (first ~ 7 min) of the event, during which the spikes were obviously stronger than the competing low-frequency continuum emission.

The polarization data are unavailable with the fast mode, thus, we are limited to the total flux data for this event. There is general flux-to-flux correspondence for this case (Figure 6.13c) providing the correlation of $R = 0.85$ (Figure 6.13d). The microwave emission is delayed by 7.3 s with respect to the spike flux at $f = 1.2$ GHz. Unlike previous events, we did not integrate the decimetric flux over a few frequency channels, because the contribution of smoothed decimetric continuum component becomes important at higher frequencies (1.4 – 2 GHz) during parts of the burst.

The correlation between $\log(F_{thick}/F_{spike})$ and α_h is quite strong and negative for this case, $R = -0.79$ (Figure 6.13d). We note that the correlation between $\log(F_{thick}/F_{spike})$ and α_h remains negative until about half-way through the second gyrosynchrotron peak at ~ 1631 UT, and then reverses to a positive correlation, which we believe is due to the spike emission giving way to a low-frequency continuum emission of another origin. Although spike clusters appear later in the burst, the gyrosynchrotron emission peaks at such a low frequency after about 1640 UT that we cannot obtain the optically thick flux density, and so cannot examine the correlation between $\log(F_{thick}/F_{spike})$ and α_h . Therefore, at least during the first 7 min of this

event where the correlation can be performed, we can classify the event as being observed at a quasi-transverse direction, similarly to two previous events, and we once again conclude that harder electron distributions are preferable for the spike generation.

6.5 Discussion

We analyzed in some detail six events producing dense spike clusters in the frequency range 1.2 – 3.4 GHz observed simultaneously with microwave gyrosynchrotron continuum.

A few new important findings are firmly established. First of all, the low-frequency part of the respective microwave bursts is considerably flatter than for the overall microwave event set. This means that there is no indication of the Razin effect operating in the microwave events accompanying the decimetric spike bursts. Consequently, the ratio ω_{Be}/ω_{pe} is large enough in the spike sources to allow operation of the ECM mechanism.

Secondly, all five events with polarization data available reveal a *high* degree of polarization in the optically thin gyrosynchrotron range significantly larger than typical mean value of $20\% \pm 16\%$ (Bruggmann & Magun 1990). This deviation is most probably related to the fast electron pitch-angle anisotropy (of the loss-cone type), which increases the degree of X-mode polarization compared with isotropic case (Fleishman & Melnikov 2003). Moreover, two of the analyzed events do not display a change of the sense of polarization from the thin to thick region, which might be related to the effect of the pitch-angle anisotropy as well (Fleishman & Melnikov 2003). Note that the high degree of polarization implies a rather non-symmetric magnetic structure at the source site, since a symmetric loop would give more equal fluxes in both polarizations, leading to smaller net polarization.

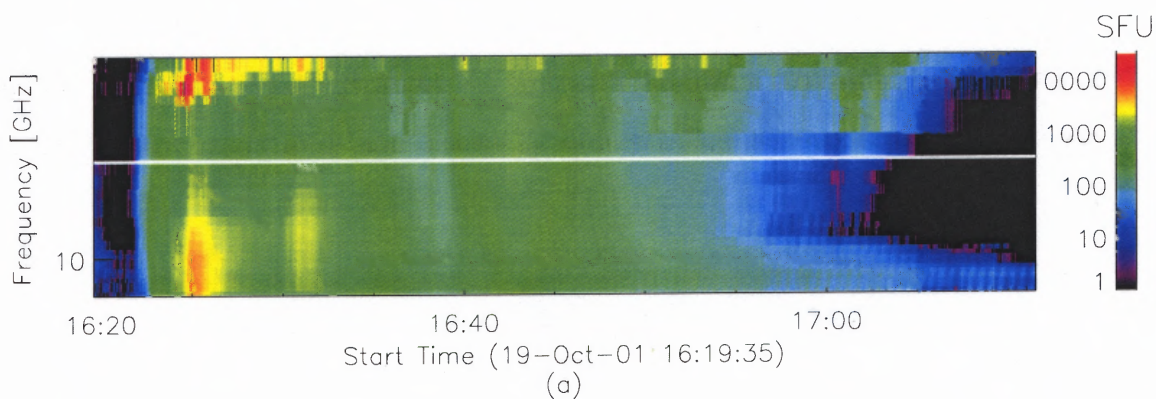


Figure 6.12 October 19, 2001: Dynamic spectrum recorded by OVSA at 22 frequencies between 1.2 and 14.8 GHz and 2 s time resolution. The solid line, 3.6 GHz, line represents the optically thick frequency used to obtain the results displayed in Fig.6.13. To analyze the spiky emission only one frequency, 1.2, GHz has been used in this case because a smoothed component becomes important for higher frequencies at the low frequency range. No polarization data are available for this event.

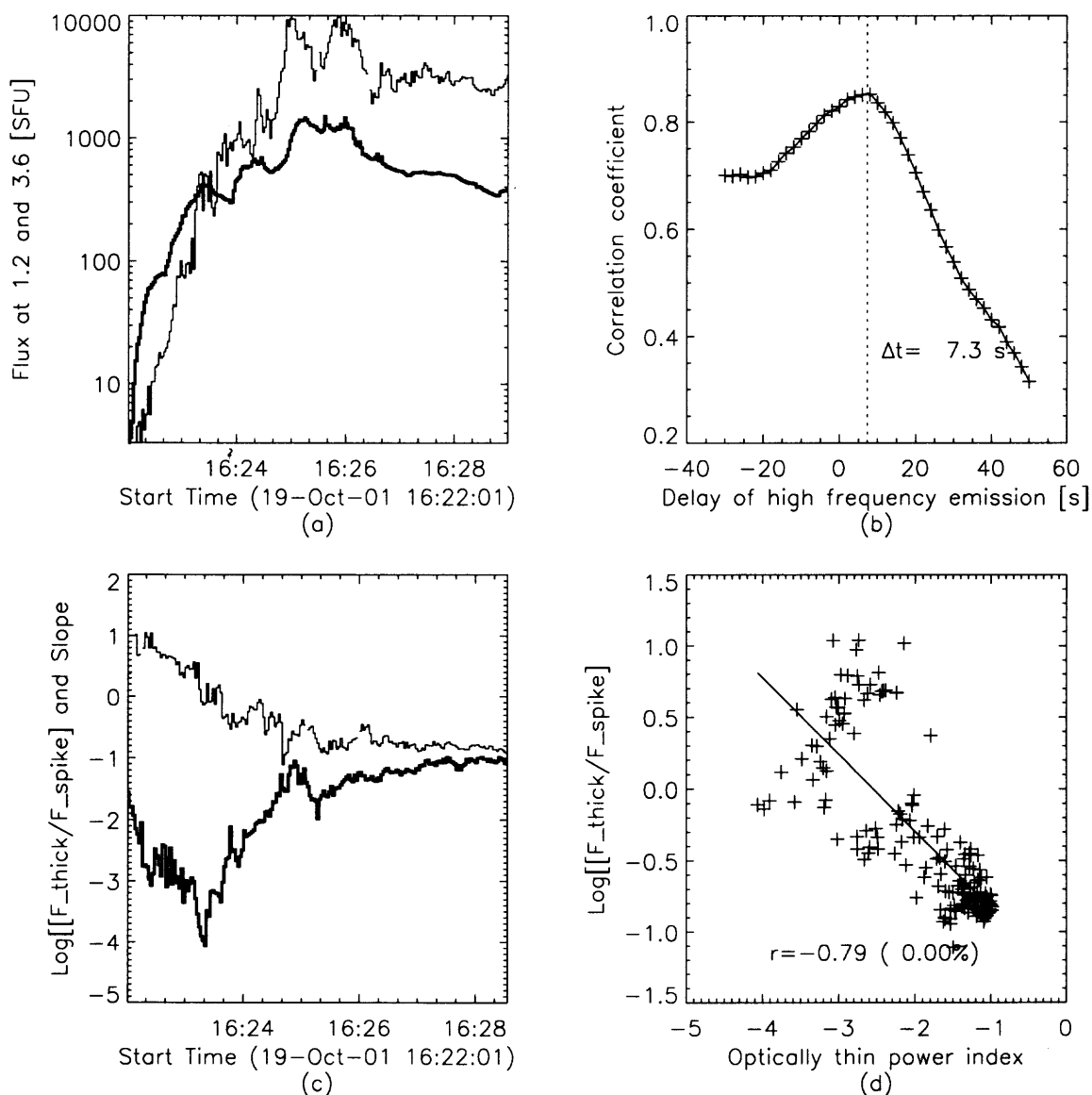


Figure 6.13 October 19, 2001: (a)-Emissions at 1.2 GHz (thin line) and the optically thick gyrosynchrotron emission at 3.6 GHz, (thick line). (b)- The linear correlation coefficient (symbols) between the magnitudes displayed in (a) for different time lags. A delay of 7.3 seconds of the high-frequency emission relative to the low-frequency emission has been estimated using a spline interpolation (solid line). (c)- The natural logarithm of the ratio between optically thick and spiky emissions (thin line) and the optically thin spectral index (thick line). (d) The correlation plot of the magnitudes displayed in (c). A linear correlation coefficient of -0.79 has been found. The probability for such a correlation coefficient to be the result of a random distribution is again 0%.

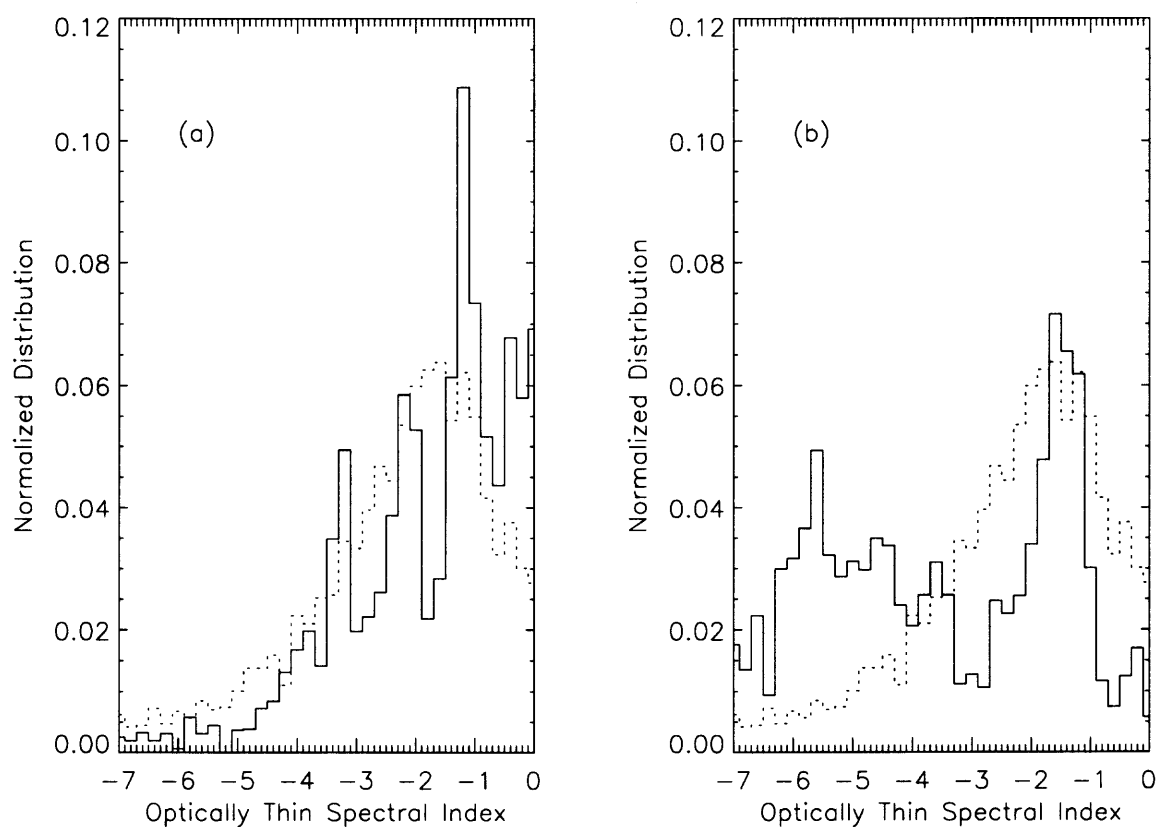


Figure 6.14 (a) Distribution of optically thin spectral index of the presumably quasi-transverse observed spike-producing bursts (solid line). (b) Distribution of optically thin spectral index of the presumably quasi-parallel observed spike-producing bursts (solid line). Both distributions are compared with that obtained for 125 gyrosynchrotron bursts above 60 sfu observed by OVSA during 2001 (dashed lines).

Thirdly, important information about the pitch-angle anisotropy of the radiating fast electrons can be obtained from the analysis of the distribution of the high-frequency microwave spectral indices. Figure 6.14a displays the distribution of spectral indices for the quasi-transverse spike-producing bursts overplotted on the overall distribution for the gyrosynchrotron bursts above 60 sfu. The average hardness of spike-producing events is similar to that for all other events (however, one could note a lack of soft $\alpha_h < -3$ values for the spike-producing events). Since α_h is related to the fast electron momentum distribution for the quasi-transverse case (Fleishman & Melnikov 2003), we can conclude that the spikes are produced by the electrons with more or less typical energy spectrum. However, for the quasi-parallel case the pitch-angle anisotropy can provide much softer gyrosynchrotron spectra for the same electron energy spectrum. Figure 6.14b displays the distribution of the spectral indices for the quasi-parallel spike-producing bursts overplotted on the overall distribution for the gyrosynchrotron bursts above 60 sfu. The respective gyrosynchrotron spectra are significantly softer than on average (one can note a strong excess in the range of $-7 < \alpha_h < -4$), which could only be ascribed to the effect of the pitch-angle anisotropy. This pitch-angle anisotropy is favorable to produce coherent ECM or plasma emission. However, the preferential X-mode polarization of the spikes together with the variations of the sense of polarization observed in many events are evidence of the ECM mechanism of spike production. The conclusion of the preferential X-mode polarization of the spikes agrees with the results of Güdel & Zlobec (1991). Since the ECM mechanism allows for both modes to be generated (Stupp 2000), the finding of Benz & Pianezzi (1997) that (for a selected set of spike observations) the original spikes are entirely O-mode polarized at their source is consistent with this model as well.

Fourthly, the analyzed events fall into two distinctive groups: those with a strong polarization of high-frequency gyrosynchrotron emission display a (positive)

correlation between $\log(F_{thick}/F_{spike})$ and α_h , while those with a weaker polarization display a (negative) anti-correlation between these two quantities. We interpret this difference as an effect of viewing angle at which the gyrosynchrotron source is observed: strong polarization corresponds to a viewing angle quasi-parallel to the magnetic field, while weaker polarization corresponds to the quasi-transverse case. For the quasi-parallel case, the gyrosynchrotron spectral index depends primarily on the pitch-angle anisotropy (Fleishman & Melnikov 2003), namely, it increases as the anisotropy increases. However, for the quasi-transverse case, the effect of pitch-angle anisotropy on the spectral index is weak, and the spectral index is specified primarily by the electron energy distribution as for isotropic case. This interpretation of these two kinds of the correlation plots is pretty consistent with the distributions of the high-frequency spectral indices (Figure 6.14) discussed above.

From the entire set of data, we therefore conclude that the millisecond solar radio spikes are generated at a source with relatively high gyro-frequency to plasma frequency ratio, during that phase of the bursts when the trapped fast electrons have the hardest energy distribution and the most anisotropic pitch-angle distribution. These properties are naturally expected within ECM theory (Fleishman & Yastrebov 1994a), while meeting large difficulties within alternative theories based on various modifications of the plasma mechanism (Fleishman & Melnikov 1998). Moreover, the pitch-angle anisotropy of the trapped electrons suggested by the data is in favor of the local trap model (Fleishman & Melnikov 1998), while inconsistent with foot-point source models of spike generation.

The incoherent microwave emission is found to be delayed significantly (by 5–30 s) with respect to averaged spike flux density. Combining this finding with the result of Aschwanden & Güdel (1992) that the averaged spike flux is delayed by 2–5 s in respect to simultaneous HXR peaks, we conclude that HXR emission arrives first, then the spike emission and finally the incoherent gyrosynchrotron emission. This

sequence is related to underlying kinetics of fast electrons: the directly precipitating electrons produce HXR emission, low-energy trapped electrons produce spikes and higher-energy trapped electrons produce incoherent gyrosynchrotron emission. This is consistent with the delays (of a few seconds to a few tens of seconds) between HXR peaks and microwave bursts found earlier (Melnikov 1994).

Aschwanden & Güdel (1992) found that sometimes there is very tight correlation between the averaged spike flux and the respective HXR flux, but sometimes there is no good flux-to-flux correlation. We found here the same property when considering the microwave emission in place of HXR emission. However, *each* spike-producing burst reveals a significant correlation between $\log(F_{thick}/F_{spike})$ and high-frequency slope α_h of the microwave gyrosynchrotron emission. This slope is related to the energy and pitch-angle distributions of the radiating fast electrons. We, thus, conclude that the spike production is directly related to the properties of the distribution function (over the momentum and pitch-angle) of the trapped electrons.

The derived properties of the distribution functions as well as source conditions (large ω_{Be}/ω_{pe} ratio) are found to be pretty consistent with those required for the ECM operation. We, therefore, can conclude that the performed study gives rise to new important evidence that millisecond solar radio spikes are produced by electron cyclotron maser mechanism.

Nevertheless, we feel that some important additional studies are necessary. For example, spatially resolved data are strongly desirable to locate the spike source in respect to the microwave source and to respective magnetic field. Also, the combined analysis of the spike, microwave and HXR bursts observed for the same events can be exceedingly helpful to constrain the involved parameters and use the spike emission for further diagnostic purposes. From this point of view, some additional work should be done to specify the gyro-harmonics providing the main contribution to the radio spike emission.

CHAPTER 7

CONCLUSION

We have examined the statistical properties of the flux density distribution of 40 years of solar radio bursts collected by the NOAA National Geophysical Data Center. The time period covered by the data includes more than 3 complete solar activity cycles (cycle 20, 21 and 22). We find that the distributions are well fit by power laws over a wide range of flux densities, but diverge from a power law at both high and low flux densities. The divergence of the distribution from the fit at low flux density probably is due to sensitivity limits of the recording instruments. This limit ranges from about 10 sfu during solar minimum to nearly 20 sfu at solar maximum. At high flux densities, the number of observed bursts again falls off relative to the fit, which may be due to instrumental limitations (e.g. saturation), or may be due to solar limitations such as the physical size of the interaction region, or total number of electrons available for energization.

During the course of our study, we found evidence that the database undercounts the true number of bursts by up to a factor of two, despite the world-wide coverage. We used the time of day distribution of reports to quantify the missed number of bursts, assuming that the peak of this distribution corresponds to longitudes where 100% of the bursts were observed. Thus, our *geographical correction factor* is a lower limit to the true correction. Even so, the correction factors we deduced average around 1.7, indicating that almost half of all events were not observed. An investigation of a non-stationary Poissonian waiting time between events using Wheatland's (2000*b*) model remarkably predicts the same factor of 1.7 based on the ratio of observed (135 min) to predicted (81 min) mean waiting times.

We developed a new approach to fitting the power-law distributions that is better for data obeying Poissonian statistics than the more widely used least squares method. The key result is that it provides a self-consistent criterion for choosing

the appropriate range over which to fit the powerlaw function based on agreement of the fits for the density and cumulative distributions. Without such a criterion, the fitting parameters depend on the arbitrary choice of fit range.

The observed occurrence rate was examined during periods of solar maximum and solar minimum, as well as separately for the three complete solar cycles. The average waiting time between occurrences of >1000 sfu events, before geographical correction, is 6 days at solar maximum, and 33 days at solar minimum. This is consistent with the estimate of one event every 10-20 days given by Bala et al. (2002). After correction these become 3.5 days and 18.5 days, respectively. Table 2.3, with equation (2.20) allows precise calculation of rates for any frequency range.

We searched for a systematic trend in the distributions as a function of epoch and frequency. We found no significant change in the power-law index from one solar cycle to the next, or phase of the solar cycle. The power-law index remained remarkably constant near -1.8 , which is also remarkably close to the slope found for hard X-ray bursts. Bai (1993) reported a slight solar-cycle dependence in power-law index at two phases of the solar cycle, amounting to a difference of 0.07 from 1980-1981 to 1982-1984. He further investigated changes on a 153.8 day cycle. Our analysis over a wider range of time failed to verify a solar cycle dependence in the radio data. We did not investigate changes on the 153.8 day timescale. Significantly, however, we did find a clear trend in power-law index as a function of frequency. Low (< 2 GHz) and high (> 15 GHz) frequencies displayed a shallower slope of near -1.7 , while the distribution in the range 4.9-7 GHz is steeper with a slope of -1.9 . This same trend appears to account at least partially for a deficit in number of bursts with flux density > 1000 sfu in the 4.9-7 GHz range.

We have investigated the microwave spectra of 412 solar radio bursts observed by OVSA during the years 2001-2002 at 40 frequencies in the 1.2–18 GHz frequency range with 4 s time resolution. For each spectrum, we have identified the main

spectral and temporal components. Each spectral component has been analyzed and the main spectral parameters, i.e peak frequency, peak flux density, and the spectral slopes below and above the peak frequency, have been derived at any instant of time.

We found the distribution of these parameters to be the result of a superposition of at least two distinct populations: the dm radio emission, which has a upper frequency limit of about 2.6 GHz and no characteristic flux size, and the cm radio emission, which in 50% of the cases has its spectral peak in the range defined by [4.9, 9.0] GHz and [26, 137] sfu limits, and has a frequency dependent limit of the peak flux density described by a $\sim \nu^2$ power law with an offset of ~ 300 sfu at 1 GHz. We found the superposition of these two populations to be responsible for the lack of strong radio emission at intermediate frequencies and for the frequency dependence of the peak flux distribution power-law slope, previously reported by Nita et al. (2002). We found the power-law slope of the peak flux number density distribution to be -1.42 ± 0.09 for the dm events, and -1.73 ± 0.04 for the cm ones, consistent with the Nita et al. (2002) results.

The increase of the average peak frequency with the increasing flux density of the cm emission, previously reported by Castelli & Guidice (1972), is now confirmed by the OVSA data set. Some 50% of the cm bursts have an absolute peak frequency in the [4.7, 8.1] GHz range, when their absolute peak flux is below 100 sfu, but this rises to [5.0, 10.9] GHz, for flux densities between 100 and 1000 sfu, and further to [4.9, 12.7] GHz, for flux densities above 1000 sfu.

We have also found an evident spectral flattening on both optically thick and optically thin sides of the gyrosynchrotron spectra for increasing peak flux density ranges. The 50% probability ranges are [1.3, 2.9] for the low frequency spectral slope and $[-3.6, -1.9]$ for the high frequency spectral slope below 100 sfu, [1.0, 2.4] and $[-2.8, -1.5]$ between 100 and 1000 sfu, [1.0, 1.8] and $[-2.4, -1.5]$ above 1000 sfu. We interpret this result as an indication that statistically the strongest flares come from

the most inhomogeneous sources (which flattens the low-frequency slope) and are simultaneously produced by electrons with statistically harder energy distributions (which flattens the high-frequency slope).

We have divided our data base into three main spectral classes based on the frequency range of the absolute peak frequency, below or above the empirical 2.6 GHz dividing line: (1) the pure cm bursts, C-type, (2) the pure dm bursts, D-type, and (3) the composite CD-type. We have carried out a detailed analysis of the spectral and temporal characteristics of these classes, presenting tables that list the most probable spectral and temporal parameters of each class in different frequency and intensity ranges.

We find that the pure cm C-type is mainly composed by impulsive bursts, while the pure dm D-type contains two populations corresponding to smooth or rapidly changing times profiles. Remarkably, we find that the frequency-dependent flux-density limit seen for cm emission also limits the peak flux of pure dm D-type bursts. In contrast, all dm bursts peaking above this limit, i.e. > 1000 sfu, are low-frequency counterparts of composite CD-bursts, and thus satisfy the criteria to be classified as U-shaped bursts (Cliver, McNamara & Gentle 1985). We interpret this finding as an indication that the gyrosynchrotron emission mechanism may produce the weaker dm bursts, with a flux density limit unlikely to exceed ~ 300 sfu at 1 GHz, while the coherent emission mechanisms, which are likely responsible for the rest of the dm bursts, seem not to be very efficient except when accompanied by a cm- λ counterpart.

We have investigated the properties of multi-spectral component bursts and find that the percentage of CD-type bursts, 17% for the whole database, increases with the flux density of the microwave bursts, being 12% below 100 sfu, 19% between 100 and 1000 sfu, and 60% above 1000 sfu. These percentages may be even larger when taking into account the possibility of undetected low frequency components

below the 1.2 GHz lower frequency limit of OVSA. We find no significant evidence for the harmonic structure of multi-component bursts previously suggested by Stähli, Gary & Hurford (1990). However, we find in most cases a strong correlation between peak fluxes of the spectral components of multi-component bursts, which suggests a physical connection between them, investigated in detail elsewhere (Fleishman, Gary & Nita 2003; Fleishman, Nita & Gary, in preparation).

Dynamical changes in the peak frequency of the GS spectrum of intense microwave bursts have been analyzed using data on more than 300 bursts obtained in 2001-2002 with OVSA. We find that the dynamical changes show a few distinct behaviors, which we have interpreted in terms of two competing effects: a) GS self-absorption and b) Razin suppression.

Observationally, we find that for a majority of simple bursts the peak frequency is very well correlated with the intensity of microwave bursts, at least near the burst maximum. The peak frequency increases on the rise phase in $\sim 84\%$ of bursts in our sample, and decreases on the decay phase in $\sim 64\%$ of bursts, in qualitative agreement with GS self-absorption as the origin of the low frequency turnover of the spectrum. For some bursts of this type, however, we find a faster than expected decrease of f_{peak} on the decay phase. This behavior is correlated with flattening of the high-frequency slope (increasing α_h) of the microwave spectrum, which is indicative of hardening of the electron energy distribution. The presence in many bursts of a positive or negative time difference between the maxima of f_{peak} and S_{peak} time profiles is also shown to be due to GS self-absorption under evolution (usually hardening but sometimes softening) of the electron spectral index.

However, we also find that for $\sim 30\text{-}36\%$ of bursts the peak frequency increase near the burst maximum is much smaller than expected or even may be entirely absent. Typically in these bursts f_{peak} starts at a rather high frequency in the very beginning of the burst and remains almost constant during a considerable (factor of

~ 10) increase and decrease of the burst intensity. We explain this temporal behavior as follows: In the beginning of the rise phase and during the late decay phase the radio source is optically thin at low frequencies due to the Razin effect. But briefly, near the maximum, when the column density of nonthermal particles becomes high enough, the source becomes nearly optically thick at $f \leq f_{peak}$, despite of the Razin suppression, and the spectral evolution of f_{peak} takes on the characteristics for GS self-absorption.

About 70% of bursts show a gradual increase in f_{peak} starting at some point in the decay phase. We show that this behavior can easily be explained by Razin suppression together with either hardening of the high energy electron spectrum or an increase in Razin parameter (due to an increase in plasma density or a decrease in magnetic field strength in the microwave source). Again, the evidence for electron spectral hardening comes directly from the observed flattening of the microwave high frequency spectral slope. An increase in f_{peak} in the late phase that is unaccompanied by microwave spectral flattening may thus be a direct signature of chromospheric evaporation and/or evolution of the source to greater heights where the magnetic field strength is lower.

Using numerical calculations from GS theory, including the effect of the medium, we have confirmed that the wide range of evolutionary behavior can be interpreted as an interplay between GS self-absorption and Razin suppression. We can say that Razin suppression plays an important role in the spectral dynamics of more than 70% of bursts, at least on their decay phase. For the Razin effect to be important for a relatively large number of bursts (with average $f_{peak} \sim 6$ GHz), we require that the magnetic field in the source be relatively weak (100-300 G for a corresponding plasma density $(1 - 10) \times 10^{10} \text{ cm}^{-3}$). The changes in f_{peak} can be used quantitatively as a further constraint on the evolution of plasma parameters, especially ambient density and magnetic field strength. Together, the combination

of spectral measures (1) temporal evolution of f_{peak} , (2) R , the logarithm of the ratio of flux densities above and below f_{peak} , and (3) the high-frequency slope α_h , relative to the flux density at spectral maximum, S_{peak} provide a new, valuable diagnostic for microwave bursts of GS origin.

To be of greatest diagnostic power, the spectral dynamics should be measured in brightness temperature, i.e. using spatially resolved spectra. This requires simultaneous spatial and spectral resolution over a wide band of frequencies. The work of Belkora (1997) is the only published example that showed Razin suppression in a brightness temperature spectrum. Such observations will be possible routinely with a new generation radio facility, the Frequency Agile Solar Radiotelescope (FASR), now being designed. For more comprehensive application of these new diagnostics to flaring loops, such microwave data should be analyzed in combination with diagnostics from EUV, X-ray and gamma-ray data.

We calculate parameters of nonthermal electrons in solar flares from the microwave flux spectra of 412 flares measured with the Owens Valley Solar Array (OVSA) in 2001-2002. The parameters are: power-law index δ of the electron energy distribution and total number and energy of the electrons integrated over energy and space. We have selected the events with spectral/temporal behaviors indicative of nonthermal gyrosynchrotron radiation so that gyrosynchrotron formulae apply.

We use the measured spectral index to determine the power-law index, the peak frequency ν for column density of nonthermal electrons, and finally the peak flux S_ν for the total number of the electrons. We also employ an empirical relationship between area and flux that we found from the Nobeyama Radioheliograph data to complement the OVSA data.

The total nonthermal energy integrated above 10 keV from 588 bursts peaks forms a power-law distribution with index around -1.2 , extending over a wide range from $\sim 10^{25}$ erg to $\sim 10^{34}$ erg. The corresponding total numbers of nonthermal

electrons are $\sim 10^{34}$ and $\sim 10^{42}$, respectively. There is an apparent trend that softer events show larger numbers of electrons concentrated at low energy interval (10-100 keV) and thus total energy content exceeding that of harder events. This trend, however, vanishes or reverses if we restrict the number integration to higher energies (≥ 100 keV). We therefore conclude that a plausible acceleration mechanism should have no preferred value of δ in terms of efficiency of nonthermal electron production.

The derived flare parameters are best correlated with the observed peak flux divided by the square of the peak frequency, so that the total nonthermal energy integrated above 100 keV is well approximated by $\sim 2 \times 10^{24} (S_\nu / \nu^2)^{-2.7}$ ergs where S_ν is in sfu and ν , in GHz. We compare our results mainly with previous hard X-ray studies and briefly discuss their implications for electron acceleration.

The present result for the upper limit in the distribution of total energy ($\sim 10^{33}$ ergs for $E_0 = 25$ keV) is within an order of magnitude the previously known energy from HXR: $\sim 10^{32}$ erg above 25 keV for the 1972 August series flares (Lin & Hudson 1971, 1976) or $\sim 4 \times 10^{32}$ erg for the 2002 July 23 flare (Lin et al. 2003). This is somewhat contrary to our expectation that the energy from HXR diagnostics is obtained by integrating the observed flux over the flare duration, and would thus be higher than inferred from our microwave diagnostic, which pertains to the instantaneous energy at the peak time. By chance, we might have both results comparable to each other if a flare is so impulsive that the energy deposition rate is mostly confined to the peak time.

Another simple resolution can be argued based on the fact that microwaves represent electrons trapped in the corona while HXR are due to the precipitating electrons. The numbers can differ by a finite ratio depending on the mirror ratio and pitch angles (see, for a review, Lee 2003). Suppose that 10% of the accelerated electrons precipitate into the chromosphere to emit thick target bremsstrahlung at the footpoints while the other 90% remain in the corona to emit microwaves. The

factor of ten difference could then be explained. However, our results are based on a number of assumptions that, while statistically justified for the population as a whole, may become suspect when extrapolated to the largest events. Therefore, the discrepancy in numbers and energy may not be significant. To improve the comparison, we will need spatially resolved observations with measured brightness temperatures. A more careful analysis may also be needed that takes into account the acceleration and loss time scales (Lin & Hudson 1971) or conversion of the microwave flux to nonthermal energy production rate (Gary 1985).

The total nonthermal energy that we derived in the present study obeys a power law with index ~ -1.2 , which is considerably flatter than the corresponding result (~ -1.53) obtained with the HXRBS/SMM data (Crosby et al. 1993). We do not have a clear explanation for the difference, also it may be due in part to the differences in the ratio of the trapped electrons to the precipitating electrons discussed above, so that the microwave diagnostic may systematically extend the distribution to higher energies, leading to a shallower slope. Alternatively, the difference may have something to do with the weighting of the microwaves to electrons of higher energies than for the HXR emission. However, we consider our power law measurement to be robust, in the sense that the law holds over a wide energy range, and only weakly depends on the low energy bound E_0 .

We note, however, that a power-law index near -1.8 is found for directly observed microwave fluxes. At radio wavelengths, monochromatic flux at a fixed frequency (Akabane 1956) or the maximum flux distribution at the peak frequency (Chapter 3) shows such a power law index around -1.7 , and the scaled flux, S_ν/ν^2 , in the present study shows a power-law index around -1.6 . A series of flare parameter studies based on the same HXR data set (HXRBS/SMM) presented slightly differing slopes depending on the selection criterion (Crosby et al. 1993). Also a relatively low slope was found for a derived quantity such as total energy in HXR emitting electrons,

which is derived after multiplication of energy deposition rate and duration, each of which has its own distribution. In the present case, the mean energy and area showed much steeper distributions with index -3.6 ± 0.34 and -2.57 ± 0.23 , respectively. Presumably the (much steeper) distributions of these auxiliary parameters such as mean energy and area play a role in shaping the resulting distribution of total electron energy. Therefore, a more careful determination of these parameters could be important to establish the universality of the power-law distribution of major flare parameters (cf. Wheatland & Sturrock 1996).

We finally discuss our result for the electron power-law index δ as a potentially important issue in electron acceleration. We found that the strong events ($y > 30$) tend to show a hard spectrum with a relatively narrow range of δ , whereas weaker events ($y < 3$) appear in a much wider range (Fig.5.4). There are, in fact, a few HXR studies that presented HXR spectral index distributions consistent with this result. On the other hand, our finally derived total energy (integrated above 100 keV) shows no good correlation with δ (Fig.5.6). The latter is a result confining our investigation to moderately harder events $2 < \delta < 6$ in which case the numbers of strong ($y > 30$), moderate ($y < 30$) and weak ($y < 3$) events distribute more uniformly with δ . Contrary to our naive speculation that softer events would have less nonthermal energy, **they** can have a large total number of electrons within a relatively low energy range (say 10–100 keV) and, as a result, can have a total energy as large as another event with harder, but fewer electrons. With the present result alone, there seems to be no preferred value of δ for strong flares in terms of total nonthermal electrons.

We briefly compare this result to the stochastic electron acceleration model by Hamilton & Petrosian (1991) which predicts a detailed shape of the electron energy distribution in phase space, $n(E)$ in our notation. The model shows that $n(E)$ at the peak time is not necessarily in single power law, although under our assumption we

nevertheless approximate it as one. But we can at least expect that this acceleration mechanism can produce δ in the wide range that we find, with no apparent effect on the total energy content. We repeat that δ inferred from HXR and microwaves may represent properties of $n(E)$ in differing energy ranges. Because the electron distribution at relatively low energies (10–100 keV) tends to be strongly influenced by Coulomb collisions whereas at high energies ($\gtrsim 200$ keV) it is largely determined by the accelerator, our result from microwaves may better reflect the accelerator properties. In that case, our result that E_{tot} is insensitive to δ could be a property associated with the acceleration process.

We analyzed in some detail six events producing dense spike clusters in the frequency range 1.2 – 3.4 GHz observed simultaneously with microwave gyrosynchrotron continuum.

A few new important findings are firmly established. First of all, the low-frequency part of the respective microwave bursts is considerably flatter than for the overall microwave event set. This means that there is no indication of the Razin effect operating in the microwave events accompanying the decimetric spike bursts. Consequently, the ratio ω_{Be}/ω_{pe} is large enough in the spike sources to allow operation of the ECM mechanism.

Secondly, all five events with polarization data available reveal a *high* degree of polarization in the optically thin gyrosynchrotron range significantly larger than typical mean value of $20\% \pm 16\%$ (Bruggmann & Magun 1990). This deviation is most probably related to the fast electron pitch-angle anisotropy (of the loss-cone type), which increases the degree of X-mode polarization compared with isotropic case (Fleishman & Melnikov 2003). Moreover, two of the analyzed events do not display a change of the sense of polarization from the thin to thick region, which might be related to the effect of the pitch-angle anisotropy as well (Fleishman & Melnikov 2003). Note that the high degree of polarization implies a rather non-

symmetric magnetic structure at the source site, since a symmetric loop would give more equal fluxes in both polarizations, leading to smaller net polarization.

Thirdly, important information about the pitch-angle anisotropy of the radiating fast electrons can be obtained from the analysis of the distribution of the high-frequency microwave spectral indices. Figure 6.14a displays the distribution of spectral indices for the quasi-transverse spike-producing bursts overplotted on the overall distribution for the gyrosynchrotron bursts above 60 sfu.

The average hardness of spike-producing events is similar to that for all other events (however, one could note a lack of soft $\alpha_h < -3$ values for the spike-producing events). Since α_h is related to the fast electron momentum distribution for the quasi-transverse case (Fleishman & Melnikov 2003), we can conclude that the spikes are produced by the electrons with more or less typical energy spectrum. However, for the quasi-parallel case the pitch-angle anisotropy can provide much softer gyrosynchrotron spectra for the same electron energy spectrum.

Figure 6.14b displays the distribution of the spectral indices for the quasi-parallel spike-producing bursts overplotted on the overall distribution for the gyrosynchrotron bursts above 60 *sfu*. The respective gyrosynchrotron spectra are significantly softer than on average (one can note a strong excess in the range of $-7 < \alpha_h < -4$), which could only be ascribed to the effect of the pitch-angle anisotropy. This pitch-angle anisotropy is favorable to produce coherent ECM or plasma emission. However, the preferential X-mode polarization of the spikes together with the variations of the sense of polarization observed in many events are evidence of the ECM mechanism of spike production. The conclusion of the preferential X-mode polarization of the spikes agrees with the results of Güdel & Zlobec (1991). Since the ECM mechanism allows for both modes to be generated (Stupp 2000), the finding of Benz & Pianezzi (1997) that (for a selected set of spike

observations) the original spikes are entirely O-mode polarized at their source is consistent with this model as well.

Fourthly, the analyzed events fall into two distinctive groups: those with a strong polarization of high-frequency gyrosynchrotron emission display a (positive) correlation between $\log(F_{thick}/F_{spike})$ and α_h , while those with a weaker polarization display a (negative) anti-correlation between these two quantities. We interpret this difference as an effect of viewing angle at which the gyrosynchrotron source is observed: strong polarization corresponds to a viewing angle quasi-parallel to the magnetic field, while weaker polarization corresponds to the quasi-transverse case. For the quasi-parallel case, the gyrosynchrotron spectral index depends primarily on the pitch-angle anisotropy (Fleishman & Melnikov 2003), namely, it increases as the anisotropy increases. However, for the quasi-transverse case, the effect of pitch-angle anisotropy on the spectral index is weak, and the spectral index is specified primarily by the electron energy distribution as for isotropic case. This interpretation of these two kinds of the correlation plots is pretty consistent with the distributions of the high-frequency spectral indices (Figure 6.14) discussed above.

From the entire set of data, we therefore conclude that the millisecond solar radio spikes are generated at a source with relatively high gyro-frequency to plasma frequency ratio, during that phase of the bursts when the trapped fast electrons have the hardest energy distribution and the most anisotropic pitch-angle distribution. These properties are naturally expected within ECM theory (Fleishman & Yastrebov 1994a), while meeting large difficulties within alternative theories based on various modifications of the plasma mechanism (Fleishman & Melnikov 1998). Moreover, the pitch-angle anisotropy of the trapped electrons suggested by the data is in favor of the local trap model (Fleishman & Melnikov 1998), while inconsistent with foot-point source models of spike generation.

The incoherent microwave emission is found to be delayed significantly (by 5–30 s) with respect to averaged spike flux density. Combining this finding with the result of Aschwanden & Güdel (1992) that the averaged spike flux is delayed by 2–5 s in respect to simultaneous HXR peaks, we conclude that HXR emission arrives first, then the spike emission and finally the incoherent gyrosynchrotron emission. This sequence is related to underlying kinetics of fast electrons: the directly precipitating electrons produce HXR emission, low-energy trapped electrons produce spikes and higher-energy trapped electrons produce incoherent gyrosynchrotron emission. This is consistent with the delays (of a few seconds to a few tens of seconds) between HXR peaks and microwave bursts found earlier (Melnikov 1994).

Aschwanden & Güdel (1992) found that sometimes there is very tight correlation between the averaged spike flux and the respective HXR flux, but sometimes there is no good flux-to-flux correlation. We found here the same property when considering the microwave emission in place of HXR emission. However, *each* spike-producing burst reveals a significant correlation between $\log(F_{thick}/F_{spike})$ and high-frequency slope α_h of the microwave gyrosynchrotron emission. This slope is related to the energy and pitch-angle distributions of the radiating fast electrons. We, thus, conclude that the spike production is directly related to the properties of the distribution function (over the momentum and pitch-angle) of the trapped electrons.

The derived properties of the distribution functions as well as source conditions (large ω_{Be}/ω_{pe} ratio) are found to be pretty consistent with those required for the ECM operation. We, therefore, can conclude that the performed study gives rise to new important evidence that millisecond solar radio spikes are produced by electron cyclotron maser mechanism.

Nevertheless, we feel that some important additional studies are necessary. For example, spatially resolved data are strongly desirable to locate the spike source in respect to the microwave source and to respective magnetic field. Also, the combined

analysis of the spike, microwave and HXR bursts observed for the same events can be exceedingly helpful to constrain the involved parameters and use the spike emission for further diagnostic purposes. From this point of view, some additional work should be done to specify the gyro-harmonics providing the main contribution to the radio spike emission.

REFERENCES

- [Akabane (1956)] Akabane, K. 1956, PASJ, 8, 173
- [Altyntsev et al. (1995)] Altyntsev, A. T., Grechnev, V. V., Zubkova, G. N., Lesovoi, S. V., Lisyian, E. G., Treskov, T. A., Rosenraukh, Y. M., & Magun, A., 1995, A&A, 303, 249
- [Altyntsev et al. (1996)] Altyntsev, A. T., Grechnev, V. V., Kononov, S. K., Lesovoi, S. V., Lisyian, E. G., Treskov, T. A., Rosenraukh, Y. M., & Magun, A., 1996, ApJ, 469, 976
- [Antonucci (1982)] Antonucci, 1982, Observatory, 102, 121
- [Aschwanden (1990)] Aschwanden, M. J., 1990, Astron. Astrophys. Suppl. 85, 1141
- [Aschwanden & Güdel (1992)] Aschwanden, M. J., & Güdel, M., 1992 ApJ, 401, 736
- [Aschwanden et al. (1995)] Aschwanden, M. J., Benz, A. O., Dennis, B. R., & Schwartz, R. A., 1995, ApJ, 455, 347
- [Aschwanden et al. (2000)] Aschwanden, M. J., Tarbell, T. D., Nightingale, R. W., Schrijver, C. J., Title, A., Kankelborg, C. C., Martens, P., & Warren, H. P. 2000, ApJ, 535, 1047
- [Aschwanden, Dennis & Benz (1998)] Aschwanden, M. J., Dennis, B. R., & Benz, A. O. 1998, ApJ, 497, 972
- [Bai (1986)] Bai, T., 1986, ApJ, 308, 912
- [Bai (1993)] Bai, T. 1993, ApJ, 404, 805
- [Bak, Tang & Wiesenfeld (1988)] Bak, P., Tang, C., & Wiesenfeld, K. 1988, Phys. Rev. A, 38, 364
- [Bala et al. (2002)] Bala, B., Lanzerotti, L. J., Gary, D. E., & Thomson, D. J. 2002, Radio Science, 37 (2), 1018
- [Barta & Karlický (2001)] Barta, M., & Karlický, M., 2001, A&A, 379, 1045
- [Bastian, Bentz & Gary (1998)] Bastian, T. S., Benz, A. O. & Gary, D. E. 1998, ARA&A, 36, 131
- [Belkora (1997)] Belkora, L., 1997, ApJ, 481, 532
- [Benz (1985)] Benz, A. O., 1985, Sol. Phys., 96, 357
- [Benz (1986)] Benz, A. O., 1986, Sol. Phys., 104, 99
- [Benz (1993)] Benz, A. O., 1993, *Plasma astrophysics: Kinetic processes in solar and stellar coronae*, Dordrecht: Kluwer

- [Benz & Güdel (1987)] Benz, A. O., & Güdel M., 1987, *Sol. Phys.*, 111, 175
- [Benz & Pianezzi (1997)] Benz, A. O., & Pianezzi, P., 1997, *A&A*, 323, 250
- [Benz, Zlobec & Jaeggi (1982)] Benz, A. O., Zlobec, P., & Jaeggi, M., 1982, *A&A*, 109, 305
- [Berghmans, Clette & Moses (1998)] Berghmans, D., Clette, F., & Moses, D. 1998, *A&A*, 336, 1039
- [Bevington & Robinson (1992)] Bevington, P. R. & Robinson, D. K. 1992, *Data Reduction and Error Analysis for the Physical Sciences*, New York: McGraw-Hill
- [Biesecker (1994)] Biesecker, D. A. 1994, Ph.D.Thesis, University of New Hampshire
- [Boffeta et al. (1999)] Boffeta, G., Carbone, V., Giuliani, P., Velti, P., & Vulpiani, A., 1999, *Phys. Rev. Lett.*, 83, 4662
- [Bromund, McTiernan & Kane (1995)] Bromund, K. R., McTiernan, J. M., & Kane, S. R. 1995, *ApJ*, 455, 733
- [Brown (1982)] Brown, J. C., 1971, *Sol. Phys.*, 18, 489
- [Brown & Hoyng (1975)] Brown, J. C.; Hoyng, P., 1975, *ApJ*, 200, 734
- [Bruggmann & Magun (1990)] Bruggmann, G., & Magun, A.. 1990, *A&A*, 239, 347
- [Bruggmann et. al. (1990)] Bruggmann, G., Benz, A. O., Magun, A., & Stehling, W. 1990, *å*, 240, 506
- [Castelli & Guidice (1972)] Castelli, J. P.& Guidice, D. A. 1972, AFCRL-72-0049
- [Cliver, McNamara & Gentle (1985)] Cliver, E. W.,McNamara, L. F., & Gentle, L. C., AFGL-TR-85-0180
- [Covington (1951)] Covington, A. E., 1951, *JRASC*, 45, 49
- [Crosby, Aschwanden & Dennis (1993)] Crosby, N. B., Aschwanden, M. J., & Dennis, B. R., 1993, *Sol. Phys.*, 143, 275
- [Csillaghy & Benz (1993)] Csillaghy, A., & Benz, A. O., 1993, *A&A*, 274, 487
- [Dennis (1985)] Dennis, B. R., 1985, *Sol. Phys.*, 100, 465
- [Dodson, Hedeman & Covington (1954)] Dodson, H. W., Hedeman, E. R., Covington, A. E., 1954, *AJ*, 58, 213
- [Drake (1971)] Drake, J. F., 1971, *Sol. Phys.*, 16, 152
- [Dulk (1985)] Dulk85 Dulk, G. A. 1985, *ARA&A*, 23, 169

- [Dulk & K (1982)] Dulk, G. A., Kiplinger, A. L., & Winglee, R. M. 1992, ApJ, 389, 756
- [Dulk & Marsh (1982)] Dulk, G. A. & Marsh, K. A., 1982, ApJ, 259, 350
- [Dulk, Kiplinger, Winglee (1992)] Dulk, G. A., Kiplinger, A. L., & Winglee, R. M., 1992, ApJ, 389, 756
- [Fitzenreiter, Fainberg & Bundy (1976)] Fitzenreiter, R. J., Fainberg, J., & Bundy, R. B., 1976, Sol. Phys., 46, 465
- [Fleishman (1994)] Fleishman, G. D., 1994, Sol. Phys., 153, 367
- [Fleishman & Arzner (2000)] Fleishman, G. D., & Arzner, K., 2000, A&A, 358, 776
- [Fleishman & Melnikov (1998)] Fleishman, G. D., & Melnikov, V.F., 1998, Physics - Uspekhi, 41, 1157
- [Fleishman & Melnikov (2003)] Fleishman, G. D., & Melnikov, V. F., 2003, ApJ, 587, 823
- [Fleishman & Platonov (1999)] Fleishman, G. D., & Platonov, K.Yu., 1999, Proc. 9th European Meeting on Solar Physics, "Magnetic Fields and Solar Processes", Florence, Italy, 12-18 September 1999. ESA SP-448, December 1999, 2, 809
- [Fleishman & Yastrebov (1994a)] Fleishman, G. D., & Yastrebov, S. G., 1994a, Solar Phys. 153, 389
- [Fleishman & Yastrebov (1994b)] Fleishman, G. D., & Yastrebov, S. G., 1994b, Sol. Phys., 154, 361
- [Fleishman, Gary & Nita (2003)] Fleishman, G. D., Gary D. E., & Nita G. M. 2003, ApJ, 573
- [Fleishman, Nita & Gary (in preparation)] Fleishman, Nita G. M., & G. D., Gary D. E.
- [Güdel (1990)] Güdel, M., 1990, A&A, 239, L1
- [Güdel & Benz (1990)] Güdel, M., & Benz, A. O., 1990, A&A, 231, 202
- [Güdel & Zlobec (1991)] Güdel, M., & Zlobec, P., 1991, A&A, 245, 299
- [Güdel, Aschwanden & Benz (1991)] Güdel, M., Aschwanden, M.J., & Benz, A. O., 1991, A&A, 251, 285
- [Gary (1985)] Gary, D. E., 1985, ApJ, 297, 799
- [Gary & Hurford (1994)] Gary, D. E. & Hurford, G. J., 1994, ApJ, 420, 903

- [Gary & Hurford (1998)] Gary, D. E., & Hurford, G. J., 1998, Proc. of the Nobeyama Symposium, Kiyosato, Japan, Oct. 27-30, Eds.: T. S. Bastian, N. Gopalswamy & K. Shibasaki, NRO Report No. 479., 429, 2000
- [Gary, Hurford & Flees (1991)] Gary, D.E., Hurford, G.J., & Flees, D.J., 1991, ApJ, 369, 255
- [Georgoulis, Vilmer & Crosby (2001)] Georgoulis, M. K., Vilmer, N., & Crosby, N. B. 2001, A&A, 367, 326
- [Ginzburg (1953)] Ginzburg, V. L., 1953, Vspekhi Fiz. Nauk, 51, 343
- [Guidice & Castelli (1975)] Guidice, D. A., & Castelli, J. P., 1975, Sol. Phys., 44, 155
- [Hamilton & Petrosian (1992)] Hamilton, R.J. & Petrosian, V. 1992, ApJ, 398, 350
- [Holman & Benka (1992)] Holman, G. D. & Benka, S. G., 1992, ApJ, 400, L79
- [Holman et al. (2003)] Holman, G. D., Sui, L., Schwartz, R. A., & Emslie, A. G., 2003, ApJ, 595, L97
- [Huang (1987)] Huang, G.-L., 1987, Sol. Phys., 114, 363
- [Hudson, Peterson & Schwartz (1969)] Hudson, H. S., Peterson, L. E., Schwartz, D. A., 1969, ApJ, 157, 389
- [Hurford, Read & Zirin (1984)] Hurford G. J., Read R. B., Zirin H., 1984, Sol. Phys., 94, 413
- [Islaker & Benz (2001)] Islaker, H. & Benz, A. O. 2001, A&A, 375, 1040
- [Kai (1968)] Kai, K. 1968, PASJ, 20, 140
- [Kakinuma, Yamashita & Enome (1969)] Kakinuma, T., Yamashita, T., & Enome, S. 1969, Proc. Res. Instit. Atmospheric (Nagoya: Res. Instit. Atmospheric), 16, 12
- [Kane & Anderson (1970)] Kane, S. R. & Anderson, K. A., 1970, ApJ, 162, 1003
- [Karlický (1984)] Karlický, M., 1984, Sol. Phys., 92, 329
- [Karlický, Sobotka & Jiricka (1996)] Karlický, M., Sobotka, M., & Jiricka, K., 1996, Sol. Phys., 168, 375
- [Klein (1987)] Klein, K.-L., 1987, A&A, 183, 341
- [Krucker & Benz (1994)] Krucker, S., & Benz A. O., 1994, A&A, 285, 1038
- [Krucker & Benz (1998)] Krucker, S. & Benz, A. O., 1998, ApJ, 501, L213

- [Kucera et al. (1997)] Kucera, T. A., Dennis, B. R., Schwartz, R. A., & Shaw, D. 1997, ApJ, 475, 338
- [Kuijpers, Van der Post & Slottje (1981)] Kuijpers, J., Van der Post, P., & Slottje, C., 1981, A&A, 103, 331
- [Kundu (1965)] Kundu M. R., 1965, *Solar Radio Astronomy*, New York: Interscience, 1965
- [Kundu & Valhos (1982)] Kundu M.R., & Vlahos L., 1982, Space Sci. Rev., 32, 405
- [Lanzerotti, Thomson & Maclellan (1999)] Lanzerotti, L. J., Thomson, D. J. & Maclellan, C. G. 1999, Modern Radio Sci.
- [Ledenev (1998)] Ledenev, V.G., 1998, Sol. Phys., 179, 405
- [Lee (2003)] Lee, J. 2003, in Solar and Space Weather Radiophysics (Ed.) Dale E. Gary and Christoph O. Keller, Astrophysics and Space Science Library series, Kluwer Academic Publishers, Chapter 8
- [Lee & Gary (1994)] Lee, J., & Gary, D. E., 1994, Sol. Phys., 153, 347
- [Lee & Gary (2000)] Lee, J., & Gary, D. E., 2000, ApJ, 543, 457
- [Lee et al. (2003)] Lee, J., Gallagher, P.T., Gary, D.E., Nita, G.M., Choe, G. S., Bong, S-C., & Yun, H.S. 2003, ApJ, 585, 524
- [Lee et al.(1994)] Lee, J., Gary, D. E., & Zirin, H., 1994, Sol. Phys., 152, 409
- [Lee, Gary & Zirin (1994)] Lee, J., Gary, D. E., & Zirin, H., 1994, Sol. Phys., 152, 409
- [Lee, Nita & Gary (in preparation)] Lee, J., Nita G. M., & Gary D. E.
- [Li (1986)] Li, H.W., 1986, Sol. Phys.104, 131
- [Lin & Hudson (1971)] Lin, R. P. & Hudson, H. S., 1971, Sol. Phys., 17, 412
- [Lin & Hudson (1976)] Lin, R. P. & Hudson, H. S., 1976, Sol. Phys., 50, 153
- [Lin et al (1984)] Lin, R. P., Schwartz, R. A., Kane, S. R., Pelling, R. M., & Hurley, K. C., 1984, ApJ, 283, 421
- [Lin et al. (2003)] Lin, R. P., Krucker, S., Hurford, G. J., Smith, D. M., Hudson, H. S., Holman, G. D., Schwartz, R. A., Dennis, B. R., Share, G. H., Murphy, R. J., Emslie, A. G., Johns-Krull, C., Vilmer, N., 2003, ApJ, 595, L69
- [Lin, Feffer & Schwartz (2001)] Lin, R. P., Feffer, P. T., & Schwartz, R. A. 2001, ApJ, 557, L125
- [Lu & Hamilton (1991)] Lu, E. T., & Hamilton, R. J., 1991, ApJ, 474, L65

- [Lu et al. (1993)] Lu, Edward T.; Hamilton, Russell J., McTiernan, J. M., Bromund, Kenneth R., 1993, ApJ, 412, 841
- [McLean, Nelson & Dulk (1985)] McLean, D. J., Nelson, G. J., & Dulk, G. A., 1985, *Solar radiophysics: Studies of emission from the sun at metre wavelengths*, Cambridge and New York, Cambridge University Press, 53
- [McTiernan & Petrosian (1991)] McTiernan, J. M., & Petrosian, V., 1991, ApJ, 379, 381
- [Melnikov (1994)] Melnikov, V. F., 1994, Radiophys. & Quant.Electr., 37 (7), 557
- [Melnikov & Magun (1996)] Melnikov, V. F., Magun, A., 1996, Radiophys. & Quant.Electr., 39, 971
- [Melnikov & Magun (1998)] Melnikov, V. F., Magun, A., 1998, Sol. Phys., 178, 153
- [Melnikov et al. (2003)] Melnikov, V. F., Reznikova, V.E., & Shibasaki, K., 2003, ApJ(submitted)
- [Melnikov, Gary & Nita (in preparation)] Melnikov V. F., Gary D. E., & Nita G. M.
- [Melrose & Dulk (1982)] Melrose, D. B., Dulk, G. A., 1982, ApJ, 259, 41
- [Mercier & Trottet (1997)] Mercier, C. & Trottet, G. 1997, ApJ, 474, L65
- [Messerotti, Nonino & Zlobec (1985)] Messerotti, M., Nonino, M., & Zlobec, P., 1985, Mem. Soc. Astron. Italiana, 56, 795
- [Messmer & Benz (2000)] Messmer, P. & Benz, A. O., 2000, A&A, 354, 287
- [Meszarosova et al. (2002)] Meszarosova, H., Veronig, A., Zlobec, P., & Karlický, M., 2002 Proc. 10th European Solar Physics Meeting, "Solar Variability: From Core to Outer Frontiers", Prague, Czech Republic, 9-14 September 2002 (ESA SP-506, December 2002), 1, 347.
- [Miller et al. (1997)] Miller et. al., 1997, J. Geophys. Res., 102, 14631
- [Moon et al. (2001)] Moon, Y., Choe, G. S., Yun, H. S., & Park, Y. D. 2001, JGR, in press
- [Nita et al. (2002)] Nita, G. M., Gary, D. E., Lanzerotti, L. J., & Thomson, D. J., 2002, ApJ, 570, 423
- [Nita, Gary & Lee (submitted)] Nita, G. M., Gary, D. E., & Lee, J.
- [Parnell & Jupp (2000)] Parnell, C. E. & Jupp, P. E. 2000, ApJ, 529, 554
- [Petrosian (1981)] Petrosian, V., 1981, ApJ, 251, 727

- [Platonov & Fleishman (2001)] Platonov, K. Yu., & Fleishman, G. D., 2001, *Astron. Zh.*, 78, 238 (transl.: *Astronomy Repts.*, 45, 203)
- [Priest (1981)] Priest, E. R., 1982, *Solar Magnetohydrodynamics*, New York: Gordon and Breach
- [Priest & Forbes (2002)] Priest, E. R., & Forbes, T. G., 2002, *ARA&A*, 10 (4), 313
- [Ramaty (1994)] Ramaty, R., Schwarz, R. A., Enome, S., and Nakajima, H., 1994, *ApJ*, 436, 941
- [Ramaty (1969)] Ramaty, R., 1969, *ApJ*, 158, 753
- [Razin (1960a)] Razin, V. A., 1960a, *Izv. VUZov Radiofizika*, 3, 584
- [Razin (1960b)] Razin, V. A., 1960b, *Izv. VUZov Radiofizika*, 3, 921
- [Rosner & Vaiana (1978)] Rosner, R., Vaiana, G. S., 1978, *ApJ*, 222, 1104
- [Sharma & Vlahos (1984)] Sharma, R.R., & Vlahos, L., 1984, *ApJ*, 280, 405
- [Sharma, Vlahos & Papadopoulos (1982)] Sharma, R.R., Vlahos, L., & Papadopoulos, K., 1982, *A&A*, 112, 377
- [Shimizu & Tsuneta (1997)] Shimizu, T., & Tsuneta, S. 1997, *ApJ*, 486, 1045
- [Silva (1995)] Silva, A. V. R., 2000, Ph.D.Thesis, University of California at Berkely
- [Silva, Wang & Gary (2000)] Silva, A. V. R., Wang, H., Gary, D. E., 2000, *ApJ*, 545, 1116
- [Stähli & Magun (1986)] Stähli, M., & Magun, A., 1986, *Sol. Phys.*, 104, 117
- [Stähli, Gary & Hurford (1989)] Stähli, M., Gary, D. E., & Hurford, G. J., 1989, *Sol. Phys.*, 120, 351
- [Stähli, Gary & Hurford (1990)] Stähli, M., Gary, D. E., & Hurford, G. J., 1990, *Sol. Phys.*, 125, 343
- [Stepanov (1978)] Stepanov, A.V., 1978, *AZh Pis'ma*, 4, 193
- [Stupp (2000)] Stupp, A., 2000, *MNRAS*, 311, 251
- [Svestka (1976)] Svestka, Z., 1976, *Solar Flares*, Dordrecht: Reidel
- [Takakura (1972)] Takakura T., 1972, *Sol. Phys.*, 26, 151
- [Takakura & Kai (1961)] Takakura, T., & Kai, K., 1961, *PASJ*, 13, 94
- [Takakura & Kai (1966)] Takakura, T., & Kai, K., 1966, *PASJ*, 18, 57
- [Tanaka (1982)] Tanaka, K., Watanabe, T., Nishi, K., & Akita, K., 1982, 254, 59

- [Tandberg-Hanssen & Emslie (1988)] Tandberg-Hanssen, E., Emslie, A. G., 1988, *The physics of solar flares*, Cambridge and New York, Cambridge University Press
- [Trimble & Aschwanden (2003)] Trimble, V., & Aschwanden, M. J., 2003, *PASP*, 115 (807), 514
- [Twiss (1954)] Twiss, R.Q., 1954, *Philos. Mag.*, 45, 249
- [Vlasov, Kuznetsov & Altyntsev (2002)] Vlasov, V. G., Kuznetsov, A. A., & Altyntsev, A. T., 2002, *A&A*, 382, 361
- [Wang, Yan & Fu (2002)] Wang, S.J., Yan, Y.H., & Fu, Q., 2002, *Sol. Phys.*, 209, 185
- [Wheatland (2000a)] Wheatland, M. S., 2000, *ApJ*, 532, 1209
- [Wheatland (2000b)] Wheatland, M. S., 2000, *ApJ*, 536, L109
- [Wheatland & Glukhov (1998)] Wheatland, M. S. & Glukhov, S., 1998, *ApJ*, 494, 858
- [Wheatland & Sturrock (1996)] Wheatland, & Sturrock, 1996, *ApJ*, 471, 1044
- [White et al. (2003)] White, S. M., Krucker, S., Shibasaki, K., Yokoyama, T., Shimojo, M.; Kundu, M. R., 2003, *ApJ*, 595, L111
- [Wiehl et al. (1985)] Wiehl, H., Batchelor, D. A., Crannel, C. J., Dennis, B. R., Price, P. N., Magun, A., 1985, *Sol. Phys.*, 96, 339
- [Winglee & Dulk (1986)] Winglee, R.R., & Dulk, G.A., 1986, *Sol. Phys.*, 104, 93
- [Winglee, Dulk & Pritchett (1988)] Winglee, R.R., Dulk, G.A., & Pritchett, P.L., 1988, *ApJ*, 328, 809
- [Zlobec & Karlický (1998)] Zlobec, P., & Karlický, M., 1998, *Sol. Phys.*, 182, 477